

University of Mississippi

eGrove

Electronic Theses and Dissertations

Graduate School

2012

Advanced Design Methodologies and Novel Applications of Reflectarray Antennas

Payam Nayeri

Follow this and additional works at: <https://egrove.olemiss.edu/etd>



Part of the [Electromagnetics and Photonics Commons](#)

Recommended Citation

Nayeri, Payam, "Advanced Design Methodologies and Novel Applications of Reflectarray Antennas" (2012). *Electronic Theses and Dissertations*. 207.

<https://egrove.olemiss.edu/etd/207>

This Dissertation is brought to you for free and open access by the Graduate School at eGrove. It has been accepted for inclusion in Electronic Theses and Dissertations by an authorized administrator of eGrove. For more information, please contact egrove@olemiss.edu.

ADVANCED DESIGN METHODOLOGIES
AND NOVEL APPLICATIONS OF
REFLECTARRAY ANTENNAS

A Dissertation
presented in partial fulfillment of requirements
for the degree of Doctor of Philosophy
in Engineering Science
The University of Mississippi

by

PAYAM NAYERI

July 2012

Copyright Payam Nayeri 2012

ALL RIGHTS RESERVED

ABSTRACT

Reflectarray antennas combine the numerous advantages of printed antenna arrays and reflector antennas and create a hybrid high-gain antenna with a low-profile, low-mass, and diversified radiation performance. Reflectarrays are now emerging as the new generation of high-gain antennas for long-distance communications. In this dissertation, some advanced concepts demonstrating novel features of reflectarray antennas are presented.

- First, various approaches for radiation analysis of reflectarray antennas are described and implemented. Numerical results are then presented for a variety of systems and the advantages, limitations, and accuracy of these approaches are discussed and compared with each other.
- A broadband technique by using sub-wavelength elements is proposed and prototypes are fabricated and tested. This technique enables the reflectarray to achieve a significant bandwidth improvement with no additional cost.
- Infrared reflectarrays antennas are studied for possible applications in concentrating solar power systems. Material losses, an important design issue at infrared frequencies, are investigated and reflectarrays consisted of dielectric resonant elements are proposed with low-loss features at infrared.
- Multi-beam reflectarray antennas are studied and it is demonstrated that by optimizing the phase of the elements, a desirable multi-beam performance can be achieved using a single-feed. Local and global phase-only optimization techniques have been

implemented. Two Ka-band quad-beam prototypes with symmetric and asymmetric beams have been fabricated and tested.

- Different approaches for beam-scanning with reflectarray antennas are also reviewed and it is shown that for moderately wide angle beam-scanning, utilizing a feed displacement technique is more suitable than an aperture phase tuning approach. A feed displacement beam-scanning design with novel aperture phase distribution is proposed for the reflectarray antenna, and is further optimized to improve the performance. A high-gain Ka-band prototype achieving 60 degrees scan range with side-lobe levels below 15 dB is demonstrated.
- The feasibility of designing reflectarray antennas on conformal surfaces is also studied numerically. A generalized analysis approach is presented and the radiation performance of reflectarray antennas on singly-curved conformal cylindrical platforms are studied and compared with their planar counterpart. It is revealed that conformal reflectarray antennas are a suitable choice for a high-gain antenna where curved platforms are required.

In summary, different challenges in reflectarray analysis and design are addressed in this dissertation. On the element design challenges, bandwidth improvement and infrared operation of reflectarray antennas have been studied. On the system level challenges, multi-beam designs, beam-scanning performance, and conformal platforms have been investigated. Several prototypes have been fabricated and tested, demonstrating the novel features and potential applications of reflectarray antennas.

ACKNOWLEDGMENTS

This dissertation would not have been possible without the help, advice, and encouragement of many people whom it is my pleasure to thank them. I am eternally grateful to my parents for their constant support and encouragement throughout my education. I am greatly indebted to my advisors, Professor Fan Yang and Professor Atef Z. Elsherbeni, for their support and selfless efforts in advising me during my Ph.D. studies. Their in-depth knowledge in this field and their encouragement throughout my studies at the University of Mississippi have been the key components that helped me in completing this dissertation. I would like to thank Professor Yahya Rahmat-Samii, and Professor Glenn D. Boreman for their collaboration. I would also like to thank Professor Allen W. Glisson, Professor Richard K. Gordon, and Professor Gerard Buskes for serving as my advisory committee. Thanks are also given to Dr. Ang Yu, Dr. Chye Hwa Loo, Mr. Martye Hickman, and Mr. Junling Zhao for their technical support.

TABLE OF CONTENTS

I.	Introduction	1
1.1	An Overview of Reflectarray Antenna Development and State of the Art Research.....	1
1.2	Contributions of this Dissertation.....	3
II.	Design and Radiation Analysis of Reflectarray Antennas.....	6
2.1	Overview of Reflectarray Antenna Design.....	6
2.2	Phase Distribution on Reflectarray Aperture.....	8
2.2.1	Element Design for Reflectarray Antennas.....	8
2.2.1.1	Full-Wave Simulation Models.....	10
2.2.1.2	Analytical Models.....	11
2.2.2	Phasing Element Selection for Reflectarray Antennas.....	12
2.2.2.1	Aperture Phase Requirement and Element Selection.....	12
2.2.2.2	Sources of Phase Error in Reflectarray Antenna Design.....	14
2.3	Radiation Analysis of Reflectarray Antennas.....	16
2.3.1	Feed Antenna and Aperture Illumination.....	16
2.3.1.1	Idealized Radiation Patterns of Horn Feeds.....	16
2.3.1.2	Feed Positioning, Illumination and Aperture Efficiency.....	17
2.3.1.3	Fields on the Reflectarray Aperture.....	19
2.3.2	Array Theory Approach for Radiation Analysis.....	20
2.3.3	Aperture Field Approach for Radiation Analysis.....	23
2.3.4	Far-Field Parameters of Interest.....	27
2.3.4.1	Radiation Patterns in the Principal Planes.....	27
2.3.4.2	Co- and Cross-Polarized Radiation Patterns.....	30
2.3.4.3	Antenna Directivity and Gain.....	31

2.3.5	Spectral Transforms and Computational Speedup.....	36
2.4	Design Examples and Comparison of Analysis Approaches.....	38
2.4.1	A Reflectarray Antenna with a Broadside Beam	39
2.4.2	A Reflectarray Antenna with an Off-Broadside Beam	42
2.4.3	Comparison of Calculated Directivity versus Frequency.....	45
2.4.4	Comparison of Classical Methods and Full-Wave Simulations.....	46
2.4.5	Considerations for the Array Theory and Aperture Field Analysis Approaches...50	
III.	Sub-Wavelength Element Technique for Bandwidth Improvement	53
3.1	Bandwidth Limitation in Reflectarray Antennas.....	54
3.2	Reflection Properties of Sub-Wavelength Elements.....	56
3.3	Phase Error Analysis of Sub-Wavelength Elements.....	58
3.3.1	Element Phase Error Analysis.....	58
3.3.2	Aperture Phase Error Analysis.....	61
3.4	Design of <i>Ka</i> -band Reflectarrays Using Sub-Wavelength Elements.....	64
3.4.1	Prototype Fabrication.....	64
3.4.2	Measurement of Prototypes.....	65
3.5	<i>Ka</i> -band Reflectarrays Using Double-Layer Sub-Wavelength Elements.....	70
3.5.1	Fabrication Considerations and the Multi-Layer Technique.....	70
3.5.2	Phase Error Analysis and Bandwidth Study.....	73
IV.	THz/Infrared Reflectarray Antennas.....	77
4.1	Reflectarray Antennas for Concentrating Solar Power Systems	77
4.2	Properties of Materials at THz/Infrared Frequencies.....	79
4.2.1	Optical Measurements and Electromagnetic Parameters.....	79
4.2.2	Calculating Drude Model Parameters for Conductors	82
4.3	Losses in Reflectarray Elements at THz/Infrared Frequencies.....	85

4.3.1	Conductor Losses.....	86
4.3.2	Dielectric Losses.....	91
4.3.3	Effect of Losses on Reflection Properties of Elements.....	92
4.4	Circuit Model Analysis.....	93
4.4.1	Circuit Theory and Loss Study.....	93
4.4.2	Zero-Pole Analysis of Element Performance	94
4.5	Dielectric Resonator Elements for THz/Infrared Frequencies.....	96
4.5.1	Limitations of Conventional Patch Element Designs.....	96
4.5.2	Low-Loss Dielectric Resonator Reflectarray Elements.....	97
4.5.3	Design of a CSP System Using Reflectarray Elements.....	99
V.	Single-Feed Multi-Beam Reflectarray Antennas.....	104
5.1	Introduction to Multiple Beam High-Gain Reflectarray Antennas	105
5.2	Direct Design Methods.....	105
5.2.1	Geometrical Approach for Multi-Beam Design.....	105
5.2.2	Superposition Approach for Multi-Beam Design.....	108
5.2.3	Comparison of Direct Design Methods for Multi-Beam Reflectarray.....	110
5.3	Optimization Methods for Single-Feed Multi-Beam Reflectarray Antenna Design.....	113
5.3.1	Alternating Projection Method.....	113
5.3.2	Particle Swarm Optimization.....	118
5.4	Design and Measurement of Single-Feed Multi-Beam Reflectarray Antennas.....	125
5.4.1	A Quad-Beam <i>Ka</i> -band Reflectarray with Symmetric Beams.....	125
5.4.2	A Quad-Beam <i>Ka</i> -band Reflectarray with Asymmetric Beams.....	131
VI.	Beam-Scanning Reflectarray Antennas.....	134
6.1	Introduction to High-Gain Beam Scanning Antennas	134
6.2	Beam-Scanning Approaches for Reflectarray Antennas.....	135

6.2.1	Feed Displacement Approach.....	136
6.2.2	Aperture Phase Tuning Approach.....	137
6.2.3	Summary.....	142
6.3	Feed Displacement in Reflectarray Antennas.....	143
6.3.1	Axial and Lateral Feed Displacement.....	143
6.3.2	Feed Displacement along a Circular Arc.....	147
6.4	Bifocal Reflectarray Antennas.....	148
6.4.1	Principles of a Bifocal System Design.....	148
6.4.2	Scanning Properties of Bifocal Reflectarrays.....	150
6.5	Optimization Approach for Beam-Scanning Reflectarray Design.....	153
6.6	Design and Measurement of <i>Ka</i> -Band Beam-Scanning Reflectarray Antennas.....	158
6.6.1	Element Selection and Radiation Performance Analysis.....	158
6.6.2	Fabrication and Measurement of Prototypes.....	163
VII.	Conformal Reflectarray Antennas.....	170
7.1	Advantages of Conformal Array Antennas.....	170
7.2	Radiation Analysis of Conformal Reflectarray Antennas.....	171
7.2.1	Radiation Pattern Calculations.....	171
7.2.2	Gain Calculations	175
7.3	Radiation Characteristics of Singly-Curved Conformal Reflectarrays.....	176
7.3.1	Radiation Patterns in the Principal Planes.....	177
7.3.2	Effects of Conformal Surface on Beamwidth and Side-lobe level.....	178
7.3.3	Gain and Bandwidth of Conformal Reflectarray Antennas.....	181
7.4	Beam-Scanning Properties of Conformal Reflectarrays.....	182
VIII.	Conclusion.....	185
8.1	Contributions of this Dissertation.....	185

8.2 Future Work.....	187
Bibliography.....	189
Appendix I: Full-Wave Simulation of Reflectarray Phasing Elements.....	196
AI.1 Method of Moments (Ansoft Designer)	197
AI.2 Finite Element Method (Ansys HFSS)	198
AI.3 Finite Integral Time-Domain Method (CST MWS)	200
AI.4 Simulation Results for a Ka-band Patch Element.....	201
Appendix II: Mask Generation for Reflectarray Antennas.....	203
AII.1 Data Files for Reflectarray Elements.....	204
AII.2 DXF Mask Generation.....	205
Appendix III: Measured Horn Antenna Patterns and Analytical Models.....	208
AIII.1 Ka-band Horn Antenna Measurement.....	209
AIII.2 Expanded Analytical Model (Co- and Cross-Polarization Modeling)	211
Appendix IV: Design of a Potter Horn Antenna for Reflectarray Feed.....	213
AIV.1 Basic Properties of Potter Horn Antennas.....	214
AIV.2 An Optimized Design with a $\text{Cos}^{6.5}\theta$ Radiation Pattern.....	216
Appendix V: Full-Wave Simulation of Reflectarray Antennas using FEKO.....	219
AV.1 Modeling the Reflectarray Antenna in FEKO and Far-Field Radiation Patterns....	220
AV.2 Near-Field Study and Aperture Phase Diagnostics.....	224

CHAPTER I

INTRODUCTION

1.1 An Overview of Reflectarray Antenna Development and State of the Art Research

Since the revolutionary breakthrough of printed circuit technology in the 1980's, microstrip reflectarrays have emerged as the new generation of high-gain antennas for long distance communications. They are similar in principal to parabolic reflectors, while the bulky curved surface of the parabolic reflector is replaced with a planar antenna array, which results in a low-profile, low-mass, and low-cost antenna.

The concept of the reflectarray was initially introduced using waveguide technology in the 60's [1]. Later in the 70's the spiraphase reflectarray was developed [2], but the reflectarray didn't receive much attention until the development of microstrip reflectarrays in the late 80's [3]. The elements of the reflectarray are designed to reflect the EM wave with a certain phase to compensate for the phase delay caused by the spatial feed. The phase shift of the elements is realized using various methods such as variable size elements, phase-delay lines, and element rotation techniques. The infinite array approach is used to calibrate the element phase versus element change [4]. Due to the very large number of elements involved in a reflectarray, full-wave simulation of the entire reflectarray antenna is still challenging. On the other hand, different theoretical models have been developed for the analysis of reflectarrays, such as the array theory formulation and the aperture field analysis technique, which show a good agreement with measured results. Moreover, implementing the spectral transform in these calculations

allows for fast calculation of the radiation characteristics of the antenna, which is a considerable advantage for synthesis design problems using iterative procedures.

Single and multi-layer reflectarrays have been designed to achieve broad band and multi-band performance from microwave frequencies up to the THz range [5]. Considerable improvements have been made to these designs over the years and many practical designs have been demonstrated. One of the main challenges in reflectarray designs is improving the bandwidth of the antenna, which is the major drawback of all printed structures [6]. Different bandwidth improvement techniques such as using multi-layer designs [7], true time-delay lines [8], and sub-wavelength elements [9] have been studied and bandwidths of more than 20% have been reported.

On the other hand, the direct control of the phase of every element in the array allows multi-beam performance with single or multiple feeds [10]. The design of contoured beam reflectarrays is also a challenging field [11]. A phase-only synthesis process is used to obtain the required element phase shift from any given mask. Multi-feed multi-beam contoured beam designs have been demonstrated [12]; however, the performances of these designs are slightly inferior to the shaped beam parabolic reflectors. Another advantage of reflectarrays is the ability of the antenna to scan the main beam to large angles off broadside. Beam scanning reflectarrays are designed by using low-loss phase shifters in every element of the array [13]. These beam scanning reflectarrays require a switch board to control the main beam direction and are well suited for radar applications and some models have been demonstrated; however, considerable challenges lie in improving the performance of these beam scanning antennas.

In addition to the numerous capabilities and potentials reflectarray antennas have demonstrated, a great deal of interest now is the practical implementation of reflectarray

antennas for space applications. Since the common considerations for space antennas are size, weight, and power (SWaP), because of limitations imposed by the satellite launch capabilities [14], the reflectarray antenna shows significant advantages over conventional high-gain space antennas, which are typically reflectors/lenses and arrays. These momentous promises make the reflectarray antenna a suitable low-cost choice for the new generation of space antennas.

1.2 Contributions of this Dissertation

In the second chapter, the basics of reflectarray antenna design and analysis are presented. Various analysis methods are described and the advantages, limitations and accuracy of each method are discussed. Chapters 3 to 7 summarize the main contributions of our work on reflectarray antennas.

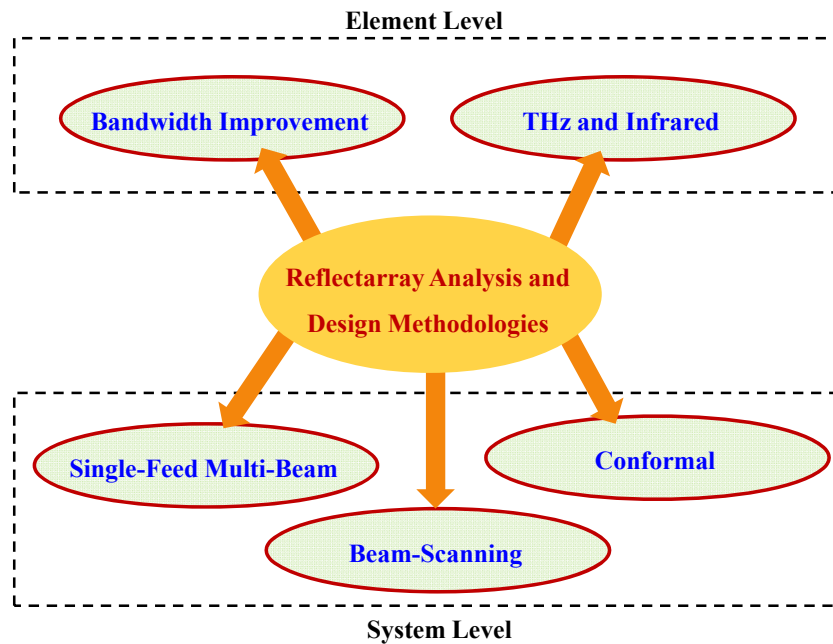


Fig. 1-1 A pictorial view of the contributions of this dissertation.

In chapter 3, a phase error analysis method to study the bandwidth of reflectarray antennas is

proposed. The sub-wavelength element technique for bandwidth improvement is investigated using this analysis approach and Ka-band prototypes are fabricated and tested, demonstrating the bandwidth improvement capability of this technique. Furthermore, to mitigate fabrication challenges in the design of sub-wavelength elements at high frequencies, a novel two-layer sub-wavelength configuration is proposed. Reflectarray designs at infrared (IR) frequencies are investigated in chapter 4. Material losses at the short-wavelength region are an important consideration in reflectarray designs. Both conductor and dielectric losses of reflectarray elements at high frequencies are studied, and an equivalent circuit model is proposed to understand this phenomenon. Based on the investigation, alternative design methods for infrared reflectarrays are suggested to lower the loss effect.

The contributions in the first two chapters can be classified into the element level problems. Chapters 5 to 7 in this dissertation are the novel designs proposed on system level challenges in reflectarray design. In chapter 5 various designs of multi-beam reflectarray antennas are first studied and then two single-feed quad-beam prototypes are then fabricated and tested. The first prototype is designed to achieve four symmetric beams, while the second prototype was designed to achieve four beams with asymmetric beam directions and beam levels. To the authors' knowledge, this is the first design of a single-feed multi-beam reflectarray antenna with asymmetric beams. In chapter 6, first different approaches for beam-scanning with reflectarray antennas are reviewed. It is shown that for moderately wide angle beam-scanning, utilizing the feed displacement technique is more suitable than the aperture phase tuning approach. A novel feed displacement beam-scanning design with a novel aperture phase distribution is proposed for the reflectarray antenna, and is further optimized to improve the performance. A high-gain Ka-band prototype achieving 60 degrees scan range with side-lobe levels below 15 dB is

demonstrated. To the authors' knowledge, this is the first design of a single-reflector high-gain beam scanning reflectarray antenna using the feed displacement technique. In chapter 7, the feasibility of designing reflectarray antennas on conformal surfaces is studied numerically. A generalized analysis approach is presented to compute the radiation pattern of conformal reflectarray antennas, and reflectarray antennas on singly-curved conformal cylindrical platforms are studied. The performances of these conformal reflectarrays are compared with their planar counterpart and it is shown that a conformal reflectarray antenna can be a suitable choice for a high-gain antenna where curved platforms are required.

CHAPTER II

DESIGN AND RADIATION ANALYSIS OF REFLECTARRAY ANTENNAS

In this chapter detailed descriptions of the practical approaches in designing an efficient reflectarray are discussed. First the basics of aperture phase distribution and phasing element selection for reflectarray antennas are described. Next two methods for analysis of reflectarray antennas radiation performance, array theory and aperture field, are described and the advantages and limitations for each method are discussed. Finally numerical results are presented for different reflectarray configurations using these classical approaches and compared with full-wave simulation results. The good agreement between these classical analysis methods and full-wave simulations show that these approaches are time-efficient methods which can accurately calculate the reflectarray antenna pattern shape, main beam direction, beam-width, side-lobe and cross-polarization level. As such, these methods can be efficient tools for antenna engineers to design and analyze reflectarray antennas.

2.1 Overview of Reflectarray Antenna Design

Designing a reflectarray antenna is usually carried out in several stages, and as such can be viewed as a system design. The main stages in this process are: designing the phasing elements, aperture selection and phase distribution design, and feed antenna design and positioning. In addition for most designs, several optimizations are required to satisfy the system requirements. While the optimization goals vary depending on the design requirements, the parameter that is

optimized is usually the phase of the reflectarray elements. A systematic design procedure for reflectarray antenna design is given in Fig. 2-1.

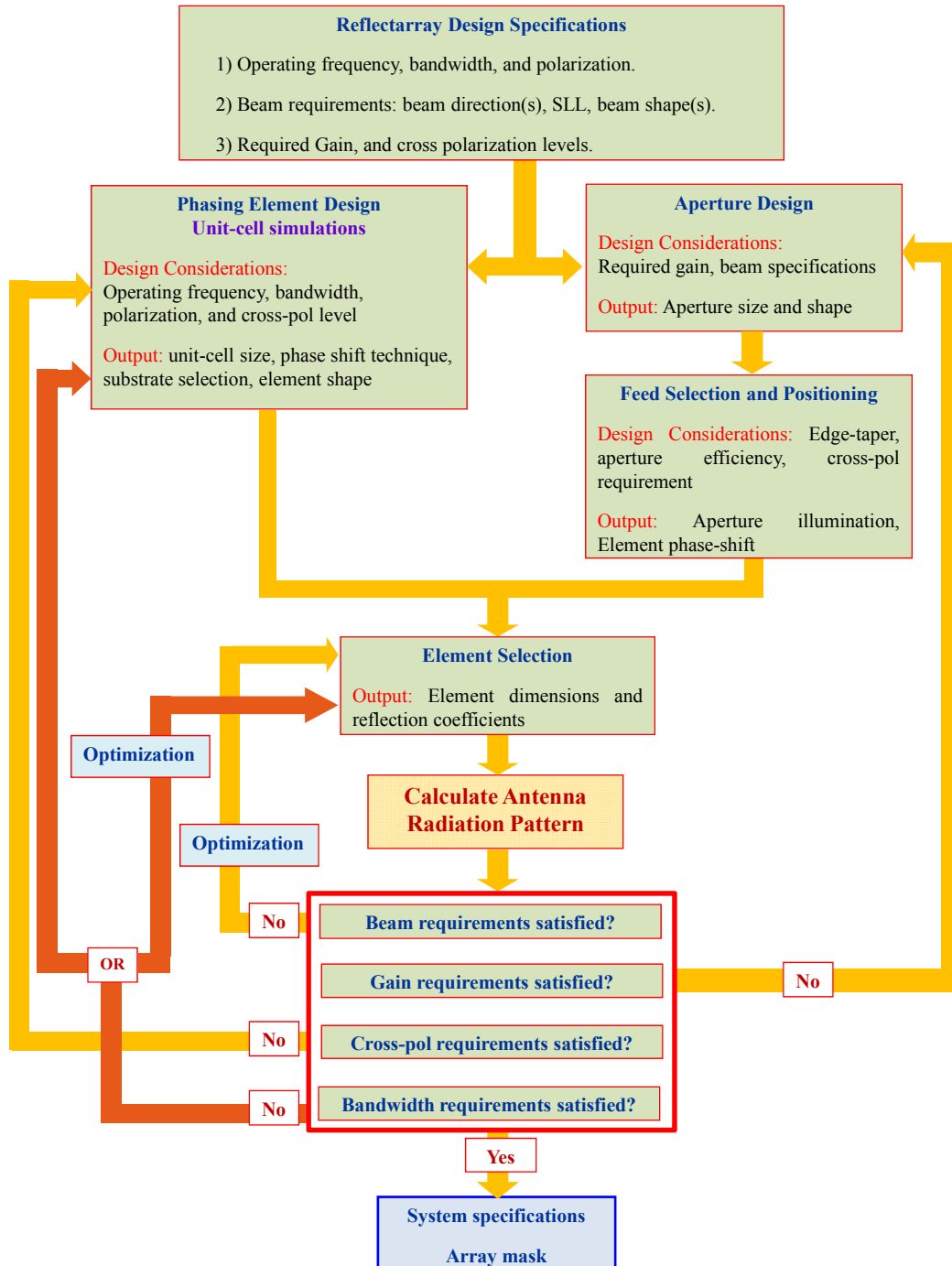


Fig. 2-1 The road map for reflectarray antenna design.

Once the reflectarray design specifications are obtained, two separate steps must be carried out first: (1) designing the phasing elements, and (2) designing the reflectarray aperture phase distribution. A feed antenna is then designed (or selected) and positioned according to the requirements of the design. With the feed and aperture specified, the phasing elements are then selected based on the phase requirements. In the next step the radiation pattern of the initial design is computed at the design frequency and the beam requirements, gain level and cross-polarization levels are compared with the design specifications. If these requirements are not satisfied, optimization routines are implemented to obtain the desired performance. In the final step, the frequency responses of the selected phasing elements are obtained and the reflectarray bandwidth is calculated. Similarly if the bandwidth specification is not satisfied, another optimization or a new element design needs to be carried out here. Once all design requirements are satisfied, the final reflectarray mask and system specifications can be obtained.

2.2 Phase Distribution on Reflectarray Aperture

2.2.1 Element Design for Reflectarray Antennas

A key feature of microstrip reflectarray implementation is how the individual elements are designed to scatter electromagnetic waves with the desired phases. Different methods have been demonstrated over the years to control the reflection phase of the elements such as microstrip patches of the same size with stubs of variable length, printed dipoles or patches with variable size, and element rotation techniques, which are applicable for circularly polarized designs. In the first technique, the electrical length of the stub controls the element's reflected phase. In the variable size technique, a small shift in the resonant frequency of an element is introduced, which has the effect of changing the phase of the reflected field. For circularly polarized designs,

the element is rotated from its original position by ψ degrees, which will advance or delay the reflection phase of the element (depending on the rotation direction) by 2ψ degrees.

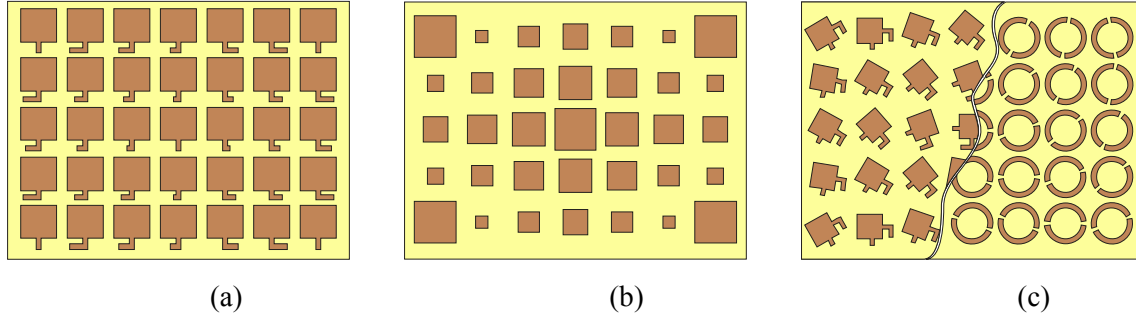


Fig. 2-2 Phase change schemes for reflectarray elements: (a) phase/time-delay lines, (b) variable size elements, (c) element rotation.

Regardless of the choice of the phasing elements, one of the most important parts of the reflectarray analysis and design is the accurate characterization of the phasing elements. Considering practical limitations in full wave simulation of a total reflectarray antenna system, the reflection phase of the phasing elements is obtained by some degree of approximation. A first order approximation is by assuming that no coupling exists between the reflectarray phasing elements and the radar cross section (RCS) of a single patch element is considered for each phasing element. A more accurate approximation assumes that the reflection from an individual patch surrounded by patches of different sizes can be approximated by the reflection from an infinite array of patches of equal size. This approximation is quite acceptable if the patch dimensions don't vary significantly between adjacent elements. Another argument for the validity of this approach is that many reflectarray antennas have been demonstrated using this technique. Ideally, if it is computationally possible, a full-wave simulation of an entire reflectarray antenna will give an accurate characterization of the performance of the phasing elements in the real environment.

The reflection characteristics of the reflectarray phasing elements are obtained from full-wave electromagnetic analysis or analytical circuit models. It should be noted that for a reflectarray antenna design, the reflection coefficients of the phasing elements should be calculated at the top surface of the element. To obtain the required reflection characteristics of the phasing elements, usually a parametric study has to be performed depending on the phase change scheme, which should also take into account the fabrication capabilities. In most cases it is sufficient to assume normal incidence for the unit-cell analysis, however, depending on the design, it might be necessary to model the element excitation angles accurately.

2.2.1.1 Full-Wave Simulation Models

Three models are available for reflectarray element analysis that can take into account the mutual coupling between the elements by means of a periodic approximation.

Unit-cell waveguide approach: In this method the element is placed in an idealized TEM waveguide. The side boundaries are set as perfect electric conductor (PEC) and perfect magnetic conductor (PMC) based on the direction of the incident electric field. The incident electric field (modeled as a plane wave) is normal to the PEC boundaries. For a normally incident wave, this configuration is equivalent to an infinite array [15].

Infinite array approach: In this method the element is simulated in a unit-cell with linked periodic boundary conditions [16]. This approach is more general than the waveguide approach, since it can mimic the periodic environment of the element more accurately, and can be used to obtain the reflection properties for oblique excitation angles. The excitation can be a plane wave or a Floquet port [17].

Waveguide Simulator approach: The element (or elements) is placed in a rectangular

waveguide where mutual coupling between the elements is taken into account as a consequence of the image principle. The main advantage of this approach is that it can also be implemented experimentally [18].

Most electromagnetic (EM) simulators have the capability to analyze the reflection characteristics of reflectarray phasing elements. While the analysis model that can be used generally depends on the software capabilities, the infinite array approach is usually the conventional method for reflectarray element analysis. More discussion on modeling reflectarray elements with commercial software is given in Appendix I.

2.2.1.2 Analytical Models

The unit-cell structure can also be modeled as a transmission line circuit. In this approach, first one has to determine the grid impedance for the periodic surface. Once the impedance of the surface (Z_s) is known, the reflection coefficient Γ of an incident plane wave on the unit-cell can be calculated using transmission line theory, i.e.

$$\Gamma = \frac{Z_s - Z_o}{Z_s + Z_o}, \quad (2-1)$$

where Z_o is the free space impedance. As an example, for square patch elements, the metallic patches act as parallel capacitors with the adjacent cells while the short circuited unit-cell ground can be modeled as a parallel inductor. This circuit model has previously been implemented for lossless reactive impedance substrates [19]. The loss in the dielectric substrate can be modeled by a parallel resistor, i.e., the total unit-cell is modeled as a parallel RLC circuit. To model the conductor loss in the patch, a resistor will be series connected to the capacitor [20]. The circuit-model for these elements is given in Fig. 2-3.

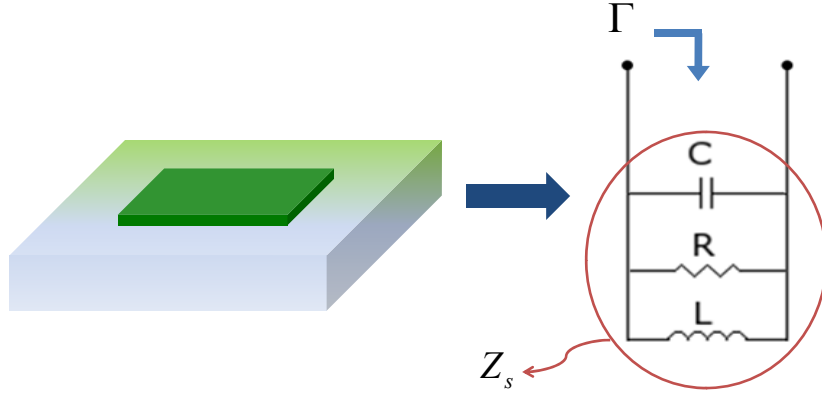


Fig. 2-3 The circuit model for the unit-cells.

It is implicit that the main challenge in the circuit model analysis is the correct analytical calculation of the transmission line parameters for different elements. It is also possible to obtain these coefficients by designing a resonant circuit at the operating frequency and then tuning these values so that the circuit model reflection curves fit the curves obtained by the full wave unit-cell simulations. It should be pointed out that the circuit model analysis is general, and the transmission line parameters can also be obtained for oblique incidence angles.

2.2.2 Phasing Element Selection for Reflectarray Antennas

2.2.2.1 Aperture Phase Requirement and Element Selection

The reflection phase of a reflectarray element is designed to compensate for the spatial phase delay from the feed horn to that element; thus a certain phase distribution can be achieved on the reflectarray aperture so that the radiation beam will point at a specific direction. The geometry of the reflectarray system is given in Fig. 2-4. The reflection phase ψ_i of the i^{th} element is calculated as:

$$\psi_i = k_0 (R_i - \bar{r}_i \cdot \hat{r}_o) + \psi_0, \quad (2-2)$$

where R_i is the distance from the feed horn to the i^{th} element, \vec{r}_i is the position vector of the i^{th} element, and \hat{r}_o represents the main beam direction. A constant phase ψ_0 is added here, indicating that a relative reflection phase rather than the absolute reflection phase is required for reflectarray design. It should be noted that while (2-2) gives the required phase distribution on the aperture for a single beam scanned to any arbitrary direction, the phase distribution for multi-beam or shaped beam designs are obtained differently [21]. In all designs, however, the phasing elements of the reflectarray antenna must take into account the spatial phase delay ($k_0 R_i$) associated with the feed.

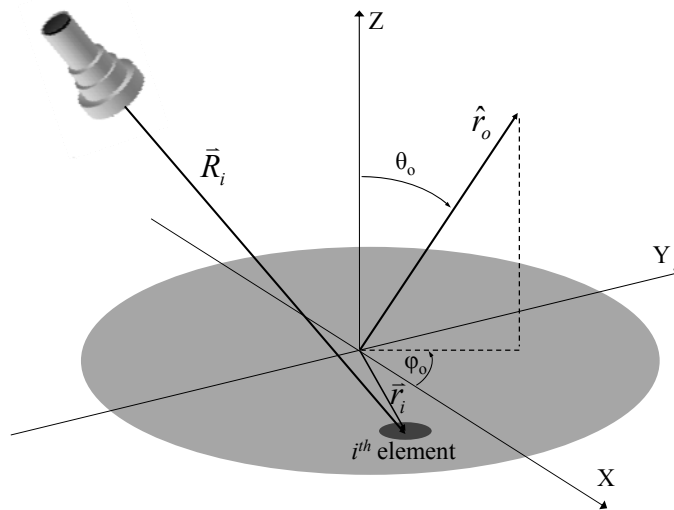


Fig. 2-4 The geometry of a reflectarray antenna.

Once the required element phase shift for every element on the reflectarray aperture is calculated, the phasing elements of the reflectarray can be selected using the phase versus element change curve which is obtained from the unit-cell analysis. While the shape of the curve generally depends on the element design scheme, generally this is an S-shaped curve with nonlinear relationship. A typical S-curve for reflectarray elements is given in Fig. 2-5.

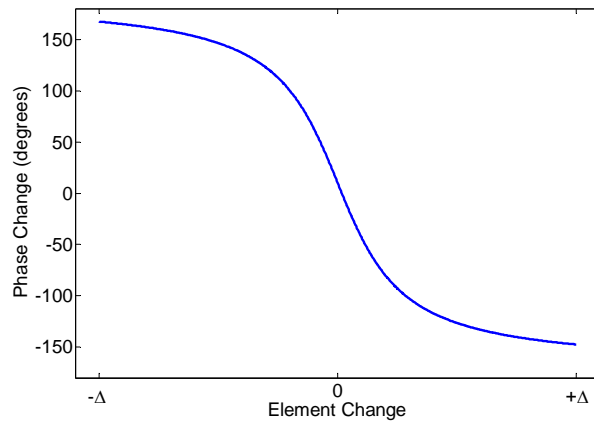


Fig. 2-5 Typical S-curve of a reflectarray element phase change versus element change.

The task is then to select the element which would provide the necessary phase shift. Once the dimensions or rotations of every element are known, the reflectarray mask can be generated. A typical data file for a reflectarray mask should include the location and dimensions of all the phasing elements on the aperture. More discussions on the mask design are given in Appendix II.

2.2.2.2 Sources of Phase Error in Reflectarray Antenna Design

The phasing elements of the reflectarray antenna are a key component in the design. Therefore it is important to note that the accuracy of the unit-cell data used for the design is susceptible to errors arising from the design method, fabrication, or approximations in the analysis. A brief description of each of these element errors is given here.

Quantization Errors: It is obvious that in practice, fabrication accuracy plays a significant role in the element's performance. The dimensions or rotations of the elements are changed by a certain amount depending on the fabrication precision, and as such, a continuous phase control is not possible. For each element on the aperture, a phasing element is selected that provides the closest quantized phase with respect to the ideal phase shift. The difference between the ideal

element phase and the quantized phase of the selected element is categorized as quantization error.

Phase Range Errors: Another important factor in element selection is the available phase range of the elements. Typically single layer phasing elements have a phase range below 360° . Although this problem can be avoided by using multi-resonance elements, if the phase range is smaller than the complete cycle, some elements will inevitably have unattainable phase shifts. While the element selection routine minimizes these errors by selecting the closest quantized values, these errors are in nature different from the quantization errors and are categorized as errors due to limited phase range.

Normal/Oblique Approximation: In most cases the reflection phase response of reflectarray elements are obtained under normal incidence approximation. While in many cases, especially for thin substrates, the effect of the oblique excitation angle on the reflection coefficients is small, this approximation is also a source of element error.

Infinite Array Approximation: As discussed earlier, the infinite array approach is used to obtain the unit-cell data, which means that the dimensions (or rotations) of the adjacent elements should be similar or at least very close. In conventional single-beam reflectarrays with variable size elements, the required phase, and therefore dimensions of adjacent elements, grow gradually in each Fresnel zone. When the zone is complete, a phase wrap is observed and the element dimension jumps from a maximum size to a minimum size or vice versa, which violates the periodic approximation and results in some error. Similar conditions are observed for other phase control schemes.

2.3 Radiation Analysis of Reflectarray Antennas

2.3.1 Feed Antenna and Aperture Illumination

The far-field radiation characteristics of a reflectarray antenna cannot be determined without a proper description of the feed characteristics. The reflectarray aperture illumination is dependent on the radiation pattern of the feed antenna and its position. In addition, an optimum illumination of the aperture increases the efficiency of the reflectarray antenna [22], thus it holds significant importance in the design.

2.3.1.1 Idealized Radiation Patterns of Horn Feeds

Usually a horn antenna is used as feed and its radiation pattern is modeled as a $\cos^q(\theta)$ function. The radiation pattern of an ideal feed horn [23] with a fixed phase center is given by

$$E^{Fx}(\theta, \varphi) = A_0 \left[\hat{\theta} C_E(\theta) \cos \varphi - \hat{\phi} C_H(\theta) \sin \varphi \right] \frac{e^{-jkr}}{r} \quad \text{for x polarized} \quad (2-3)$$

$$E^{Fy}(\theta, \varphi) = A_0 \left[\hat{\theta} C_E(\theta) \sin \varphi + \hat{\phi} C_H(\theta) \cos \varphi \right] \frac{e^{-jkr}}{r} \quad \text{for y polarized} \quad (2-4)$$

$$E^{Fcp}(\theta, \varphi) = A_0 e^{j\tau\varphi} \left[\hat{\theta} C_E(\theta) + \hat{\phi} j\tau C_H(\theta) \right] \frac{e^{-jkr}}{r} \quad \text{for circular polarized} \quad (2-5)$$

where A_0 is a complex constant and C_E and C_H are defined as

$$C_E(\theta) = (\cos \theta)^{q_E} \quad \text{E plane pattern of the horn} \quad (2-6)$$

$$C_H(\theta) = (\cos \theta)^{q_H} \quad \text{H plane pattern of the horn} \quad (2-7)$$

For the circular polarized feed horn pattern, the parameter τ determines the sense of polarization. For a left-handed (LH) CP feed $\tau = +1$ and for right-handed (RH) CP feed $\tau = -1$. Note that this equation represents a perfect circular polarized wave only in the main beam direction ($\theta = 0$) of the feed coordinate system. Away from this direction it is generally elliptically polarized unless

$q_E = q_H$. The shape of the pattern is controlled by q_E and q_H , which are determined by matching C_E and C_H to the measured pattern of the feed horn antenna.

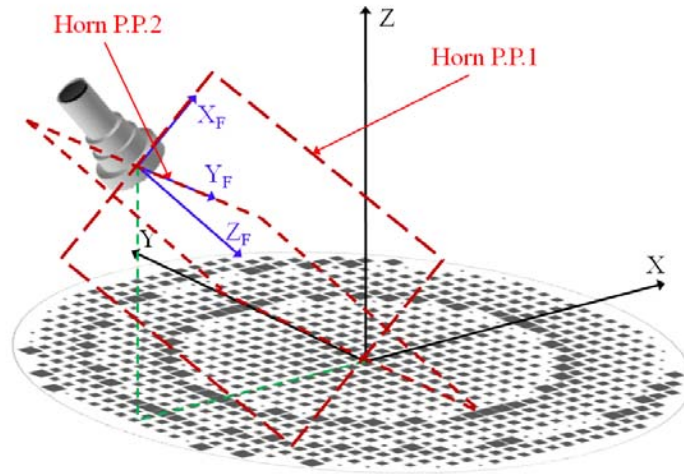


Fig. 2-6 The coordinate systems for the feed and reflectarray.

It should be noted that the coordinate variables used in equations (2-3) to (2-7) are defined with respect to the feed coordinate system (F), defined by axes X_F , Y_F , Z_F . Generally the definition of the E and H planes of the horn antenna depend on the polarization and orientation of the horn, however the principal planes (P. P.) of the horn are shown in Fig. 2-6.

2.3.1.2 Feed Positioning, Illumination and Aperture Efficiency

The correct positioning of the feed horn is of critical importance in reflector antenna design. The feed horn position controls the aperture efficiency of the reflectarray antenna which is directly related to the aperture illumination. The aperture efficiency used in this dissertation follows the approach described in [24]. While it is desirable to increase the aperture efficiency it is also critical to control the illumination at the array edges, i.e. the edge taper (ET). A high ET results in a strong diffraction at the array edges which will significantly deteriorate the

performance of the reflectarray antenna. Usually to minimize diffractions it is desirable to have an ET below -10 dB. The optimum feed horn position is then determined based on two criteria, first to control the ET in the design in order to minimize diffraction at the array edges, and second to achieve maximum aperture efficiency. It should be noted that with an offset feed the ET will not be uniform across the aperture. In addition, since the horn antenna radiation pattern is frequency dependent, aperture illumination and efficiency can be calculated as a function of frequency over the band of interest.

The efficiency analysis approach discussed here also provides the means to select the optimum shape for the reflectarray aperture. While in general it is possible to design rectangular or elliptical apertures, the common choices for a reflectarray antenna are squares and circles. To compare the effect of aperture shape on the efficiency of the reflectarray antenna we consider two designs: 1) a square $20\lambda \times 20\lambda$ aperture, and 2) a circular aperture with a diameter of 20λ , where both designs use a prime focus feed positioned with an F/D of 0.75. The efficiency of these two reflectarray systems is given in Fig. 2-7 as a function of q .

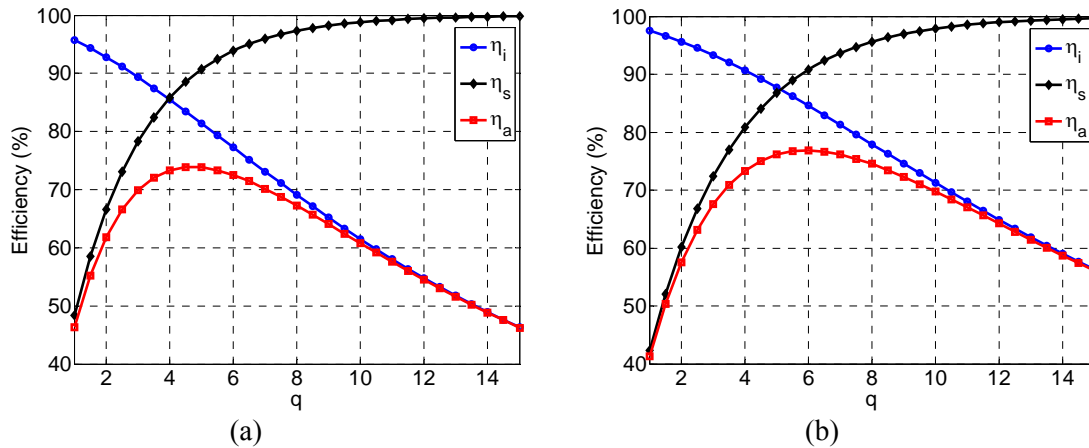


Fig. 2-7 Aperture efficiency of reflectarray antennas: (a) square aperture, (b) circular aperture.

First, the optimum q for the feed depends on the aperture shape; where in comparison square

apertures require a smaller value for q ; and second, circular apertures achieve a higher efficiency than square apertures. In the designs studied here the optimum value for q is 4.5 and 6.0, for square and circular apertures, which correspond to an aperture efficiency of 73.86%, and 76.83%, respectively. In general circular apertures achieve a higher efficiency due to the fact that the spherical wave front of the feed can be matched perfectly to a circular aperture, by selecting the optimum q . From this comparative study it can be seen that circular aperture reflectarrays will be preferable over square apertures due to efficiency considerations. In addition, square apertures also show higher side lobes in comparison with circular apertures, which is due to the fact that illumination of a square aperture is quite poor towards the edges. It is worthwhile to point out that in many practical cases where an available feed horn is to be used, not designed; the value of q is fixed and the optimum feed position (F/D) has to be determined for the reflectarray system.

2.3.1.3 Fields on the Reflectarray Aperture

The next step is to determine the field radiated by the feed at each reflectarray element in terms of the Cartesian components in the reflectarray coordinate system. First the incident field is calculated at the center point of each reflectarray element using (2-3) to (2-5) depending on the polarization of the feed. Note that in these equations r represents the radial distance from the phase center of the feed horn to each element in the array. Then the field is transformed into Cartesian components using the following equations

$$\begin{bmatrix} E_x^F \\ E_y^F \\ E_z^F \end{bmatrix} = \begin{bmatrix} \sin \theta^F \cos \varphi^F & \cos \theta^F \cos \varphi^F & -\sin \varphi^F \\ \sin \theta^F \sin \varphi^F & \cos \theta^F \sin \varphi^F & \cos \varphi^F \\ \cos \theta^F & -\sin \theta^F & 0 \end{bmatrix} \begin{bmatrix} 0 \\ E_\theta^F \\ E_\varphi^F \end{bmatrix} \quad (2-8)$$

In this equation (θ^F, ϕ^F) are the spherical angles of the reflectarray elements in the feed coordinate system. Since the spherical angles change with position of the element, this transformation is carried out for each element of the reflectarray.

Transformation from the feed coordinate to the reflectarray coordinates can be accomplished using the rotation functions described in [25]. The three functions **rotx(array, α)**, **roty(array, β)**, **rotz(array, γ)** rotate the Cartesian coordinates of the feed horn back to the array coordinate system. A flowchart of these transformations is given in Fig. 2-8. Here N_x and N_y are the number of elements in each direction on the reflectarray.

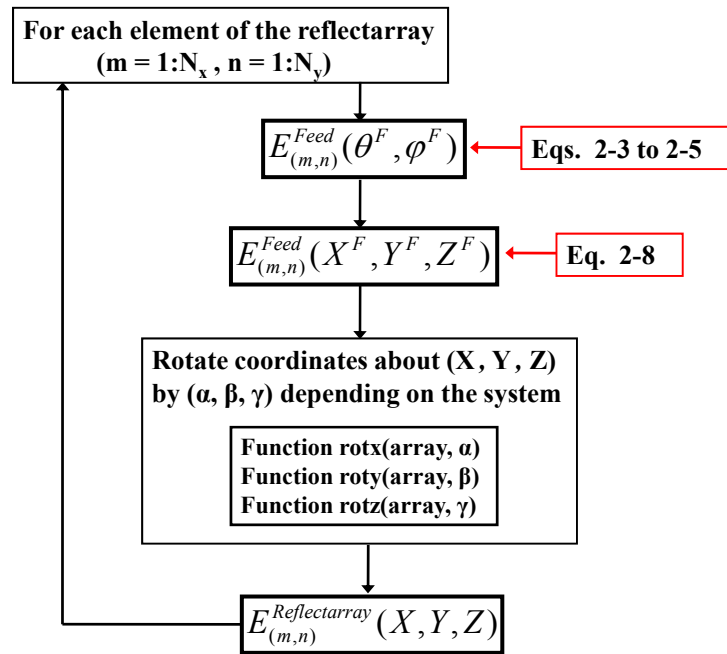


Fig. 2-8 Flowchart of the transformations from feed to array coordinates.

2.3.2 Array Theory Approach for Radiation Analysis

The conventional array theory can be implemented to calculate the far-field radiation pattern of the reflectarray antenna. The radiation pattern of a two-dimensional planar array with $M \times N$

elements can be calculated as

$$\begin{aligned}\vec{E}(\hat{u}) &= \sum_{m=1}^M \sum_{n=1}^N \vec{A}_{mn}(\hat{u}) \cdot \vec{I}(\vec{r}_{mn}), \\ \hat{u} &= \hat{x} \sin \theta \cos \varphi + \hat{y} \sin \theta \sin \varphi + \hat{z} \cos \theta,\end{aligned}\tag{2-9}$$

where A is the element pattern vector function, I is the element excitation vector function, and \vec{r}_{mn} is the position vector of the mn^{th} element [26]. The coordinate system for the reflectarray antenna is given in Fig. 2-9.

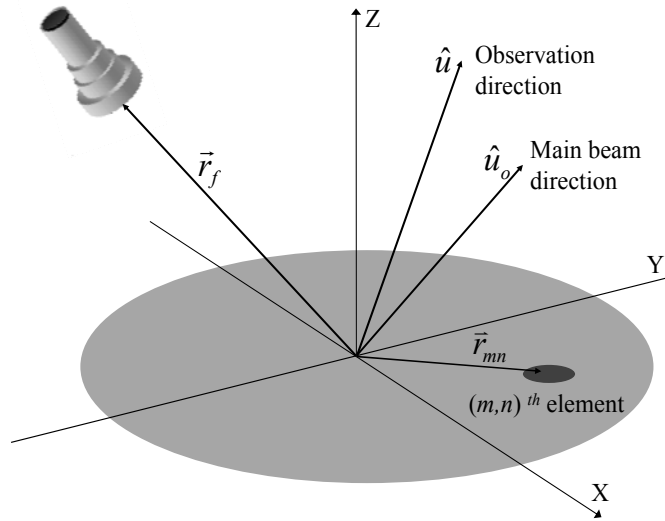


Fig. 2-9 The coordinate system for the reflectarray antenna.

To simplify calculations usually one uses scalar functions in the analysis. For the element pattern function A , a scalar approximation considers a cosine q model for each element with no azimuth dependence, i.e.,

$$A_{mn}(\theta, \varphi) \approx \cos^{q_e}(\theta) \cdot e^{jk(\vec{r}_{mn} \cdot \hat{u})}.\tag{2-10}$$

The element excitation function $I(m,n)$, is determined by the incident field and element property. By approximating the feed horn pattern function using a cosine q model and taking into account the Euclidian distance between the feed horn and the element, the illumination of the aperture

can be obtained. The element excitation can then be expressed as

$$I(m, n) \approx \frac{\text{Cos}^{q_f} \theta_f(m, n)}{|\bar{r}_{mn} - \bar{r}_f|} \cdot e^{-jk(\bar{r}_{mn} - \bar{r}_f)} \cdot |\Gamma_{mn}| e^{j\phi_{mn}}. \quad (2-11)$$

Here, θ_f is the spherical angle in the feed coordinate system and \bar{r}_f is the position vector of the feed. In addition, for each element this excitation can take into account the receive mode pattern, i.e., $|\Gamma_{mn}|$. This pattern is also modeled by a cosine q function based on the local element coordinates, i.e.,

$$|\Gamma_{mn}| = \text{Cos}^{q_e} \theta_e(m, n). \quad (2-12)$$

It should be noted that this definition of $|\Gamma_{mn}|$ is for the receive/transmit (R/T) model, and in the scattering model analysis approach, this value is obtained directly from the unit-cell analysis. The required phase delay of the mn^{th} element, ϕ_{mn} , is designed to set the main beam in the \hat{u}_o direction. It should be noted that since the infinite-array approach is often used for analysis of reflectarray elements, ϕ_{mn} in (2-11) does contain the mutual coupling effects in an infinite array environment. With these approximations, the radiation pattern from (2-9) can be simplified to the scalar form

$$E(\theta, \varphi) = \sum_{m=1}^M \sum_{n=1}^N \text{Cos}^{q_e} \theta \frac{\text{Cos}^{q_f} \theta_f(m, n)}{|\bar{r}_{mn} - \bar{r}_f|} e^{-jk(\bar{r}_{mn} - \bar{r}_f - \bar{r}_{mn} \cdot \hat{u})} \text{Cos}^{q_e} \theta_e(m, n) e^{j\phi_{mn}}. \quad (2-13)$$

The radiation pattern calculation method described here uses a conventional array summation technique. In general, the array theory formulation will yield good main beamwidth, beam direction, and general pattern shape; however, since the polarization of the feed horn and elements are not accounted for in the simplified cosine q model, the cross-polarization of the reflectarray antenna is not calculated in this procedure. In summary, the advantages and

disadvantages of this approach are:

Advantages:

- Simplicity of the formulation and program development
- Fast computational time

Limitations:

- Cross-polarization is not modeled

2.3.3 Aperture Field Approach for Radiation Analysis

In this method, the radiation pattern of the reflectarray is calculated from the aperture fields using the equivalence principle. First, the electric fields on the aperture surface are obtained using (2-8) while considering the polarization of the feed horn. From the incident fields on the reflectarray aperture, the reflected fields for every element in the array is obtained using the generalized scattering matrix relating the Cartesian components of incident and reflected fields in the periodic cell, i.e.,

$$\begin{bmatrix} E_x^{ref}(m,n) \\ E_y^{ref}(m,n) \end{bmatrix} = \begin{bmatrix} \Gamma_{xx} & \Gamma_{xy} \\ \Gamma_{yx} & \Gamma_{yy} \end{bmatrix} \begin{bmatrix} E_x^{inc}(m,n) \\ E_y^{inc}(m,n) \end{bmatrix}. \quad (2-14)$$

The phase shift produced for each element depends on the polarization of the feed and, also, takes into account the cross-polarized reflected fields. The Cartesian components of the tangential currents on the reflectarray can then be expressed as

$$J_{sx}(x,y) = H_y^i(x,y), \quad J_{sy}(x,y) = -H_x^i(x,y), \quad (2-14)$$

$$M_{sx}(x,y) = E_y^i(x,y), \quad M_{sy}(x,y) = -E_x^i(x,y), \quad (2-15)$$

where the magnetic fields are obtained using Maxwell's equations. From the tangential currents on the reflectarray surface, the far-field radiation pattern can be calculated using the vector

potentials as described in [27].

The E and H field components in the far-field are written as

$$\begin{aligned}
 E_r &= 0 & H_r &= 0 \\
 E_\theta &= -\frac{jke^{-jkr}}{4\pi r} (L_\theta + \eta N_\theta) & H_\theta &= +\frac{jke^{-jkr}}{4\pi r} \left(N_\theta - \frac{L_\theta}{\eta} \right) \\
 E_\phi &= +\frac{jke^{-jkr}}{4\pi r} (L_\phi - \eta N_\phi) & H_\phi &= -\frac{jke^{-jkr}}{4\pi r} \left(N_\phi + \frac{L_\phi}{\eta} \right)
 \end{aligned} \tag{2-16}$$

where N and L are functions which are evaluated directly from the tangential currents on the reflectarray surface. For the reflectarray coordinate system in Fig. 2-6, the functions N and L are given as

$$N_\theta = \iint_S (J_x \cos \theta \cos \phi + J_y \cos \theta \sin \phi) e^{jk(x'u+y'v)} ds' \tag{2-17a}$$

$$N_\phi = \iint_S (-J_x \sin \phi + J_y \cos \phi) e^{jk(x'u+y'v)} ds' \tag{2-17b}$$

$$L_\theta = \iint_S (M_x \cos \theta \cos \phi + M_y \cos \theta \sin \phi) e^{jk(x'u+y'v)} ds' \tag{2-17c}$$

$$L_\phi = \iint_S (-M_x \sin \phi + M_y \cos \phi) e^{jk(x'u+y'v)} ds' \tag{2-17d}$$

where u and v are the angular coordinates, ($u = \sin \theta \cos \phi$, $v = \sin \theta \sin \phi$). In general the double integration must be extended to the entire plane $z = 0$, but it is always limited to the reflectarray surface, because it is assumed that the tangential currents are zero outside the reflectarray. In order to evaluate these integrals element by element, some change of parameters is required. The coordinates of the central point of each reflectarray element can be given by

$$x' = x'_e + md_x - \left(\frac{N_x - 1}{2}\right)d_x; \quad m = 0, 1, 2, \dots, N_x - 1 \tag{2-18a}$$

$$y' = y'_e + nd_y - \left(\frac{N_y - 1}{2}\right)d_y; \quad n = 0, 1, 2, \dots, N_y - 1 \tag{2-18b}$$

where N_x and N_y are the maximum number of elements in each direction and d_x and d_y represent the periodicity of the reflectarray elements in the x and y directions, respectively. It should be noted that it is assumed that the tangential currents are constant on each element of the reflectarray and also x'_e and y'_e are limited to the unit-cell, i.e.,

$$\left(-\frac{d_x}{2} \leq x'_e \leq \frac{d_x}{2}, -\frac{d_y}{2} \leq y'_e \leq \frac{d_y}{2} \right).$$

To simplify the formulation, we first define a constant K_I as $K_I = e^{-j\frac{k}{2}[(N_x+1)ud_x+(N_y+1)vd_y]}$.

As mentioned earlier, since the tangential currents on each reflectarray element are assumed to be constant, they are pulled out of the integrals. The constant terms which need to be evaluated for all the integrals can then be expressed in the form of sinc functions.

$$\int_{-d_x/2}^{d_x/2} \int_{-d_y/2}^{d_y/2} e^{jk(x'_e u + y'_e v)} ds'_e = d_x d_y \operatorname{sinc} \left(\frac{ku d_x}{2} \right) \operatorname{sinc} \left(\frac{kv d_y}{2} \right). \quad (2-19)$$

Substituting these parameters in equation (2-19), the functions N and L can then be evaluated as

$$\begin{aligned} N_\theta(\theta, \varphi) &= K_I d_x d_y \operatorname{sinc} \left(\frac{kud_x}{2} \right) \operatorname{sinc} \left(\frac{kvd_y}{2} \right) \\ &\cdot \sum_{m=1}^{N_x} \sum_{n=1}^{N_y} (J_x(x'_e, y'_e) \cos \theta \cos \varphi + J_y(x'_e, y'_e) \cos \theta \sin \varphi) e^{jk[mud_x + nvd_y]} \end{aligned} \quad (2-20a)$$

$$\begin{aligned} N_\varphi(\theta, \varphi) &= K_I d_x d_y \operatorname{sinc} \left(\frac{kud_x}{2} \right) \operatorname{sinc} \left(\frac{kvd_y}{2} \right) \\ &\cdot \sum_{m=1}^{N_x} \sum_{n=1}^{N_y} (-J_x(x'_e, y'_e) \sin \varphi + J_y(x'_e, y'_e) \cos \varphi) e^{jk[mud_x + nvd_y]} \end{aligned} \quad (2-20b)$$

$$\begin{aligned} L_\theta(\theta, \varphi) &= K_I d_x d_y \operatorname{sinc} \left(\frac{kud_x}{2} \right) \operatorname{sinc} \left(\frac{kvd_y}{2} \right) \\ &\cdot \sum_{m=1}^{N_x} \sum_{n=1}^{N_y} (M_x(x'_e, y'_e) \cos \theta \cos \varphi + M_y(x'_e, y'_e) \cos \theta \sin \varphi) e^{jk[mud_x + nvd_y]} \end{aligned} \quad (2-20c)$$

$$L_{\varphi}(\theta, \varphi) = K_1 d_x d_y \sin c\left(\frac{kud_x}{2}\right) \sin c\left(\frac{kvd_y}{2}\right) \sum_{m=1}^{N_x} \sum_{n=1}^{N_y} (-M_x(x'_e, y'_e) \sin \varphi + M_y(x'_e, y'_e) \cos \varphi) e^{jk[mud_x + nvd_y]} \quad (2-20d)$$

It should be noted that this summation is extended to a rectangular grid with N_x and N_y elements, but for circular or elliptical reflectarrays, the tangential fields for the elements outside the aperture boundary have to be set to zero. By using (2-20) in (2-16) the far-field radiation pattern of the reflectarray antenna can be obtained.

The formulation presented here is the general aperture field analysis method where the first principle of equivalence is used to obtain the fields on the reflectarray aperture and the corresponding far-field radiation pattern. It is worthwhile to mention that to simplify the calculations usually only the electric field components are used in the analysis which corresponds to the second principle of equivalence. Alternatively the magnetic field components may also be used to compute the far-field radiation pattern of the reflectarray antenna. More discussion on this topic will be given in a section 2.4.

The advantages and disadvantages of this approach are:

Advantages:

- Accurate modeling of feed and element polarization.

Limitations:

- Complicated formulation and program development.
- Increased computational time.

2.3.4 Far-Field Parameters of Interest

2.3.4.1 Radiation Patterns in the Principal Planes

The previous sections discuss calculating the radiation pattern of the antenna in the entire space. However, it is more interesting to view the radiation pattern in the principal planes with respect to the main beam direction [28]. While for a broadside radiation, the principal planes are the xz - and yz - planes, for off-broadside beams the principal plane positions do not lie on the spherical coordinate axis. Consider the coordinate system in Fig. 2-10, which shows a main beam in an arbitrary direction of (θ_m, φ_m) .

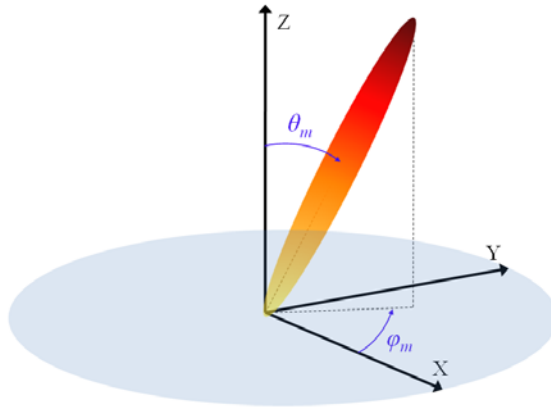


Fig. 2-10 Far-field Coordinate system for the reflectarray antenna.

It is necessary to choose the plane cuts that best capture the features of the 3-D patterns. For any arbitrary beam direction (θ_m, φ_m) it is possible to align the axis of the coordinate system with the main beam direction by defining two coordinate rotations. First a rotation of $\gamma = \varphi_m$ about the z -axis, and next a rotation of $\beta = \theta_m$ about the y -axis. By using these two rotations the main beam will be in the direction of z'' -axis in the new coordinate system (x'', y'', z'') . These coordinate rotations are shown pictorially in Fig. 2-11.

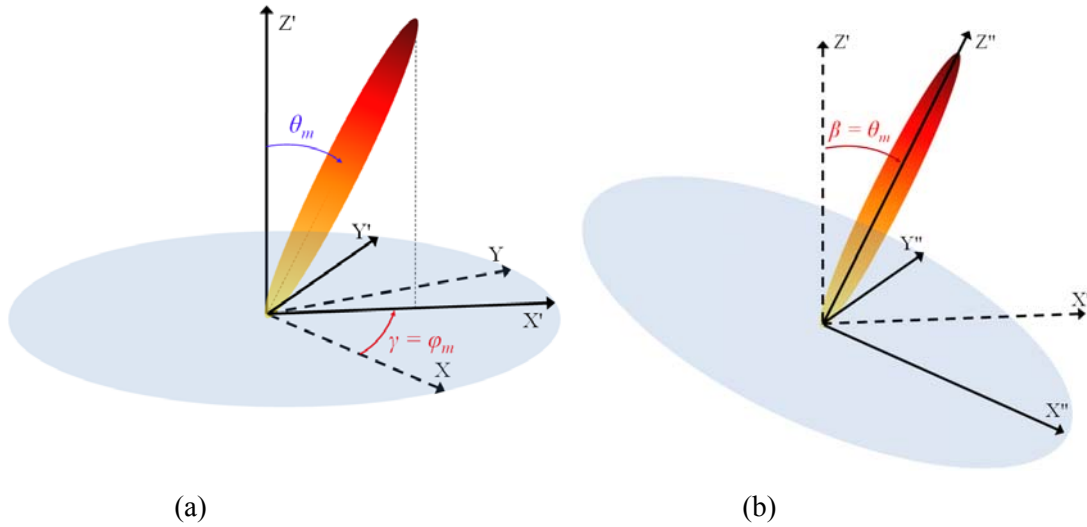


Fig. 2-11 Coordinate rotations used for the reflectarray system: (a) rotation of $\gamma = \varphi_m$ about the z-axis, (b) rotation of $\beta = \theta_m$ about the y-axis.

In this new coordinate system, the principal planes (P.P.1, P.P.2) are simply defined as $x''z''$ and $y''z''$ planes, respectively. The 2-D radiation patterns can then be plotted using the principal plane angles defined as α_1 and α_2 for P.P.1 and P.P.2. The principal planes and the corresponding angles are shown in Fig. 2-12.

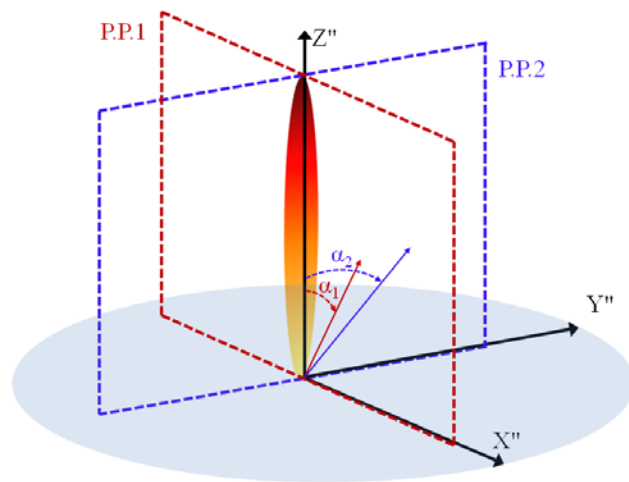


Fig. 2-12 Principal planes of the reflectarray antenna.

The task here is to calculate the principal plane angles in terms of the initial coordinate system. As discussed earlier two coordinate rotations are used here. These transformations can be expressed in terms of matrix multiplications which transform the original coordinate system (x, y, z) to the new coordinate system (x'', y'', z'').

$$\begin{bmatrix} x'' \\ y'' \\ z'' \end{bmatrix} = \begin{bmatrix} \cos \theta_m & 0 & -\sin \theta_m \\ 0 & 1 & 0 \\ \sin \theta_m & 0 & \cos \theta_m \end{bmatrix} \cdot \begin{bmatrix} \cos \varphi_m & \sin \varphi_m & 0 \\ -\sin \varphi_m & \cos \varphi_m & 0 \\ 0 & 0 & 1 \end{bmatrix} \cdot \begin{bmatrix} x \\ y \\ z \end{bmatrix}. \quad (2-21)$$

With this matrix transform a direct relation between the original and new coordinate system can be obtained as

$$\begin{bmatrix} x'' \\ y'' \\ z'' \end{bmatrix} = \begin{bmatrix} \cos \theta_m (x \cos \varphi_m + y \sin \varphi_m) - z \sin \theta_m \\ -x \sin \varphi_m + y \cos \varphi_m \\ \sin \theta_m (x \cos \varphi_m + y \sin \varphi_m) + z \cos \theta_m \end{bmatrix}. \quad (2-22)$$

Since the radiation patterns are usually expressed in terms of the spherical or angular coordinates, we can use the formula

$$\begin{aligned} x &= u = \sin \theta \cos \varphi \\ y &= v = \sin \theta \sin \varphi \\ z &= w = \cos \theta \end{aligned} \quad (2-23)$$

to obtain the principal plane angles α_1 and α_2 . From Fig. 2-12 it can be seen that for P.P.1

$$\begin{aligned} x'' &= u'' = \sin \theta'' \cos \varphi'' = \pm \sin \alpha_1 \\ y'' &= 0 \\ z &= w'' = \cos \theta'' = \cos \alpha_1. \end{aligned} \quad (2-24)$$

Similarly for P.P.2

$$\begin{aligned} x'' &= 0 \\ y'' &= v'' = \sin \theta'' \sin \varphi'' = \pm \sin \alpha_2 \\ z &= w'' = \cos \theta'' = \cos \alpha_2. \end{aligned} \quad (2-25)$$

Using (2-24) and (2-25) in (2-22) the spherical or angular coordinates corresponding to the

principal plane angles can be calculated. For P.P.1 one obtains

$$\begin{aligned} u &= \cos \theta_m \cos \varphi_m (\cos \alpha_1 \tan \theta_m \pm \sin \alpha_1) \\ v &= u \tan \varphi_m. \end{aligned} \quad (2-26)$$

Similarly for P.P.2 one obtains

$$\begin{aligned} u &= \sin \theta_m \cos \varphi_m (\cos \alpha_2 \pm \sin \alpha_2 \tan \varphi_m \sin \theta_m) \\ v &= u \tan \varphi_m \mp \frac{\sin \alpha_2}{\cos \varphi_m}. \end{aligned} \quad (2-27)$$

Equations (2-26) and (2-27) provide a complete description of the principal planes in terms of the angular coordinates (u, v) . For any arbitrary beam direction P.P.1 is a straight line passing through the center, while P.P.2 is generally a curved line in the (u, v) plane. For example the principal planes of a reflectarray antenna with a main beam in the direction of $(\theta_m = 26^\circ, \varphi_m = 40^\circ)$ are given in Fig. 2-13.

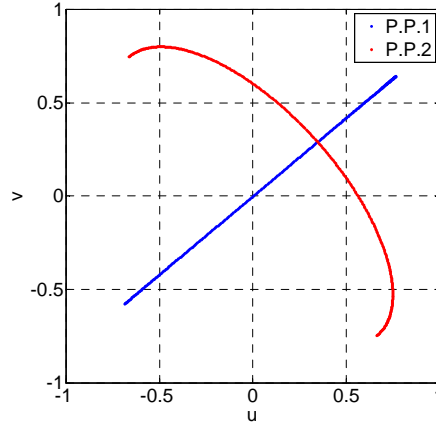


Fig. 2-13 Principal planes of a reflectarray antenna in the angular coordinates with a main beam at the direction of $(\theta_m = 26^\circ, \varphi_m = 40^\circ)$.

2.3.4.2 Co- and Cross-Polarized Radiation Patterns

The radiation patterns obtained here (Eq. 2-16) are expressed in terms of θ and φ components, however it is more common to use the co-polar and cross-polar components of the fields

according to Ludwig's third definition [29].

For an x-polarized feed (see Fig. 2-6), the transformation from θ and φ to co-polar (E_{co-pol}) and cross-polar (E_{x-pol}) components are given by

$$\begin{bmatrix} E_{co-pol}^x \\ E_{x-pol}^x \end{bmatrix} = \begin{bmatrix} \cos \varphi & -\sin \varphi \\ -\sin \varphi & -\cos \varphi \end{bmatrix} \begin{bmatrix} E_\theta \\ E_\varphi \end{bmatrix}, \quad (2-28)$$

and for a y-polarized feed by

$$\begin{bmatrix} E_{co-pol}^y \\ E_{x-pol}^y \end{bmatrix} = \begin{bmatrix} \sin \varphi & \cos \varphi \\ \cos \varphi & -\sin \varphi \end{bmatrix} \begin{bmatrix} E_\theta \\ E_\varphi \end{bmatrix}. \quad (2-29)$$

For circular polarized feeds, the co- and cross- polar components are defined in terms of the sense of rotation where

$$E_{RHCP} = \frac{1}{\sqrt{2}}(E_\theta + jE_\varphi), \quad E_{LHCP} = \frac{1}{\sqrt{2}}(E_\theta - jE_\varphi). \quad (2-30)$$

These equations formulated here allow for an accurate calculation of the co- and cross-polar radiation patterns of the reflectarray antenna. This includes all possible sources of cross-polar radiation from the feed horn, the geometrical projections and even the reflectarray phasing elements. For the latter case here the cross polarization of the phasing elements has to be obtained from the unit-cell simulations.

2.3.4.3 Antenna Directivity and Gain

Once the radiation pattern of the antenna is obtained from any of the methods described in the previous section, the antenna directivity can be obtained using

$$D_0 = \frac{4\pi |E(\theta_m, \varphi_m)|^2}{\int_0^{2\pi} \int_0^\pi |E(\theta, \varphi)|^2 \sin \theta d\theta d\varphi} \quad (2-31)$$

In the equation above θ_m, φ_m are the direction of the main beam. The calculated directivity in (2-31) takes into account the illumination (taper efficiency) of the array, and the effect of projected aperture for off-broadside beams. Typically the main challenge in directivity calculations is the evaluation of the denominator in (2-31) which is done numerically. It is important to point out here, that if the radiation patterns are computed in the angular coordinates (u, v) rather than the spherical coordinates (θ, φ) , it will be necessary to use Jacobi transforms for the directivity calculations. The differential relation between angular and spherical coordinates is

$$\begin{aligned} u &= \sin \theta \cos \varphi, \quad v = \sin \theta \sin \varphi \\ du &= \frac{\partial u}{\partial \theta} d\theta + \frac{\partial u}{\partial \varphi} d\varphi, \quad dv = \frac{\partial v}{\partial \theta} d\theta + \frac{\partial v}{\partial \varphi} d\varphi. \end{aligned} \quad (2-32)$$

The matrix relation is then obtained as

$$\begin{bmatrix} d\theta \\ d\varphi \end{bmatrix} = \begin{bmatrix} \frac{\cos \varphi}{\cos \theta} & \frac{\sin \varphi}{\cos \theta} \\ -\frac{\sin \varphi}{\sin \theta} & \frac{\cos \varphi}{\sin \theta} \end{bmatrix} \begin{bmatrix} du \\ dv \end{bmatrix} \quad (2-33)$$

Using equation (2-33), the beam solid angle can be expressed in terms of the angular coordinates as

$$d\Omega = \sin \theta d\theta d\varphi = \frac{1}{\cos \theta} (\cos \varphi du + \sin \varphi dv)(-\sin \varphi du + \cos \varphi dv) \quad (2-34)$$

From this equation it can be observed that for the case of $\theta = 90^\circ$ the beam solid angle shows a singular behavior. Two methods can be used to mitigate this problem where both approaches basically omit the singular points. The first method avoids the calculation of the integral at $\theta =$

90°. The second method removes this singularity in terms of the angular components. First the beam solid angle expression in (2-34) is expressed completely in terms of the angular components, i.e.

$$d\Omega = \frac{1}{\cos \theta} \left(\cos 2\varphi du dv + \frac{1}{2} \sin 2\varphi (dv^2 - du^2) \right) = \frac{1}{\sqrt{1 - (u^2 + v^2)}} \left(\frac{u^2 - v^2}{u^2 + v^2} du dv + \frac{uv}{u^2 + v^2} (dv^2 - du^2) \right) \quad (2-35)$$

In this method the singularity is removed for the case where $u^2 + v^2 = 1$. It is worthwhile to mention that since most reflectarrays are designed to generate a beam that is not far from the broadside direction, the numerical singularity is actually occurring in a region where the radiated power is almost zero.

Once the reflectarray directivity is calculated, the antenna gain can be obtained by taking into account the aperture efficiency. For an accurate calculation of the reflectarray antenna gain it is imperative to determine the overall aperture efficiency of the antenna. Different kinds of efficiency factors are considered in conventional reflector antennas [30]. Amongst these efficiency factors, however, the major terms that influence the reflectarray antenna gain are the spillover and taper efficiency. The formulation presented in the previous section for calculating the radiation pattern accurately takes into account the illumination of the aperture. In other words, the effect of taper efficiency is already taken into account when one calculates the radiation pattern directivity using (2-31). Therefore, one only needs to evaluate the spillover efficiency to determine the reflectarray antenna gain. By definition, spillover efficiency (η_s) is the percentage of radiated power from the feed that is intercepted by the reflecting aperture. For the spillover efficiency calculation we followed the approach in [24]. The gain of the reflectarray antenna is given as

$$G = \eta_s D. \quad (2-36)$$

Here D is the maximum directivity of the reflectarray antenna, which is defined as the maximum radiation intensity of the antenna over the average, and is calculated using (2-31). It should be noted that the gain calculations discussed here don't include the factors associated with the feed loss, and blockage; however, in most cases for reflectarrays with offset feed and low-loss substrates, these factors don't contribute much to the overall loss of the system [4].

The reflectarray antenna gain can also be computed from the far field radiation patterns while using the input power of the feed horn antenna as the reference. The antenna gain is defined as

$$G = 4\pi \frac{\text{intensity of the antenna in direction } (\theta, \varphi)}{\text{power incident at the antenna}} = 4\pi \frac{U(\theta, \varphi)}{P_{feed\ horn}} \quad (2-37)$$

The radiation intensity is defined as

$$U(\theta, \varphi) = \frac{1}{2} \text{Re} \{ E(\theta, \varphi) \times H^*(\theta, \varphi) \} r^2 \hat{r}. \quad (2-38)$$

The gain of the reflectarray antenna can then be evaluated as

$$G(\theta, \varphi) = 4\pi \frac{|E(\theta, \varphi)|^2 r^2}{2\eta_0 P_{feed\ horn}}, \quad (2-39)$$

where η_0 is the intrinsic impedance of the free-space. Assuming the losses in the feed horn antenna are negligible, the total power radiated by the feed horn antenna can be computed as

$$P_{feed\ horn} = \int_{\varphi=0}^{2\pi} \int_{\theta=0}^{\pi} \frac{|E^F(\theta, \varphi)|^2}{2\eta_0} r^2 \sin \theta d\theta d\varphi. \quad (2-40)$$

In this equation, E^F is the radiation pattern of the horn antenna, which is given by equations (2-3) to (2-5) depending on the polarization of the feed.

For an x-polarized feed horn, the amplitude squared for the horn radiation pattern is

$$\left|E^{Fx}(\theta, \varphi)\right|^2 = E^{Fx}(\theta, \varphi) \left(E^{Fx}(\theta, \varphi)\right)^* = |A_0|^2 \left(C^2_E(\theta) \cos^2 \varphi + C^2_H(\theta) \sin^2 \varphi\right). \quad (2-41)$$

Similarly for a y-polarized feed horn, the amplitude squared for the horn radiation pattern is

$$\left|E^{Fy}(\theta, \varphi)\right|^2 = E^{Fy}(\theta, \varphi) \left(E^{Fy}(\theta, \varphi)\right)^* = |A_0|^2 \left(C^2_E(\theta) \sin^2 \varphi + C^2_H(\theta) \cos^2 \varphi\right). \quad (2-42)$$

Assuming that $q_E = q_H = q$ in the cosine q models used for the functions C_E and C_H , (2-41) and (2-42) can both be expressed as

$$\left|E^{Fx}(\theta, \varphi)\right|^2 = \left|E^{Fy}(\theta, \varphi)\right|^2 = |A_0|^2 \cos^{2q} \theta. \quad (2-43)$$

Substituting this in (2-40) and evaluating the integral, the total power radiated by a linearly polarized feed horn can be calculated as

$$P_{feed\ horn} = \frac{|A_0|^2 \pi r^2}{\eta_0} \frac{2}{(2q+1)}. \quad (2-44)$$

Using (2-44) in (2-39), the gain of a linearly polarized reflectarray antenna is given as

$$G(\theta, \varphi) = \frac{1}{|A_0|^2} (2q+1) |E(\theta, \varphi)|^2. \quad (2-45)$$

It is implicit that if the complex constant A_0 was taken into account in the calculation of the radiation patterns of the antenna, it will be cancelled out in the gain computations.

For a circularly polarized feed horn

$$\left|E^{Fc}(\theta, \varphi)\right|^2 = E^{Fc}(\theta, \varphi) \left(E^{Fc}(\theta, \varphi)\right)^* = |A_0|^2 \left(C^2_E(\theta) + C^2_H(\theta)\right), \quad (2-46)$$

for both right hand and left hand polarizations. Considering that for an ideal circular polarized feed horn $q_E = q_H = q$, the total power radiated from the horn antenna can then be calculated as

$$P_{feed\ horn} = \frac{|A_0|^2 \pi r^2}{\eta_0} \frac{4}{(2q+1)}. \quad (2-47)$$

Using (2-47) in (2-39), the gain of a circularly polarized reflectarray antenna is given as

$$G(\theta, \varphi) = \frac{1}{|A_0|^2} \frac{(2q+1)}{2} |E(\theta, \varphi)|^2, \quad (2-48)$$

which as expected is one half of that of the linear polarized antenna (2-45). It is important to mention that the co-polarized pattern of the reflectarray antenna should be used in (2-45) and (2-48) for gain calculations.

Both formulas used for the gain calculations, (2-36) and (2-37), correctly take into account the losses due to aperture projection, illumination taper, and spillover. However, (2-37) is more general since in addition to the polarization, the effect of element losses on the antenna gain is also evaluated directly, given that they are included in the radiation pattern calculations.

2.3.5 Spectral Transforms and Computational Speedup

In the previous sections it was shown that both approaches require evaluation of a double summation for far-field calculations, namely (2-13) and (2-20). This double summation can be replaced by a 2D inverse discrete Fourier transform (IDFT), defined as

$$f(p, q) = \frac{1}{N_x N_y} \sum_{m=0}^{N_x-1} \sum_{n=0}^{N_y-1} F(m, n) e^{j \frac{2mp\pi}{N_x}} e^{j \frac{2nq\pi}{N_y}}. \quad (2-49)$$

Here the spectral functions will be obtained in a discrete number of angular coordinates. These points in the (u, v) plane are defined by the Fourier transform as:

$$\begin{aligned} u &= \frac{2\pi}{N_x d_x k_0} p; \quad p = 0, 1, 2, \dots, N_x - 1, \\ v &= \frac{2\pi}{N_y d_y k_0} q; \quad q = 0, 1, 2, \dots, N_y - 1. \end{aligned} \quad (2-50)$$

The main advantage of using spectral functions in the calculations is a significant reduction of computational time, which is simply achieved by replacing the double summations with Fourier transforms. It should be noted that the definition of the propagating wave direction determines

whether the discrete Fourier transform (DFT) or IDFT is to be used for the transforms. In the formulation presented here, we followed the definition in [3], where the IDFT is used to replace the double summation in the spectral functions. It should be noted here that the condition which needs to be satisfied here is that the sets (m,n) and (p,q) must have a one on one relation. This condition can be satisfied by setting the number of far-field points that are calculated equal to the number of elements on the array.

With these constraints defined it is possible to replace the double summation with the 2D inverse discrete Fourier transform. By using the 2D inverse fast Fourier transform (2D-IFFT) algorithm available in Matlab, it is possible to calculate the radiation patterns of the reflectarrays very efficiently. Some important considerations about implementing the 2D-IFFT are listed below.

- A. The 2D-IFFT routine described here cannot be implemented if the radiation pattern is being calculated in terms of the spherical coordinates (θ,φ) . This is due to the fact that (θ,φ) don't satisfy the one on one condition with (m,n) . It is trivial that once the pattern is calculated in the angular coordinates it is possible to transform it to any other coordinate system.
- B. The spectral functions are obtained in a discrete number of angular coordinates. It is possible to make this range symmetric by defining a shift in the variables. The range of (u,v) is typically defined as

$$-\frac{\lambda_0}{2d_x} \leq u \leq \frac{\lambda_0}{2d_x}, \quad -\frac{\lambda_0}{2d_y} \leq v \leq \frac{\lambda_0}{2d_y}, \quad (2-51)$$

It should be pointed out that if the periodic cell is $\lambda_0/2$, the radiation pattern will be computed in the whole visible range which is defined by the circle $u^2 + v^2 \leq 1$. In addition note that in this case the absolute value of the range of u and v will be smaller than 1, due

to the $\frac{N_x - 1}{N_x}, \frac{N_y - 1}{N_y}$ factors in (2-50). For periodic cells smaller than $\lambda_o/2$, the radiation

patterns will be computed in a larger range while periodic cells larger than $\lambda_o/2$, the radiation patterns will be computed in a smaller range.

- C. The number of points in the (u,v) plane for radiation pattern calculations are equal to the number of elements on the array. For a higher resolution in pattern calculations it is possible to increase the number of points by extending the grid on the reflectarray surface. This extended grid can be viewed as a virtual reflectarray surface where the amplitude of all the elements outside of the reflectarray is set to zero. With this definition of extended grid it is possible to obtain high resolution radiation patterns for small size arrays.
- D. The implementation of the 2D-IFFT routine in Matlab also requires some discussion. The FFT routine generally has only one zero frequency point. For the pattern calculations here this point is actually representing the center point in the (u,v) plane which is $(0,0)$. To satisfy this condition it is necessary to use an odd number of points for radiation pattern calculations. In addition Matlab's 2D-IFFT command swaps the coordinates so that the zero frequency point is located at the lower left corner. After the 2D-IFFT command (`ifft2`) is executed it is necessary to correct the obtained results by using the `fftshift` command which corrects the quadrants so that the center of the (u,v) plane is placed in the center of the matrix.

2.4 Design Examples and Comparison of Analysis Approaches

The techniques presented in this chapter are applied to Ka-band reflectarrays for comparison of

these methods. We consider a Ka-band reflectarray with a circular aperture and a diameter of 17λ at the design frequency. The phasing elements, used in this study, are variable size square patches with a unit-cell periodicity of $\lambda/2$ at the design frequency of 32 GHz and are fabricated on a 20 mil Rogers 5880 substrate. The reflection phase response (S-curve) of the phasing elements obtained using the infinite array approach, is generated using Ansoft Designer [31], and is given in Fig. 2-14. It can be seen that the reflection characteristics of the phasing elements are angle dependent; however, for this design, normal incidence can present good approximations for oblique incidence angles up to 30° . Thus, the reflectarrays here are designed based on the simulated reflection coefficients obtained with normal incidence. In addition the element losses and cross-polarization are also negligible here and are ignored in the computations.

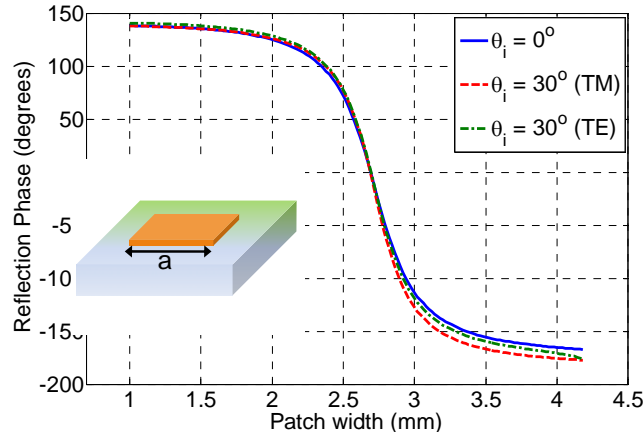


Fig. 2-14 Reflection phase versus patch width for the reflectarray elements.

2.4.1 A Reflectarray Antenna with a Broadside Beam

In this design, the reflectarray phasing elements are designed to generate a beam in the broadside direction. The reflectarray aperture is circular and has a diameter of 17 wavelengths at the center design frequency. The x-polarized prime-focus feed horn is positioned with an F/D

ratio of 0.735, although as discussed previously, in the array theory calculations, the polarization of the feed horn is not modeled. For the horn model used in this study, the power q of the feed radiation pattern is 6.5 at 32 GHz. The aperture taper and the ideal phase requirement for the reflectarray elements are given in Fig. 2-15.

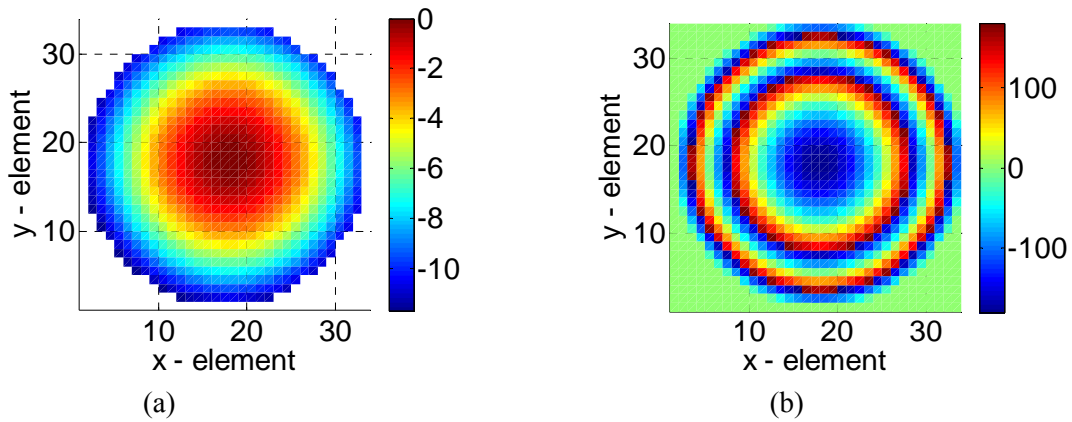


Fig. 2-15 (a) Aperture taper, (b) Phase requirement on the aperture.

For this system, the spillover and illumination efficiency are 93.009% and 81.983%, respectively. This corresponds to an aperture efficiency of 76.252%. In the next stage, the dimensions of the patch elements are selected from the S-curve in Fig. 2-14 to match the required phase distribution on the aperture. The mask of the reflectarray antenna and the obtained reflection phase of the elements are given in Fig. 2.16.

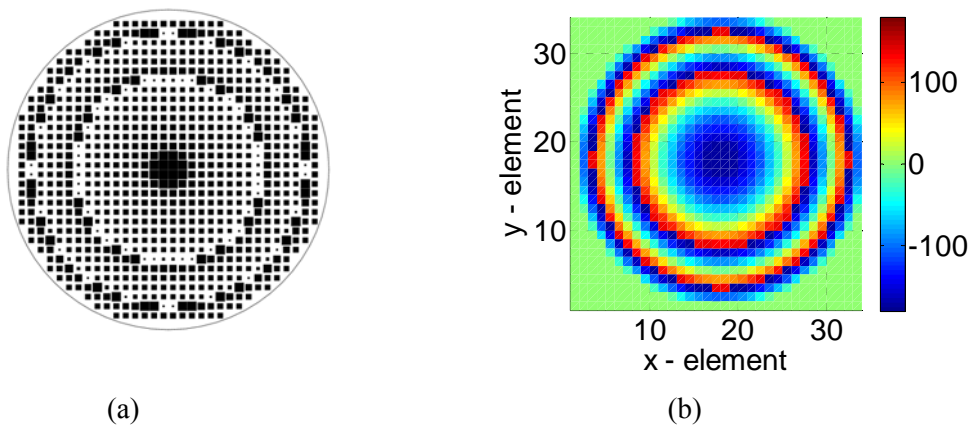


Fig. 2-16 (a) Mask of the reflectarray antenna, (b) Reflection phase of the elements on the reflectarray aperture.

It can be seen the phase distribution obtained from the variable size patch elements shows a close agreement with the ideal phase, i.e. Fig. 2-15 (b). Now that all the system parameters are determined, the radiation performance of the reflectarray antenna can be computed using the analysis approaches described in the previous section. The principal plane (P.P.1 and P.P.2) radiation patterns of the reflectarray antenna, calculated by both methods are given in Fig. 2-17 at 32 GHz. It should be noted that with this design the cross-polarized pattern obtained using the aperture field formulation is almost zero in the principal planes. The maximum cross-polarization level for this system is -36.1 dB which occurs in the 45° planes. A contour plot of the radiation patterns obtained by the aperture field analysis approach is also given in Fig. 2-18.

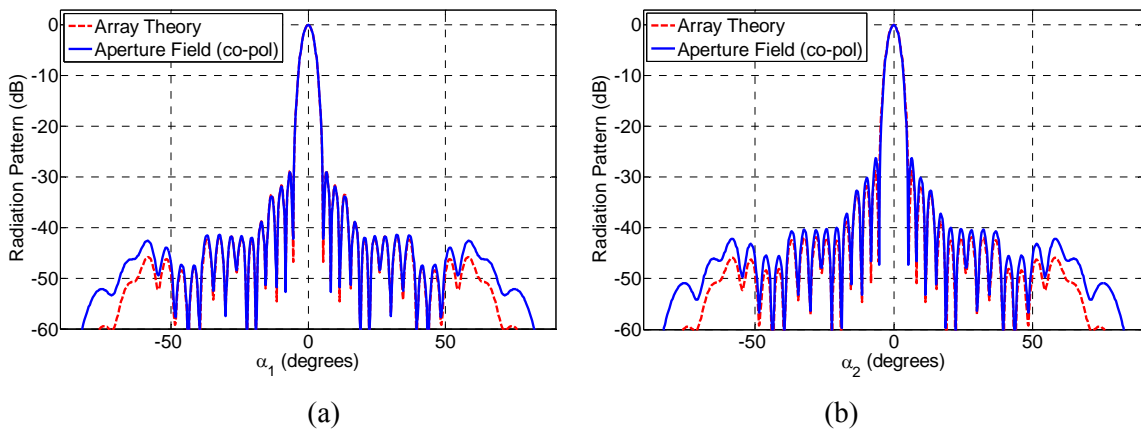


Fig. 2-17 Radiation pattern of the reflectarray with a broadside beam: (a) xz -plane, (b) yz -plane.

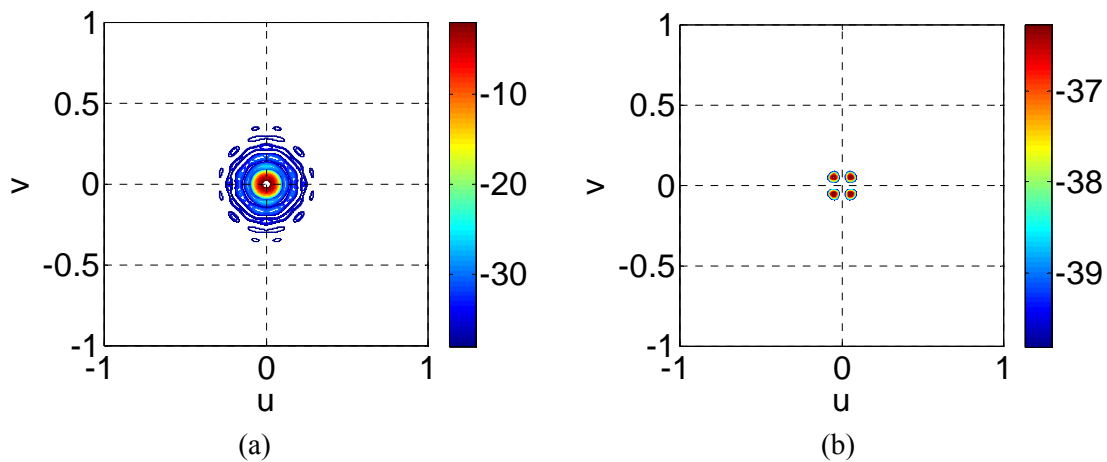


Fig. 2-18 Radiation pattern of the reflectarray with a broadside beam: (a) co-pol, (b) cross-pol.

2.4.2 A Reflectarray Antenna with an Off-Broadside Beam

For the second system, we consider designing a reflectarray with an off-broadside beam. The phasing elements are designed to generate a beam in the direction of $(\theta, \varphi) = (25^\circ, 0^\circ)$. The offset feed horn position is $X_{feed} = -45.9 \text{ mm}$, $Y_{feed} = 0 \text{ mm}$, $Z_{feed} = 98.4 \text{ mm}$ based on the coordinate system in Fig. 2-6. The feed horn is LHCP and the power q of the feed radiation pattern is 6.5 at 32 GHz. The aperture taper and the ideal phase requirement for the reflectarray elements are given in Fig. 2-19.

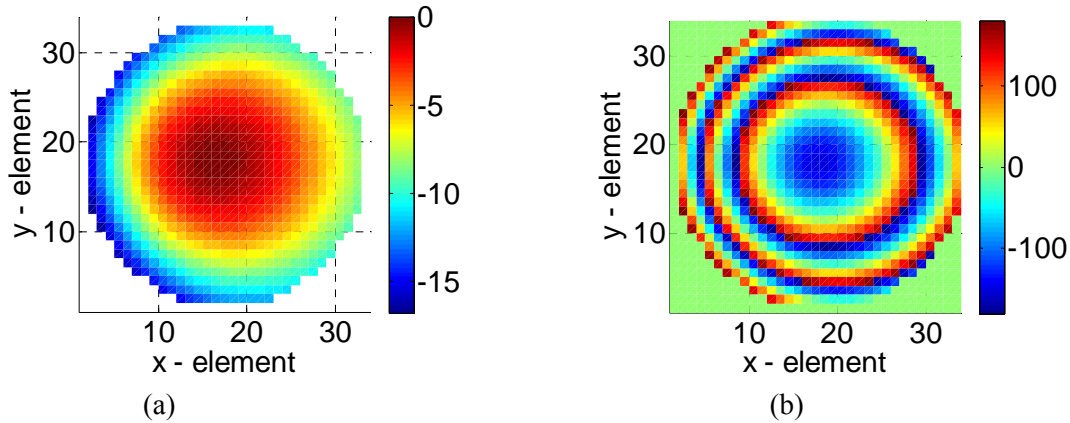


Fig. 2-19 (a) Aperture taper, (b) Phase requirement on the aperture.

For this system, the spillover and illumination efficiency are 92.194% and 77.920%, respectively. This corresponds to an aperture efficiency of 71.837%. Similar to the previous design, the dimensions of the patch elements can now be selected from the S-curve in Fig. 2-14 to match the required phase distribution on the aperture. The mask of the reflectarray antenna and the obtained reflection phase of the elements are given in Fig. 2.20. Similarly, it can be seen the phase distribution obtained from the variable size patch elements show a close agreement with the ideal phase, i.e. Fig. 2-19 (b).

As discussed earlier, the polarization of the feed is correctly modeled in the aperture field analysis approach. It would be interesting to observe the field distribution on the aperture for

both incident and reflected fields. The incident electric fields on the reflectarray aperture are given in Fig. 2-21.

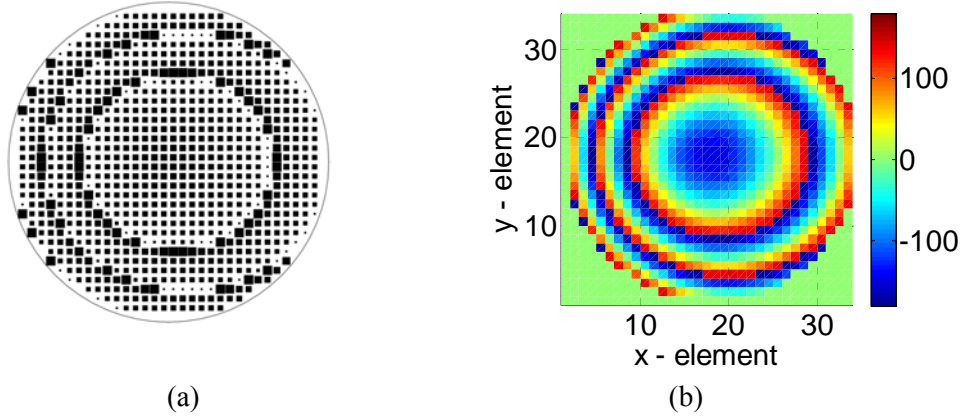


Fig. 2-20 (a) Mask of the reflectarray antenna, (b) Reflection phase of the elements on the reflectarray aperture.

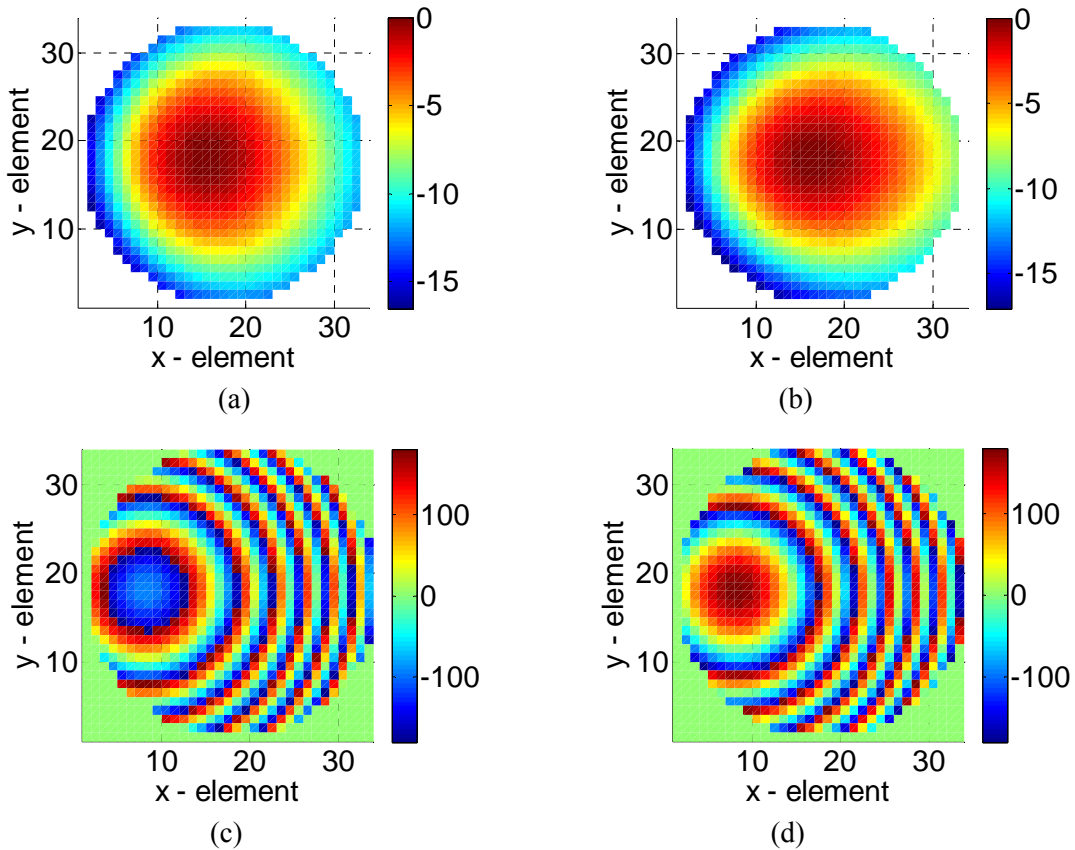


Fig. 2-21 Incident electric fields on the reflectarray aperture: (a) $|E_x|$ (dB), (b) $|E_y|$ (dB), (c) phase of E_x , (d) phase of E_y .

To generate a collimated beam, the reflected phase, after element phase compensation, should be flat along the y -axis and progressive in the direction of the scanned beam (x -axis). These results are given in Fig. 2-22, where indeed such a phase distribution can be observed. It should be noted that the reflectarray elements used in the design here have a reflection coefficient magnitude close to unity, thus the magnitude of the reflected field remains almost the same as that of the incident field, and are not shown here for brevity.

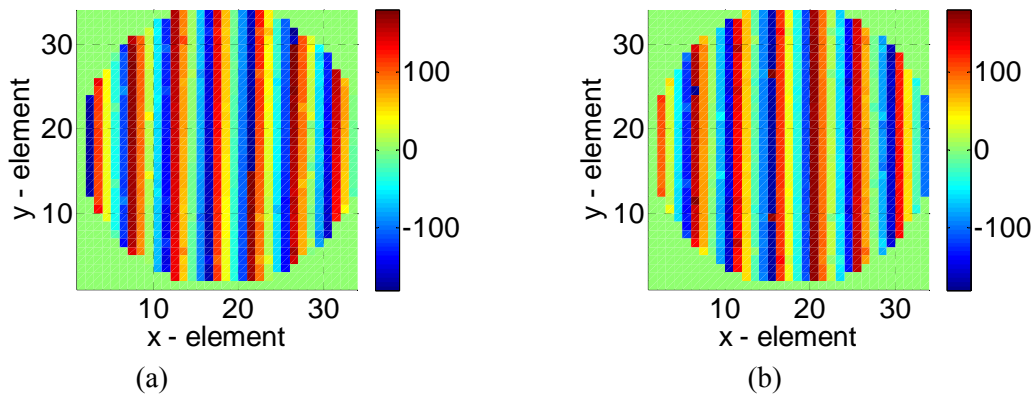


Fig. 2-22 Reflected electric fields on the reflectarray aperture: (a) phase of E_x , (b) phase of E_y .

The radiation performance of this reflectarray antenna is computed using the analysis approaches described in the previous section. The radiation patterns in the principal planes at 32 GHz are given in Fig. 2-23. For this system the cross-polarized radiation pattern is also observed in both principal planes, where the maximum cross-polarization level is -30.0 dB.

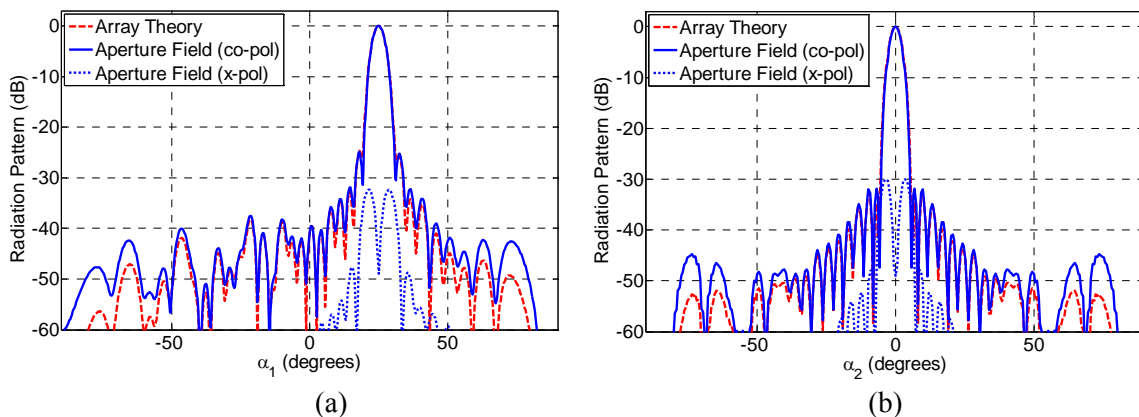


Fig. 2-23 Radiation pattern of the reflectarray with an off-broadside beam: (a) P.P.1, (b) P.P.2.

2.4.3 Comparison of Calculated Directivity versus Frequency

From the results given in Figs. 2-17 and 2-23 for the two reflectarray systems, it can be seen that the calculated radiation pattern obtained by both methods are in close agreement with each other. In particular, the main beam direction, beamwidth, and general pattern shape are almost identical, however a slight difference is observed in the side-lobe regions.

The antenna directivity is a suitable measure to compare the calculated radiation performance of these methods in the entire 3D space. In order to accurately model the reflectarray directivity versus frequency, the frequency behavior of the feed horn pattern and the element reflection characteristics are implemented into this calculation routine. For the phasing elements, the frequency behavior of the reflection phase is obtained across the band from full-wave simulations. For the horn model used in this study, the power q of the feed radiation pattern varies almost linearly from 5 at 30 GHz to 8.3 at 34 GHz according to the measured data [10]. For the two reflectarray systems studied in the previous section, the directivity versus frequency is given in Fig. 2-24. It can be seen that the computed directivity versus frequency obtained by both methods also shows a close agreement. At the center frequency of 32 GHz, the difference in computed directivity is less than 0.1 dB for both designs. It should be noted here that, as expected, the off broadside system shows a lower directivity and a slightly larger bandwidth.

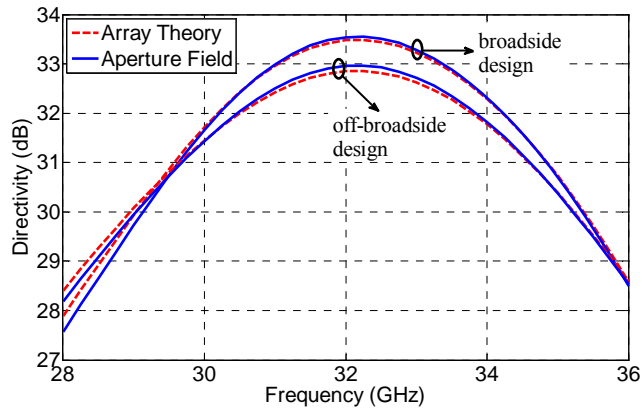


Fig. 2-24 Directivity versus frequency for the two reflectarray systems.

It is worthwhile to point out that a possible reason for the slightly lower directivity obtained with the array theory approach is the effect of the element receive mode pattern. In the aperture field method the reflection coefficients of the elements are obtained under normal incidence approximation. In other word, an omni-directional element receive pattern is assumed in the aperture field analysis.

One other topic that merits some attention is the comparison of the two gain computation approaches, namely equations 2-36 and 2-39. For the broadside and off-broadside reflectarray systems studied, the computed gain at 32 GHz using the first approach is 33.2244 dB and 32.5981 dB, respectively. With the second approach the computed gain values are 33.0885 dB and 32.4708 dB, respectively. It can be seen that in both cases the values obtained with the second method are slightly smaller. A possible reason for this is that with the second approach, the polarization of the feed horn is correctly taken into account during gain computations.

2.4.4 Comparison of Classical Methods and Full-Wave Simulations

Comparison of both classical analysis approaches showed that the radiation patterns computed by both methods are in close agreement with each other. However, as discussed earlier, several approximations are considered in these approaches. In addition, the reflectarray phasing elements are analyzed with an infinite array approach, which is also an approximation. As a result of these approximations in the analysis, it is expected that the radiation pattern obtained by these approaches may show some discrepancy with practical results. The aim of the study here is to analyze the accuracy of the reflectarray radiation pattern computed using these approaches by comparing them with full-wave simulations. For this comparative study, full-wave simulations will be more advantageous than measured results, since measurement results are susceptible to

both fabrication and measurement errors.

We consider a Ka-band reflectarray with a circular aperture and a diameter of 14.5λ at the design frequency of 32 GHz. The feed is positioned at $X_{feed} = -45.90 \text{ mm}$, $Y_{feed} = 0 \text{ mm}$, $Z_{feed} = 98.44 \text{ mm}$ based on the coordinate system in Fig. 2-6. The elements phase are designed to generate a beam in the direction of $(\theta, \varphi) = (25^\circ, 0^\circ)$. Similarly for the reflectarray phasing elements, the variable size square patches are selected from the S-curve data in Fig. 2-14. The 609 element reflectarray antenna is modeled using the commercial electromagnetic software FEKO [32]. For the excitation of the reflectarray, a point source feed model with a $\cos^{6.5}\theta$ radiation pattern is used. The advantage of using a point source rather than a feed horn here is that a point source model does not have a blockage aperture, which makes it more suitable for comparison purpose, since blockage is typically not modeled in the classical methods. For this design 568,435 unknown basis functions have to be calculated for the FEKO method of moments (MoM) solution. Considering the large number of unknowns, the multilevel fast multi-pole method (MLFMM) solver in FEKO was selected for this simulation. More discussion on full-wave simulations using FEKO is given in the appendix. The geometry of the reflectarray antenna modeled in FEKO and the simulated 3D radiation pattern is shown in Fig. 2-25. The full-wave simulation here will take into account all approximations in reflectarray element design and mutual coupling, in addition to edge diffraction effects. Therefore comparing these simulation results with the results obtained using classical approaches, can provide a good measure in terms of the accuracy of these approaches.

The principal plane (P.P.1 and P.P.2) radiation patterns of the reflectarray antenna calculated using the aperture field method and the full-wave simulation are given in Fig. 2-19. The computed directivity and gain of the reflectarray antenna is 30.476 dB and 29.682 dB,

respectively. To accurately model the cross-polarization of the reflectarray antenna in the aperture field analysis, the incident fields on the reflectarray aperture obtained from the full-wave simulations were used in these calculations.

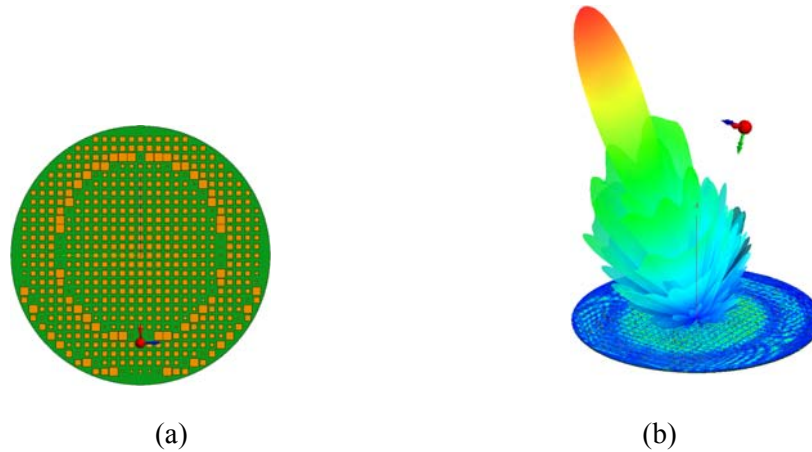


Fig. 2-25 Reflectarray antenna simulated using FEKO, (a) top view of the reflectarray, (b) 3D radiation pattern of the reflectarray.

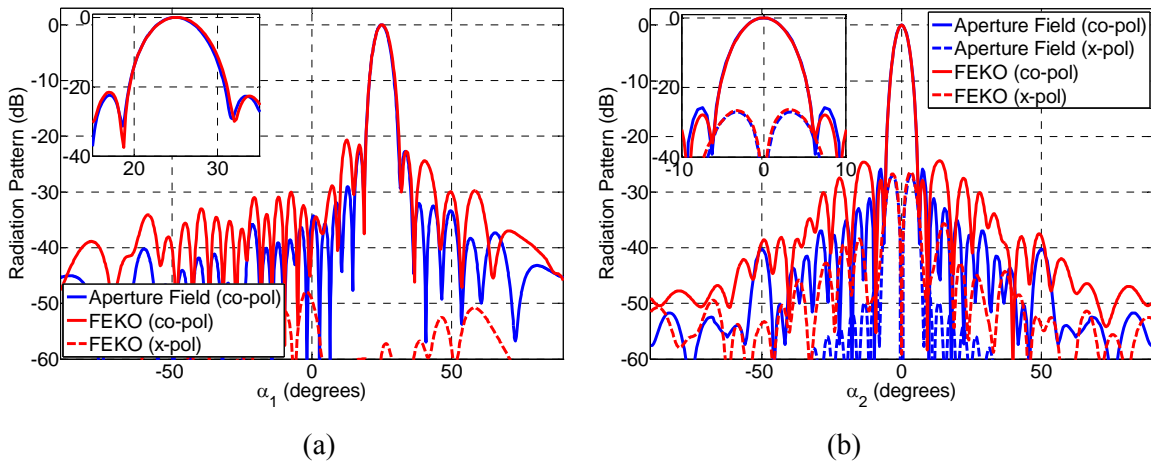


Fig. 2-26 Radiation patterns of reflectarray antenna: (a) P.P.1, (b) P.P.2.

It should be noted that the calculated co-polarized radiation pattern of the reflectarray antenna obtained using the array theory approach was similar to the aperture field results, and is not shown in this section for the sake of brevity.

Comparison of the results given here show that the analysis approaches presented in this

chapter accurately calculate: the general pattern shape, main beam direction, beam-width, and the side-lobe and cross-polarization level in the main beam area. Outside the main beam area, however, some discrepancies are observed between these results. These are primarily due to element design approximations, mutual coupling, and edge diffraction effects that are not taken into account in the analysis approaches. In particular, comparison between the ideal phase shift and the phase shift obtained by the reflectarray elements, Fig. 2-27, indicates that while the reflectarray aperture does indeed generate a phase shift which creates the collimated beam, this difference in phase shift is the primary reason for the discrepancies in the radiation pattern.

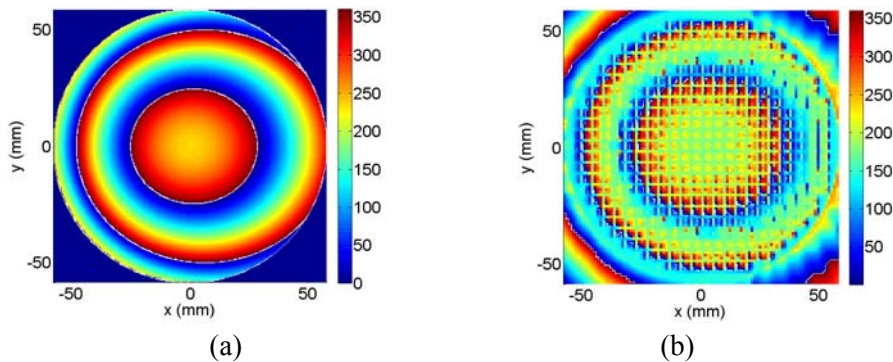


Fig. 2-27 Phase shift on the reflectarray aperture, (a) ideal phase shift, (b) phase shift obtained by the reflectarray elements.

To better observe the difference between the ideal phase shift and the phase shift obtained by the reflectarray elements, the phase distribution along the x-axis ($y=0$) is also given in Fig. 2-28.

It is implicit that a full-wave simulation will provide accurate results; however, the main disadvantage of full-wave simulations is the high computational time and resources required. In total, the full-wave simulation here required 29.56 GB of memory with a CPU time of 26.97 hours on an 8 core 2.66 GHz Intel(R) Xeon(R) E5430 computer. In comparison, the CPU time for the array theory and aperture field calculations were 1.78 sec. and 46.4 sec. on the same computer using a single core, respectively. It is worthwhile to point out that in general the classical approaches have limited accuracy, and when accurate radiation pattern computation in

the entire 3D space is required, full-wave simulation of the reflectarray system is necessary.

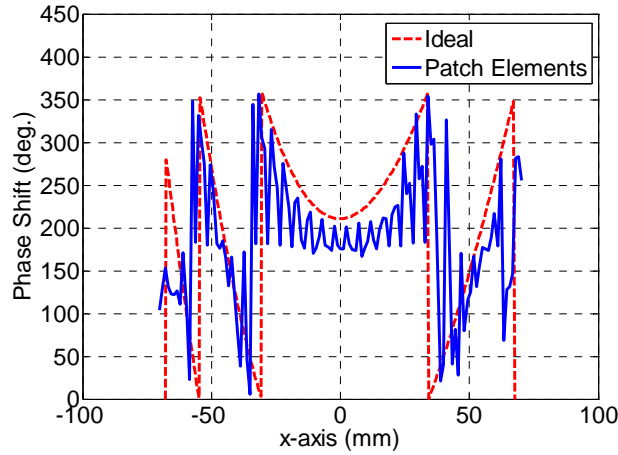


Fig. 2-28 The progressive phase shift on the reflectarray aperture.

2.4.5 Considerations for the Array Theory and Aperture Field Analysis Approaches

In the array theory formulation, the radiation pattern of the reflectarray antenna is computed using (2-13), which takes into account the element receive (R_x) and transmit (T_x) patterns. As discussed earlier, the elements are modeled with a cosine q_e radiation pattern, where in most cases $q_e = 1$. In general an isotropic element pattern may be assumed for the elements of large reflectarrays. However, it is interesting to observe the effects of element pattern on the radiation pattern of the reflectarray antenna. To study this effect we consider the same off-broadside system studied in section 2.4.2. The radiation pattern in the principal plane is given in Fig. 2-29 for four different cases.

From these results it can be seen that although the radiation patterns show a close agreement around the area of the main beam, a noticeable difference in the pattern shape is observed in the off-main beam areas. In particular, the element transmit pattern plays an important role here, where in comparison almost 10 dB difference is observed in the minor lobes. Similar results were observed in the other principle plane. In addition note that when the element transmit mode

pattern is ignored, the antenna beam width is slightly wider, which would also correspond to a higher computed directivity.

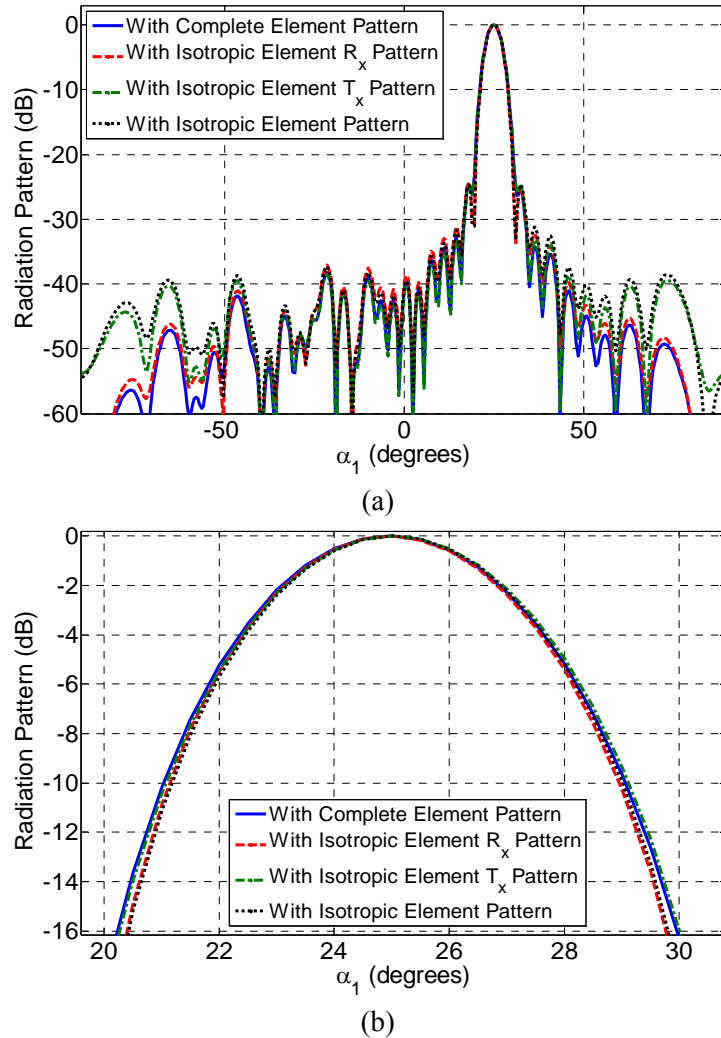


Fig. 2-29 Radiation pattern of the reflectarray antenna and the effect of element pattern: (a) P.P.1, (b) P.P.1 zoomed view.

The aim of this study was to place emphasis on the importance of the element pattern shape in the radiation analysis of reflectarray antennas. While for the square type patch elements studied here the element pattern was a simple cosine model, accurately determining the element pattern shape is essential before one computes the radiation pattern. More discussion on this topic is given in Chapter 7.

The aperture field approach is based on the principle of equivalence. It was discussed earlier that the radiation pattern of the antenna can be obtained using any of the three variations of equivalence principle, i.e., only magnetic currents, only electric currents, and both electric and magnetic currents. To study this numerically, we consider the same off-broadside reflectarray system studied in section 2.4.2. The radiation pattern in the principal plane is given in Fig. 2-30 for the three cases. Similar results were observed in the other principle plane.

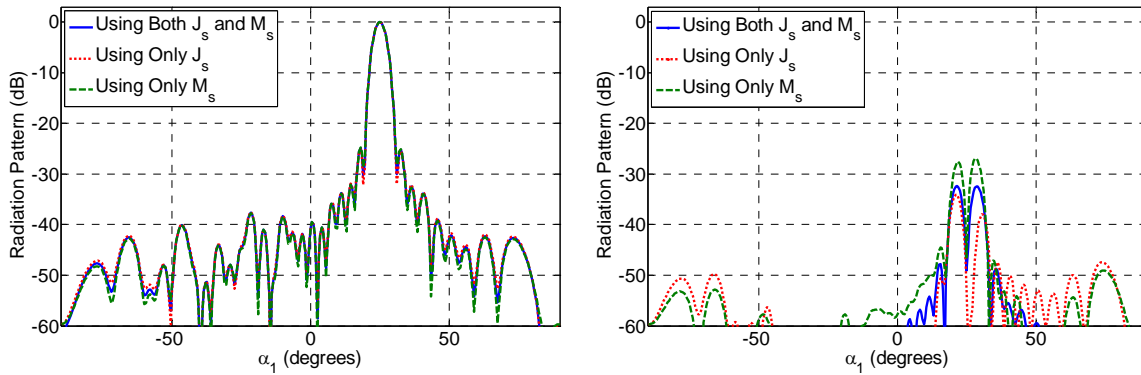


Fig. 2-30 Radiation pattern of the reflectarray antenna and the effect of aperture currents in equivalence principle.

These results show that as expected the co-polarized radiation pattern obtained by these three methods are almost identical and either approach can be applied. On the other hand, some difference is observed in the cross-polarized radiation patterns. In general, using both electric and magnetic fields on the aperture yields a better representation of the problem, and as such it is expected that using the first equivalence of principle is the most accurate analysis approach. This was also observed in the results given in Fig. 2-26 where the analytical results were compared to full-wave simulations.

CHAPTER III

SUB-WAVELENGTH ELEMENT TECHNIQUE FOR BANDWIDTH IMPROVEMENT

In this chapter, a novel broadband technique is introduced for reflectarray antenna elements. This is achieved by designing sub-wavelength elements instead of the conventional half-wavelength designs. A new definition of phase error is introduced to analyze the phase behavior of reflectarray elements. Numerical studies are then performed to understand the broadband mechanism of sub-wavelength elements. Based on these studies two Ka-band reflectarrays are designed using variable size square patches. One is designed using the conventional $\lambda/2$ elements, and the other one with $\lambda/3$ elements. While both antennas demonstrated good performance, the reflectarray designed with closely spaced elements showed a 36% increase in the gain bandwidth. To further improve the practical fabrication barriers of sub-wavelength designs at high frequencies, double-layer sub-wavelength reflectarray elements are also studied. It is demonstrated that combining the multi-layer approach with the sub-wavelength technique can increase the bandwidth of the antenna while considering practical fabrication tolerances. The gain bandwidths of reflectarray antennas using single- and double-layer elements with half-wavelength and sub-wavelength unit-cells are investigated numerically. A Ka-band reflectarray with a gain of 32.5 dB at 32 GHz, and a 1 dB gain bandwidth of 19.1% has been demonstrated using double-layer elements with a periodicity of $\lambda/4$.

3.1 Bandwidth Limitation in Reflectarray Antennas

As discussed earlier, microstrip reflectarrays offer several advantageous features compared to parabolic reflectors. They are low profile, low mass, easy to fabricate and transport, and most notably its printing process results in a low fabrication cost. On the other hand, despite all these advantages, the major drawback of reflectarray antennas is its inherent narrow band characteristic. While the bandwidth of the reflectarray antenna generally depends on several factors, such as aperture size, element design, and focal length, it is no match for a parabolic reflector, which theoretically has an infinite bandwidth. The bandwidth of a reflectarray is limited by two factors. The first is the bandwidth of the patch elements, and the second is the differential spatial delay.

The bandwidth limitation caused by the radiating elements is the major concern for moderate size reflectarrays. Microstrip patches on a thin dielectric layer are usually used as radiating elements, and their narrowband characteristics limit the bandwidth of the reflectarray. For patch elements using phase/time delay lines, the element bandwidth is normally determined by the matching of the input impedance of the element [33]. The same phenomenon has been observed in aperture-coupled patches [34]. For variable size patch elements, the input impedance bandwidth makes no sense, since the phase shift is obtained by varying the resonant length of printed patches. For these designs the limitation usually arises from the fact that one has to use a very thin dielectric in order to achieve a sufficient range of phase shift ($> 300^\circ$). In summary, reflectarray antennas have a narrow bandwidth because the nonlinear S-shape curve of the elements phase response is very sensitive to frequency variations near resonance. Therefore various approaches have been demonstrated over the years to improve the bandwidth of the reflectarray antenna elements, such as multi-layer structures [8], single-layer multi-resonant

designs [35], and aperture coupled lines.

For large size reflectarrays, the bandwidth is mainly influenced by the effect of the differential spatial delay. To illustrate this effect, let's consider the differential spatial phase delay for two arbitrary elements on the reflectarray aperture. Here, ΔS , is the phase difference between the two paths S_1 and S_2 from the feed to the two elements. This ΔS can be many multiples of the wavelength (λ_0) at the center operating frequency, which can be expressed as

$$\Delta S = (N + d)\lambda_0. \quad (3-1)$$

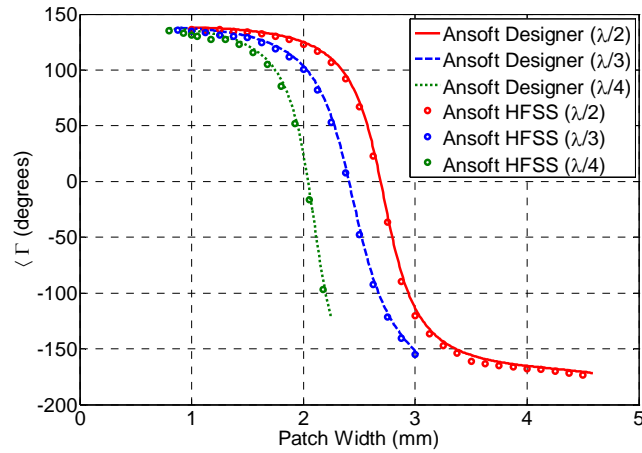
Here N is an integer and d is a fractional number of a free space wavelength. In traditional reflectarray element design, d is compensated by an appropriate phase shift, which is achieved by the reflectarray element at the center design frequency. As the frequency changes, the differential phase delay will also change. At an off-center frequency, the differential spatial delay becomes $(N + d)(\lambda_0 + \Delta\lambda)$, however, the compensated phase is fixed only for the center frequency. In other words, the amount of phase change required for the element at the off-center frequency will be $(N + d)(\Delta\lambda)$, which can be a significant portion of the wavelength. As a result, a frequency excursion phase error will be generated on the reflectarray aperture. This phenomenon is observed in all planar reflectarray antennas; however, the amount of frequency excursion error increases as the aperture size increases, and becomes the major factor in bandwidth limitation for large reflectarrays. To reduce this, the integer number N must be reduced. Several techniques have been introduced to address this problem, such as time-delay lines, which use $(N + d)\lambda_0$ for phase delay compensation at the center frequency [9]. Other approaches use large f/D ratios, or piecewise-flat curved reflectarrays [36] to minimize the path difference.

3.2 Reflection Properties of Sub-Wavelength Elements

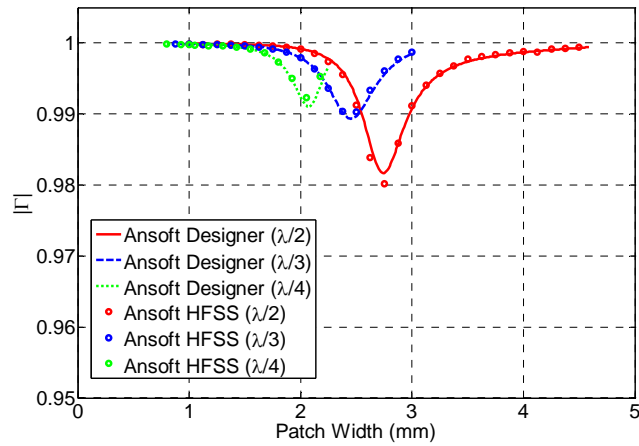
Traditionally the reflectarray phasing elements are designed with unit-cell sizes around $\lambda/2$. Recent advances on metamaterials [37] reveal that similar reflection phase response can also be realized using sub-wavelength elements. For a reflectarray design, as long as a sufficient phase range is obtained with the element, smaller unit-cell periodicities can be used for the design. The aim of the study here is to compare the reflection properties of reflectarray phasing elements with periodicities smaller than half-wavelength. Variable size approach is used in these element designs, and the main difference is the selection of element periodicity. In particular, $\lambda/2$, $\lambda/3$, and $\lambda/4$ are selected as the periodicities for this study. Although smaller periodicities such as $\lambda/10$ can be selected in the analysis and design, it will bring difficulties to the fabrication tolerance and increase the fabrication cost.

A 20 mil Rogers 5880 substrate ($\epsilon_r = 2.2$) is used here for this study. The commercial electromagnetic software packages Ansoft Designer and Ansys HFSS are used for the unit-cell analysis. The reflection coefficients versus patch size at the design frequency (32 GHz) for normal incidence are given in Fig. 3-1. It can be seen that the results obtained from both software packages are in close agreement with each other. Comparison between the reflection magnitudes of the elements shows that as the unit-cell size decreases, the element loss also decreases. While the reflection coefficients for all the elements in this study are larger than 98%, mainly due to the low-loss properties of the substrate, sub-wavelength elements can potentially reduce the element losses [38]. On the other hand, comparison between the reflection phases of the elements shows that as the unit-cell size decreases the phase range is reduced and the slope inclination becomes more vertical, essentially increasing the quantization error in the fabrication. More discussion on the phase range of sub-wavelength elements and the effect of gap size between the patches will

be given in a subsequent section. It is important to point out that in general the reflection characteristics are angle dependent and oblique incidence needs to be considered, however, it has been shown that normal incidence can present good approximations for incidence angles up to 30° .



(a)



(b)

Fig. 3-1 Reflection coefficients versus patch size at the center frequency 32 GHz for $\lambda/2$, $\lambda/3$, and $\lambda/4$ unit-cells with normal incidence: (a) phase, (b) magnitude.

In the unit-cell analysis here a periodic boundary condition is being used to account for the coupling between the unit-cell elements. The coupling between the elements is a function of the

patch size and the gap between the patches. For a fixed unit-cell size, the coupling between the patch elements increases by reducing the spacing between them. However, if the size of the unit-cell is reduced, a closer spacing between the patch elements is required to achieve the same level of coupling for larger unit-cell sizes. Consequently, this would mean that smaller unit-cell sizes with the same gap size would have a weaker coupling between the elements, which would reduce the phase range versus patch size for these elements.

3.3 Phase Error Analysis of Sub-Wavelength Reflectarrays

3.3.1 Element Phase Error Analysis

Regardless of the choice of phasing elements used for the design, reflectarray elements are selected to satisfy the required phase at the design frequency. However, as the frequency changes, the required phase between any two elements in the array will also change. This will ultimately introduce phase errors in the array, which result in pattern deterioration, gain reduction, and ultimately bandwidth limitations of the antenna. It's worthwhile to point out that the frequency behavior of the phase difference is important here rather than the reflection phase of an individual element, since in a reflectarray design, only the phase difference between the elements is important to obtain the desired radiation pattern. Consequently, defining an element bandwidth for reflectarray phasing elements is not practical without considering the relative phase requirements of all the reflectarray elements. It is, however, possible to study the phase error by considering the frequency behavior of the reflectarray elements for certain relative phase requirements.

Without loss of generality, we first consider a reflectarray with a main beam at the broadside direction ($\vec{r}_i, \hat{r}_o = 0$). The geometrical center of the reflectarray surface (point 1) is selected as a

phase reference and the center point of an arbitrarily element (point 2) is selected on the reflectarray surface to explain the required phase relation. The phase difference between these two points at the center frequency (f_0) satisfies the following relation:

$$\psi_2(f_0) - \psi_1(f_0) = k_0 \cdot (R_2 - R_1). \quad (3-2)$$

As the frequency changes, the phase difference will also change. An ideal phase relation is:

$$\psi_2(f) - \psi_1(f) = k \cdot (R_2 - R_1). \quad (3-3)$$

Combining (3-2) with (3-3), one can obtain:

$$\frac{\psi_2(f) - \psi_1(f)}{f} = \frac{\psi_2(f_0) - \psi_1(f_0)}{f_0} = \frac{2\pi}{c} \times (R_2 - R_1). \quad (3-4)$$

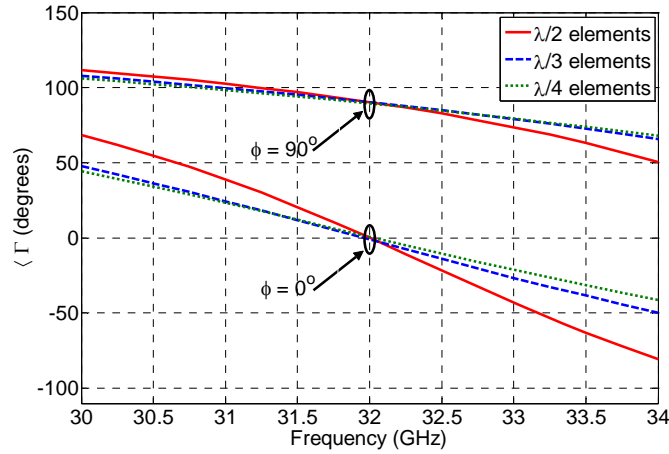
It is clear from above equations that the phase difference ($\Delta\psi(f) = \psi_2(f) - \psi_1(f)$) should be a function of frequency. When the frequency increases, the phase difference should also increase. In practice, this ideal frequency behavior of the phase difference cannot be satisfied. Depending on the element designing methods, phase errors will occur with frequency, which reduces the reflectarray gain and narrows the reflectarray bandwidth. To study this effect quantitatively, a phase error (PE) term is defined as follows:

$$PE(f) = \{\psi_2(f) - \psi_1(f)\} - k \cdot (R_2 - R_1). \quad (3-5)$$

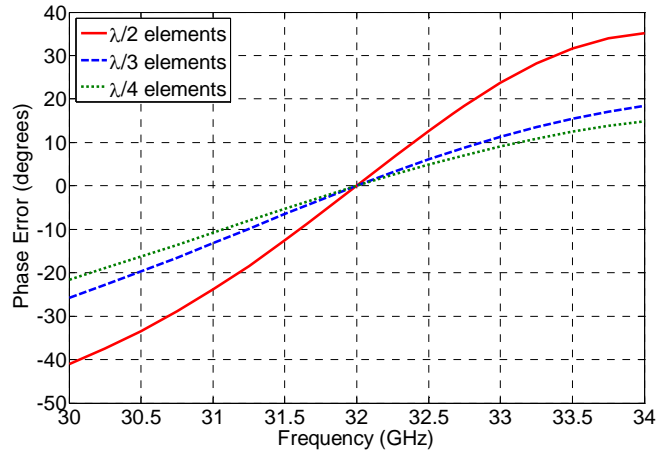
In this equation, the first term represents the frequency behavior of the elements, while the second term is the required spatial phase delay. In total this equation represents the phase error of elements relative to a certain phase requirement. Thus, it provides a good measure to compare different element design methods: the smaller the phase error, the wider the reflectarray bandwidth. It should be pointed out that in this phase error formula, the quantized phase of the reflectarray elements will result in a non-zero phase error at the center frequency (f_0), however, quantization phase error is usually small in comparison.

It has been shown that reflectarray antennas using sub-wavelength aperture-coupled reflectarray elements can improve the bandwidth of the antenna [39]. In addition, in a theoretical study it was shown that a reflectarray using closely spaced patch elements can also improve the bandwidth of the antenna [10]. While no analytical explanation is presented in either reference, the main reason for this bandwidth improvement is attributed to the fact that sub-wavelength elements don't operate near the resonance mode. To get a better understanding on why the sub-wavelength elements can improve the bandwidth of reflectarray antennas, we analyze the frequency response of half-wavelength and sub-wavelength reflectarray elements.

Consider the case where two elements on the aperture are required to have a 90° relative phase difference. Using the element data in Fig. 3-1, for a zero degree reflection phase, the patch size will be 2.69, 2.41, and 2.04 mm for $\lambda/2$, $\lambda/3$, and $\lambda/4$ designs. When a 90° reflection phase is required, the patch size should be 2.41, 2.1, and 1.81 mm. Fig. 3-2 (a) shows how the reflection phases of these 0° and 90° elements vary with frequency. It is observed that $\lambda/2$, $\lambda/3$, and $\lambda/4$ designs have different frequency behaviors for the element reflection phase. When the frequency changes, the closely spaced elements show a smaller phase variation with frequency. As discussed previously, it is the frequency behavior of the phase difference that determines the reflectarray bandwidth. Thus, the phase error curves of the $\lambda/2$, $\lambda/3$, and $\lambda/4$ designs, as defined in (3-5), are obtained and plotted in Fig. 3-2 (b). It is clear from this figure that the closely spaced elements have a smaller phase error over the frequency than the half-wavelength elements. Similar studies have been performed on the reflectarray elements with different relative phase requirements, and the same observation is obtained. Therefore, it is clear that the reflectarray bandwidth can be increased by using closely spaced elements.



(a)



(b)

Fig. 3-2 (a) Reflection phases versus frequency for 0° and 90° elements for $\lambda/2$, $\lambda/3$, and $\lambda/4$ unit-cells. (b) Phase errors for a 90° relative phase difference versus frequency for $\lambda/2$, $\lambda/3$, and $\lambda/4$ unit-cells.

3.3.2 Aperture Phase Error Analysis

Using the formulation presented in the previous section, the phase error between any two elements with an arbitrary phase requirement can be calculated. However, to get a better understanding on the bandwidth performance of a reflectarray antenna, it is necessary to observe the phase error performance for all the elements with respect to a certain reference point. Theoretically, the relative phase requirement on an array surface can be calculated with respect to any element in the array. However, since in most reflectarray designs the feed is pointing to

the geometrical center of the array, we consider this point as the reference for phase calculations.

The general formula for an ideal phase relation is defined as

$$\psi_i(f) - \psi_{ref}(f) = k \cdot \left\{ R_i - R_{ref} - (\bar{r}_i \cdot \hat{r}_o - \bar{r}_{ref} \cdot \hat{r}_o) \right\}. \quad (3-6)$$

Since the center element is used as the phase reference, $|\bar{r}_{ref}| = 0$. The relative phase error (*PE*)

for the i^{th} element in the array with respect to the center of the array can then be calculated as

$$PE_i(f) = \left\{ \psi_i(f) - \psi_{ref}(f) \right\} - k \cdot \left\{ R_i - R_{ref} - \bar{r}_i \cdot \hat{r}_o \right\}. \quad (3-7)$$

This definition of phase error on the array surface takes into account the relative phase requirements for every element of the array for a general array geometry and beam direction. To further expand this phase error formulation for a practical case, the feed illumination must also be taken into account. The reason is that the excitation of each element will determine the overall effect of the phase error of that individual element on the reflectarray performance. The illumination of a reflectarray antenna is calculated using the normalized radiation pattern of the feed horn simulated as a $Cos^q(\theta)$ function, which is the widely adopted model to approximate practical feed patterns. The weighted phase error (*WPE*) is then defined as the product of the phase error and the normalized array illumination, i.e.,

$$WPE_i(f) = PE_i(f) \cdot \text{Normalized Illumination}_i(f). \quad (3-8)$$

To quantitatively analyze the performance of the sub-wavelength phasing elements, we consider a practical example of a Ka-band reflectarray. A circular aperture reflectarray with a diameter of 159 mm is designed for the operating frequency of 32 GHz to generate a beam in the direction of $(\theta, \varphi) = (25^\circ, 0^\circ)$. The offset feed horn position is $X_{feed} = -45.9 \text{ mm}$, $Y_{feed} = 0 \text{ mm}$, $Z_{feed} = 98.4 \text{ mm}$ based on the array coordinate system in Fig. 2-3. For the horn model used in this study, the power q of the feed radiation pattern varies linearly from 5 at 30 GHz to 8.3 at 34

GHz. From the system design specifications, the location of all the array elements, the required element phase shift, and the illumination on the array surface can be calculated. The patch dimensions are then determined from the unit-cell simulations at the center design frequency of 32 GHz. From these patch size dimensions, the frequency behavior of the elements reflection phase is obtained across the band. The weighted phase error on the array surface can then be calculated at any specified frequency using (3-8).

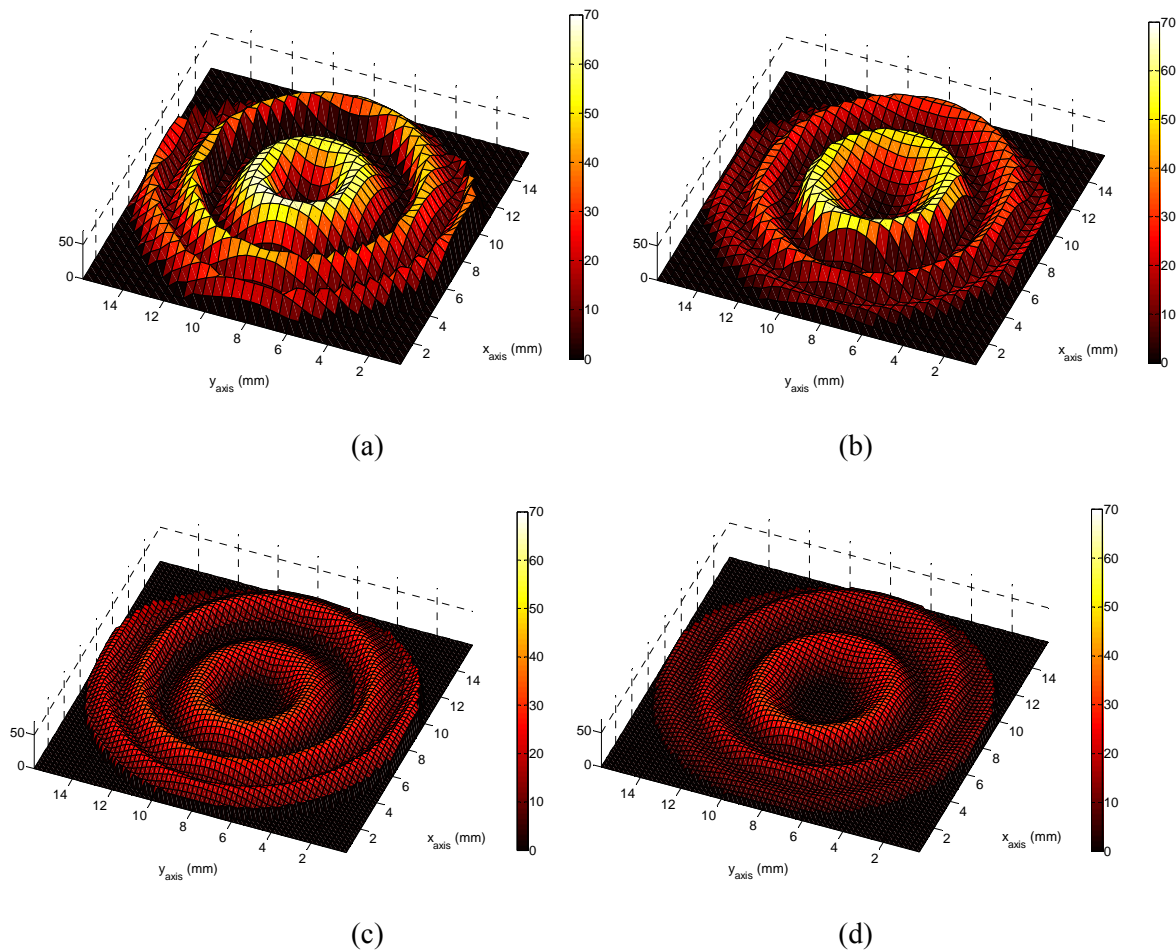


Fig. 3-3 Absolute value of weighted phase error on the reflectarray aperture: (a) $\lambda/2$ elements – 30 GHz, (b) $\lambda/2$ elements – 34 GHz, (c) $\lambda/4$ elements – 30 GHz, (d) $\lambda/4$ elements – 34 GHz.

The weighted phase error on the array surface at two off-center frequencies (30 and 34 GHz) is given in Fig. 3-3 for two designs. One design uses the conventional $\lambda/2$ elements, while the other

reflectarray is designed with $\lambda/4$ unit-cell periodicity. It can be seen that in comparison between the two designs, the sub-wavelength design shows a significantly smaller phase error over the reflectarray aperture, demonstrating the bandwidth improvement of this technique. Similar results were observed at different frequencies across the band. It should be noted that in these results, the aperture phase errors at off-center frequencies are normalized to the center frequency. In other words, the quantization errors associated with the design are not taken into account. Although as mentioned earlier, the effect of quantization errors is not significant in these designs.

3.4 Design of Ka-band Reflectarrays Using Sub-Wavelength Elements

3.4.1 Prototype Fabrication

The minimum gap size between the patch elements is a critical factor in controlling the maximum achievable phasing range. In our designs a minimum gap size of 0.1 mm was dictated by the size of the smallest drill bit in our LPKF ProtoMat S62 milling machine. By enforcing this fabrication limit in the unit-cell simulations, the phasing range of the elements is reduced to 310° , 290° , and 247° for $\lambda/2$, $\lambda/3$, and $\lambda/4$ elements, respectively. Typically, a phasing range around 300° is required for a reflectarray design. This achievable phasing range of elements, which is directly related to fabrication tolerance of the gap sizes, should be viewed as the lower limit in selecting sub-wavelength elements for the reflectarray with variable size patches. As the phase range of the elements is decreased, the antenna gain decreases and the sidelobe level increases; however, the antenna bandwidth is mainly determined by the frequency behavior of the phasing elements. Considering the phase range of elements studied here, our analysis showed that going from $\lambda/2$ to $\lambda/3$ elements did not result in any gain reduction or increase in sidelobes. For a $\lambda/4$ design however, the reduction of phase range resulted in almost 0.5 dB loss in antenna gain and 6 dB increase in sidelobe level relative to the $\lambda/2$ design. This 0.5 dB loss is acceptable

relative to the high gain reflectarray, since this $\lambda/4$ design is adding an additional advantage of a wider reflectarray bandwidth; however, this design was not suitable for demonstration purposes. In summary there is a tradeoff between the reflectarray gain and bandwidth if one would use sub-wavelength elements.

Based on the above considerations, two Ka-band microstrip reflectarrays are designed and fabricated for the operating frequency of 32 GHz. One is designed using the conventional $\lambda/2$ elements and the other one is designed using $\lambda/3$ elements. Both antennas have a circular aperture with a diameter of 17λ at the design frequency and are fabricated on a 20 mil Rogers 5880 substrate. The offset feed horn ($\theta_i = 25^\circ$) is positioned at $X_{feed} = -45.9 \text{ mm}$, $Y_{feed} = 0 \text{ mm}$, $Z_{feed} = 98.4 \text{ mm}$ based on the array coordinate system in Fig. 2-3. The total number of square patch elements is 848 and 1941 for the $\lambda/2$ and $\lambda/3$ arrays, respectively, and the elements phase is adjusted to scan the main beam 25° off broadside to minimize feed blockage. Photographs of the fabricated reflectarrays are shown in Fig. 3-4.

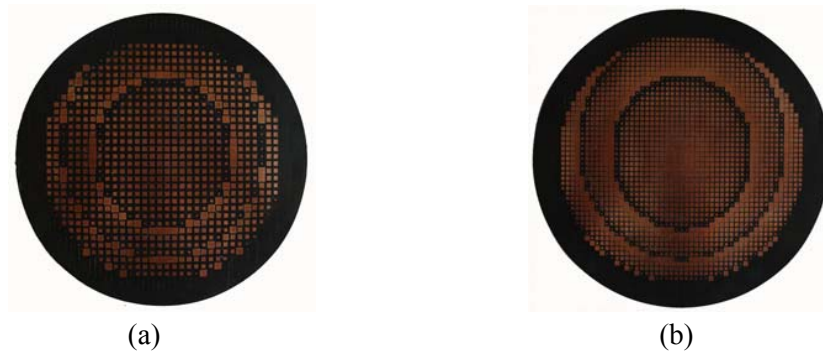


Fig. 3-4 Photographs of the fabricated arrays: (a) $\lambda/2$ array with 848 square patches, (b) $\lambda/3$ array with 1941 square patches.

3.4.1 Measurement of Prototypes

Photographs of the reflectarray systems are shown in Fig. 3-5. The feed antenna is a circularly polarized (LHCP) corrugated conical horn. A wooden frame is designed to support both the array plane and the horn. Both prototypes are measured by the NSI system. The antennas performances

were measured over the frequency range from 30.0 to 35.0 GHz which was set by the limits of the feed horn and the Ka-band measurement probe of our NSI near-field system. The setup parameters for the measurements are listed in Table 3-1.



Fig. 3-5 Photographs of the fabricated arrays: (a) $\lambda/2$ array with 848 square patches, (b) $\lambda/3$ array with 1941 square patches.

Table 3-1 Measurement setup for the NSI system

Variable	Value	Description
Z (input)	16.5 inch (44.7 λ @ 32 GHz)	distance between the array and the sampling plane
θ (input)	45°	angle range of the far field
f_H (input)	35 GHz	highest frequency
L_x	20.0 inch (54.186 λ @ 32 GHz)	length of sampling plane
L_y	20.0 inch (54.186 λ @ 32 GHz)	width of sampling plane
N_x	125	number of sampling points in x
N_y	125	number of sampling points in y
n_x	0.16129 inch (2.3 samples per λ)	sampling rate in x direction
n_y	0.16129 inch (2.3 samples per λ)	sampling rate in x direction

The near-field patterns of both prototypes at 32 GHz are given in Figs. 3-6 and 3-7. It can be seen that in the main beam area (magnitude peaks), the phases of both components show a parallel phase distribution, indicating that a parallel phase front is formed by the phase shift of the reflectarray elements.

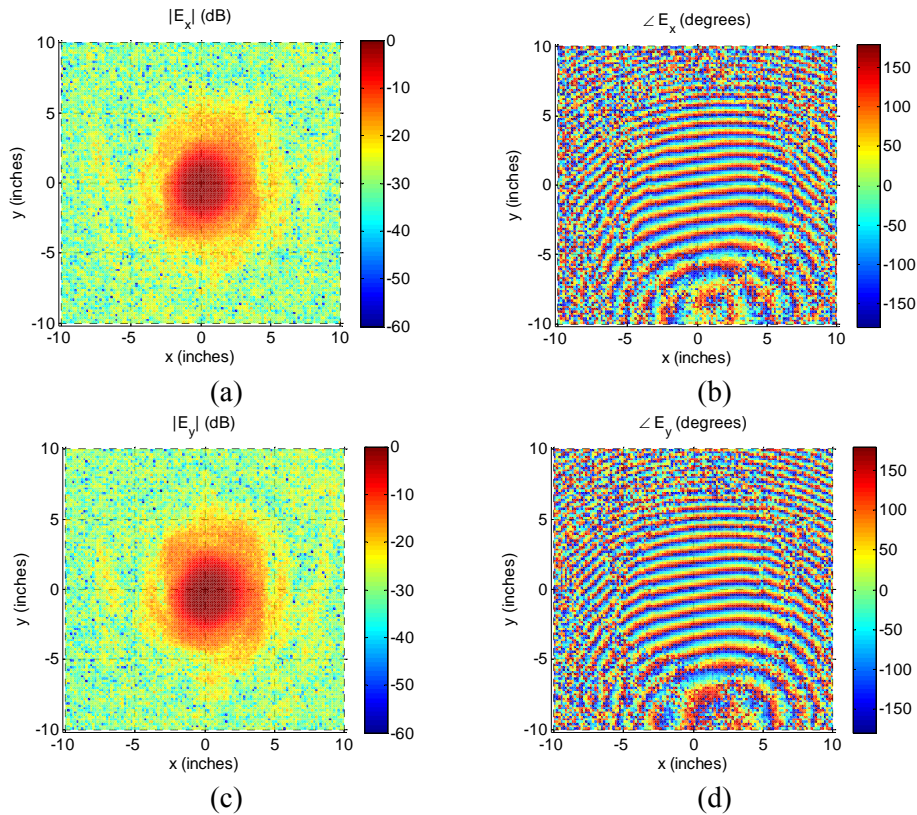


Fig. 3-6 Measured near-field components of the $\lambda/2$ prototype at 32 GHz: (a) magnitude of E_x , (b) phase of E_x , (c) magnitude of E_y , phase of E_y .

The vertical plane radiation patterns at 32 GHz for both antennas are shown in Fig. 3-8. Note that the main beam is correctly scanned to 25° and the sidelobe levels are below -22 dB for both antennas. The simulated results here were obtained using the array theory formulation described in chapter 2. It can be seen that the measured and simulated results show a good agreement in the main lobe; however, some discrepancies exist in the side lobe region. These are primarily due to the phase errors (fabrication and approximations in the unit-cell simulations) and alignment

errors. Similar results were also observed in the horizontal plane. At 32 GHz the measured -3dB beamwidth for the $\lambda/2$ array is 4.5° and 4.6° for vertical and horizontal planes, respectively, and the measured gain is 30.99 dB, which corresponds to an overall aperture efficiency of 44.0%. For the $\lambda/3$ array the measured -3dB beamwidth at 32 GHz is 4.4° and 4.6° for vertical and horizontal planes, respectively, and the measured gain is 30.95 dB, which corresponds to an overall aperture efficiency of 43.6%.

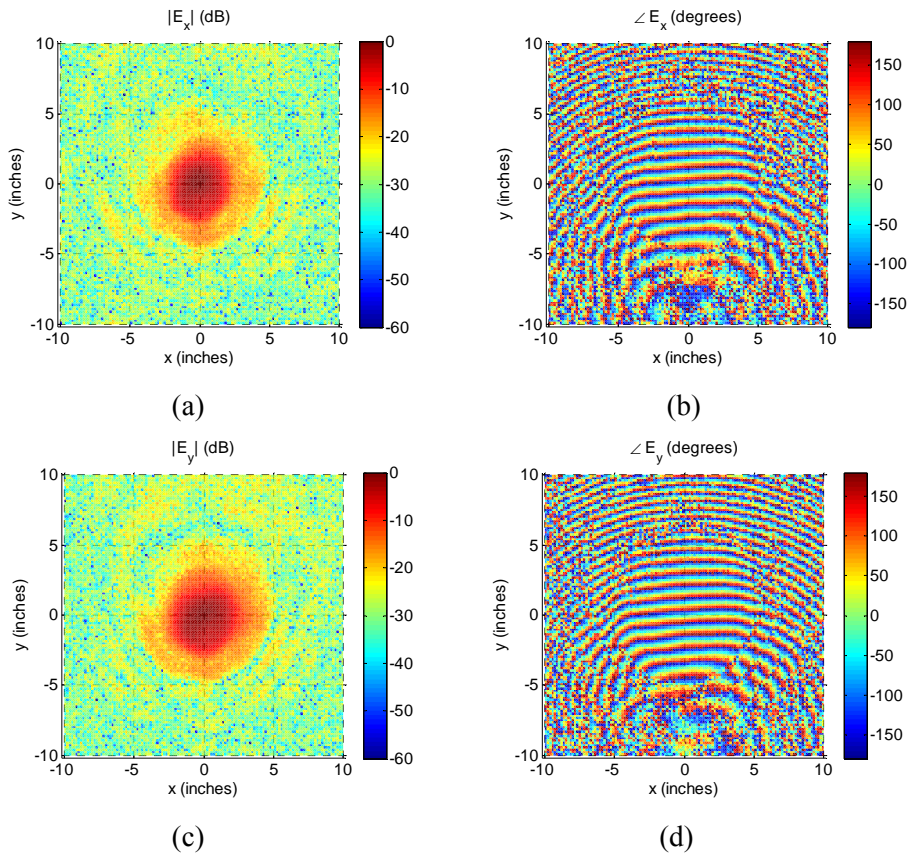


Fig. 3-7 Measured near-field components of the $\lambda/3$ prototype at 32 GHz: (a) magnitude of E_x , (b) phase of E_x , (c) magnitude of E_y , phase of E_y .

The frequency response of the antennas was also measured across the frequency range of 30 to 34 GHz. The measured gain and aperture efficiency of the antennas are given in Fig. 3-9. To observe the bandwidth improvement of the sub-wavelength element technique, a direct

comparison between the measured gains of the prototypes is also given in Fig. 3-10.

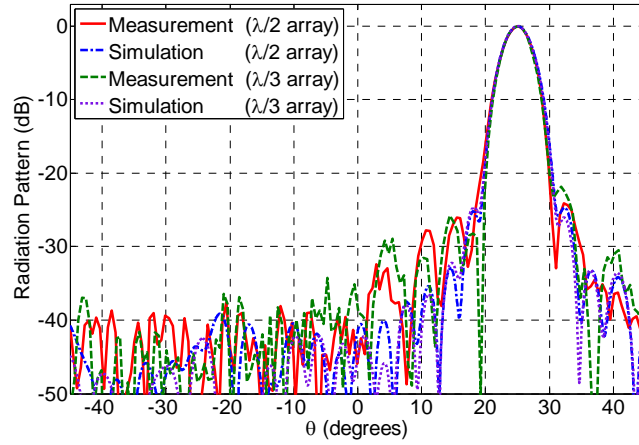


Fig. 3-8 Measured and simulated radiation patterns of the reflectarray antennas at 32 GHz in the elevation plane.

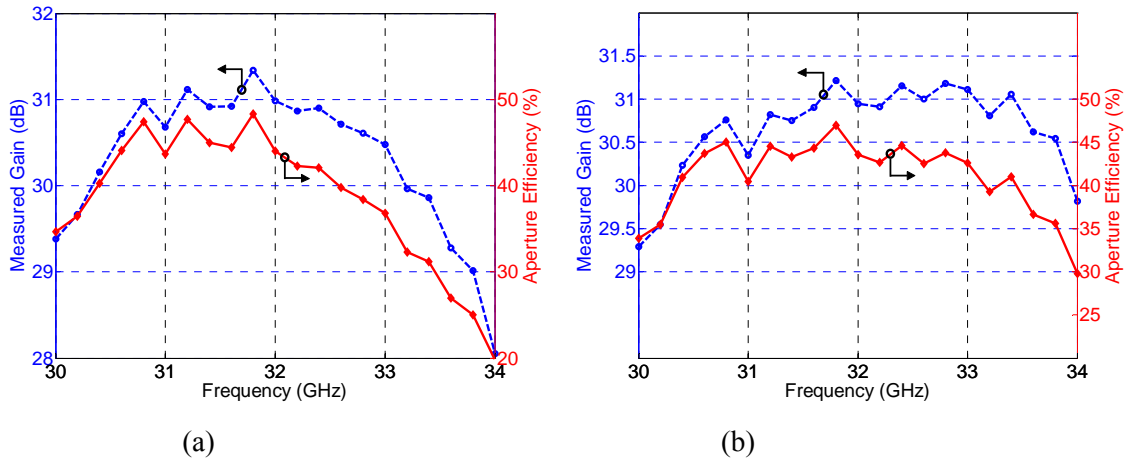


Fig. 3-9 Measured gain and aperture efficiency versus frequency for the prototypes: (a) $\lambda/2$ array, (b) $\lambda/3$ array.

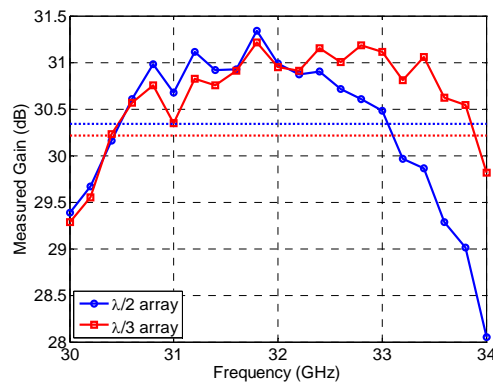


Fig. 3-10 Comparison between the measured gain versus frequency for the $\lambda/2$ and $\lambda/3$ array.

The 1 dB gain bandwidth of the $\lambda/2$ array is 8.0% and this antenna achieves its max gain of 31.34 dB at 31.8 GHz. The measured results also show that the $\lambda/3$ array achieves a considerable bandwidth improvement, where the 1 dB gain bandwidth has been increased to 10.9%. Similarly this antenna achieves its max gain of 31.22 dB at 31.8 GHz. The measured radiation patterns show a similar performance across the entire band except for a slight increase in sidelobe level at the extreme frequencies. It should be noted that the measured gain of the feed horn is 14.2 dB at 32 GHz and the variation across the 30 to 34 GHz band is less than 0.5 dB.

It is worthwhile to point out that as discussed earlier; the bandwidth of a reflectarray antenna is limited by two different factors, the bandwidth of the element and the bandwidth limitation by spatial phase delay. The sub-wavelength broadband technique studied here improves the reflectarray element bandwidth. Consequently this broadband technique is applicable to small size reflectarray antennas. As the size of the aperture increases the broadband effect of the sub-wavelength elements would be less effective due to the effect of the spatial phase delay which will become dominant. Our numerical results showed that for this Ka-band reflectarray going from $\lambda/2$ elements to $\lambda/3$ elements, the percentage of bandwidth improvement will be significantly reduced as the aperture diameter is increased. These numerical results are summarized in Table 3-2.

Table 3-2 Performance of sub-wavelength elements as a function of aperture size

Aperture diameter	10λ	20λ	30λ	40λ
Relative bandwidth improvement	61.63%	36.28%	22.25%	15.47%

3.5 Ka-band Reflectarrays Using Double-Layer Sub-Wavelength Elements

3.5.1 Fabrication Consideration and the Multi-Layer Technique

As discussed earlier, conventionally, the phasing elements of reflectarray antennas are

designed with unit-cell size on the order of $\lambda/2$. The sub-wavelength technique can improve the narrowband effects associated with the conventional designs, since the elements don't operate near the self-resonant dimensions. In fact the field distribution of sub-wavelength elements is indicative of a coupled-resonant behavior between the elements [38]. Although there is no theoretical limit on using smaller unit-cells in reflectarray designs, the fabrication tolerance of the patches becomes a critical factor at high frequencies. In particular, since most of the reflection phase range occurs for patches with very thin gaps, the fabrication tolerance of the gap sizes controls the smallest unit-cell dimensions which can be etched reliably.

To study the effect of the minimum gap size on the phase range of elements, we consider Ka-band reflectarray elements using variable patch sizes as shown in Fig. 3-11.

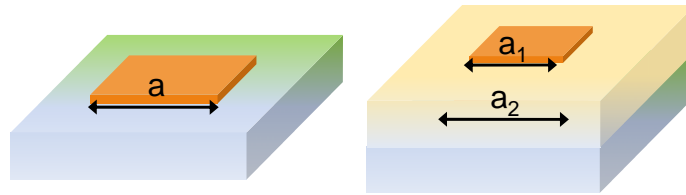


Fig. 3-11 Geometry of single-layer and double-layer reflectarray phasing elements.

The phase ranges of these elements with different unit-cell periodicities are obtained using Ansoft Designer and the results are summarized in Table 3-3. It should be noted that the results presented here are based on normal incidence approximation. It can be seen that for most single-layer designs with a very small gap size (0.001 mm) between the elements, a sufficient phase range (typically around 300°) can be achieved. However, practical fabrication tolerance limits the achievable phase range of elements. The minimum gap size of 0.1 mm used in practical designs is based on the fabrication capabilities of our LPKF ProtoMat S62 milling machine. For these Ka-band elements, reducing the unit-cell size from $\lambda/2$ to $\lambda/6$ results in an almost 200° loss of phase range. Furthermore, the limited fabrication tolerance of the patch sizes will also increase

the phase quantization errors within the above phase range. As a result, reflectarrays designed using single-layer sub-wavelength elements will show significant phase errors that degrade the antenna performance. In other words, the bandwidth improvement achieved by means of sub-wavelength elements will be accompanied by a reduction in antenna gain that is undesirable.

Table 3-3 Phase Range of Reflectarray Elements at 32 GHz

Design \ Unit-cell size	$\lambda/2$	$\lambda/3$	$\lambda/4$	$\lambda/6$
Single-layer (0.001 mm gap)	312.6°	304.8°	294.9°	261.8°
Single-layer (0.1 mm gap)	310.0°	292.5°	258.3°	100.3°
Double-layer (0.1 mm gap)	583.9°	323.0°	277.0°	214.5°

Another broadband technique that has received considerable attention is by the use of stacked patches [8]. This multi-resonance design can increase the phase range of the elements and improve the slope linearity of the phase curve. By integrating multi-resonance elements with sub-wavelength unit-cells we can take advantage of both broadband techniques. In addition, the phase range of the elements can be improved with the same fabrication tolerance. Comparing the phase range of single- and double-layer designs in Table 3-3, it is observed that the double layer designs can increase the achievable phase range of the elements as expected. The maximum element loss (including both dielectric and Ohmic losses) is less than 0.2 dB in all designs studied here. It is important to point out that as the unit-cell size decreases, the reflection loss decreases for both single- and double-layer designs. In addition the double-layer designs have a relatively smaller loss than the single-layer designs. It should be noted that for double-layer designs, the top patch size is usually considered to be a fraction of the lower patch size. Our parametric analysis showed that for the unit-cell periodicities studied here, a ratio of $a_1 = 0.7a_2$ provided a sufficient phase range. This ratio is used throughout this section for the double-layer

designs. In this study, each layer is a 20 mil Rogers Duroid 5880 substrate.

3.5.2 Phase Error Analysis and Bandwidth Study

To quantitatively analyze the performance of the double-layer sub-wavelength phasing elements we consider the same reflectarray system studied in section 3.3. The weighted phase error on the array surface is calculated using (3-8) at two off-center frequencies (30 and 34 GHz). These results are shown in Fig. 3-12 for two double-layer designs. One design uses $\lambda/2$ elements, while the other reflectarray is designed with $\lambda/4$ unit-cell periodicity. Comparing these with the results given in Fig. 3-3 for single-layer designs, it can be seen that as expected the double-layer designs show a significantly lower phase error on the aperture.

To observe the phase performance of double-layer sub-wavelength designs, let's compare the maximum aperture phase error of this design with the single-layer half-wavelength design. At 30 GHz, the maximum phase error for the single-layer $\lambda/2$ design is 70.47° , while for the double-layer $\lambda/4$ design this error is 21.16° . It can be seen that the double-layer phasing elements with $\lambda/4$ unit-cell periodicity show a much smaller phase error over the reflectarray aperture. Similar results were observed at different frequencies across the band.

To further illustrate the frequency response of the phase error, we define the average phase error of a reflectarray antenna as

$$\text{Average Phase Error}(f) = \frac{1}{N} \sum_{i=1}^N WPE_i(f). \quad (3-9)$$

Here N is the number of phasing elements of the reflectarray antenna. The average phase error defined here provides a single phase error number for any reflectarray system at every frequency. Using this definition it is possible to compare the performance of reflectarrays designed with different element design methods. These results are given in Fig. 3-13 for four reflectarrays

designed with single- and double-layer phasing elements.

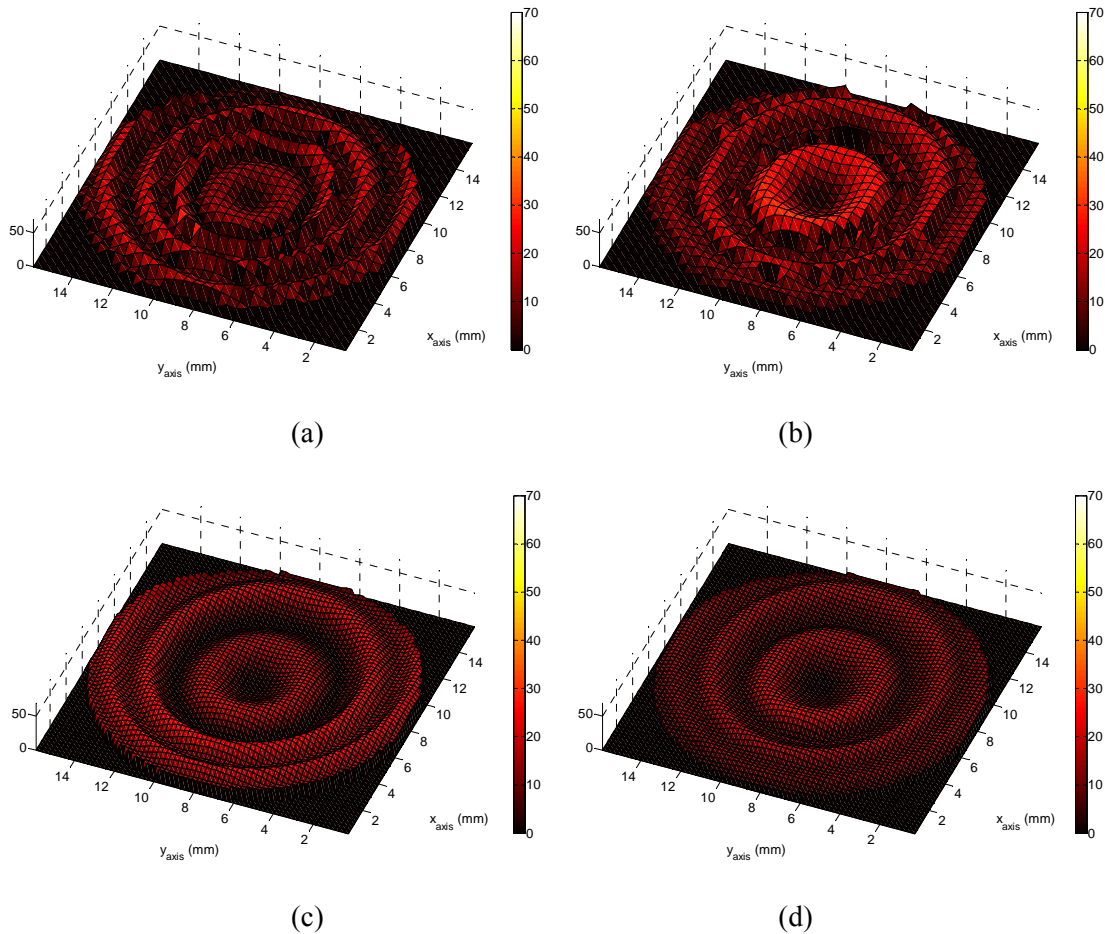


Fig. 3-12 Absolute value of weighted phase error on the reflectarray aperture for double-layer designs: (a) $\lambda/2$ elements – 30 GHz, (b) $\lambda/2$ elements – 34 GHz, (c) $\lambda/4$ elements – 30 GHz, (d) $\lambda/4$ elements – 34 GHz.

These results clearly demonstrate that the reflectarray designed with double-layer sub-wavelength elements has the best performance. A significantly reduced phase error is observed across the band which would result in a notable bandwidth improvement of the antenna.

To verify the broad-band behavior of double-layer sub-wavelength designs, the gain bandwidth of the reflectarray antennas is computed using the aperture field formulation described in chapter 2. The calculated gain here includes the spillover losses and the element losses in the

reflectarray. In addition the frequency behavior of the feed horn pattern and elements reflection characteristics are implemented into this calculation routine. Due to the limited phase range of Ka-band elements with a periodicity of $\lambda/6$ (Table 3-3), only $\lambda/2$ and $\lambda/4$ elements are studied here for the reflectarray gain comparison. The gain versus frequency is given in Fig. 3.14.

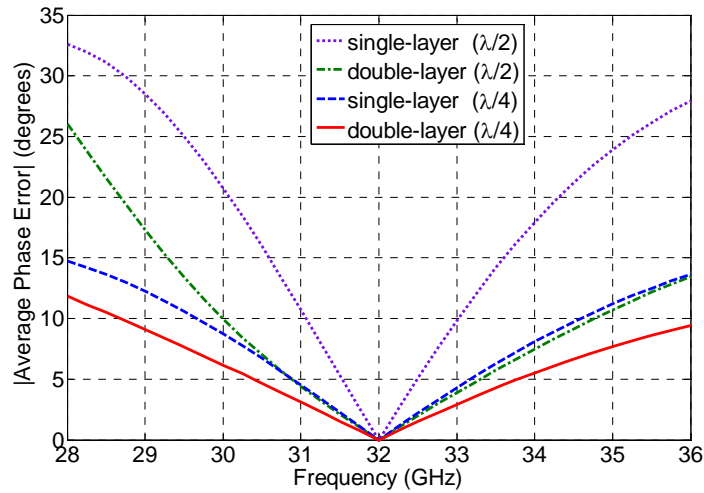


Fig. 3-13 Average phase error of the reflectarray antenna as a function of frequency for single and double-layer elements.

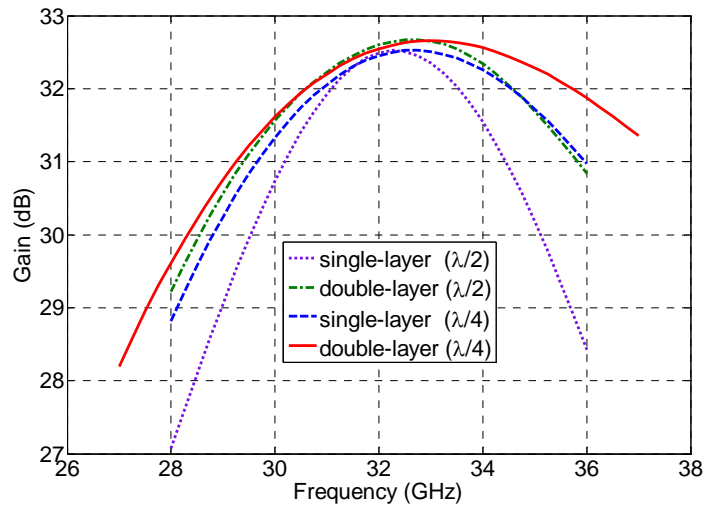


Fig. 3-14 Gain vs. frequency for single and double-layer reflectarrays using $\lambda/2$ and $\lambda/4$ elements.

From these results it is clear that a sub-wavelength double-layer reflectarray shows a significant

improvement in bandwidth where the bandwidth has been increased by more than 80% in comparison with a conventional single-layer half-wavelength design. The results are summarized in Table 3-3.

Table 3-4 Bandwidth Performance of the Reflectarray Antennas

Design	1 dB Gain Bandwidth (GHz)	Gain at 32 GHz
Single-layer ($\lambda/2$)	30.61 – 34.02 (10.55%)	32.49 dB
Double-layer ($\lambda/2$)	30.14 – 35.02 (14.98%)	32.60 dB
Single-layer ($\lambda/4$)	30.23 – 35.29 (15.45%)	32.45 dB
Double-layer ($\lambda/4$)	30.07 – 36.43 (19.13%)	32.55 dB

Comparing the antenna gain at 32 GHz, it is also observed that, for both unit-cell sizes, going from single-layer to double-layer increases the antenna gain by about 0.1 dB. This increase in antenna gain is mainly due to the fact that double-layer designs have a smaller reflection loss. It should be noted here that all phasing elements are designed with a minimum gap size of 0.1 mm.

CHAPTER IV

THz / INFRARED REFLECTARRAY ANTENNAS

In this chapter, reflectarray designs at infrared (IR) frequencies are investigated. At the short-wavelength region, material loss becomes an important consideration in reflectarray designs. Based on the measured properties of conductors and dielectrics at infrared frequency, the loss effects on the reflection magnitude and phase of reflectarray elements are investigated. It is revealed that when the material loss exceeds a certain limit, the element reflection phase will vary within a narrow phase range instead of a full 360° phase range. An equivalent circuit model is used to understand this phenomenon. Based on the investigation, alternative design methods for infrared reflectarrays are suggested to lower the loss effect. The low loss reflectarrays have great potential for infrared and visible range applications, such as a low profile planar concentrator for solar energy systems.

4.1 Reflectarray Antennas for Concentrating Solar Power Systems

Electromagnetic waves cover a wide frequency spectrum, including microwaves and optics. The wave behavior at both microwave and optical frequencies follows Maxwell's equations; hence many microwave concepts have been extended to optics, and in turn a lot of optical designs have been translated to microwave frequencies. For example, the invention of optical fiber [40], a kind of dielectric waveguide, has greatly propelled the development of optical communications and the Internet. In addition, resonant optical antennas [41], are recently being

studied that could contribute to the improvement of light emitters in the future.

Concentrating solar power (CSP) systems use mirrors or lenses to concentrate a large area of sunlight onto a small area. Compared to conventional solar panels, the CSP system has a significant cost advantage, since the solar collector is less expensive than an equivalent area of solar cells. In most cases CSP systems using mirrors are preferable to lenses, mainly because they have a lower cost. These mirrors are either parabolic or Fresnel reflectors that focus the sunlight at the reflector's focal point. In comparison between these two types of reflectors, flat mirrors allow more reflective surface in the same amount of space as a parabolic reflector, thus capturing more of the available sunlight, and they are much cheaper than parabolic reflectors.

The aim of the study here is to investigate the feasibility of using reflectarray antennas as reflectors for CSP systems. The reflectarray has a flat plane and therefore a larger reflective surface compared to a parabolic reflector, and it has a much higher efficiency compared to a Fresnel reflector. In addition, low-profile and planar reflectarrays are easy to fabricate and integrate, and the individually controlled element phase increases the focusing flexibility and enhances the system capability. For example, reflectarrays can focus the solar energy onto a specified area with high concentration and uniform distribution instead of focusing all energy at a specific point. This feature is desirable in a CSP system because it avoids over-illumination at a specific point and provides high efficiency over the entire solar cell surfaces. On the other hand, several challenges and technological limitations exist here which need to be resolved. For a practical system design, efficiency, bandwidth, and fabrication capabilities are of major concerns and must be investigated. While several methods to improve the efficiency and bandwidth of reflectarrays are available in the literature, currently a major concern for optical designs is the fabrication limitations. The practical barrier for a CSP system design is generally the fabrication

capability at a competitive cost. In recent years, nanotechnology has emerged as a revolutionary technological breakthrough, which has led to the creation of many new materials and devices with a wide range of applications in medicine, electronics, and energy production. Thanks to the latest progress in nano-fabrication techniques, the fabrication accuracy has been significantly improved at an affordable cost [42]. Therefore, it is now possible to design a reflectarray antenna with nanometer accuracy for far-infrared ($\lambda \sim 10 \mu\text{m}$) applications. It is believed that with the rapid growth of nano-fabrication techniques, this concept would be extended to optical frequencies in the near future.

4.2 Properties of Materials and THz/Infrared Frequencies

Reflectarray antenna design at terahertz and optical frequencies is a rather new and challenging study [43]. To design a reflectarray operating at infrared frequency with a $10 \mu\text{m}$ wavelength, the size of reflectarray element is around $5 \mu\text{m}$ (half wavelength). Material loss is always a concern in reflectarray designs [44]. At microwave frequencies, since a high conductivity is obtained for conductors and a low loss tangent can be achieved for substrates, the gain loss of a reflectarray due to the materials is relatively small. At optical frequencies however, the losses in substrates and conductors can be severe, and their effects on reflectarray element designs could become a critical issue. Thus it is important to understand the loss mechanism for the elements and accurately model the losses in the system.

4.2.1 Optical Measurements and Electromagnetic Parameters

Ellipsometry is an optical technique for measurement of the dielectric properties of materials. The analysis is based on the change of polarization of light that is reflected off a sample. From these measurements the complex index of refraction of materials can be determined across the

frequency band of interest. Electromagnetic simulations however require material property definitions as complex dielectric constants. Therefore, the measured data from the ellipsometer needs to be converted using

$$\tilde{\epsilon}_r(\lambda) = \tilde{n}^2(\lambda), \quad (4-1)$$

where $\tilde{n} = n + jk$ is the complex index of refraction. For dielectric materials the dielectric constant and loss tangent are calculated as

$$\epsilon_c = \epsilon_0(\epsilon'_r + j\epsilon''_r) = \epsilon_0(n^2 - k^2 + j2nk), \quad (4-2)$$

$$\tan \delta_e = \frac{\epsilon''_r}{\epsilon'_r} = \frac{2nk}{n^2 - k^2}. \quad (4-3)$$

In these equations, the $e^{-j\omega t}$ time convention is assumed. For conductors the electromagnetic property of interest is the conductivity, which is related to the index of refraction as

$$\sigma = j\omega\epsilon_0(1 - \tilde{n}^2) = \omega\epsilon_0[2nk + j(1 - n^2 + k^2)]. \quad (4-4)$$

These optical properties of materials can now be directly implemented in electromagnetic (EM) simulators. The optical properties of materials used in our work here were measured using a Woollam variable angle spectroscopic ellipsometer (IR-VASE) [45]. It should be pointed out that as with any measurement data, the IR-VASE is susceptible to measurement and post processing errors. However, by detailed analysis of the standard deviation of the measured response and material model errors, the measured optical properties should be within $\pm 5\%$ of their actual values.

Measured material properties of some conductors and dielectrics used at infrared frequencies are shown in Figure 4-1. Here benzo-cyclo-butene (BCB) is a spin-on polymer (Dow Cyclotene).

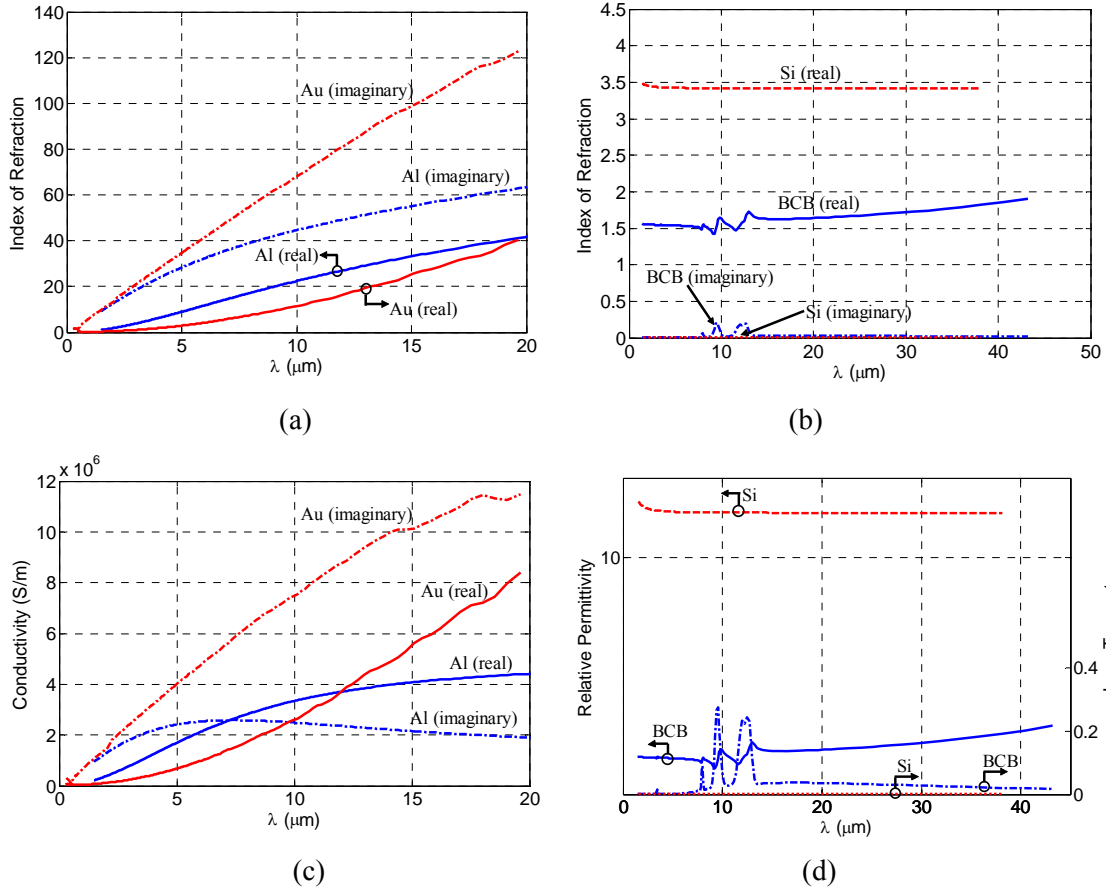


Fig. 4-1 Measured properties of various materials at infrared.

To reduce metallic losses, gold is typically used as conductors at high frequencies; however, it can be seen that the conductivity of gold at infrared is on the order of one tenth of its nominal value. On the other hand, for the dielectric materials, the loss tangent is not very high in this frequency range and they show less dispersive behavior in comparison with the conductors. In general these results indicate that the major material concern at THz frequencies is the performance of the conductor. It should be noted that in comparison between the dielectrics, although Si shows a superior low loss performance, BCB tends to be a better candidate for the reflectarray substrate due to its lower dielectric constant.

4.2.2 Calculating Drude Model Parameters for Conductors

To study the propagation of electromagnetic waves in mediums, we consider the time-harmonic case. The applied electric field varies harmonically with time with the factor $e^{j\omega t}$. The assumption is that the motions of the electrons in the medium have the same harmonic dependence. Usually for isotropic dielectrics, the effects of polarization on the propagation of light through a medium are studied. For conducting media, however, the effects of conduction on the propagation of light through a medium are studied. While different types of media such as Lorentz or Debye have been used to characterize dielectric media, in most cases the Drude model is more suitable for conductors.

The Drude model was proposed to explain the transport properties of electrons in materials (especially metals). This classical model, which is an application of kinetic theory, assumes that the microscopic behaviors of electrons in a solid may be treated by considering the instantaneous collision between free electrons and ions (as solid spheres).

The significant results of the Drude model are: 1) equation of motion in the medium, 2) a linear relationship between current density and electric field. The Drude model predicts the current as a response to a time-dependent electric field in which

$$\sigma = \frac{\sigma_0}{1 - j\omega\tau}. \quad (4-5)$$

Here $\sigma_0 = \frac{ne^2\tau}{m}$ is the DC conductivity, τ is the average time of electron collisions, n is the free electron density, e is the electron charge, and m is the effective mass of the electrons. The current can then be defined using

$$E(t) = \text{Re}\{Ee^{-j\omega t}\}, \quad J(t) = \text{Re}\{\sigma(\omega)Ee^{-j\omega t}\}. \quad (4-6)$$

The imaginary part indicates that the current lags behind the electric field, which happens

because the electrons need roughly a time τ to accelerate in response to a change in the electric field.

The Drude model dielectric function is $\varepsilon(\omega) = \varepsilon_0 + i \frac{\sigma(\omega)}{\omega}$, where ε_0 is directly related to the DC conductivity ($\sigma_0 = \varepsilon_0 \tau \omega_p^2$) by the plasma frequency of metals. The plasma frequency is usually given in rad/s units. Separating the real and imaginary parts for the Drude model dielectric function, one can obtain

$$\varepsilon(\omega) = \varepsilon_0 + i \frac{\sigma(\omega)}{\omega} = \varepsilon_0 \left(1 - \frac{\omega_p^2 \tau^2}{1 + \omega^2 \tau^2} + i \frac{\omega_p^2 \tau}{\omega(1 + \omega^2 \tau^2)} \right). \quad (4-7)$$

Typically this Drude model dielectric function is used to obtain a fit for the data. The damping (collision) frequency for the material is defined as $\omega_\tau = 1/\tau$, with the unit s^{-1} . With this definition, the Drude model can be written as

$$\varepsilon_r(\omega) = \varepsilon_r' + i\varepsilon_r'' = 1 - \frac{\omega_p^2}{\omega_\tau^2 + \omega^2} + i \frac{\omega_p^2 \omega_\tau}{\omega^3 + \omega \omega_\tau^2}. \quad (4-8)$$

It should be noted that the plasma frequencies of metal are typically in the visible and near ultraviolet regions. The material is opaque (bulky) at frequencies below ω_p and transparent at higher frequencies.

To determine the Drude model parameters for a material, one has to obtain the damping and plasma frequencies based on the measured results. The procedure [46] is as follows:

- 1) The equations are solved for the damping frequency (ω_τ), eliminating ω_p . This equation is solved for (ω_τ) at some frequency:

$$\omega_\tau = \frac{\omega \varepsilon_r''}{1 - \varepsilon_r'} \quad (4-9)$$

- 2) The plasma frequency ω_p is obtained using

$$\omega_p^2 = (1 - \varepsilon_r')(\omega^2 + \omega_\tau^2) \quad (4-10)$$

- 3) This is repeated for several values of ω to obtain several pairs of ω_τ and ω_p , which produce the best eyeball fit to the data.

Using this approach, the Drude parameters for gold used in our studies were determined over the band of interest. The plasma and damping frequency of gold are 1.3468×10^{16} (rad/s) and 6.501×10^{13} (1/s), respectively. These correspond to an average collision time of 1.5382×10^{-14} seconds and a DC conductivity of 2.4704×10^7 S. Using these values, the material properties of gold are calculated using the Drude model and are given in Fig. 4-2. It can be seen that a close agreement between the measured data and Drude model are obtained. Using this approach, the plasma and damping frequency for aluminum were calculated to be 1.2159×10^{16} (rad/s) and 2.5184×10^{14} (1/s), respectively.

Using this model, the complex value of conductivity can now be modeled in the simulation software. How the material is modeled, however, depends on the software. To model complex conductivity in Ansys HFSS we use the real part of the dielectric constant (which is negative) along with the value of dielectric loss tangent, which is obtained using $\tan \delta_e = \varepsilon_r'' / \varepsilon_r'$. These results have to be imported as a data file for every frequency point. In other words, the conductor is simulated with a dielectric model. It should be noted that the dielectric constant is a positive number since it represents the loss in the material. To model complex conductivity in CST MWS we can directly use the plasma and damping frequencies for the material. The software then generates the material properties for every frequency simulation point using the Drude model.

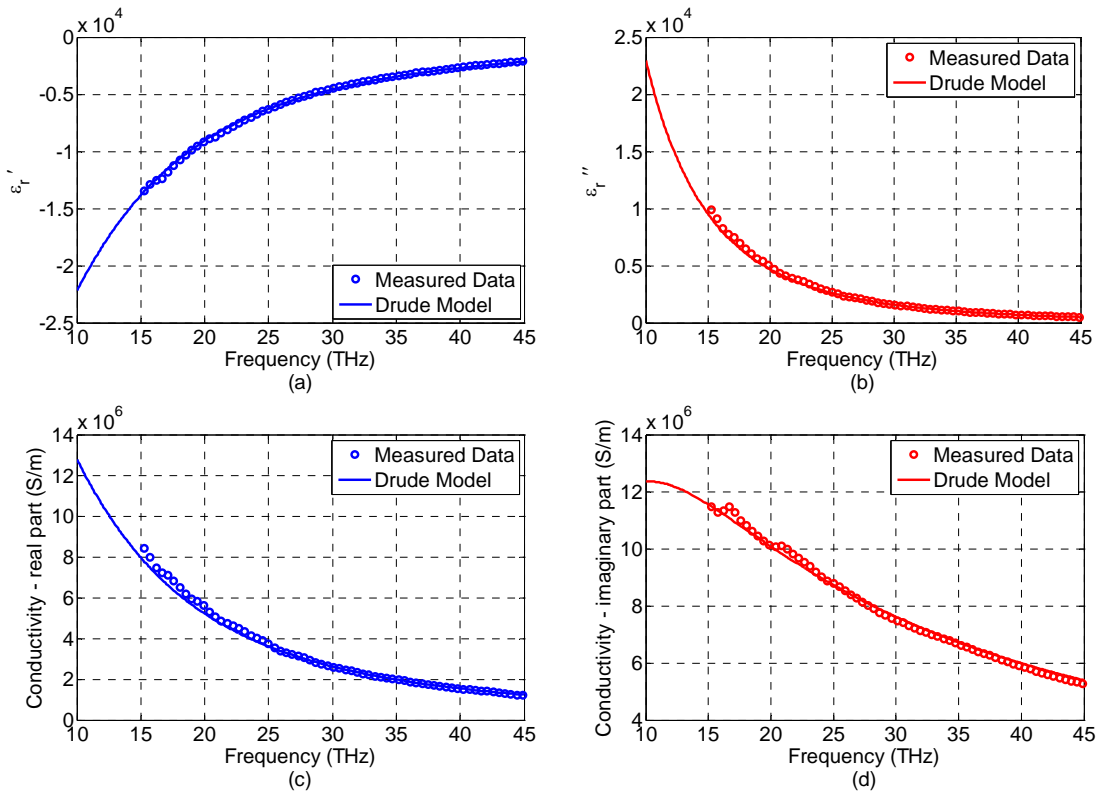


Fig. 4-2 Comparison between the Drude model and measured results for gold.

4.3 Losses in Reflectarray Elements at THz/Infrared Frequencies

The aim of the study here is to understand the loss mechanism in reflectarray unit-cells, so to simplify the problem the effects of the conductor loss in the metal patch and dielectric loss in the substrate are investigated separately. Furthermore, it is assumed that the ground plane is a perfect electric conductor (PEC). For the reflectarray elements studied here, the dielectric substrate ($\epsilon_r = 2.2$) has a thickness of 450 nm, the unit-cell periodicity is 5.54 μm , and a 3 \times 3 μm square patch is used as the phasing element. It should be noted that in the analysis here, the dynamic reflection properties of the elements will be studied. For a practical design, however, the reflection properties of the elements are required at a fixed frequency, or at least over a relatively narrow frequency range, when the patch size changes. While there is a strong relationship between these

two methods, the main advantage of the dynamic analysis here is that from a circuit model viewpoint, one value of C and L is sufficient to analyze the performance of the unit-cells. In addition for the resonance patch element ($3 \times 3 \mu\text{m}$) studied in this section, the dynamic reflection properties essentially represent the highest loss of the element at the center frequency, which is quite advantageous for the loss study. The unit-cell simulations were carried out using commercial electromagnetic software Ansys HFSS [47] and CST MWS [48].

4.3.1 Conductor Losses

To study the conductivity effect, we consider a lossless dielectric ($\tan \delta_e = 0$) and investigate the reflection characteristics of the unit-cells using different conductors for the patch. It is important to point out that when modeling conductors at THz and optical frequencies a zero thickness approximation will be inaccurate for practical designs. Furthermore, the conductivity has to be modeled as a complex number, unlike microwave frequencies where typically only the real value of conductivity is used for simulations.

A. Effect of Conductor Thickness

As mentioned earlier, an important consideration in the simulations here is the impact of metal thickness on the performance of the elements. While thin films in the nanometer range can be fabricated, an important consideration is to ensure that the conductor is optically bulky (opaque). While this generally depends on both the plasma frequency of the metal and the thickness [49], in the frequency range of study here, a 100 nm thick patch is sufficient to ensure good reflection properties.

Two sets of simulations are studied here to observe the reflection properties of elements with different conductivities and thicknesses. For both cases here, only the real part of conductivity is

used for the metal and it is assumed to be non-dispersive. A good agreement between the simulation results was observed with both softwares, hence only the results obtained by Ansys HFSS are reported for brevity. The reflection coefficients of reflectarray unit-cells with zero thickness conductors are given in Fig. 4-3.

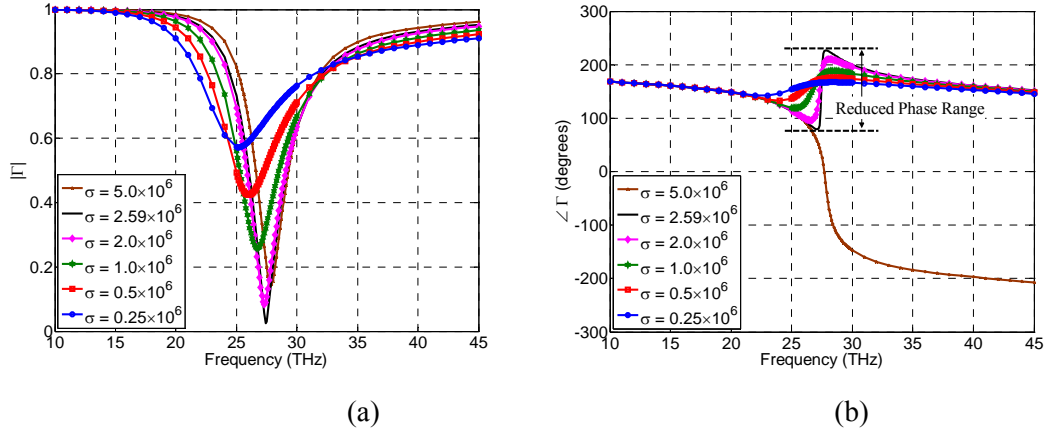


Fig. 4-3. Reflection coefficients for infrared reflectarray elements with a zero thickness patch: (a) magnitude, (b) phase.

From these results it can be seen that as the metal conductivity decreases, the magnitude of reflection coefficient decreases as well, indicating an increasing loss in the unit-cell. When the conductivity (σ) is equal to 2.59×10^6 S/m, almost total loss is observed at the resonance frequency. The phase response of this case also seems to be completely different from the typical S-curve. Instead of a 360° phase range, a reduced range of 150° is observed. When the real part of conductivity is further reduced to 1×10^6 S/m, it is interesting to observe that reflection magnitude increases now, indicating a decreasing energy loss. With this conductivity, the phase range becomes even smaller. It should be pointed out here that the values of conductivity used in the study here are not for any particular material. The aim here is to show the trend for reflection properties of elements for low-loss and high-loss cases. For the zero thickness patches studied here it can be seen that a proper phase curve is observed for high value of conductivity while an

improper phase wrap is observed when the conductivity is below a certain value (referred to as critical conductivity value). For this case, the critical conductivity value is between 2.59×10^6 and 5.0×10^6 . The reflection coefficients of reflectarray unit-cells with a patch thickness of 100nm are given in Fig. 4-4.

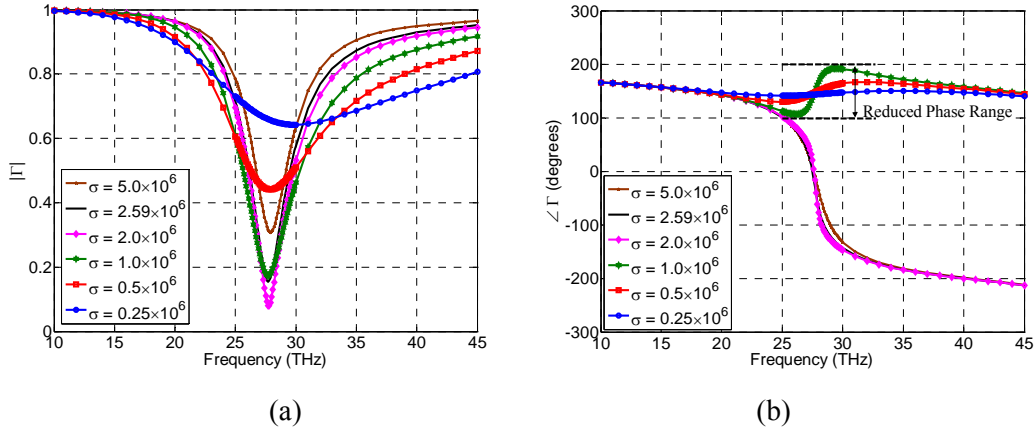


Fig. 4-4. Reflection coefficients for infrared reflectarray elements with a 100 nm thick patch modeled with only the real part of conductivity (non-dispersive): (a) magnitude, (b) phase.

Similar to Fig. 4-3, it is observed that while for high values of conductivity a proper phase curve is observed, as the conductivity decreases an improper phase wrap will be observed. However, the critical conductivity value for this 100 nm thick case is between 2.0×10^9 and 1.0×10^9 , which is different than that of a zero thickness patch. For a specific value of conductivity such as 2.59×10^9 , the improper phase wrap occurs for zero thickness and does not appear for 100 nm thickness.

B. Effect of Complex Conductivity

As discussed earlier, for an accurate modeling of conductors in the optical range, the complex value of conductivity and the dispersive properties must be taken into account. To model complex and dispersive conductivity in the electromagnetic software, the Drude models obtained

from measured data are used in this section. The reflection coefficients of reflectarray unit-cells with a patch thickness of 100nm are given in Fig. 4-5 for various conductors.

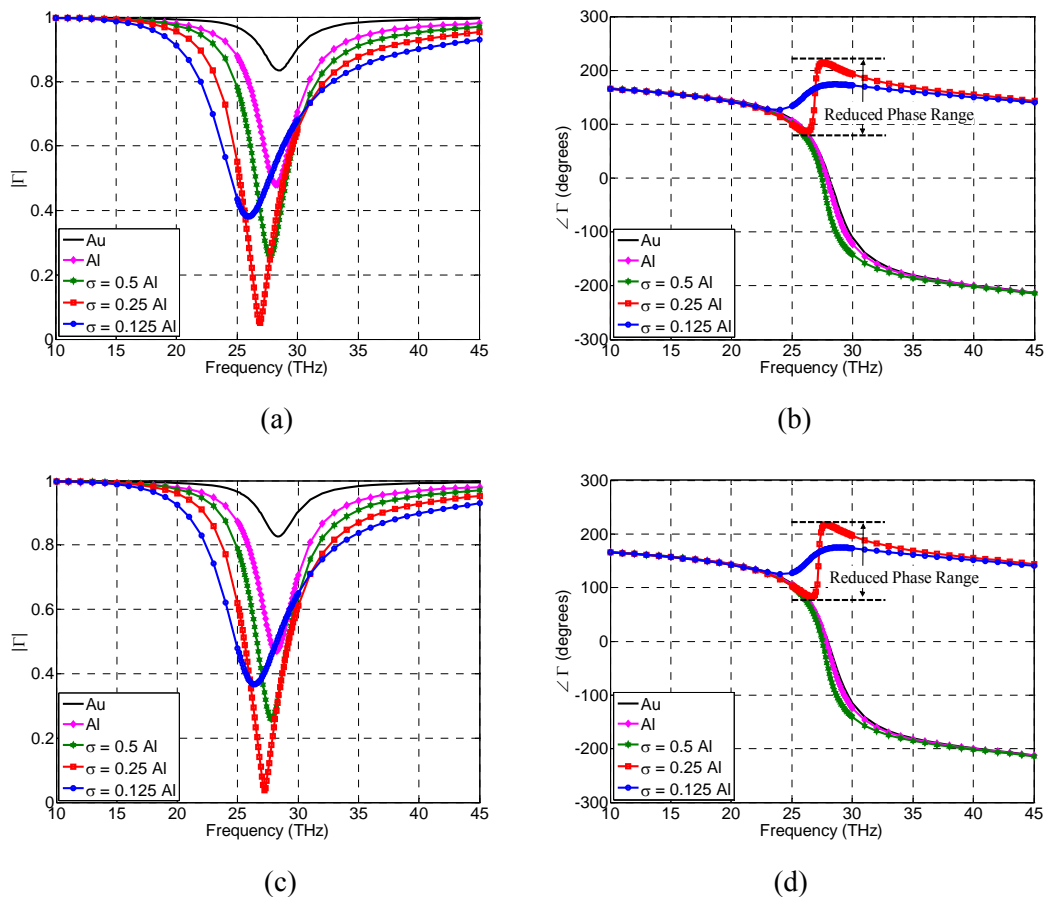


Fig. 4-5. Reflection coefficients for infrared reflectarray elements with a 100 nm thick patch using the Drude model for conductors: (a) magnitude (HFSS), (b) phase (HFSS), (c) magnitude (CST), (d) phase (CST).

From these results it can be seen that while the performance of a gold patch is quite acceptable in this frequency range, when an aluminum patch is used for the phasing element, less than half of the incident field will be reflected back from the elements. To study the effects of lower values of conductivity, we use the Drude models with values proportional to the aluminum case. It can be seen that as the metal conductivity decreases, the losses will increase. When the

conductivity is reduced to one quarter of the value of conductivity for aluminum, almost a total loss of power will be observed. The phase response of this case is completely different from the typical S-curve. Instead of a 360° phase range, a reduced range of 150° is observed. Similar to the previous cases, it can be observed that while for high values of conductivity a proper phase curve is observed, as the conductivity decreases an improper phase wrap is observed for the elements. In this case, the critical value is between $\frac{1}{2}$ and $\frac{1}{4}$ of the conductivity of aluminum, which is lower than the previous two cases. A comparison between the results obtained using Ansys HFSS and CST MWS is given in Fig. 4-6 for a small conductivity case ($\sigma = \frac{1}{4} \sigma_{aluminum}$) and a large conductivity case ($\sigma = \frac{1}{2} \sigma_{aluminum}$).

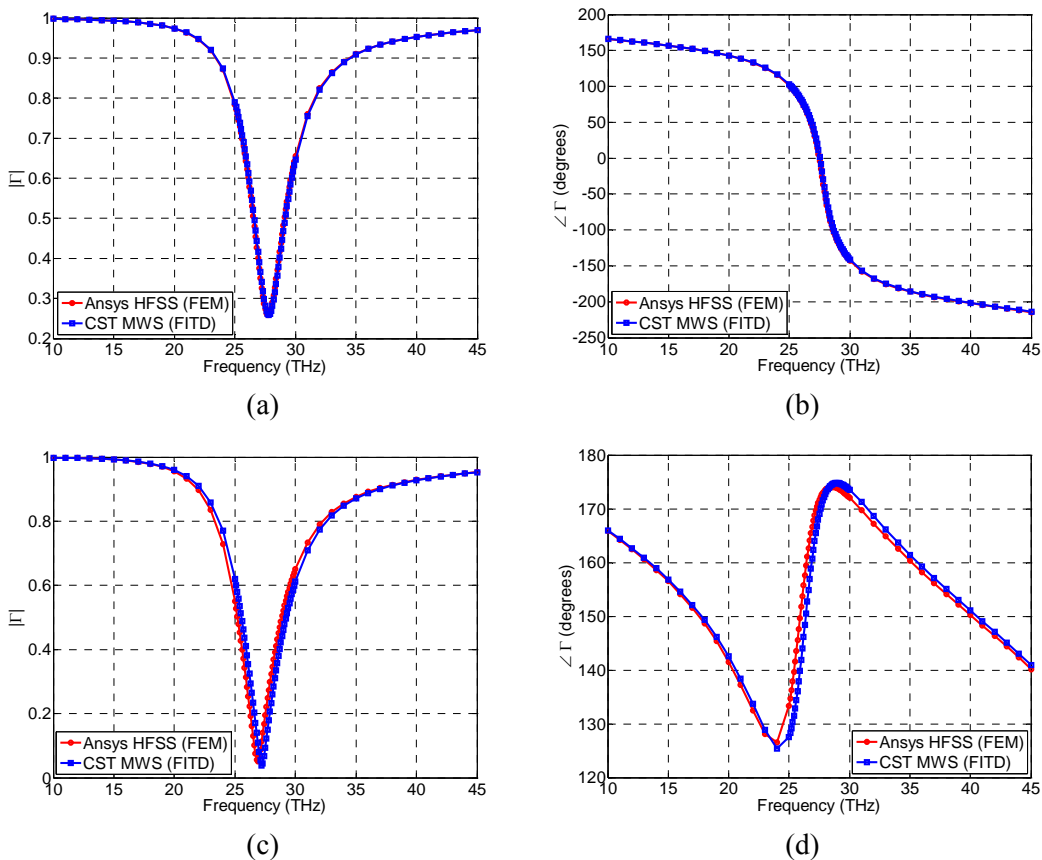


Fig. 4-6. Comparison of reflection coefficients for infrared reflectarray elements with a 100 nm thick patch using the Drude model for conductors: (a) magnitude for the large-conductivity case, (b) phase for the large-loss case, (c) magnitude for small-conductivity case, (d) phase for small conductivity case.

It can be seen that a close agreement is observed between the results, verifying the concept that when the conductivity is below a certain threshold level, an improper phase response will be observed.

From this study, we can make following conclusions:

- When a large conductivity is used as the patch material, a proper phase curve that changes monotonically from 180° to -180° is observed. When the conductivity reduces below a threshold level, an improper phase wrap is observed and the phase range cannot cover the required 360° phase range.
- When the metal patch is modeled using zero thickness, finite thickness with real conductivity, and finite thickness with complex conductivity, the above behavior can all be observed. However, the critical conductivity values are different in these three cases.

4.3.2 Dielectric Losses

To study the effect of dielectric losses in the unit-cell we consider the case of a PEC patch on different dielectric substrates with a thickness of 450 nm and various loss tangents. Similarly we use a $3 \times 3 \mu\text{m}$ square patch in a unit-cell with periodicity of $5.54 \mu\text{m}$. For this study we have assumed that the dielectric properties are constant over the frequency band. It is implicit that in practical designs the dispersive nature of the parameters must be taken into account for accurate calculation of the reflection coefficients. However, for dielectrics this effect is not significant. The reflection coefficients of reflectarray unit-cells with different values of dielectric loss tangent are given in Fig. 4-7.

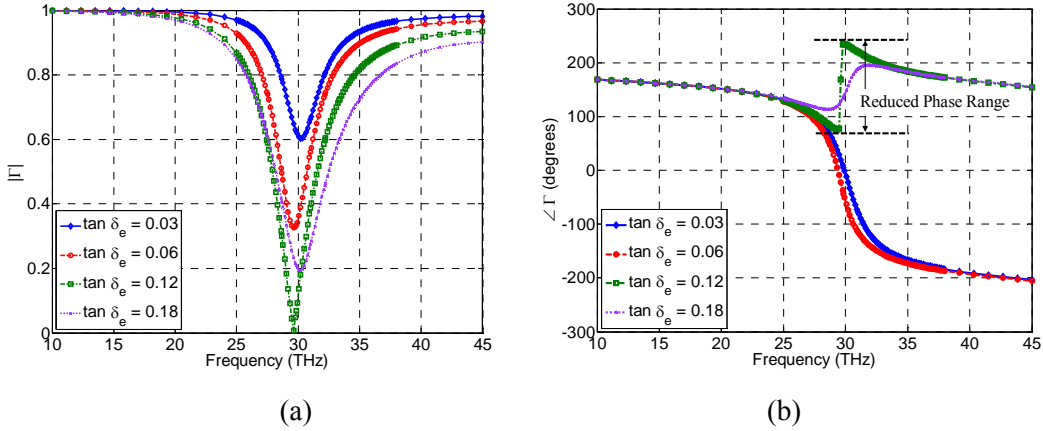


Fig. 4-7. Reflection coefficients for infrared reflectarray elements with various values of dielectric loss tangent: (a) reflection magnitude. (b) reflection phase.

It can be seen that as the loss tangent increases, the losses in the element increase and for $\tan \delta_e = 0.12$ almost total loss is observed at the resonance frequency. When the dielectric losses are increased beyond this critical limit the losses in the unit-cell decrease; however, the reflection phase does not return back to the typical S-curve.

4.3.3 Effect of Losses on Reflection Properties of Elements

In summary, two lossy situations exist in the reflectarray unit-cells. When the metal conductivity is above a certain limit or the dielectric loss tangent is below a certain value, the phase of reflection coefficient varies with a 360° range. In this situation when the conductor and dielectric losses increase but do not exceed the limit, the element loss will increase, but it will not affect the phase range. On the other hand, when the metal conductivity is decreased or the dielectric loss tangent is increased beyond the limits, a new phase curve is observed with a limited angular range. In this situation when metal conductivity decreases or the dielectric loss tangent increases, the phase range becomes even smaller. The traditional reflectarray design at microwave frequency has the loss situation in the first category. The reflectarray design at

infrared may have both loss situations because of the high loss material properties.

4.4 Circuit Model Analysis

4.4.1 Circuit Theory and Loss Study

As discussed in chapter 2, the unit-cell structure can be modeled as a transmission line circuit, where the square metallic patches act as parallel capacitors with the adjacent cells while the short circuited unit-cell ground can be modeled as a parallel inductor. This circuit model has previously been implemented for lossless reactive impedance substrates [19]. The loss in the dielectric substrate can be modeled by a parallel resistor, i.e., the total unit-cell is modeled as a parallel RLC circuit. To model the conductor loss in the patch, a resistor will be series connected to the capacitor as shown in [50]. In this section we use the parallel RLC circuit model to understand the loss behavior associated with the dielectrics. Similar derivations can be obtained for conductor loss analysis. Using this parallel RLC model the reflection coefficient in the S-plane is calculated as

$$\Gamma(S) = -\frac{S^2 + S\left(-\frac{1}{Z_o C} + \frac{1}{RC}\right) + \frac{1}{LC}}{S^2 + S\left(\frac{1}{Z_o C} + \frac{1}{RC}\right) + \frac{1}{LC}}. \quad (4-11)$$

Using this model the reflection properties of a lossy unit-cell can be calculated directly. Let's consider two cases, the low loss ($\tan \delta_e = 0.0009$) and high loss ($\tan \delta_e = 0.15$) dielectric substrates. The values of the lumped elements in the circuit model are obtained by initially designing an RLC circuit resonating at 28.3 THz and then tuning these values so that the circuit model reflection curve fits the curve obtained by the full wave unit-cell simulations. The comparison of full wave simulation and circuit model are shown in Fig. 4-8.

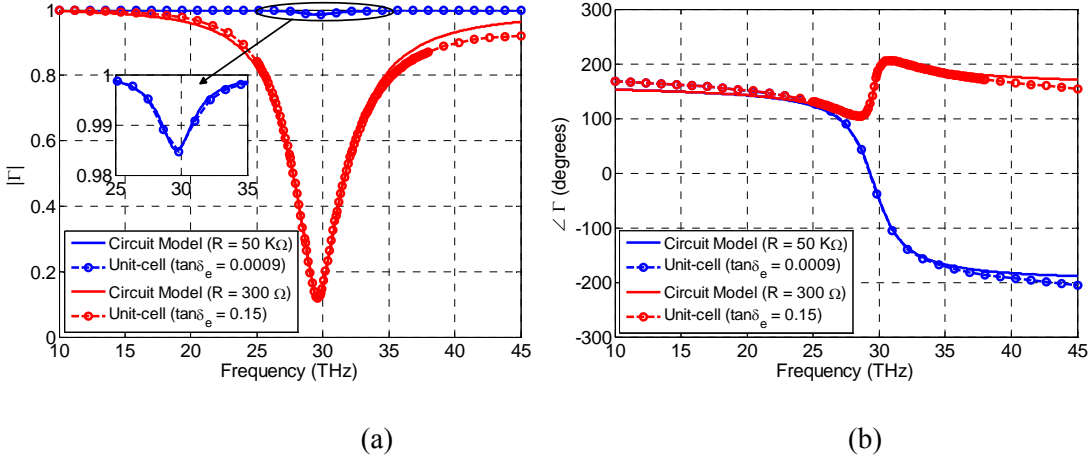


Fig. 4-8. Comparison between circuit-model and unit-cell simulations for low loss and high loss cases: (a) reflection magnitude, (b) reflection phase.

It can be seen that the circuit model shows good agreement with the full wave simulations in both cases where the values used for the capacitor and inductor are 0.134 fF and 0.215 pH , respectively. It should be pointed out that these lumped element values are for the case of normal incidence on the unit-cell. However, a similar derivation can be obtained for the oblique incidence case. Comparing the resistor values in the circuit model, it can be seen that in the low loss case the parallel resistor is quite large, so there is less power dissipated in the resistor. For the high loss case however the resistance comes close to the free space impedance and as a result of the high power transfer to the resistor, almost no power is reflected back from the system near the resonant frequency. As expected, the reflection phase of the circuit model also shows that this high loss will considerably change the reflection phase behavior of the unit-cell.

4.4.2 Zero-Pole Analysis of Element Performance

In the previous sections it was shown that when the losses in the unit-cell material increase beyond a certain limit, the typical S-curve of the reflection phase, which shows a phase range of

about 360° , is no longer observed. The high losses change the traditional S-shape phase curve and create a new phase curve that has a narrow phase range. The unit-cell circuit model provides a helpful tool to obtain an insight into this unusual behavior. Three cases are considered for the value of the resistor, $R \rightarrow \infty$, $R = Z_0$ and $R < Z_0$. In the first case, i.e., the lossless model, the reflection coefficient can be simplified to

$$\Gamma(S) = -\frac{S^2 - S\frac{1}{Z_0 C} + \frac{1}{LC}}{S^2 + S\frac{1}{Z_0 C} + \frac{1}{LC}}. \quad (4-12)$$

The function has two poles located on the left side of the S-plane and two zeros on the right side of the S-plane. As the frequency goes from $\omega = 0$ to $\omega \rightarrow \infty$, the total phase changes from 180° to -180° , indicating a complete phase range and total reflection $|\Gamma(S)| = 1$. The phases of the numerator and denominator in (4-12) and the total phase are plotted in Fig. 4-9 (a).

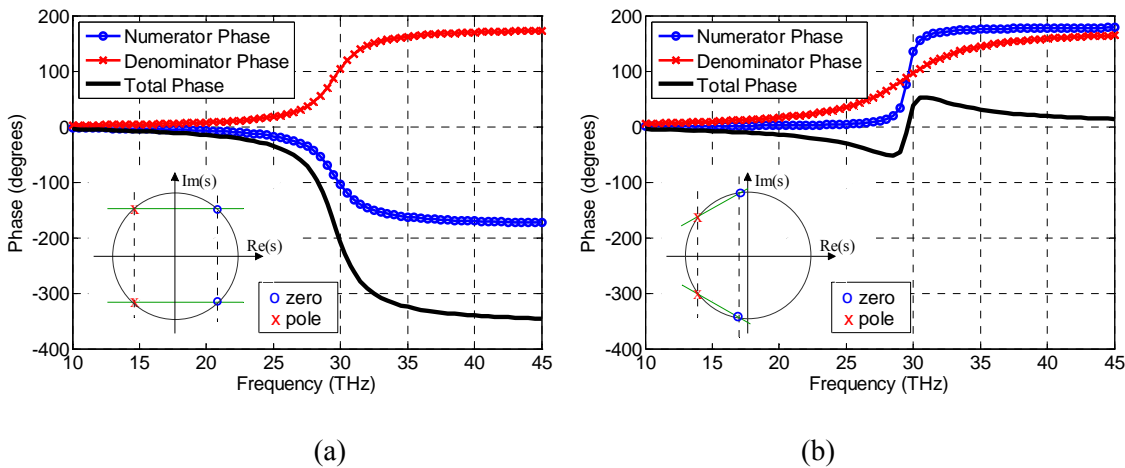


Fig. 4-9. The positions of poles and zeros in the S-plane, and the corresponding phase versus frequency:

(a) lossless case ($R \rightarrow \infty$), (b) high loss case ($R < Z_0$).

When $R = Z_0$ the reflection coefficient will be

$$\Gamma(S) = -\frac{S^2 + \frac{1}{LC}}{S^2 + S\left(\frac{2}{Z_0 C}\right) + \frac{1}{LC}}. \quad (4-13)$$

In this case the zeros of the function are on the imaginary axis in the S-plane. At the resonance frequency the reflection coefficient will be zero ($|\Gamma(S)| = 0$), i.e., a total loss and no reflected power.

When $R < Z_0$ the zeros will be located on the left side of the S-plane, as shown in Fig. 4-9 (b). The positions of the poles and zeros indicate that in this case although the magnitude of the reflection coefficient is non-zero it will have a phase range below 180° . This means that when the losses in the unit-cell go beyond the critical limit ($R = Z_0$), not only the reflected power but also the phase range will be insufficient for reflectarray unit-cells.

4.5 Dielectric Resonator Elements for THz/Infrared Frequencies

4.5.1 Limitations of Conventional Patch Element Designs

In traditional reflectarray antennas, both conductors and dielectrics are used in element designs. While in general both metallic and dielectric losses can influence the performance of the reflectarray antenna, the dominant loss term depends on the materials (metal and dielectric) used in the design. At THz frequencies, the dielectric loss may be minimized by selecting proper materials such as BCB, but the conductor loss is a major concern. Using high quality conductors such as gold significantly reduces the losses, but this runs contrary to the goal of a low-cost system. On the other hand, low-cost conductors such as aluminum have a higher loss, which will decrease the efficiency of the system. In addition while these low-cost conductors may achieve a complete phase range in the far-infrared range, at the short- and near-infrared range they will

suffer from a limited phase range, which will further reduce the efficiency of the system.

Based on the previous investigation, it is clear that the low loss reflectarray element design, which is not a major concern at the microwave frequency, becomes a critical topic at the optical frequency. The element loss results from the finite value of the metal conductivity and high loss tangent of the dielectric substrate, and becomes severe near the resonant frequency. Some conventional element design methods in the microwave frequency such as variable-size patches may suffer from significant losses, and new design methodologies need to be developed.

4.5.2 Low-Loss Dielectric Resonator Reflectarray Elements

A possible solution to the high-loss performance of patch elements at THz frequencies is to use resonant dielectric elements as reflectarray phasing elements. The idea is similar to the dielectric resonator antenna (DRA) concept in microwave and millimeter wave designs [51]. A dielectric cavity backed by a conducting ground plane will be designed as the reflectarray phasing element. The phase control will be realized by the proper design of the shape and dimensions of the dielectric resonator, hence avoiding the use of a resonant conductor patch. This dielectric resonant element approach has some resemblance to the fiber optic design except that the cavity structure is designed instead of the transmission line structure.

Here we design two types of reflectarray elements: 1) variable size square patch elements on a low-loss dielectric substrate, and 2) variable size low-loss dielectric resonator elements. The aim of this study is to compare the loss performance of these two types of reflectarray phasing elements. The elements are designed for the operating frequency of 28.3 THz and we use the same unit-cell size of $5.54 \times 5.54 \mu\text{m}$ as the previous studies. While there is a strong relationship between the dynamic phase range study conducted in the previous sections, and the variable size element design here, the later is necessary for a reflectarray design. The materials used for these

designs are selected from the data given in Fig. 4-1. For the patch design, we can use either gold or aluminum for the conductor, although as discussed earlier, aluminum patches have a higher loss. Also taking into account fabrication considerations, a thickness of 100 nm is used for the patch, and for accurate electromagnetic analysis, the complex conductivity model of the conductor is used in the simulations. For the substrate we select a 450 nm BCB slab, which is sufficient to achieve a good phase range. For the dielectric resonator (DR) element design, BCB will not be practical, since it has a relatively low dielectric constant, thus Silicon (Si) is selected for the DR element. The height of the DR is selected to be 2.5 μm which is about $5/6^{\text{th}}$ of the wavelength in the dielectric at the operating frequency. For both designs, the ground plane is assumed to be a perfect conductor. The geometry of both designs is shown in Fig. 4-10.

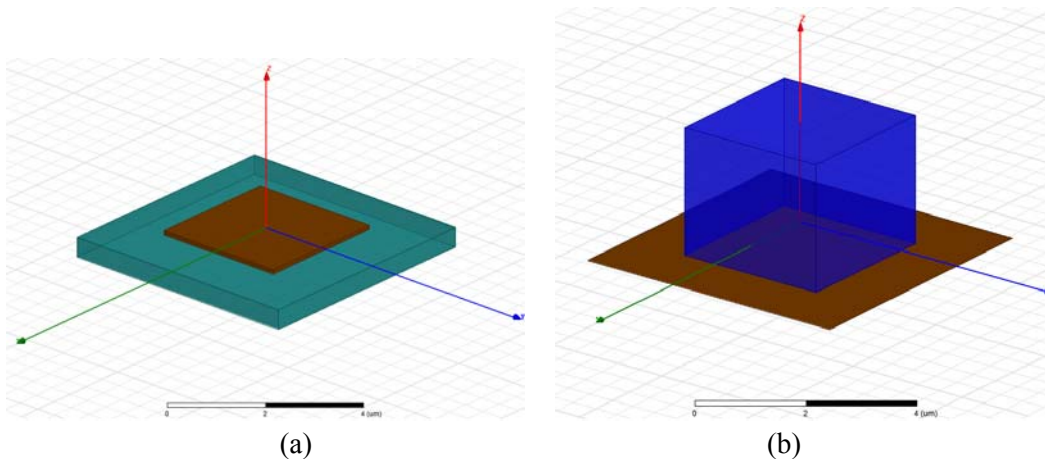


Fig. 4-10. Variable size elements for THz reflectarrays: (a) variable size square patch, (b) variable size square DR.

While the fabrication precision depends on the technology used, for the numerical study here, we consider a precision of 0.25 μm for both designs. The reflection coefficients of these elements are obtained using HFSS software and are given in Fig. 4-11.

These results clearly show that as expected, the variable size DR elements outperform the patch elements. In addition to a significant improvement in the reflection loss with DR elements,

they also show a much larger phase range, where the full phase cycle is achieved. It should be noted that the phase range obtained for the patch elements is about 320° , which is quite sufficient for a reflectarray design; however the main disadvantage is the high loss of these elements. While the losses are substantially lower for gold, both patch configurations show a very high loss at the resonance dimension. It is interesting to point out that similar to what was observed in the dynamic phase range study, the aluminum patch design here also shows a minimum reflection coefficient magnitude of about 0.5, i.e., only half of the incident field will be reflected back from the element.

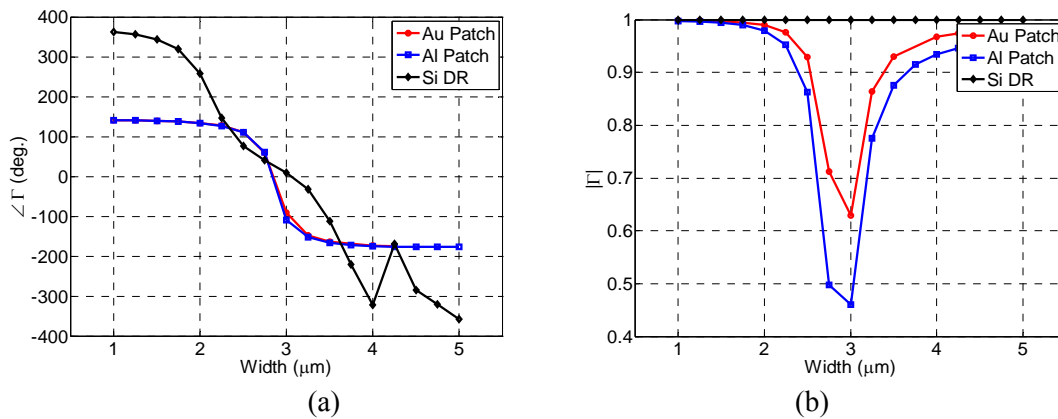


Fig. 4-11. Reflection coefficients of the variable size elements for THz reflectarrays: (a) phase, (b) magnitude.

4.5.3 Design of a CSP System Using Reflectarray Elements

As discussed earlier in this chapter, one important motivation in the THz reflectarray antenna design was to design a CSP system using a reflectarray antenna as the reflector for focusing the sunlight. A schematic view of the CSP system is given in Fig. 4-12. To accurately compute the focusing gain of a reflector antenna, a full-wave analysis is necessary. This is computationally quite challenging for a reflectarray design, given the fact that the dimensions of a CSP reflector are several hundred wavelengths, however it can be approximated using the following approach.

First, the currents on the aperture of a reflectarray antenna are computed using the formulation given in chapter 2. In the next step, using these aperture currents, the electric fields in the near-field can be calculated using the formulation presented in [27].

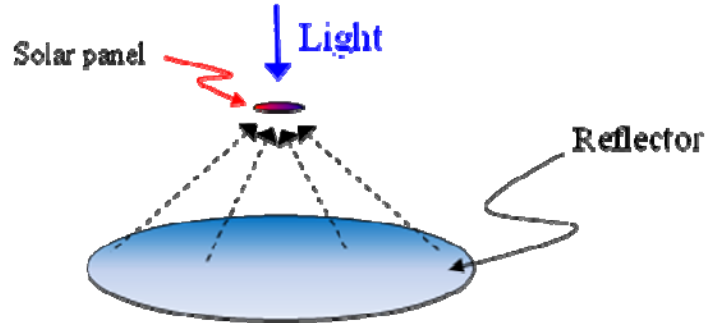


Fig. 4-12. A schematic view of the CSP system.

Without the loss of generality, for a y -directed electric current on the aperture, the electric fields in near-field are given as

$$E_x = \frac{-j\eta}{4\pi\beta} \iint_s \{(x-x')G_2 \times (y-y')J_y\} \frac{e^{-j\beta R}}{R} ds', \quad (4-11a)$$

$$E_y = \frac{-j\eta}{4\pi\beta} \iint_s \{G_1 J_y + (y-y')G_2 \times (y-y')J_y\} \frac{e^{-j\beta R}}{R} ds', \quad (4-11b)$$

$$E_z = \frac{-j\eta}{4\pi\beta} \iint_s \{(z-z')G_2 \times (y-y')J_y\} \frac{e^{-j\beta R}}{R} ds'. \quad (4-11c)$$

In these equations, G_1 and G_2 are

$$G_1 = \frac{-1 - j\beta R + \beta^2 R^2}{R^3}, \quad (4-12a)$$

$$G_2 = \frac{3 + j3\beta R - \beta^2 R^2}{R^5}. \quad (4-12b)$$

Using this formulation, the aim of the study here is to compare the focusing power of three CSP

reflectarray systems, using the elements designed in the previous section. An $F/D = 0.5$, and a diameter of 100λ at 28.3 THz is selected for the reflectors. The element dimensions are then determined from the phase curves in Fig. 4-11. It should be noted that since in most cases the CSP system also rotates mechanically depending on the direction of the sunlight in order to receive maximum power, a normal incidence approximation for the elements reflection coefficients is quite acceptable for the analysis here. The electric currents on the aperture are shown in Fig. 4-13 for the three designs. The incident electric field has a magnitude of 1 V/m.

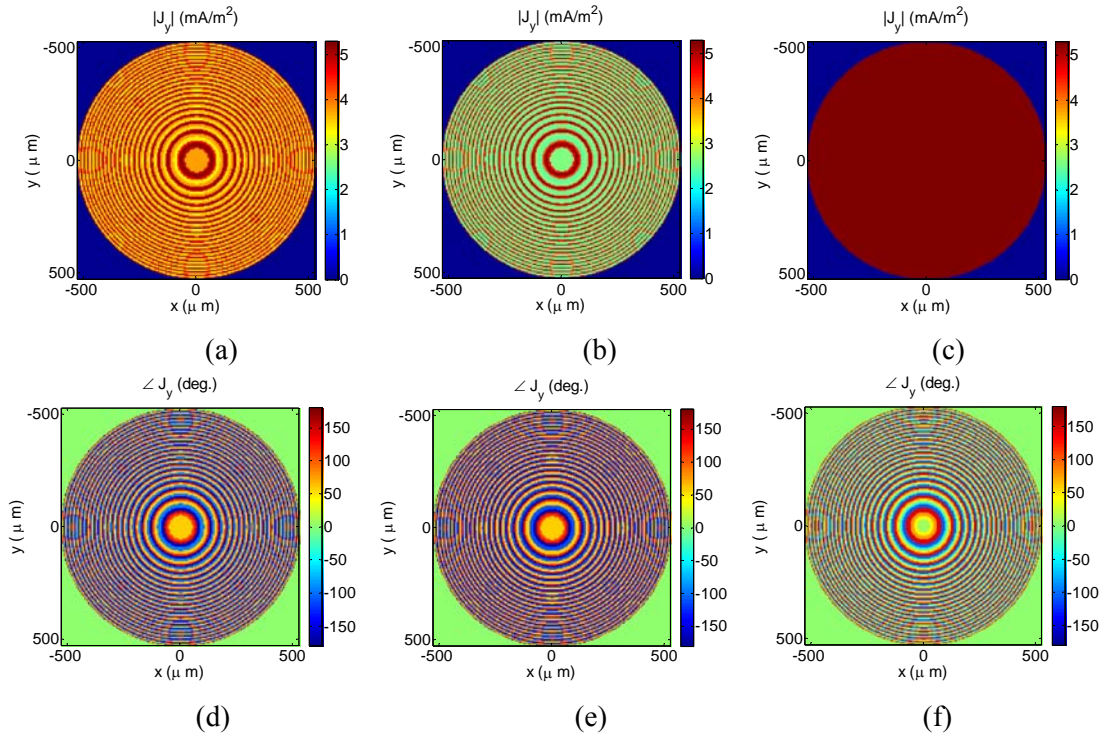


Fig. 4-13. Electric currents on the reflectarray aperture: magnitude (a) Au patch design, (b) Al patch design, (c) Si DR design, phase (d) Au patch design, (e) Al patch design, (f) Si DR design.

It can be seen that while the phase of the electric currents is almost similar in all three designs, the main difference is in the magnitude of the electric current. Due to the very low-loss performance of the Si DR elements, an almost uniform current distribution is observed on the

aperture of the DR reflectarray system. The electric near-fields along the normal axis of the reflector are obtained from these current distributions, and are given in Fig. 4-15. These results clearly demonstrate the superior performance of the DR reflectarray system design, which achieves a maximum electric field strength about 100 V/m at the focal point. A direct comparison between the electric field powers along the normal axis of the reflector in these three systems is given in Fig. 4-15. The maximum power at the focal point is 37.760, 35.884, and 40.209 dB for the Au patch design, Al patch design, and Si DR design, respectively.

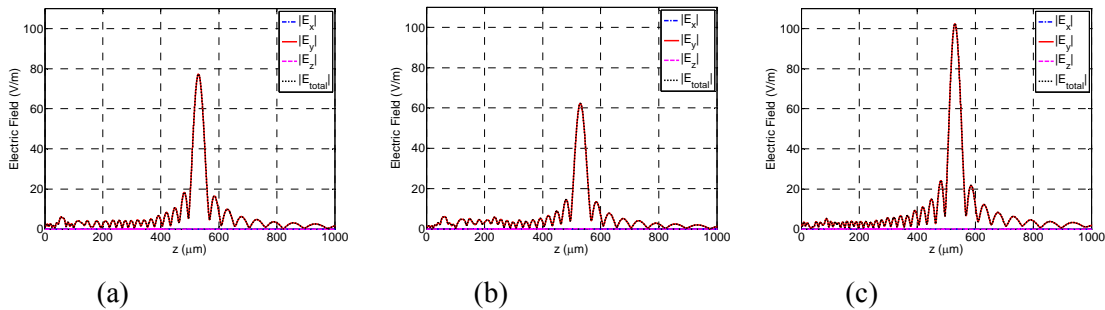


Fig. 4-14. Electric fields along the normal axis of the reflector: (a) Au patch design, (b) Al patch design, (c) Si DR design.

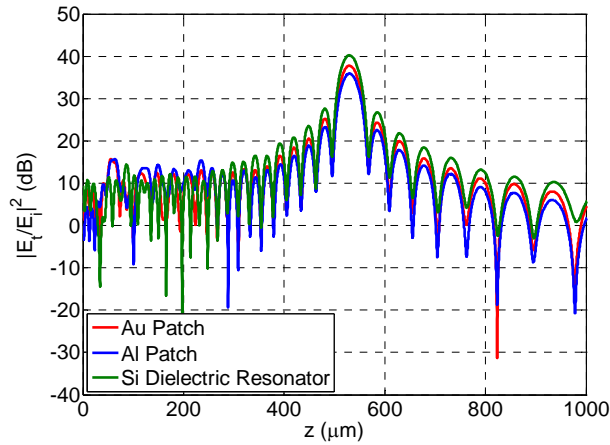


Fig. 4-15. Electric field power along the normal axis of the CSP reflectors.

It is worthwhile to point out that the approximation made in the analysis here is the fact that the reflection coefficients of the elements are a far-field quantity not a near-field quantity. Therefore

using this data in the field calculations could result in some error. Nonetheless since the peak value obtained at the focal points is about 50λ away from the reflector surface, which is basically the Fresnel zone, this approximation is quite acceptable.

CHAPTER V

SINGLE-FEED MULTI-BEAM REFLECTARRAY ANTENNAS

Several advantages of reflectarray antennas over classical reflectors and array antennas, such as low-profile, low-mass and low-cost features, were delineated in the previous chapters. In addition to these advantages that are mainly due to the use of printed circuit technology, the reflectarray allows for an individual control of the phase shift of each element in the array. As a result, the reflectarray can achieve contoured beam performance without any additional cost. Similarly, multi-beam performance can also be realized by designing the phase shift of the elements appropriately.

In this chapter, a systematic study on various design methods of single-feed multi-beam reflectarray antennas is presented. Two direct design methods for multi-beam reflectarrays, the geometrical method and the superposition method, are investigated first. It is demonstrated that although both methods could generate a multi-beam radiation pattern, neither approach provides satisfactory performance, mainly due to high side-lobe levels and gain loss in these designs. Two different optimization techniques, the alternating projection method and the particle swarm optimization method, are then implemented to optimize the phase distribution on the reflectarray surface for multi-beam performance. The mask definition and convergence condition of the optimization are studied for multi-beam reflectarray designs. Finally two Ka-band reflectarray prototypes with symmetric and asymmetric beam characteristics are fabricated and tested, both of which show a good multi-beam performance.

5.1 Introduction to Multiple Beam High-Gain Reflectarray Antennas

Multi-beam antennas have numerous applications, such as electronic countermeasures, satellite communications, and multiple-target radar systems [52]. These multi-beam antennas are typically based on reflectors with feed-horn clusters [53] or large phased arrays [54]. Horn array feeds for reflector antennas on communication satellites can provide multiple beams with tailored earth coverage patterns. For phased array antennas, multiple simultaneous beams can be generated by connecting the array to a beam-forming network with multiple ports. Considering the complexity of fabricating these antennas and deployment for space applications, these multiple beam designs are relatively high cost. The numerous advantages of reflectarrays, in particular the low-mass and low-cost features, makes the multiple beam reflectarray a suitable antenna candidate.

Reflectarrays can generate single or multiple beams with single or multiple feeds. A two-beam reflectarray prototype using a single feed was demonstrated in [55], while [56] presented a single-feed reflectarray generating four simultaneous beams. Multi-feed multi-beam reflectarrays with shaped patterns were also studied in [12]. In addition, multi-feed single-beam reflectarray antennas were investigated in [21]. In these works, different design approaches have been introduced to achieve the multi-beam performance. The main objective of this chapter is to provide a comprehensive and systematic comparison of various multi-beam design approaches, including both direct design methods and optimization techniques, which can aid the antenna engineer in selecting the suitable approach for his design. In addition, the design of single-feed asymmetric multi-beam reflectarray antennas is investigated for the first time, in this chapter.

5.2 Direct Design Methods

5.2.1 Geometrical Approach for Multi-Beam Design

The basic idea behind this method is simply to divide the reflectarray surface into N sub-arrays where each sub-array can then radiate a beam in the required direction. Although the array division and beam allocation can be arbitrary, it is feasible to define them based on the directions of the beams they are designed to generate. Since in most reflectarray designs the feed is pointing toward the geometrical center of the array, the sub-arrays can be defined by the zones corresponding to the beam direction they generate, i.e.

$$\varphi_n - \frac{\pi}{N} \leq \text{zone } n \leq \varphi_n + \frac{\pi}{N}. \quad (5-1)$$

Here φ_n is the azimuthal direction of the n^{th} beam. With this definition each sub-array will generate a beam in the direction of the zone center. It should be noted that with this approach each zone receives $1/N$ of the power from the feed horn while using $1/N$ of the aperture surface.

To demonstrate the multi-beam design capabilities of this approach we will study two multi-beam designs, a double-beam and a quad-beam reflectarray antenna. The antenna is designed for the operating frequency of 32 GHz and has a circular aperture with a diameter of 17λ at the design frequency. The element periodicity is $\lambda/2$ and we assume ideal phasing elements are used here. A prime focus feed is used for this design and is positioned with an F/D ratio of 0.735. The feed horn is circularly polarized and the power q of the feed horn $\text{Cos}^q(\theta)$ radiation pattern model is 6.5 at 32 GHz. The radiation patterns of the reflectarrays are calculated using the aperture field distribution method.

For the double-beam design, the element phase is adjusted to generate two beams in the directions of $(\theta_{1,2} = 30^\circ, \varphi_1 = 0^\circ, \varphi_2 = 180^\circ)$. Since only two beams are required in this design the reflectarray surface can be divided into two half circles where each zone generates one beam. Two different zone allocations are considered for this design. In the first case the beams are generated in the direction of the zone center (design A), i.e.,

$-90^\circ \leq zone_1 \leq 90^\circ$, $90^\circ \leq zone_1 \leq 270^\circ$. In the second case the beams are in the direction of the zone edges (design B), i.e. $0^\circ \leq zone_1 \leq 180^\circ$, $180^\circ \leq zone_1 \leq 360^\circ$. The radiation patterns of both these designs are given in Fig. 5-1.

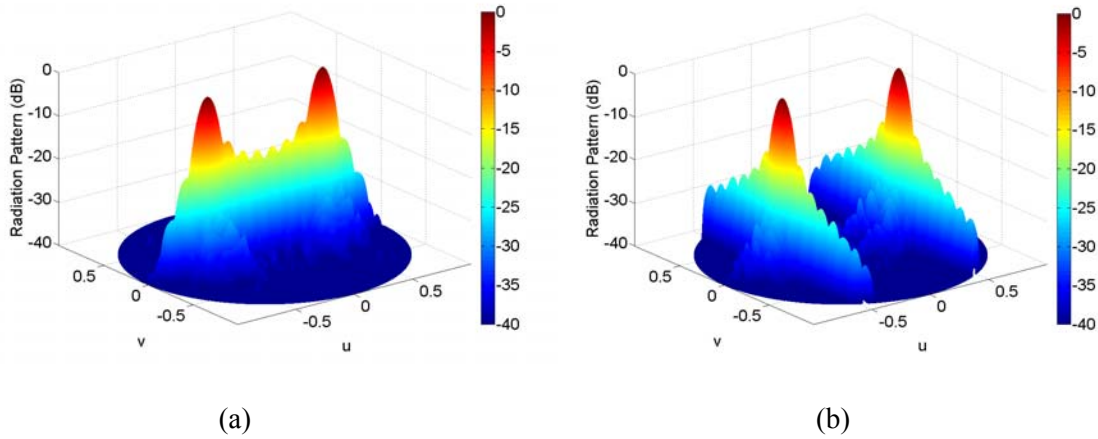


Fig. 5-1 3D radiation pattern of the double-beam reflectarray antennas designed with the geometrical approach: (a) design A, (b) design B.

From these results it can be observed that although two beams are generated in the required directions, the sidelobe levels are quite high. In addition, the beams show broadening in one direction. In both cases the direction of beam broadening corresponds to the shorter length of the sub-arrays.

The quad-beam reflectarray is designed to generate four beams in the directions of ($\theta_{1,2,3,4} = 30^\circ$, $\varphi_1 = 0^\circ$, $\varphi_2 = 90^\circ$, $\varphi_3 = 180^\circ$, $\varphi_4 = 270^\circ$). Similarly two different zone allocations are considered for the sub-arrays, namely beams pointing in the zone center direction or the zone edge. The radiation patterns for both these designs are given in Fig. 5-2. The results here show that four beams are generated in the required directions but with high side-lobe levels. While the examples here considered symmetric zone allocations with respect to the beam directions, it was observed that regardless of the choice of the zones, beam broadening will be observed in the

radiation patterns. This is mainly due to the fact that a smaller array surface is being used which would also reduce the antenna gain. Further discussions about the radiation performance of this approach will be given later in this section.

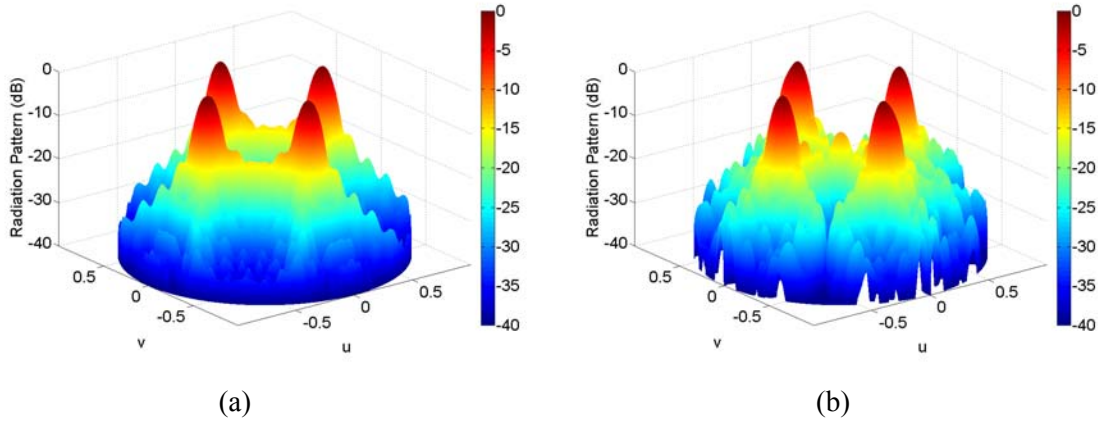


Fig. 5-2 3D radiation pattern of the quad-beam reflectarray antennas designed with the geometrical approach: (a) design A, (b) design B.

5.2.2 Superposition Approach for Multi-Beam Design

Another approach to multi-beam reflectarray designs is by using the superposition of the aperture fields associated with each beam on the reflectarray aperture. To generate N beams with a single feed, the tangential field on the reflectarray surface can simply be written as

$$E_R(x_i, y_i) = \sum_{n=1}^N A_{n,i}(x_i, y_i) e^{j\phi_{n,i}(x_i, y_i)}. \quad (5-2)$$

Here $A_{n,i}$ and $\phi_{n,i}$ are the required amplitude and phase of the i^{th} element which will radiate the n^{th} beam. In reflectarrays the amplitude of each element is fixed by the feed position and element location, which are independent of the beam direction, so

$$E_R(x_i, y_i) = A_i^{Feed}(x_i, y_i) \cdot \sum_{n=1}^N e^{j\phi_{n,i}(x_i, y_i)}. \quad (5-3)$$

The summation of the complex field distributions in (5-2) will give the overall required

amplitude and phase distributions. A basic problem exists here that is due to the fixed amplitude distribution imposed by the feed in reflectarray antennas. Although the required phase in (5-3) can be satisfied by proper element designs, the amplitude requirement cannot be satisfied in reflectarray antennas, i.e.,

$$\left| \sum_{n=1}^N e^{j\phi_{n(i)}(x_i, y_i)} \right| \neq 1. \quad (5-4)$$

As a result of this difference in the amplitude distribution on the aperture, reflectarrays designed using the superposition approach may show a degraded performance.

This amplitude error may be avoided for some simple designs; however, complicated multi-beam reflectarrays will suffer from this error. To demonstrate the multi-beam design capabilities of this approach, here we consider the quad-beam reflectarray system studied earlier. Three different normalized amplitude distributions on the aperture of the reflectarray antenna are given in Fig. 5-3. Fig. 5-3 (a) shows the summation of the complex terms, i.e. equation (5-4). Fig. 5-3 (b), shows the practical amplitude distribution of the reflectarray antenna which is set by the feed horn characteristics and position. The ideal amplitude distribution is given in Fig. 5-3 (c), which is the practical amplitude distribution multiplied by the summation of the complex terms. It is implicit that such a taper cannot be realized on the reflectarray antenna aperture, and this ideal amplitude distribution is not practical. This could result in a degradation of antenna performance, mainly by an increase in the side-lobe levels.

For the double-beam antenna, the periodic variations in the x-direction coincide with the element periodicity of $\lambda/2$. As a result, the amplitude variation is actually not seen by the phasing elements and is avoided. On the other hand, the quad-beam design shows amplitude variations that are not avoided and thus significantly alter the illumination taper of the aperture. The radiation patterns of both these multi-beam antennas are given in Fig. 5-4.

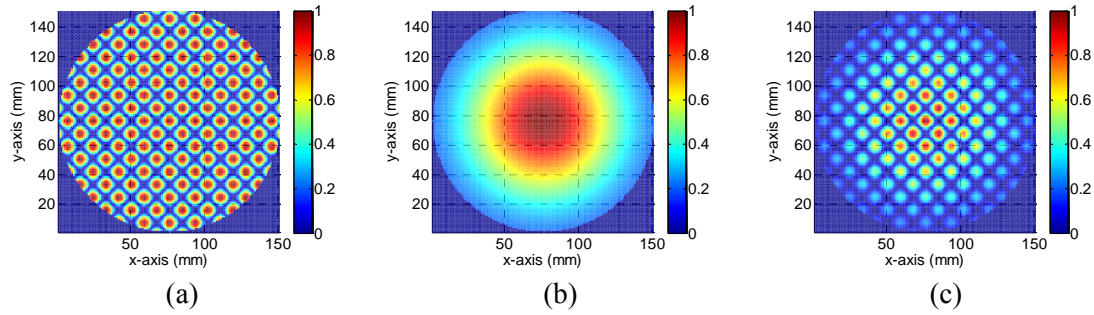


Fig. 5-3 (a) Amplitude error arising from equation (5-4). (b) Practical amplitude distribution. (c) Ideal amplitude distribution.

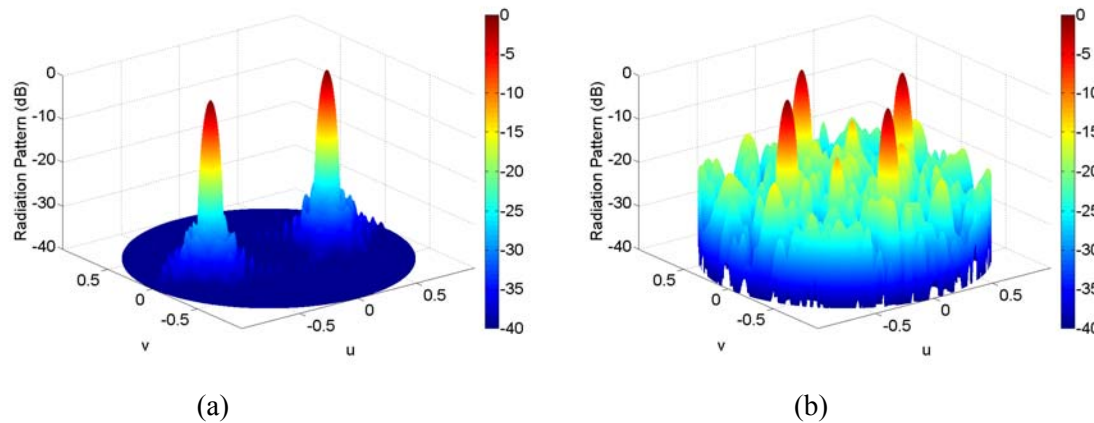


Fig. 5-4 3D radiation pattern of the multi-beam reflectarray antennas designed with the superposition approach: (a) double-beam, (b) quad-beam.

From these results it can be seen that, as expected, the double-beam design shows an ideal performance with side-lobe levels below -25 dB and beams correctly scanned to the designed directions. The quad-beam design however shows a very poor performance. Although four beams are generated, the sidelobe levels are quite high and the beams are not exactly scanned to the designed directions.

5.2.3 Comparison of Direct Design Methods for Multi-Beam Reflectarray

In order to compare the performances of these two direct design approaches for multi-beam

reflectarray design, let's study the quad-beam reflectarray antenna, introduced in the previous sections. We also design a single-beam reflectarray antenna as a reference whose beam is in the direction of $(\theta = 30^\circ, \varphi = 0^\circ)$. In Fig. 5-5 the normalized radiation pattern of this single beam design is compared with the multi-beam reflectarrays. Since the reference beam is in the $\varphi = 0^\circ$ plane, only this plane is given here, and a similar pattern was observed in the orthogonal plane. Comparison of the radiation patterns shows small beam deviations in the multi-beam reflectarray designs. The radiation patterns also show that the side-lobe level is below -11 dB for the geometrical design and below -17 dB for the superposition design. The side-lobe levels (SLL) are much higher than the reference single-beam design. Furthermore, the quad-beam antenna designed using the superposition method shows a beamwidth identical to the reference single-beam design, while in the geometrical design the beamwidth is much wider. The antenna directivity is an important measure to compare the radiation performance of these multi-beam design methods. For multi-beam reflectors using a single-feed, theoretically, the power of each beam will be reduced by $1/N$. Therefore, ideally it is expected that generating four beams will reduce the antenna directivity by 6 dB. However, the geometrical design has a directivity reduction of 11.73 dB and the superposition design exhibits a directivity reduction of 7.02 dB.

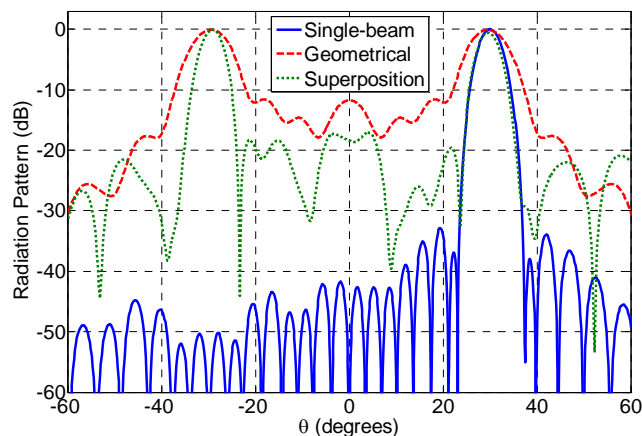


Fig. 5-5 Normalized radiation patterns of the single- and quad-beam designs.

Some important results of these three reflectarrays are summarized in Table 5-1.

Table 5-1 Calculated Radiation Characteristics of the Single-beam and Multi-beam Reflectarrays.

Antenna	Design Method	Beam Direction (deg.)	SLL (dB)	Directivity (dB)	HPBW
Single-beam		30	-32.85	32.937	5.0°
Quad-beam	Geometrical	29.44	-11.05	21.207	4.9°
	Superposition	29.57	-17.05	25.920	8.4°

For the multi-beam reflectarray designed with the geometrical approach, the amplitude distribution in each zone is maximum at the corner of that zone (near the array center) and minimum at the outer edge, which results in a significant increase in the side-lobe level. The wider beamwidth and lower directivity in the geometrical designs, however, requires further attention. The reduction in antenna directivity is the result of using one fourth of the array surface and one fourth of the power from the feed horn to generate each beam. This reduction of array surface is also the reason for the increase in beamwidth. For the multi-beam reflectarray designed using the superposition method, the high side-lobes are due to the amplitude errors, which alter the required illumination taper on the aperture. Also, in comparison of the calculated antenna directivity with the reference, this design approach shows a directivity loss about 1 dB higher than the ideal directivity reduction (6 dB), which is mainly due to the high side-lobe levels of this design.

In summary the shortcomings of both these direct design approaches are tabulated here:

Geometrical design method:

- 1) High side-lobe due to illumination taper.
- 2) Gain loss and beam broadening due to dividing the array surface into sub-arrays.

- 3) Small beam deviation.

Superposition design method:

- 1) High side-lobe due to amplitude error.
- 2) Gain loss due to the increase in side-lobe level.
- 3) Small beam deviation.

As a result of the above problems associated with the direct methods of multi-beam reflectarray design, it is necessary to implement some form of optimization routine to achieve desirable performance.

5.3 Optimization Methods for Single-Feed Multi-Beam Reflectarray Antennas

Another approach in multi-beam reflectarray design is to view this as a general array synthesis problem. In reflectarrays, however, the synthesis of radiation patterns is restricted by the fact that the amplitude of each reflectarray element is fixed by the feed properties and element location. As a result, design of multi-beam reflectarrays requires a phase only synthesis approach. In this section two different optimization approaches are briefly discussed and then implemented for designing single-feed reflectarray antennas with multiple beams.

5.3.1 Alternating Projection Method

The alternating projection method (APM), also known as the intersection approach [57], has been applied successfully to the phase synthesis of antenna arrays. A simple example of a two-beam reflectarray has been demonstrated using this method. This method is basically an iterative process that searches for the intersection between two sets, i.e., the set of possible radiation patterns that can be obtained with the reflectarray antenna and the set of radiation patterns that satisfy the mask requirements (set M). Compared to other phase synthesis methods developed for

array antennas, the main advantage of the alternating projection method is the significantly reduced computational time for convergence of the solution, which makes it suitable for large reflectarray antennas.

The pattern requirements for the design are usually defined by a mask, i.e., two sets of bound values, between which the pattern must lie. The general form of the radiation patterns that satisfy the mask requirements is

$$\text{set } M \equiv \{F(u, v) : M_L(u, v) \leq |F(u, v)| \leq M_U(u, v)\},$$

$$u = \sin \theta \cos \varphi, \quad v = \sin \theta \sin \varphi \quad , \quad (5-5)$$

where F is the far-field radiation pattern of the array and (u, v) are the angular coordinates. M_U and M_L set the upper and lower bound values of the desired pattern in the entire angular range. With set M defined, the alternating projection method can be implemented to obtain the desired radiation pattern. Implementing the alternating projection method requires definition of two projection operators: the mask projector (P_M) and the inverse projector (P_I). The mask projector uses the upper and lower bounds of the mask to correct the radiation pattern. The inverse projection (P_I) consists of a series of functions which projects the pattern back to the array excitation coefficients. It calculates new phase values for the reflectarray elements while the elements amplitude remain unchanged. A flowchart of the optimization routine is given in Fig. 5-6.

The first step is to define the mask for multi-beam operation. Typical masks for different contour beams can be found in the literature [58]; however, for multi-beam designs the mask definition is different. The required masks for multi-beam radiation patterns are typically circular contours defined in the direction of each beam. Since in this quad-beam design we don't want to change the beamwidth, which is directly related to the aperture size and illumination, the mask

upper and lower bounds in the beam area were defined according to the reference single-beam design. These upper and lower bounds are defined as

$$\begin{aligned} \text{If } (u, v) \in \text{main beam : } & M_U(u, v) = 0 \text{ dB,} \\ \text{If } (u, v) \in -3 \text{ dB beamwidth : } & M_L(u, v) = -3 \text{ dB.} \end{aligned} \quad (5-6)$$

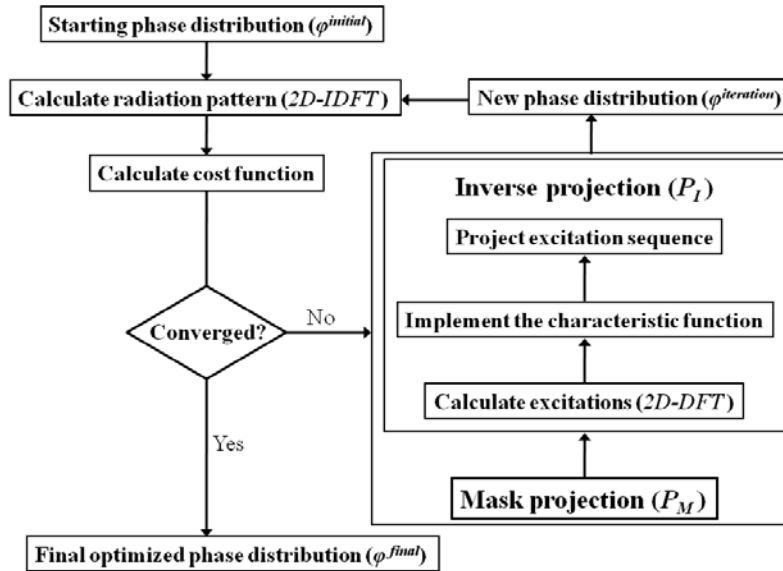


Fig. 5-6 Flowchart of the APM optimization.

The main objective of this optimization is to minimize the side-lobe level. While it is possible to control the side-lobe level by defining an upper bound (M_U) at certain values, in order to further minimize the side-lobe level, both upper and lower bounds in the side-lobe area were set to zero ($-\infty$ dB). A 2D figure of this beam mask model for the quad-beam reflectarray is plotted in Fig. 5-7 using dashed lines. It should be noted that in practice it was found that for this quad-beam reflectarray design, defining mask levels to zero or to an achievable level showed almost similar results.

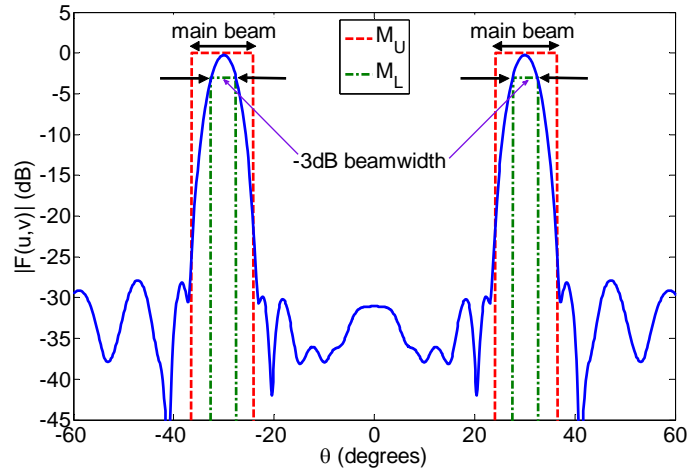


Fig. 5-7 2D view of the mask model for the quad-beam reflectarray.

In all optimization routines, it is necessary to define a cost function that should be minimized and can also control the number of iterations required for the convergence of the solution. Since in this optimization the requirements in the main beam will be satisfied by the projection operators with the bounds set in (5-6), the cost function need only to take into account the side-lobe performance of the array [59]. Thus, the cost is evaluated over every point in the (u,v) space which does not belong to the main beams using the following equation:

$$\text{If } |F(u,v)| > M_U(u,v)$$

$$\text{Cost} = \sum_{u^2+v^2 \leq 1} \sum (|F(u,v)| - M_U(u,v))^2. \quad (5-7)$$

With the mask and cost function defined, the optimized phase distribution of the reflectarray elements can be obtained with an iterative procedure. It should be noted here that the optimization is considered to be converged when the cost function becomes stable. In most cases the optimization converges with only a few iterations; however, a suitable starting point can reduce the number of iterations. In this design the phase distribution obtained by the superposition method in Section II is used as the starting point for the optimization. The

alternating projection method is then implemented to improve the reflectarray performance by optimizing the phase distribution on the reflectarray aperture. A far-field pattern of 400×400 points evenly spaced in the angular coordinates was computed for each candidate reflectarray at each cost evaluation.

For this quad-beam design, the solution converges after 23 iterations. Although the number of iterations required for the optimization generally depends on the problem at hand, in most cases the APM will converge with just a few iterations. The radiation pattern of the optimized design is given in Fig. 5-8. A quad-beam performance is obtained for the reflectarray with side-lobes below -26 dB. It can be seen that implementing the optimization here has corrected the amplitude problems associated with the initial superposition design. As a result, the side-lobe level has been reduced by about 9 dB and all four beams are exactly scanned to 30° off broadside. Also the calculated directivity for this antenna is 26.95 dB, which is about 1dB higher than the initial superposition design (Table 5-1). These results clearly demonstrate the effectiveness of the phase optimization process. The computational time for the APM optimization with 30 iterations was 456 seconds on a 2.2 GHz Intel core Duo CPU with 4GB RAM. This is to be compared with 16.5 seconds for both direct design methods.

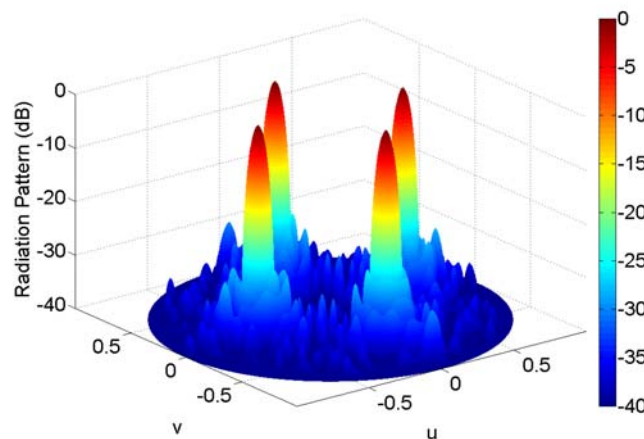


Fig. 5-8 Radiation pattern of the optimized design at 32 GHz.

It is important to point out that although in some cases the APM optimization might converge to local minima, for this symmetric quad-beam design the optimization did not get trapped and the solution converged smoothly. Similar radiation pattern results were observed when the phase distribution obtained by the geometrical approach was used for the starting point. Furthermore, the solution convergence was also observed for different side-lobe level requirements in the design. The convergence curves for different mask levels are given in Fig. 5-9 where it can be seen that in all cases, APM converges with a very few iterations.

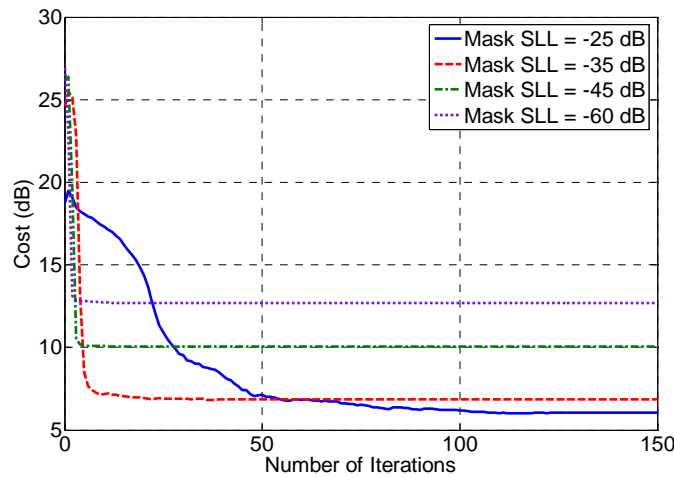


Fig. 5-9 Convergence curves for the optimization with different mask requirements.

For non-symmetric multi-beam designs, however, the problem with local minima is more challenging and some approaches that can circumvent the local minima problem may be required. To mitigate this problem, a more powerful global optimization technique is implemented in the next section.

5.3.2 Particle Swarm Optimization

The basics of the APM optimization techniques and how it can be implemented for multi-beam reflectarray antenna design were given in the previous section. While a number of multi-beam

and contour beam reflectarray antennas have been demonstrated using this approach, in many cases this method converges to local minima rather than the solution due to the non-convexity of the optimization problem. In the case of multi-beam design, if grating lobes exist in the visible range, usually the APM routine cannot optimize this design, because the solution space becomes a non-convex space. As an example a single-feed reflectarray antenna generating 2, 3, 4 and 6 beams are studied, where all four designs were optimized using the APM routine. The radiation pattern of the optimized designs is shown in Fig. 5-10. It can be seen that while for the two and four beam designs, the optimized performance is quite acceptable, for the tri- and hexa-beam designs, the grating lobes are still observed in the visible range.

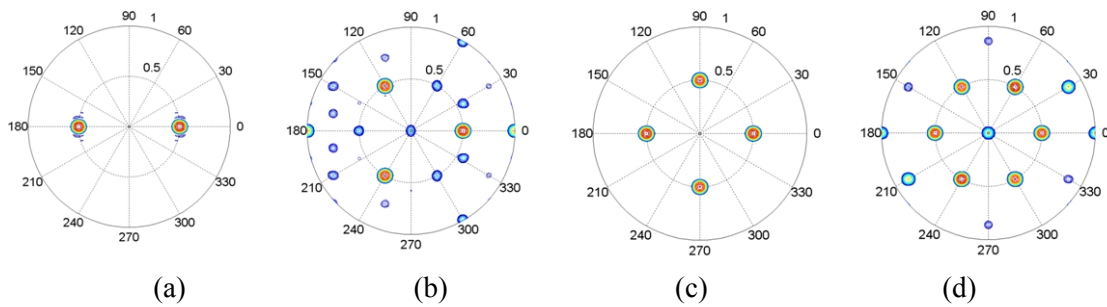


Fig. 5-10 Radiation patterns of single-feed multi-beam reflectarrays optimized with the APM routine: (a) two beams, (b) three beams, (c) four beams, (d) six beams.

This problem becomes more challenging when asymmetric multiple beam performance is required for the design. As such, the application of a global and more powerful optimization routine for multi-beam reflectarray designs is necessary.

The particle swarm optimization (PSO) has shown to be a robust optimization algorithm for many antenna design applications including array antennas [60]. To implement PSO, first an initial set of random positions and velocities are defined for the particles in the swarm. In the case of the phase optimization here, these positions are the phases of the reflectarray elements.

Each of these particle positions is then scored to obtain a scalar cost based on how well it solves the problem. The particles then fly through the N -dimensional problem space subject to both deterministic and stochastic update rules to new positions using

$$\begin{aligned} v_n &= \omega * v_n + c_1 \text{rand}() * (p_{best,n} - x_n) + c_2 \text{rand}() * (g_{best,n} - x_n), \\ x_n &= x_n + \Delta t * v_n, \end{aligned} \quad (5-8)$$

where v_n and x_n are the velocity and position of the particle in the n^{th} dimension, respectively. c_1 and c_2 are the self- and group-knowledge constants, that determine the relative pull, and ω is the inertial weight. As particles explore the problem hyperspace, each particle remembers its own personal best position (p_{best}) and also knows the best position found by any particle in the swarm (g_{best}). The swarm of particles explores the problem hyperspace, and eventually settles down near a good solution.

In order to implement the optimization, the first step is to define the far-field radiation pattern mask based on the design requirements. As discussed earlier, the required masks for multi-beam radiation patterns are typically circular contours defined in the direction of each beam. Usually for multi-beam designs the mask bounds in the beam area are defined according to the reference single-beam design. Similarly, the general form of the radiation patterns that satisfy the mask requirements is

$$F(u, v) : M_L(u, v) \leq |F(u, v)| \leq M_U(u, v), \quad (5-9)$$

where F is the far-field radiation pattern of the array and (u, v) are the angular coordinates. M_U and M_L set the upper and lower bound values of the desired pattern in the entire angular range. A 2-D figure of this mask model for a multi-beam design with different beam levels is given in Fig. 5-11.

The fitness function defined for this optimization is

$$Cost = \sum_{\substack{(u,v) \in \text{mainbeam} \\ \text{and } |F(u,v)| < M_L(u,v)}} (|F(u,v)| - M_L(u,v))^2 + \sum_{\substack{(u,v) \notin \text{mainbeam} \\ \text{and } |F(u,v)| > M_U(u,v)}} (|F(u,v)| - M_U(u,v))^2. \quad (5-10)$$

This function takes into account the performance of every point in the visible space, i.e., $u^2+v^2 \leq 1$. The first term in the fitness function takes into account the absolute difference between the radiation pattern and the lower bound, in other words the beam performance. The second term controls the side-lobe performance of the array for every point which does not belong to the main beam area. It should be noted that the radiation pattern of the reflectarray antenna is computed using the array theory formulation. Using the spectral transformation for the calculations, the radiation pattern of the reflectarray antenna can be computed quite efficiently, which is necessary for the optimization here.

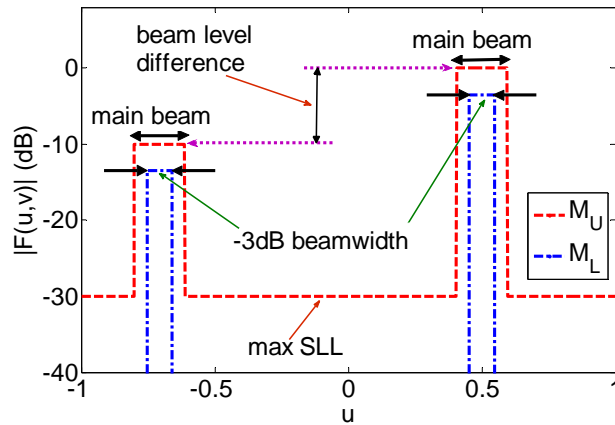


Fig. 5-11 2D view of a mask model for a multi-beam reflectarray.

To demonstrate the feasibility of the approach presented in this paper for phase optimization of multi-beam reflectarray antennas, we considered three different quad-beam reflectarray antenna designs. In all designs the antenna has a circular aperture with a diameter of 17λ at the design frequency. This corresponds to 848 phasing elements for the reflectarray with an element spacing of $\lambda/2$. The feed is prime focus and the power q of the feed horn $\cos^q \theta$ radiation pattern model is

6.5 which will give an edge taper below -12 dB. The beam requirements for the designs are summarized in Table 5-2. It should be pointed out that while in general the beamwidth and gain level for multi-beam designs are determined based on the design requirements, such as coverage area for satellite applications, in the designs studied here all beams are set to have beamwidths identical to a reference single-beam design. In addition for all three designs the required side-lobe level was -30 dB.

Table 5-2 Design Requirements for the Multi-beam Reflectarrays.

Design A

Beam	1	2	3	4
θ (degrees)	30	30	30	30
φ (degrees)	0	90	180	270

Design B

Beam	1	2	3	4
θ (degrees)	45	15	15	45
φ (degrees)	0	0	180	180

Design C

Beam	1	2	3	4
θ (degrees)	30	25	45	35
φ (degrees)	0	100	200	280
Normalized Gain (dB)	-3	-10	-5	0

For the optimization, the swarm population was set to 400 particles and 100,000 iterations were performed for each design. For the PSO parameters, the inertial weight was varied linearly from 0.9 to 0.4 over the course of the run and the self- and group-knowledge constants, c_1 and c_2 , were both set equal to 2 throughout the optimization.

The first reflectarray (Design A), represents a symmetric quad-beam design, similar to the one studied in the previous section. Four beams have equal levels and are located symmetrically in the angular space. Almost a similar performance was obtained using the APM optimization. The second reflectarray (Design B), is designed to have four simultaneous beams in one plane. This type of multiple beam antenna is primarily designed for radar applications. For this design the angular separation between adjacent beams is 30 degrees. While this design is also symmetric, the optimization problem is quite complex in this case and the APM technique was not able to achieve the required performance. The optimized phase distribution and radiation pattern for these two designs are given in Figs. 5-12 and 5-13, respectively.

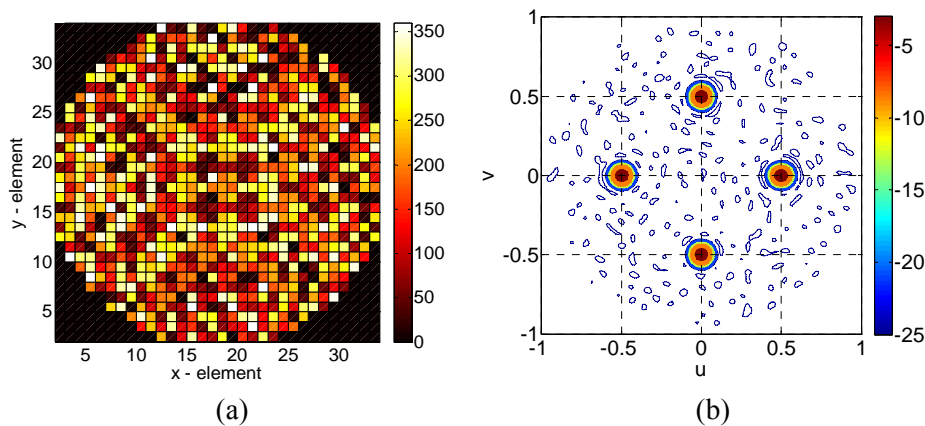


Fig. 5-12 Optimized multi-beam reflectarray (Design A): (a) phase distribution, (b) radiation pattern.

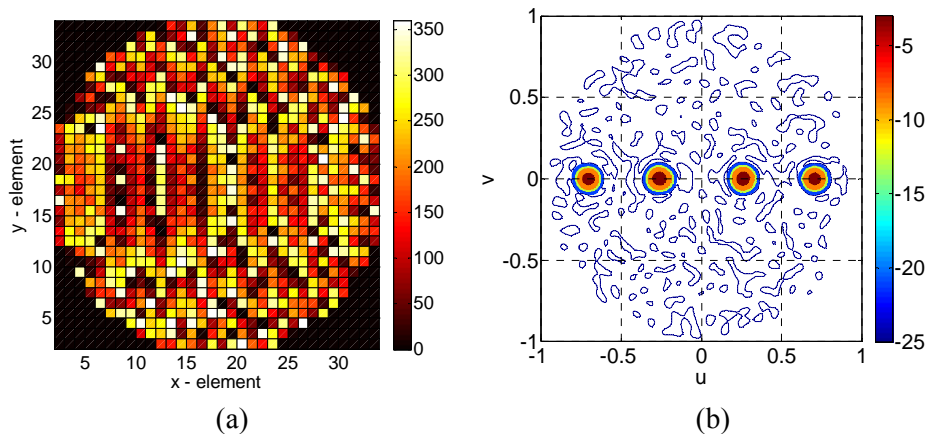


Fig. 5-13 Optimized multi-beam reflectarray (Design B): (a) phase distribution, (b) radiation pattern.

For the next case (Design C), we consider a multi-beam reflectarray with asymmetric beam directions and different gain levels. While in comparison with the previous designs, the optimization problem here is much more complicated, the number of iterations used for PSO was sufficient for convergence of the solution. The optimized phase distribution and radiation pattern for this design is given in Fig. 5-14.

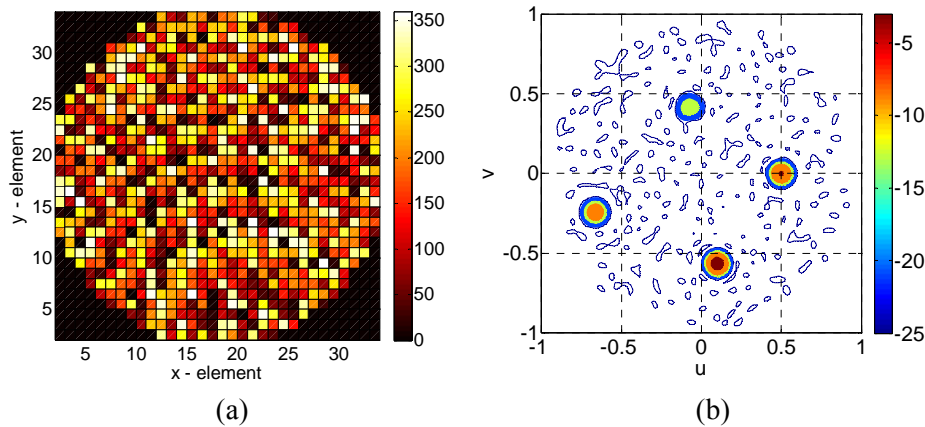


Fig. 5-14 Optimized multi-beam reflectarray (Design C): (a) phase distribution, (b) radiation pattern.

It can be seen that all three reflectarrays studied in this section achieved the design requirements, which demonstrates the effectiveness of the particle swarm optimization for multi-beam designs. It is also important to note that depending on the design requirements it is possible to utilize the symmetry of the problem to reduce the dimension of the optimization problem; however, the focus of the study here was on asymmetric multiple beam designs, therefore no symmetry boundary was implemented in the optimizations. While it is implicit that in comparison with the APM approach, the PSO method requires a much higher computational time, the main strength of the PSO is the capability to escape the traps in the optimization process. Experimental results showed that while the APM optimization could be used for simple cases such as Design A, it fails to achieve the design requirements for more complex cases such as Designs B and C. It is important to point out here that for these optimizations the convergence

curves did not show a smooth improvement, which is mainly due to the fact that the swarm population is quite small for an optimization of this size. None the less, in all designs a fitness improvement higher than 26 dB was obtained which was quite sufficient.

5.4 Design and Measurement of Single-Feed Multi-Beam Reflectarray Antennas

In this section, measurement results for two optimized quad-beam prototypes are presented. Both designs are fabricated on a 20 mil Rogers 5880 substrate. The reflectarray has a circular aperture with a diameter of 15.94 cm. The phasing elements are variable size square patches with a unit-cell periodicity of $\lambda/2$ at the design frequency of 32 GHz. The unit-cell simulations are carried out using the commercial software Ansoft Designer, where the fabrication limit of our LPKF ProtoMat S62 milling machine is also taken into account by enforcing the minimum gap size between the elements and the achievable fabrication tolerance. It is worthwhile to point out that in general the reflection characteristics of the phasing elements are angle dependent and oblique incidence needs to be considered. Our simulations showed that for these elements normal incidence can present good approximations for oblique incidence angles up to 35° ; thus the prototypes were designed based on the simulated reflection coefficients obtained with normal incidence.

5.4.1 A Quad-Beam *Ka*-Band Reflectarray Antenna with Symmetric Beams

The quad-beam reflectarray antenna here is designed to have four symmetric beams, each pointing 30 degrees off-broadside direction. The photograph of the fabricated array with 848 square patch elements is shown in Fig. 5-15. The centered prime focus LHCP feed horn is mounted on a mechanical alignment system and positioned with an F/D ratio of 0.735. To avoid blockage from the supporting strut of the feed horn, the array is rotated 45° in the reflectarray

plane so the main beams are in the directions of ($\theta_{1,2,3,4} = 30^\circ$, $\varphi_1 = 45^\circ$, $\varphi_2 = 135^\circ$, $\varphi_3 = 225^\circ$, $\varphi_4 = 315^\circ$). Since dual-linear square patch elements are used in this design, the reflected co-polarized radiation of the reflectarray system is RHCP.



Fig. 5-15 Fabricated quad-beam reflectarray antenna.

The radiation pattern is measured using our planar near-field measurement system. Comparisons of the simulated and measured co-polarized radiation patterns at 32 GHz are shown in Fig. 5-16. The simulated radiation pattern of the single beam reference design in section II is also plotted here for comparison.

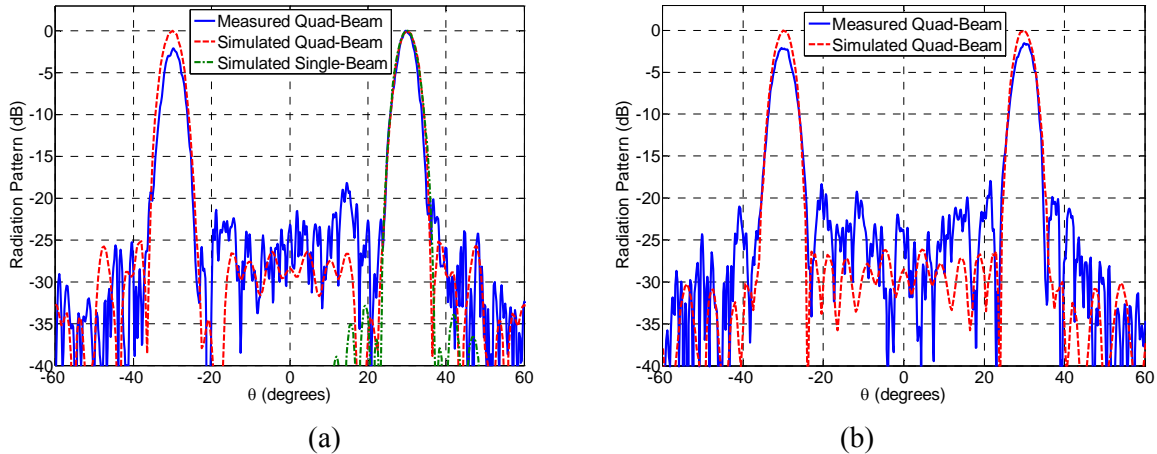


Fig. 5-16 Measured and simulated co-polarized radiation patterns of the reflectarray antenna: (a) $\varphi = 45^\circ$ plane, (b) $\varphi = 135^\circ$ plane.

For the quad-beam design, the simulated radiation patterns here also include the aperture blockage caused by the horn and the alignment system, which is calculated using the approach given in [25]. To study the blockage effect, the computed radiation pattern of the quad-beam design is imported into an EM solver (FEKO) and the blockage is approximated by a PEC disk (representing the 2D cross section of the blockage) located at the horn aperture. Although this model does not take into account multiple reflections between the feed horn and the reflectarray aperture, it can provide a first order approximation of the blockage effect. The simulated radiation patterns, with and without the blockage effect are compared with the measured results in Fig. 5-17. A much better agreement between the measured and simulated results can be observed. The blockage effect increases the SLL in the off-beam areas about 15 dB, but has negligible effect on the radiation patterns for angles larger than $\theta = 40^\circ$. Similar results were observed in the other principal plane.

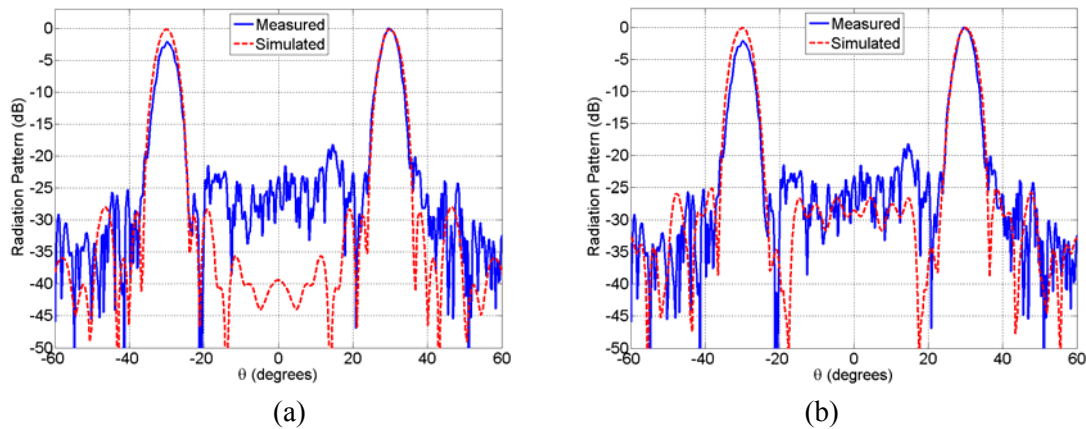


Fig. 5-17 Effect of blockage on the radiation pattern of the antenna: (a) without blockage, (b) with blockage.

The measured radiation patterns show that four beams are generated in the required directions, which are correctly scanned to 30° , and the side-lobe levels are below -18 dB. The measured and simulated results show good agreements in the main lobes, where the measured -3dB beamwidth

is 4.35° for both vertical and horizontal planes. Some discrepancies exist in the side-lobe regions, which are mainly due to fabrication errors and element design approximations. The beam level reduction is primarily due to the alignment errors of the measurement setup and the azimuth non-symmetry of the feed horn radiation pattern; however, this reduction is less than 2.15 dB for any beams. Both simulated and measured cross-polarized radiation patterns of the reflectarray are given in Fig. 5-18 for the $\varphi = 45^\circ$ plane. Almost similar results were observed in the orthogonal plane ($\varphi = 135^\circ$). The relatively high cross-polarization level of the reflectarray here is due to the high cross polarization of the feed horn. To reduce the cross polarization, one approach is to use a better feed horn with lower cross-polarization level. This was confirmed by repeating the simulations with an idealized horn antenna model. For this case the cross-polarization level of the reflectarray was reduced to -23.1 dB. Another approach is to use the element rotation technique [26] for phase compensation, since it will only compensate the phase of the co-polarized CP components to form a focused beam.

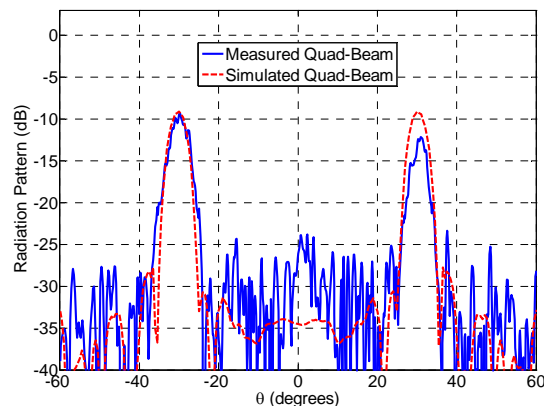


Fig. 5-18 Measured and simulated cross-polarized radiation patterns of the reflectarray antenna in $\varphi = 45^\circ$ plane.

A 3-D view of the measured co-polarized radiation pattern of this quad-beam prototype is given in Fig. 5-19.

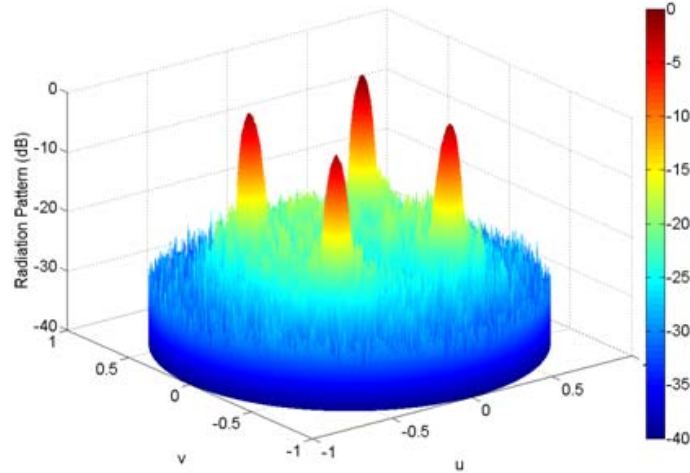


Fig. 5-19 Measured radiation patterns of the reflectarray antenna.

The measured gain and aperture efficiency vs. frequency are given in Fig. 5-15. It should be noted that although all beams showed a similar gain performance vs. frequency, the gain results presented here are for the beam in the direction of $\theta = 30^\circ$, $\varphi = 45^\circ$. At 32 GHz, the measured gain is 25.3 dB, and the 1 dB gain bandwidth is 8.6%. For multi-beam antennas, the classical definition of aperture efficiency might not be appropriate; therefore a modified definition is used here to calculate the aperture efficiency, i.e.,

$$\eta_a = \sum_{i=1}^N \frac{\lambda^2 G_i}{4\pi A}, \quad (5-11)$$

where N represents the number of beams and A is the aperture area. This definition takes into account the measured gains of all four beams, and the aperture efficiency is calculated to be 35.26%. Besides the spillover and illumination effects, the loss in the aperture efficiency comes from the cross-polarization effect, the element loss, and the feed blockage.

The bandwidth of a reflectarray antenna is usually defined by the 1 dB gain bandwidth [7]. For multi-beam reflectarrays however, the practical bandwidth of the antenna is also limited by the fact that the beams shift with frequency. This is due to the fact that the main beam direction

depends on the progressive total phase on the aperture (including all time delay effects from feed radiation and total reflection phase of the elements). It was shown in [61] that beam squint can be minimized in reflectarray antennas by enforcing the condition $\theta_o = \theta_i$, where θ_i is defined as the angle from the phase center of the feed to the center of the array and θ_o is the main beam direction. It is clear that this condition cannot be satisfied for multi-beam designs and beam squint would become a limiting factor.

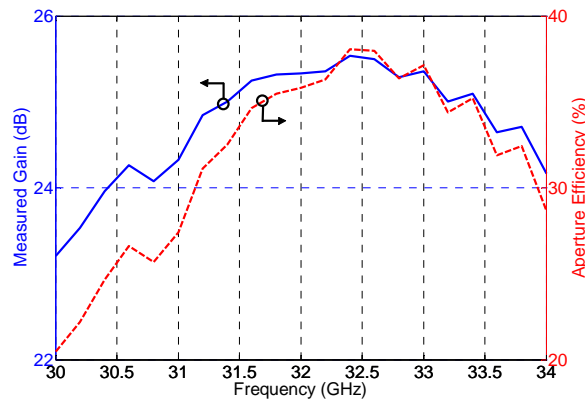


Fig. 5-20 Measured gain and efficiency of the quad-beam reflectarray antenna.

The measured radiation patterns at the center and extreme frequencies are given in Fig. 5-21 for the $\varphi = 45^\circ$ plane. Similar results were observed in the orthogonal plane. The radiation patterns show quad-beam patterns across the entire band with a slight increase in side-lobe level at the extreme frequencies. The beam squint across the 1 dB gain bandwidth of the antenna is about 2.5° . Considering that the beamwidth of the antenna is more than 4° , the effect of this beam squint is acceptable for this quad-beam prototype.

It is interesting to point out that in comparison between the multi-beam design methods, the direct geometrical approach shows the smallest beam squint. While the quad-beam prototype here did not show a very large beam squint across the band, it should be pointed out that in general multi-beam reflectarrays, beam squint could limit the operating band of the antenna.

Thus, for general multi-beam designs where a minimum beam squint requirement is specified, additional constraints over the frequency bandwidth needs to be imposed when optimizing the phase distribution of the elements.

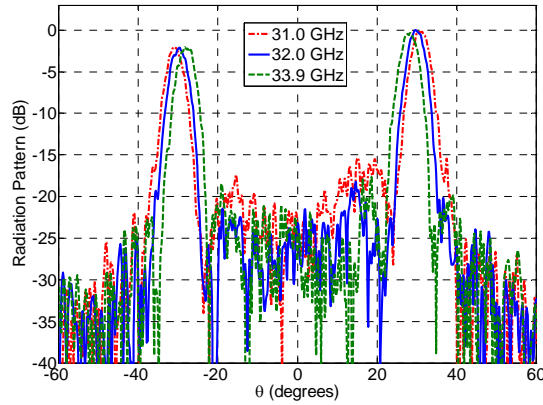


Fig. 5-21 Measured radiation patterns of the reflectarray antenna across the 1 dB gain band in the $\varphi = 45^\circ$ plane.

5.4.2 A Quad-Beam *Ka*-Band Reflectarray Antenna with Asymmetric Beams

An example of a quad-beam reflectarray antenna prototype with asymmetric beam directions and beam levels is presented here. The design requirements for the beams are summarized in Table 5-3. The photograph of the fabricated array with 848 square patch elements is shown in Fig. 5-22. The radiation pattern of this asymmetric quad-beam design is measured using our planar near-field measurement system. The measured near-field electric fields are given in Fig. 5-23.

Table 5-3 Design Requirements for the Asymmetric Multi-beam Reflectarray.

Beam	1	2	3	4
θ (degrees)	30	25	45	35
φ (degrees)	0	100	200	280
Normalized Gain (dB)	-3	-10	-5	0

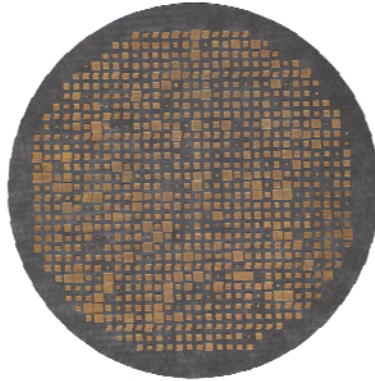


Fig. 5-22 Fabricated asymmetric quad-beam reflectarray antenna.

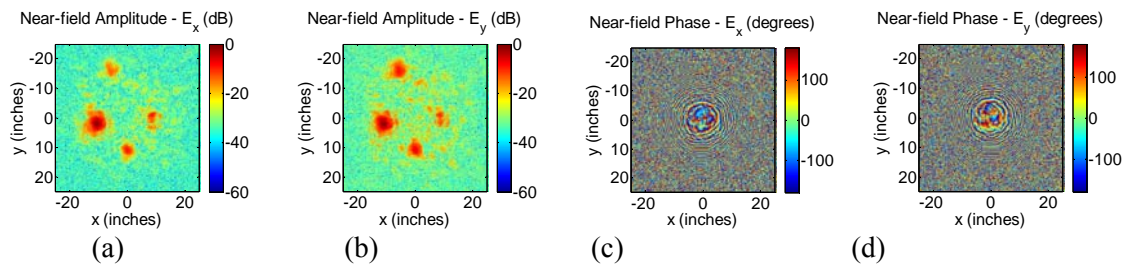


Fig. 5-23 Measured near-field electric fields of the asymmetric quad-beam prototype: (a) $|E_x|$, (b) $|E_y|$, (c) phase of E_x , (d) phase of E_y .

A contour plot of the measured and simulated radiation patterns are shown in Fig. 5-24. It can be seen that a close agreement between the measured and simulated results is observed, where the beams are correctly scanned to the required directions. The measured and simulated 3-D radiation patterns are also given in Fig. 5-25. It can be seen that while a reasonably good agreement is observed between these results, the main difference between the measurements and simulations is the increase in SLL. None the less the peak SLL in the measured results is about -20dB which is similar to what was observed in the symmetric quad-beam design.

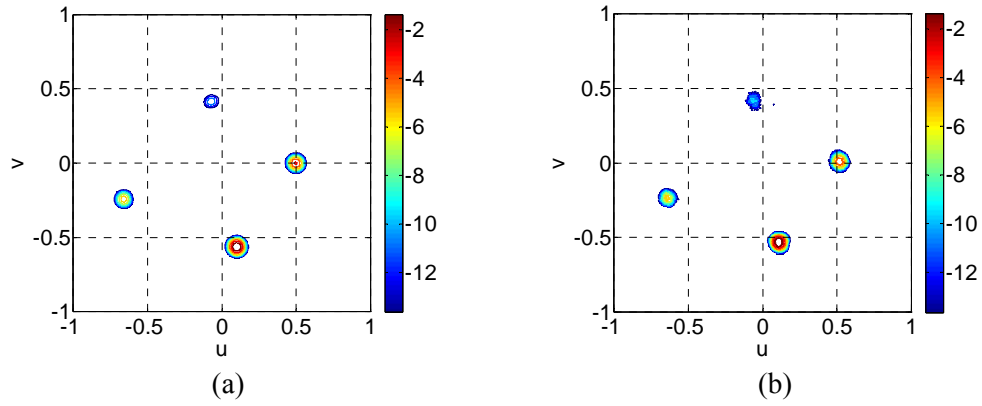


Fig. 5-24 Far-field radiation patterns of the asymmetric quad-beam prototype: (a) simulated, (b) measured.

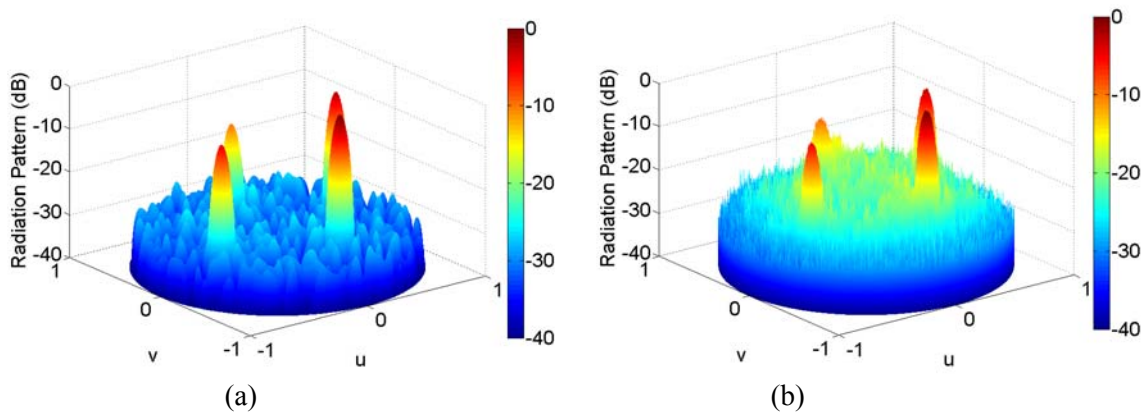


Fig. 5-25 3-D far-field radiation patterns of the asymmetric quad-beam prototype: (a) simulated, (b) measured.

CHAPTER VI

BEAM SCANNING REFLECTARRAY ANTENNAS

In this chapter, various approaches for designing beam-scanning reflectarray antennas are first reviewed and the advantages and limitations of these approaches are summarized. From this comparative study it is realized that for moderately wide angle beam-scanning, utilizing the feed displacement technique is a convenient approach. In the next stage, a novel aperture phase distribution is proposed for the reflectarray antenna, and is further optimized to improve the beam-scanning performance of the system. A high-gain Ka-band prototype achieving 60 degrees scan range with side-lobe levels below 15 dB is demonstrated.

6.1 Introduction to High-Gain Beam-Scanning Antennas

High-gain antennas are an essential part of a long distance wireless communication link. The conventional choice for the antennas in these systems are typically based on reflectors (or lenses) or arrays. Antennas with beam-scanning capability, on the other hand, add new dimensions to the system, enabling multi-function performance and improving system efficiency. A beam-scanning antenna can search or track targets for radar applications or direct beams toward distant receivers and transmitters in a communication system. The market for high-gain beam-scanning antennas is primarily dominated by military radar and tracking platforms, however, some commercial applications such as low earth orbit (LEO) satellite communications and collision warning systems also require high-gain beam-scanning antennas [62]. Owing to their hybrid nature, the

reflectarray antenna provides advantages over these two types of antennas, and is well suited for applications requiring high-gain beam-scanning antennas.

In most high-gain beam-scanning applications, the conventional choice between a reflector and a direct radiating phased array is driven by factors relating to scan rate, scan volume, and cost [63]. Electronic scanned phased arrays rely on phase shifter technology. For high-gain beam-scanning where the antenna aperture is large, active phased arrays using transmit/receive (T/R) modules are employed. While the phase shifter and T/R module technology have greatly matured over the years and the cost of active phased arrays have dropped dramatically, they still represent a considerable portion of the overall antenna cost [64]. Reflector antennas, on the other hand, are more suitable when a very high gain aperture is required and a phased array is cost prohibitive. In addition to the cost benefit advantages, they are well suited for systems which operate over a limited field of view. It should be noted that for both designs it is possible to scan the beam by mechanical movement of the aperture; however, the focus of the beam-scanning study here is to achieve a dynamic pattern. To scan the beam of these aperture antennas, the phase distribution on the aperture has to be adjusted corresponding to the direction of the scanned beam. While the concept is similar in both designs, the approaches used to realize this is distinctive for reflectors and arrays. Reflectarrays on the other hand are a hybrid antenna, and as such offer more flexibility in aperture phase control. The beam of a reflectarray antenna can be scanned by means of the reflector nature or the array nature of the antenna. In addition it is possible to utilize both approaches in a single design to improve scan performance or reduce system cost.

6.2 Beam-Scanning Approaches for Reflectarray Antennas

To achieve a dynamic radiation pattern for a reflectarray antenna, the aperture phase

distribution has to be adjusted corresponding to the direction of the scanned beam. The phase distribution for each element on the reflectarray aperture consists of two components, i.e.,

$$\phi(x_i, y_i) = -k_0 d_i + \phi_R(x_i, y_i). \quad (6-1)$$

In this equation, the first term corresponds to the spatial delay, which is the electrical distance between the phase center of the feed and the element position on the array. The second term is the reflection phase of the element on the aperture. Since in a reflectarray antenna one can control these two components almost independently, different approaches are available for beam-scanning reflectarray antennas.

6.2.1 Feed Displacement Approach

In the first approach, one changes the phase distribution on the reflectarray aperture by changing the spatial delay. This beam scanning technique is similar to what one uses to scan the beam of a reflector antenna, which is categorized here as the feed displacement approach. As pointed out earlier, the aperture placement is fixed, so the change in spatial delay is realized by displacing the feed phase center. Depending on the scan speed requirement, the availability of feed antennas, and the overall system cost, beam-switching or beam-scanning performance can be realized with this technique. A simple low-cost choice is to use a single movable feed for beam-scanning, but this mechanical feed displacement approach has a low scan speed. To achieve high-speed performance, generally a fixed array feed is used. The feed array system can be categorized into two groups: multiple feed array and phased array feed. A multiple array feed can achieve a beam-switching performance, basically on the basis of one feed per beam, while a phased array feed can provide a continuous beam-scanning.

An additional degree of freedom exists in these systems that can be utilized to further enhance the beam-scanning performance of these designs. As discussed earlier, the aperture phase distribution is fixed in these designs; however, it is possible to design an aperture that provides a better phase compensation, depending on the scan range requirement. Conventionally, reflectarray antennas are designed based on the aperture phase distribution of parabolic reflector antennas. For beam-scanning applications, however, these designs show a poor performance [65]. Reflectarrays designed based on the principle dual reflectors [66], bifocal dual reflectors [67], or spherical reflector systems [68], can significantly improve the scan performance. It is worthwhile to mention here that, in general, the reflection phase of reflectarray elements are sensitive to the excitation angle; therefore, displacement of the feed phase center will also change the second term in (6-1). However various designs are available for phasing elements which show low sensitivity to the angle of incidence, and can be used to reduce the effects of oblique excitation angles on the performance of the reflectarray antenna.

6.2.2 Aperture Phase Tuning Approach

Similar to phased array antennas, a reflectarray antenna with individual phase control for each element can achieve a dynamic pattern. As discussed earlier, a main challenge in the design of phased arrays is the feed network. While smaller phased arrays can be designed by only using phase shifters for each element, essentially a passive design, larger phased arrays require the use of T/R technology to compensate for the distribution losses in the feed network. These active phased arrays can achieve a high-gain beam-scanning performance; however, the main disadvantage of these designs is the high-cost of the system. A great strength of the reflectarray antenna is the spatial feed network of this system. A reflectarray antenna with individual phase

control for each element can achieve a dynamic pattern without the need for an RF feed network. This can potentially improve the gain and allow for greater flexibility in array configurations, since beam-scanning can be achieved by implanting low-loss phase shifters into each reflectarray element without the need for T/R modules.

Different approaches for aperture phase tuning beam-scanning reflectarray elements have been developed over the years. In general, phase control of reflectarray elements can be categorized into four groups:

- Mechanically controlled elements
- Electromechanically controlled elements
- Electronically controlled elements
- Exotic materials

Various designs of aperture phase tuning beam-scanning reflectarrays with micro-machines, MEMS actuators and switches, PIN diodes, and exotic materials have been demonstrated [69]. While in general the beam scanning speed is directly dependent on the technology used, mechanical scanning is in the order of milliseconds, and electronic scanning is typically in the nanosecond range. Particularly for the electronic scanning, an important consideration is the number of bits required for digital phase control.

Studies have shown that due to the phase front averaging in reflectarray antennas, low-bit quantization phase shifters, such as 2 or 3 bits, can achieve good far-field beam scanning resolution [3]. To demonstrate this, here we study an aperture phase tuned reflectarray system with digital phase shifters for every element, and compare it to a system with analog phase controlled elements. The reflectarray antenna has a circular aperture with a diameter of 20λ at the center frequency and 1184 phase controlled elements. F/D is set to 1, and the system is designed

for a -10 dB ET. This corresponds to a q value of 9.318 for the feed antenna. Since with this system, the feed placement is fixed, the aperture efficiency of the system which is 78.41% remains constant during beam-scanning. Furthermore the phase shifters are assumed to be lossless and ideal, and also cover the complete 360° phase cycle. For example 2-bit phase shifters will have four states with 0° , 90° , 180° , and 270° phase shift.

As discussed earlier, beam-scanning with this system is achieved by changing the phase distribution on the reflectarray aperture. The aperture phase distribution for a broadside beam, and a 60° scanned beam for the ideal analog phase controlled system is given in Fig. 6-1.

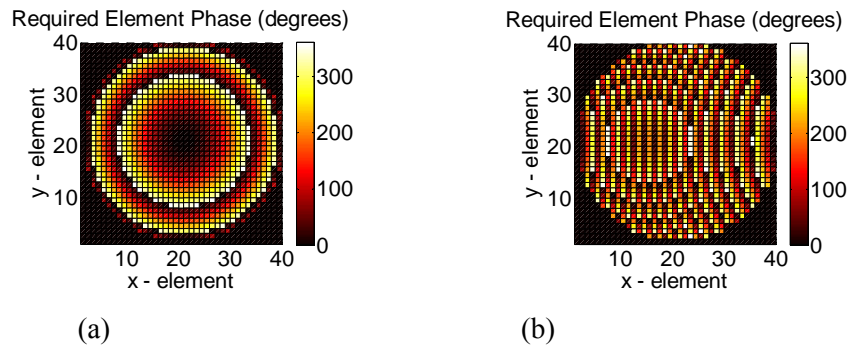


Fig. 6-1 Phase distribution on the analog phase controlled reflectarray aperture: (a) broadside beam, (b) 60° scanned beam.

To study the effect of digital phase quantization we study systems with 1- to 3-bit phase shifter elements. The aperture phase distribution for these three systems for a broadside beam, and a 60° scanned beam is given in Fig. 6-2.

From these figures it can be seen that while the 1-bit phase control doesn't appear to give a good representation of the ideal aperture phase distribution, 2- and 3-bit phase control seem to be quite sufficient.

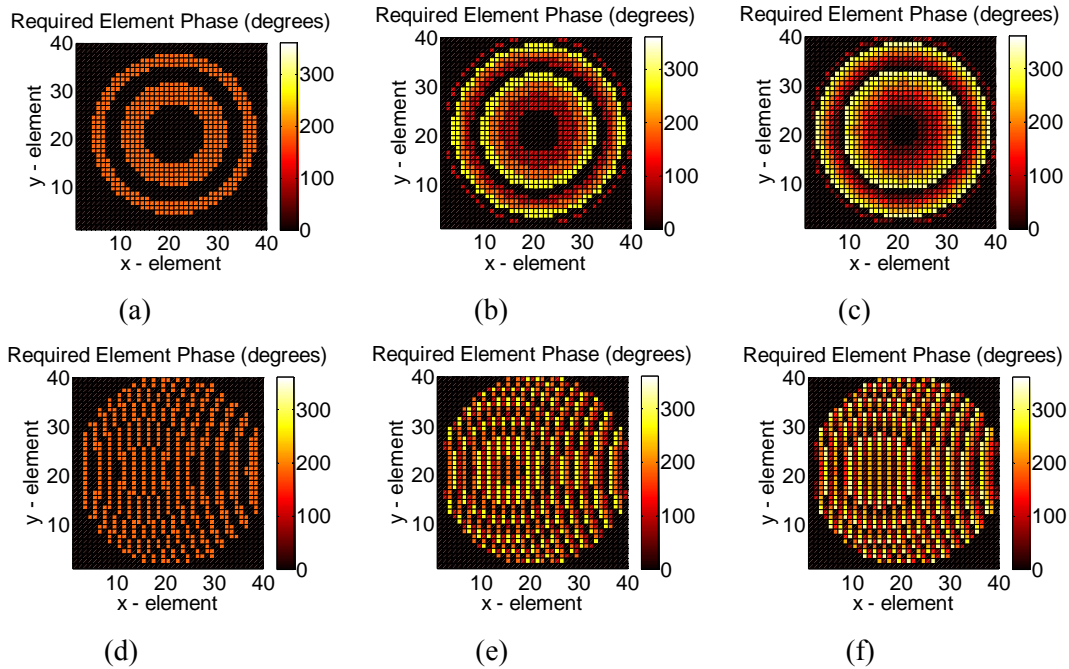


Fig. 6-2 Phase distribution on the digital phase-controlled reflectarray aperture: broadside beam (a) 1-bit, (b) 2-bit, (c) 3-bit; 60° scanned beam (d) 1-bit, (e) 2-bit, (f) 3-bit.

To properly characterize the beam-scanning performance of these systems, we study the side-lobe level and scan loss of these four systems. The normalized radiation patterns for broadside, and 60° scanned beam are given in Fig. 6-3. It can be seen that while the main beam direction and beam width is almost identical in all four designs, the primary difference is in the side lobe performance. The 1-bit system shows a very poor radiation performance where side lobes are about -23 dB for the broadside beam and increase to -17 dB as the beam is scanned. While in general, the side lobes do increase as the beam is scanned off broadside; the increase in side-lobe level for the 2- and 3-bit systems is much lower. In particular the radiation patterns for the 3-bit system shows a reasonably close agreement with the analog system. While for beam-scanning systems with very low side-lobe requirement it might be necessary to increase the number of bits, the side lobe performance of the 3-bit system studied here is quite sufficient for most applications.

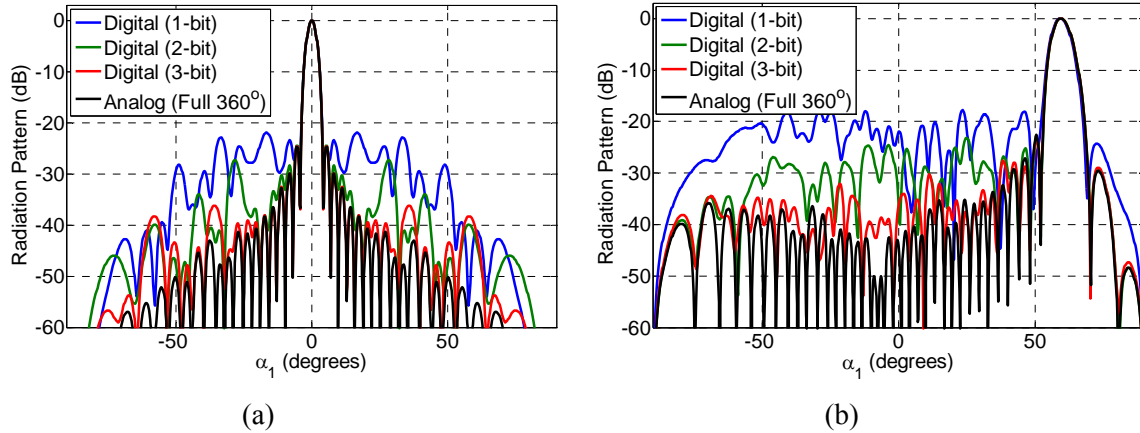


Fig. 6-3 Radiation patterns of the beam-scanning reflectarray antennas: (a) broadside beam, (b) 60° scanned beam.

One of the most important characteristics of a beam scanning antenna is the scan loss [62]. The ideal scan loss for a beam-scanning array is given by a $\cos \theta_s$ function, which is a consequence of the projected aperture size reduction. For practical systems where the array elements display some losses, scan loss is usually represented by a $\cos^n \theta_s$ function. While the array elements may exhibit a variety of both random and spatially correlated errors that degrades the system performance, in our study here the error and corresponding scan loss is solely due to phase quantization effects. The scan performances for the four designs are given in Fig. 6-4.

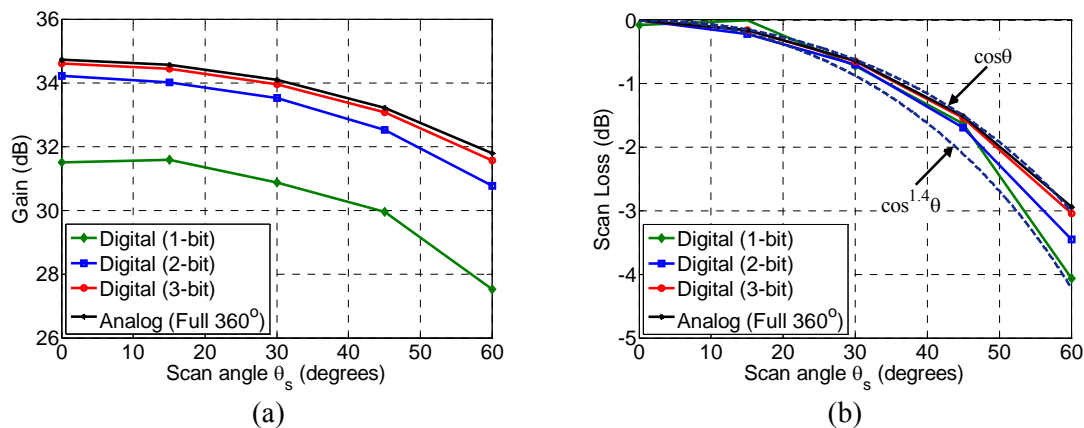


Fig. 6-4 Scan performance of the reflectarray antennas: (a) gain vs. scan angle, (b) scan loss.

Comparison of the antenna gains show that for the 1-bit system, the broadside gain is almost 3 dB lower than the analog design. This peak gain difference is reduced as the numbers of bits are increased, and for the 3-bit system it approaches 0.1 dB. On the other hand gain loss as a function of scan angle doesn't show a strong dependence on the number of bits. The results in Fig. 6-4 (b) indicate that while scan loss also improves as the numbers of bits are increased; this variation is about 1 dB for the four systems studied here. Ignoring the slight initial increase for the 1-bit system, the bounds for the scan loss envelope are $\cos^{1.0} \theta_s$ and $\cos^{1.4} \theta_s$.

The study presented in this section on the performance of analog and digital aperture phase controlled reflectarray antennas showed that, digital control with 2- or preferably 3-bits is quite sufficient for a beam-scanning system and the antenna can achieve a performance comparable to analog control designs. While analog or digital phase shifting may not be an issue for mechanically controlled elements, for electromechanical or electronic phase shifting, digitally controlled elements would be preferable since they typically exhibit a lower loss, better phase accuracy, and are less complicated to bias. It is worthwhile to point out here that generally for these beam scanning reflectarrays, apart from the spatial feed network, a control board has to be placed behind the array to supply control voltages or rotation angles to each element, and a microcontroller is used to interface the system with an external computer, which synthesizes the array.

6.2.3 Summary

Depending on the application, several system requirements maybe specified for a beam scanning reflectarray antenna. In general, however, the main parameters are scan resolution, pattern control, scan speed, control power consumption, and system cost. From a comparative

study, it is observed that for narrow beam-scanning, feed displacement approaches are the suitable choice since the loss in these systems is much lower. On the other, hand for wide angle beam-scanning, aperture phase tuned reflectarrays can achieve wide angle beam scanning, which is usually not practical with the former method. The drawback is the higher cost in these designs. It is worthwhile to point out that, from a system design view point, the phase control architecture in aperture phase tuned reflectarrays, which generally depends on the scan range requirement, determines the overall system cost.

6.3 Feed Displacement in Reflectarray Antennas

6.3.1 Axial and Lateral Feed Displacement

As discussed in the previous section, it is possible to scan the beam of a reflectarray antenna by changing the phase center of the feed antenna. To systematically study the effect of feed displacement on the radiation performance of reflectarray antennas, we follow the procedure developed for reflector antennas [22, 23], and study axial and lateral displacements of the feed independently.

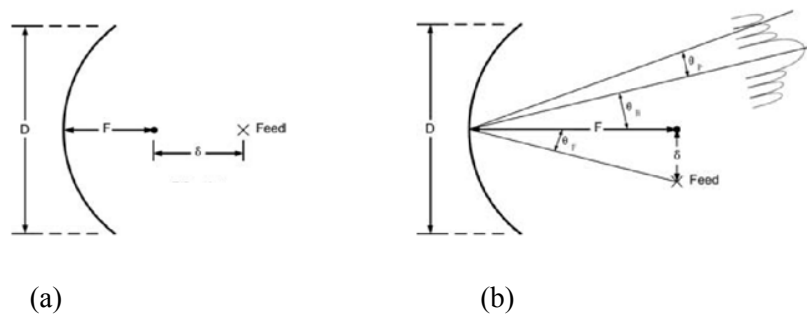


Fig. 6-5 Feed displacement paths for reflector antennas: (a) axial displacement, (b) lateral displacement.

A circular reflectarray aperture with a diameter of 20λ is considered for the study here, and in all studies the F/D and radiation pattern model (q) are designed to achieve an edge taper equal to -10

dB when the feed is at focal point. For the axial displacement study, we study the gain loss versus displacement (δ/λ) for various F/D ratios. In all studies the feed is displaced along the axial direction from -3λ to $+3\lambda$, where the negative sign indicates that the feed is moving towards the reflector. The ideal phase shift and the corresponding phase error on the aperture is given in Fig. 6-6 for F/D = 0.4.

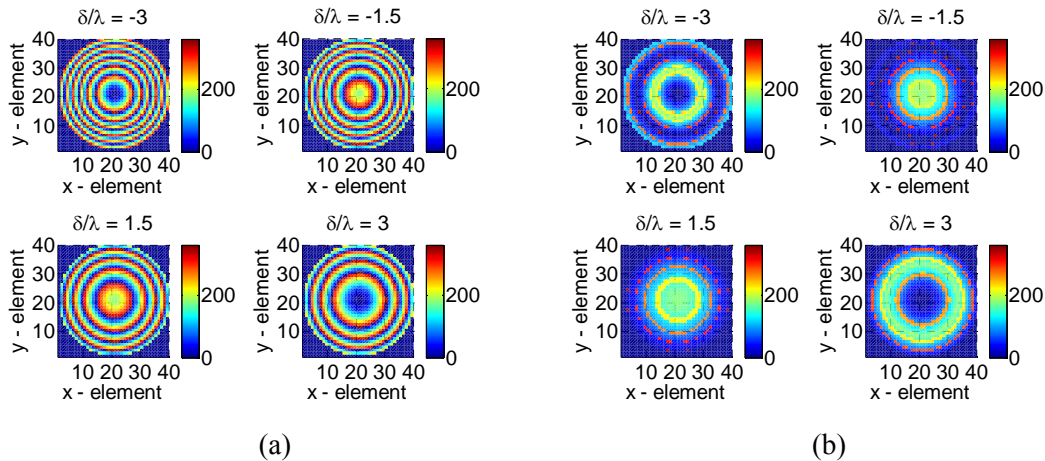


Fig. 6-6 Effect of axial displacement of the feed on the phase distribution on the aperture: (a) Ideal phase shift, (b) corresponding phase error.

These studies showed that similar to reflector antennas, the dominant effect of axial defocusing is the generation of quadratic phase error across the aperture [70]. The quadratic phase error (order 2) does not scan the beam but causes loss and a change in the side-lobe levels and the depth of the nulls between them. To further observe the effect of axial feed displacement on the radiation performance of the antenna, the gain patterns of reflectarray antennas with various values of F/D are given in Fig. 6-7.

These numerical studies showed that although axial feed displacement cannot be used to scan the beam, increasing the F/D ratio for the design will improve the performance of the design. In particular, from a fabrication and measurement viewpoint the alignment sensitivity will be reduced if a larger F/D ratio is used for the design.

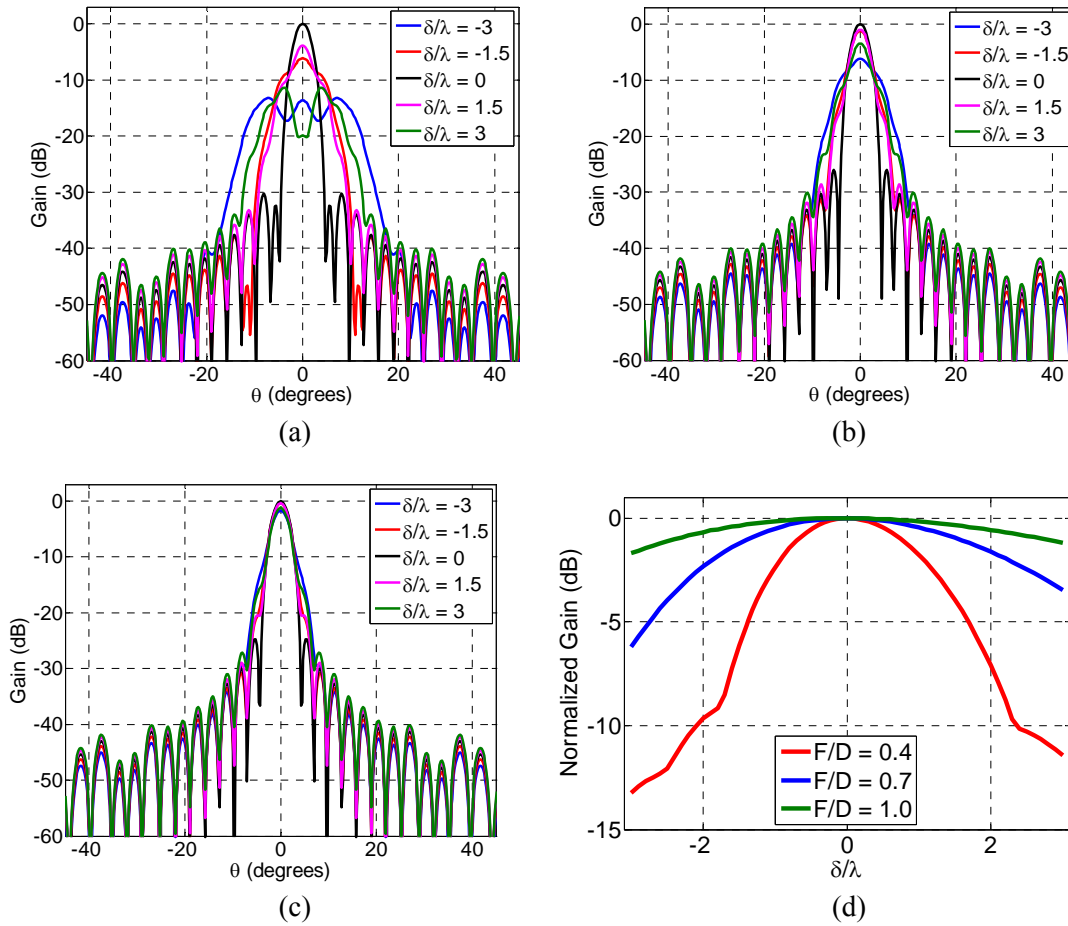


Fig. 6-7 Effect of axial displacement of the feed on the radiation performance of reflectarray antennas: (a) $F/D = 0.4$ ($q = 1.447$), (b) $F/D = 0.7$ ($q = 4.586$), (c) $F/D = 1.0$ ($q = 9.318$), (d) normalized gain versus axial displacement.

Now let's study the effect of lateral feed displacements. With reference to reflector antennas, the parameter of interest is the gain loss versus beamwidths scanned (bmws). An important parameter defined in this study is the beam deviation factor. The beam deviation factor (BDF) is the ratio between the beam direction (θ_B) and the feed angle (θ_F) in Fig. 6-1. For reflector antennas BDF is typically less than 1. Using this definition of BDF and calculating the half-power beamwidth of the antenna, the beamwidths scanned can be calculated using

$$\text{bmws} = \frac{\theta_F \cdot \text{BDF}}{\text{HPBW}} \quad (6-2)$$

The procedure to calculate the radiation pattern in terms of bmws then requires one to: (1) obtain the BDF for various feed angles (θ_F), and (2) use the values of BDF and HPBW for the design and setup a simulation to scan the beam to the required directions. Using this procedure, the effect of lateral feed displacement on the radiation performance of the antenna with various values of F/D is given in Fig. 6-8.

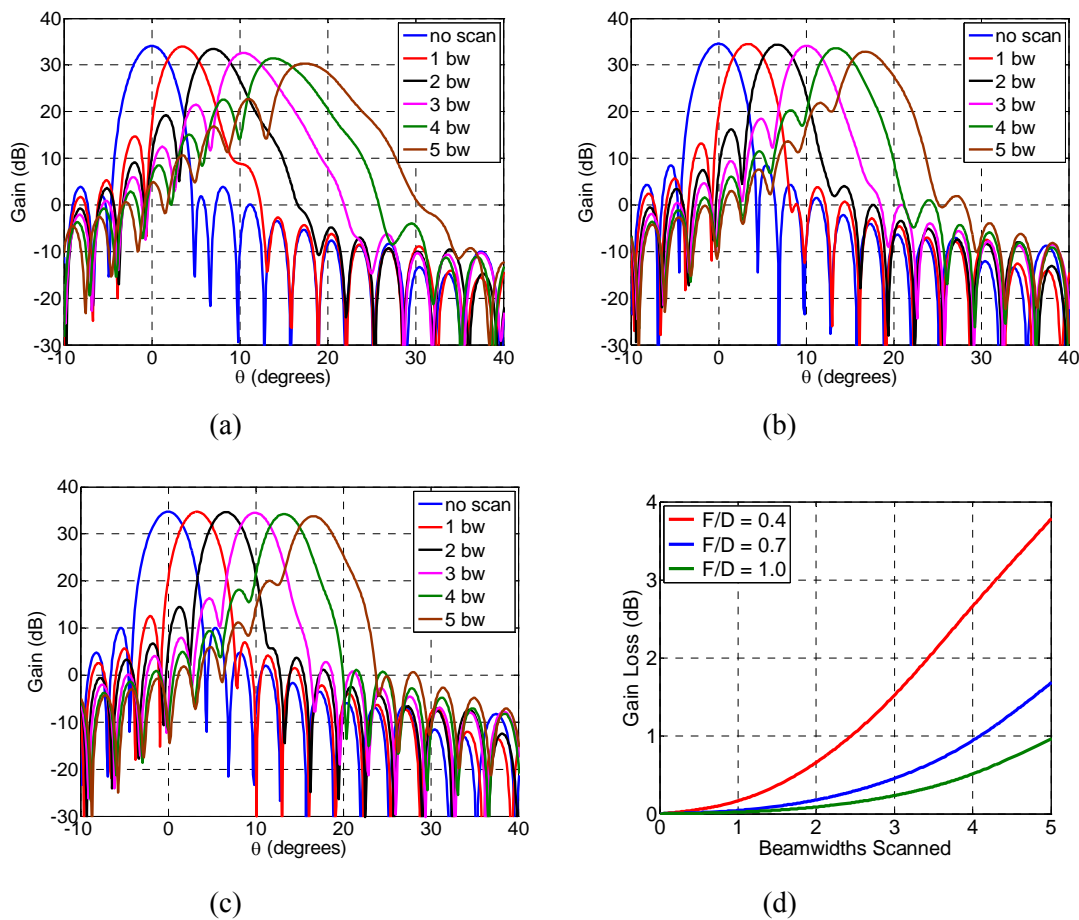


Fig. 6-8 Effect of lateral displacement of the feed on the radiation performance of reflectarray antennas: (a) F/D = 0.4 ($q = 1.447$), (b) F/D = 0.7 ($q = 4.586$), (c) F/D = 1.0 ($q = 9.318$), (d) normalized gain loss versus bmws.

The numerical studies presented here showed that lateral feed displacement can be effectively

utilized to scan the beam of a reflectarray antenna. In addition, increasing the F/D ratio for the system significantly improves the scan performance. While in the numerical studies presented here the value of q was adjusted to realize a certain edge taper for the design, in practice for an available horn antenna one has to determine the maximum F/D possible based on other design criteria such as aperture efficiency and edge taper.

6.3.2 Feed Displacement along a Circular Arc

In the previous section, it was shown that moving the feed antenna along the lateral direction can be used to scan the beam of the reflectarray antenna. In practice, however, different paths can be used for the feed movement. Since in all designs, the feed is always pointing to the geometrical center of the array, a practical path would be a circular arc as shown in Fig. 6-9. A notable advantage of the later design is that since F/D is held constant, the change in edge taper (ET) as a function of feed angle can be improved. For the 20λ aperture reflectarray (F/D = 0.7) studied in the previous section with a feed q power of 6.5, the edge taper is given in Fig. 6-10. It can be seen that for the lateral displacement path, as the feed angle increases, the change in ET shows a significant increase where the maximum ET increases to about -6 dB in the extreme case.

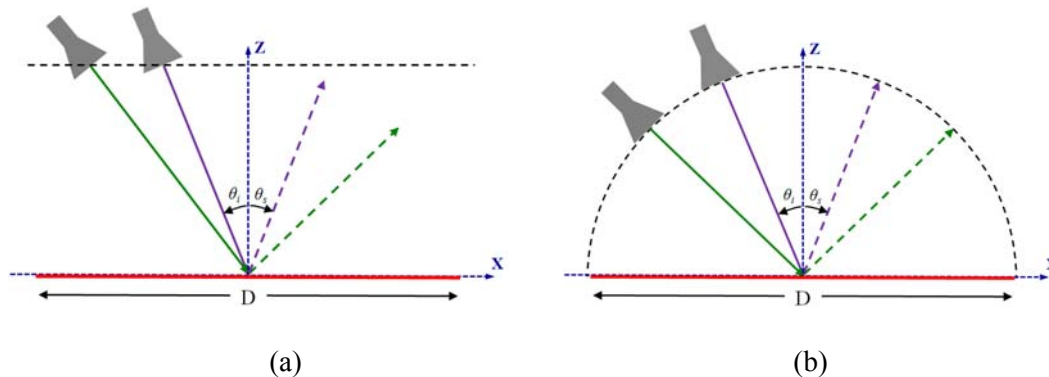


Fig. 6-9 Different paths for feed displacement: (a) lateral movement (H/D is fixed), (b) circular arc movement (F/D is fixed).

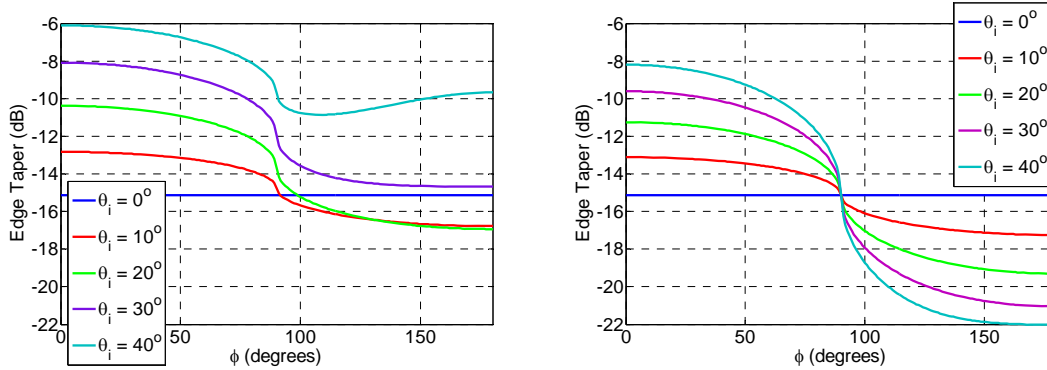


Fig. 6-10 Edge taper for various feed angles: (a) lateral movement (H/D is fixed), (b) circular arc movement (F/D is fixed).

The spillover efficiency is also significantly affected by the choice of feed path. The spillover efficiency for both designs for various feed angles is given in Table 6-1. Based on these parametric studies, the feed movement along a circular arc shows a better performance and this approach is used for the beam-scanning studies in the following sections.

Table 6-1 Spillover efficiency for different feed displacement paths.

θ_F	0°	10°	20°	30°	40°
Lateral movement	96.14%	95.39%	92.89%	87.95%	79.52%
Circular arc movement	96.14%	95.71%	94.38%	91.99%	88.33%

6.4 Bifocal Reflectarray Antennas

6.4.1 Principles of a Bifocal System Design

As discussed in the previous section, the main beam of a reflector antenna can be scanned by a lateral movement of the feed, however beam-scanning by means of a lateral displacement of the

feed is limited to a few beam widths [65]. In order to improve the scan performance of the system, we propose a new design for the aperture phase distribution of the reflectarray based on the concept of bifocal systems.

It is well known that a bifocal dielectric lens [71] has a wider scan capability than a dielectric lens with a single focus. It was also shown that a bifocal dual reflector antenna has a better scan capability than a classical Cassegrain reflector. A bifocal folded dual-reflectarray antenna using a seven element feed array was presented in [72], which showed a scan range of about 27 degrees ($\pm 13.5^\circ$). The scan range was further improved to 49 degrees ($\pm 24.5^\circ$) by designing a system with restricted apertures for each beam. While the beam-scanning performance achieved in this design is a significant improvement over the conventional parabolic type designs, the main disadvantage is the design complexity and fabrication difficulty of dual-reflector systems.

The aim of our work here is to study the feasibility of designing a bifocal single-reflector system. To formulate the problem let's consider the system parameters in Fig. 6-11.

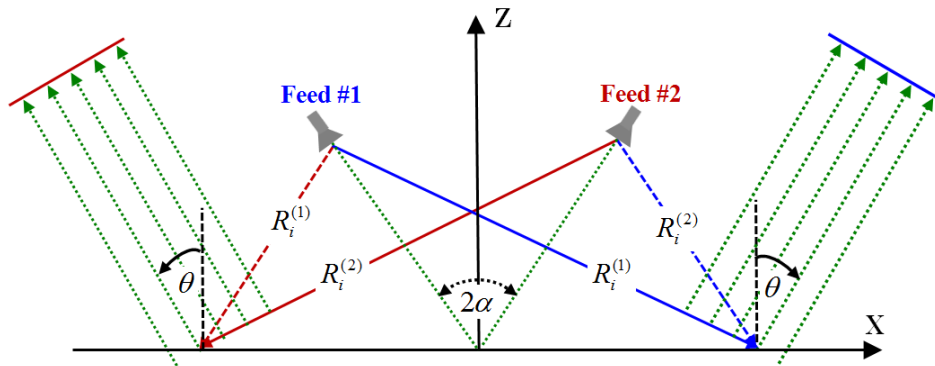


Fig. 6-11 Coordinate system for the bifocal reflectarray antenna.

The aperture phase distribution on the reflectarray antenna, which lies on the xy -plane, is given by

$$\phi_i = k_o (R_i^{(f)} - \sin \theta (x_i \cos \varphi + y_i \sin \varphi)). \quad (6-3)$$

In this equation, θ and φ represent the direction of the scanned beam. In comparison with (2-2), the main difference here is the spatial delay term, which has to be compensated for two different feed positions. To simplify the problem, let's consider a symmetric system here, i.e., when the feed is at position 1, the scanned beam is in the direction of $(\theta, \varphi = 0^\circ)$. Similarly when the feed is at position 2, the scanned beam will be in the direction of $(\theta, \varphi = 180^\circ)$. For this system, the phase requirements can then be written as

$$\begin{aligned}\phi_i^{(1)} &= k_o (R_i^{(1)} - x_i \sin \theta), \\ \phi_i^{(2)} &= k_o (R_i^{(2)} + x_i \sin \theta).\end{aligned}\tag{6-4}$$

To satisfy this condition for the design

$$\phi_i^{(1)} = \phi_i^{(2)},\tag{6-5}$$

which essentially requires that the phase distribution on the aperture be equal to the average phase delay associated with the two feed position. It is implicit that since the far-field beam direction θ is cancelled out in (6-4), the direction of the main beam of the reflectarray will now depend on the feed tilt angle, $\alpha/2$. Similar to the parabolic designs studied in the previous section, a beam deviation factor will be observed in these designs, i.e., $|\theta| < \alpha/2$. It is worthwhile to point out here that the phase requirement in (6-3) can be realized by using different polarizations for each feed point; however, this would not be a suitable approach for a beam-scanning system.

6.4.2 Scanning Properties of Bifocal Reflectarrays

To study the performance of these bifocal reflectarray systems, three Ka-band systems with 30° , 60° , 90° separation between the far-field beams were designed. For the designs here, the power q of the feed horn $\cos^q \theta$ radiation pattern model is 6.5, therefore in addition to aperture efficiency considerations an important design consideration was to minimize edge diffraction. In

all designs the feed angle (α) was set to scan the beam correctly in the required direction while achieving the maximum F/D and maintaining a maximum ET of -8 dB. The system parameters for the three designs are summarized in Table 6-2.

Table 6-2 System Parameters for Bifocal Reflectarrays.

Design	θ	α	F/D
30° scan	$\pm 15^\circ$	16.4°	0.86
60° scan	$\pm 30^\circ$	33.3°	0.724
90° scan	$\pm 45^\circ$	51.3°	0.56

The aperture phase distributions for all designs are shown in Fig. 6-12. It can be seen that as the angular separation (2α) increases the phase distribution on the aperture changes from circular concentric rings into ellipsoidal shapes.

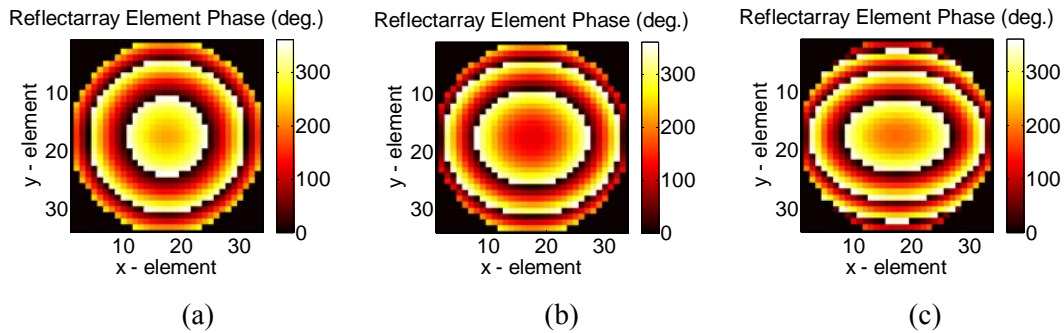


Fig. 6-12 Phase distribution on the aperture of bifocal reflectarray antennas: (a) 30° scan ($\pm 15^\circ$), (b) 60° scan ($\pm 30^\circ$), and (c) 90° scan ($\pm 45^\circ$).

The radiation pattern of these bifocal designs when the beam is directed to the maximum scan angle is given in Fig. 6-13 (a). It can be seen that although the bifocal designs show an acceptable performance when the beams are not scanned far from broadside, as the scan angle increases the coma lobe increases significantly. The beam-scanning performance of the designs,

Figs. 6-9 (b) to (d), also shows that in addition to the poor performance at the maximum scan angle, a significant beam broadening effect is observed as the scanned beam moves towards the broadside direction. Thus, the conventional bifocal design may not be suitable if wide angle beam scanning is required. It is worthwhile to point out that the computed directivity for the three designs at the maximum scan angle, i.e. 15° , 30° , 45° , are 33.64 dB, 31.99 dB, and 28.34 dB, respectively. More discussion on the scan loss of these bifocal designs is given in section 6.6.1.

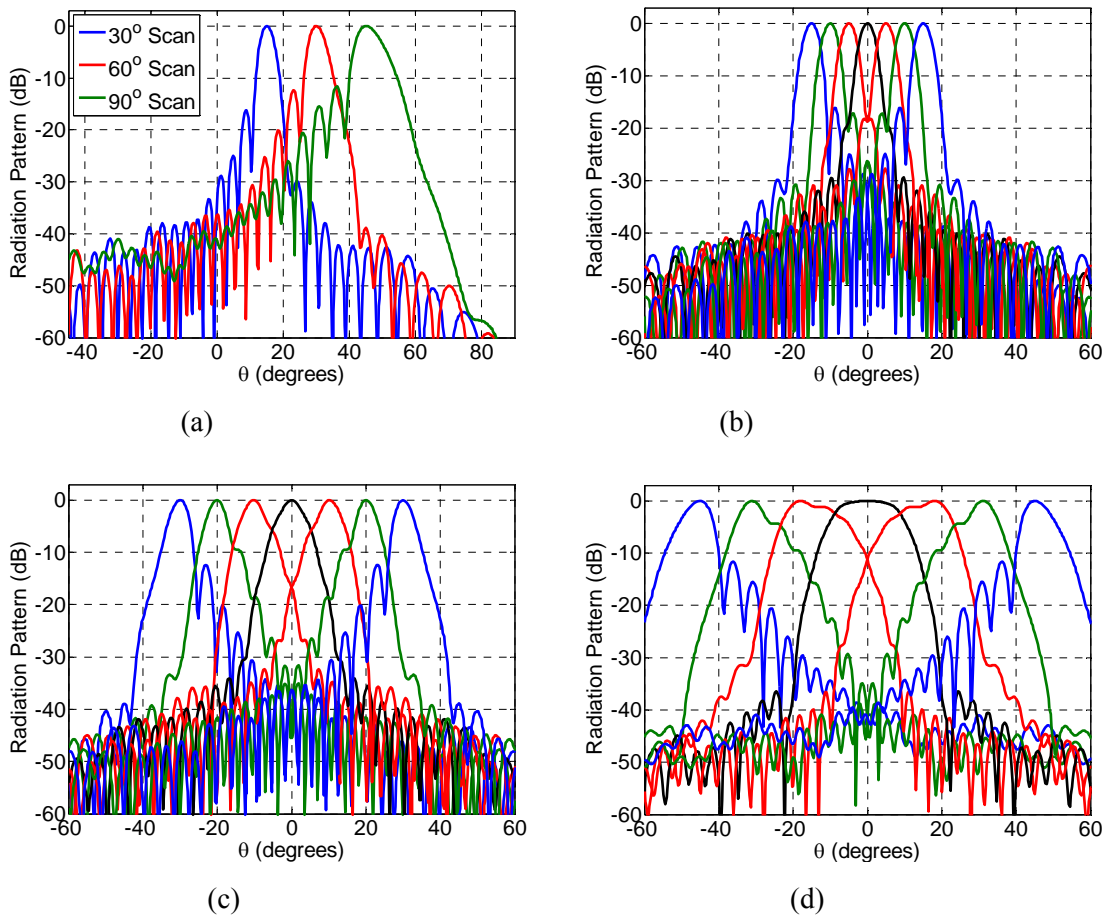


Fig. 6-13 Normalized radiation patterns of bifocal reflectarray antennas: (a) Comparison of the three designs at the maximum scan angle, (b) scanned beams for the 30° scan range design, (c) scanned beams for the 60° scan range design, (d) scanned beams for the 90° scan range design.

6.5 Optimization Approach for Beam-Scanning Reflectarray Design

The initial phase distribution obtained for the bifocal designs, equation (6-4), was based on averaging the spatial phase delay associated with the two feed positions. It is implicit that this simple approximation may not provide the optimum phase distribution. To further improve the designs, the reflectarray element phase is optimized using the particle swarm optimization method.

The basics of the PSO optimization techniques and how it can be implemented for multi-beam reflectarray antenna design were given in chapter 5. While the optimization principle is similar here, the mask definition and fitness function are quite different and require some attention. As discussed earlier, to implement PSO, the first step is to define the far-field radiation pattern mask for the problem. The primary aim of the optimization here is to reduce the side lobe level (SLL) without reducing the antenna gain. Therefore different masks and fitness functions were studied to determine a suitable setup for the optimization.

The pattern masks used for the multi-beam optimizations were designed to maintain a constant side-lobe level in the entire (u, v) space. While in general this type of mask simplifies the optimization problem, the main disadvantage is a significant increase in the antenna directivity. Shaped masks, on the other hand, designed such that the side-lobe envelope decreases outside the main beam area, can improve the antenna directivity, but they increase the complexity of the optimization problem. In addition to the shape of the mask, an additional improvement can be achieved by modifying the fitness function in the optimization. Since the primary goal is to reduce the SLL, particularly the first side-lobe, a penalty term can also be added to the fitness function to account for this. The fitness function defined for this optimization is then

$$\begin{aligned}
Cost = & \sum_{\substack{(u,v) \in \text{mainbeam} \\ \text{and } |F(u,v)| < M_L(u,v)}} \sum (|F(u,v)| - M_L(u,v))^2 + \\
& \sum_{\substack{(u,v) \notin \text{mainbeam} \\ \text{and } |F(u,v)| > M_U(u,v)}} \sum (|F(u,v)| - M_U(u,v))^2 + \\
& P \times \sum_{\substack{(u,v) \in \text{first side-lobe area} \\ \text{and } |F(u,v)| < M_L(u,v)}} \sum (|F(u,v)| - M_L(u,v))^2.
\end{aligned} \tag{6-6}$$

The term P in the cost function is the penalty term added to account for the performance of the first side-lobe.

To demonstrate the feasibility of this optimization approach, the bifocal reflectarray antenna designed for 60° scan range in the previous section is studied here. For the optimization, the swarm population was set to 100 particles and 100,000 iterations were performed for each design. For the PSO parameters, the inertial weight was varied linearly from 0.9 to 0.4 over the course of the run and the self- and group-knowledge constants, c_1 and c_2 , were both set equal to 2 throughout the optimization.

The mask in the first optimized design was set to have a constant SLL of -25 dB in the entire (u, v) space. For the other two designs, the masks linearly decrease outside the main beam area from -25dB to -45dB. While the masks in these two designs are similar, the fitness function in the third design was set to increase the penalty for the first side lobe using a value of P equal to 6. The performances of these designs are summarized in Table 6-3.

Table 6-3 Performance of optimized bifocal designs.

Design	SLL (dB)	Directivity (dB)
Bifocal	-12.35	31.989
PSO (constant SLL)	-20.7	30.522
PSO (shaped mask)	-18.3	31.499
PSO (shaped mask, P = 6)	-19.75	31.340

These results indicate that, as expected, the performance of the initial bifocal design can be significantly improved using this technique. The radiation patterns of the initial and optimized designs for a 30 degree scan are given in Fig. 6-14 (a). It can be seen that PSO has effectively improved the performance of the initial bifocal design. The coma lobe has been reduced by about 8 dB and the beam is almost symmetric along the scanned direction. The scan performance of this reflectarray system is given in Fig. 6-10 (b).

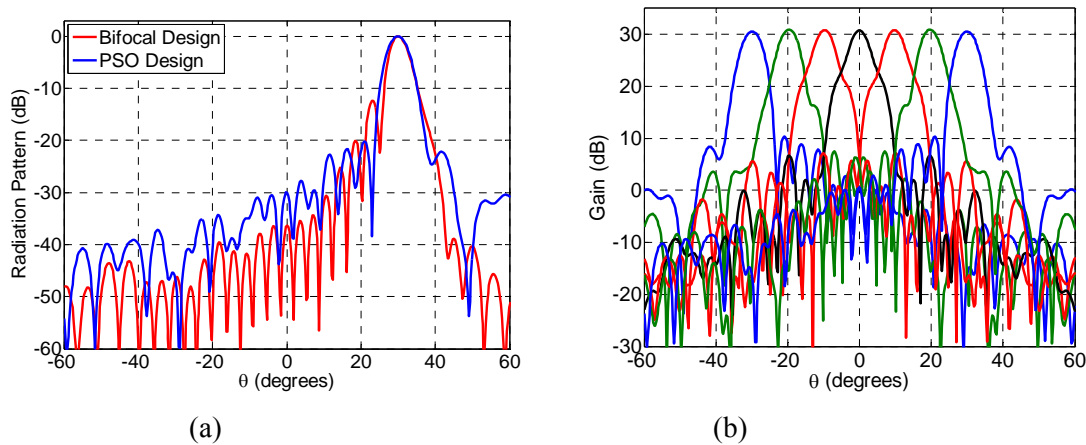


Fig. 6-14 (a) Normalized radiation patterns of the initial and optimized bifocal reflectarray antennas. (b) Scanned beams for the optimized design.

In these designs the phases of the reflectarray elements were optimized for beams at $\pm 30^\circ$. It is possible to further improve the scan performance of these systems by optimizing the antenna for other beams along the scan angles. Here we choose to optimize the beams at $\pm 10^\circ$ and $\pm 30^\circ$. Essentially such an optimization would necessitate a multi-objective fitness function, so the multi-objective PSO (MOPSO) technique is used here for the design. In general, multi-objective optimizations arise from the need for a strategy to address multiple design factors. For the optimization problem here, however, the design factors are somewhat similar, i.e., radiation patterns of the array for different scanned beams, which simplifies the problem. Therefore, the conventional weighted aggregation (CWA) method with equal weights for each objective is

adapted here. In addition, the same pattern mask used in the previous optimization is applied here for both beam directions. It should be noted that since the symmetry of the problem is utilized in the optimization problem here, the four optimized beams correspond to only two objective functions. Both objectives are evaluated using the fitness function given in (6-6). The first objective takes evaluates the performance of the 10° scanned beam, and the second evaluates the 30° scanned beam. The cost for the optimization is given in Fig. 6-15.

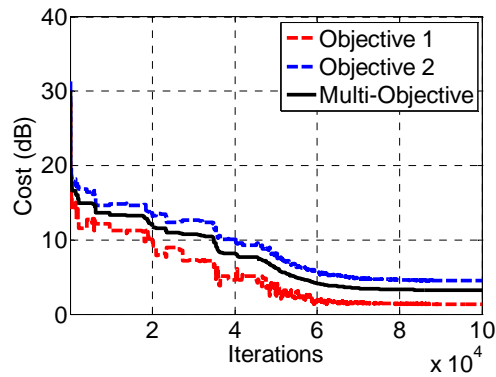


Fig. 6-15 Cost for the multi-objective optimization.

The optimized aperture phase distributions for both the PSO and MOPSO designs are given in Fig. 6-16.

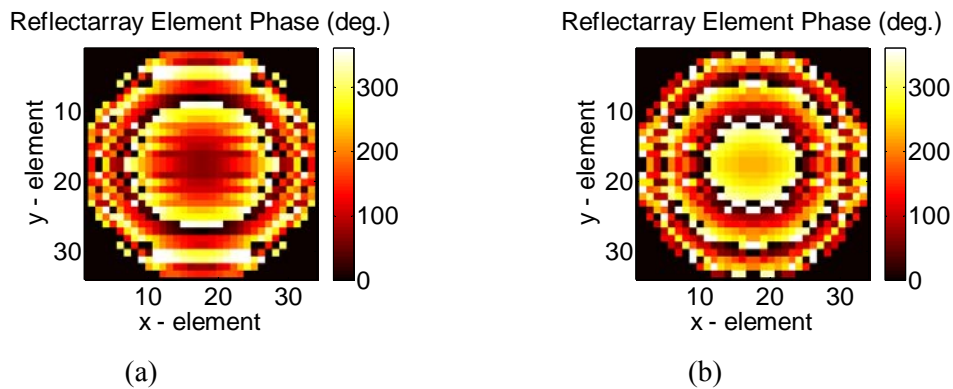


Fig. 6-16 Optimized phase distribution on the aperture of bifocal reflectarray antennas: (a) PSO design, (b) MOPSO design.

The radiation pattern of the PSO and MOPSO designs for a 10° and 30° scan are given in Fig. 6-17. It can be seen that for the 10° scanned beam, the MOPSO design shows a significant improvement in the radiation pattern. On the other hand for the 30° scanned beam, a SLL increase of about 2 dB is observed. None the less a SLL below -17.5 dB is observed across the entire scan range.

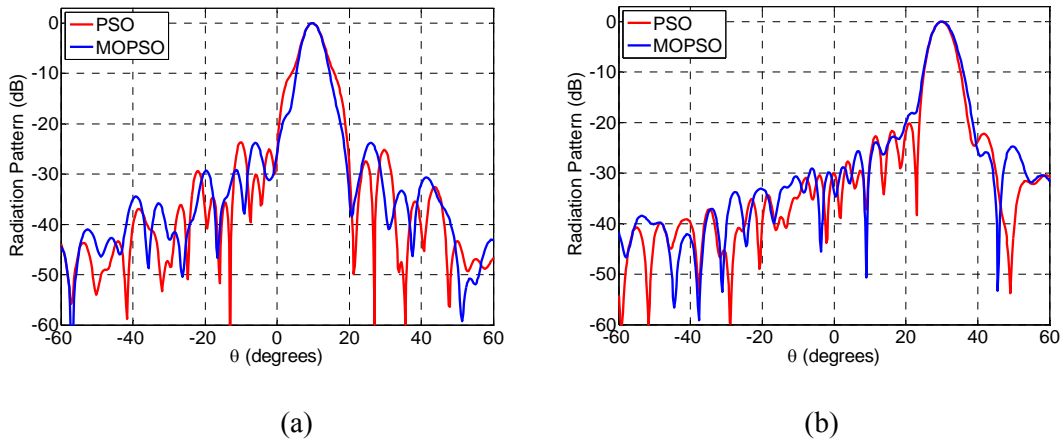


Fig. 6-17 (a) Normalized radiation patterns of the initial and optimized bifocal reflectarray antennas. (b) Scanned beams for the optimized design.

The scan performance of this optimized beam-scanning reflectarray antenna is given in Fig. 6-18.

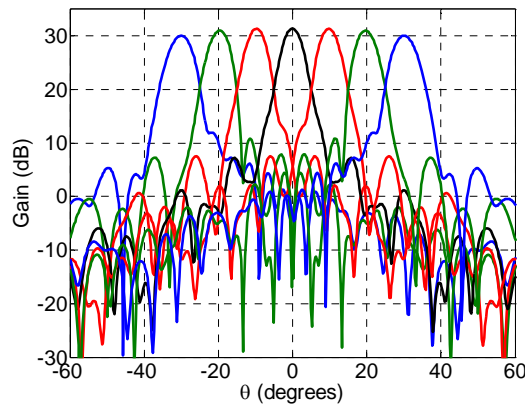


Fig. 6-18 Scanned beams for the optimized design.

6.6 Design and Measurement of a Ka-band Beam-Scanning Reflectarray Antenna

The design approaches presented in this chapter will be applied to a practical design of a Ka-band reflectarray antenna with 60° scan range. The horn antenna is an LHCP corrugated conical horn with a q value of 6.5 at the center frequency of 32 GHz. The aperture has a diameter of 17λ , corresponding to 848 elements with a unit-cell periodicity of $\lambda/2$. The feed horn is placed with an F/D ratio of 0.725 and the feed moves mechanically along a circular arc.

6.6.1 Element Selection and Radiation Performance Analysis

As discussed earlier, an important consideration for the feed displacement beam-scanning technique is the effect of oblique angles of excitation. When the feed moves along the arc, the excitation angle of the elements will also change. For the system designed here, the change in excitation angle θ_e is shown in Fig. 6-19, when the feed is at $\theta_i = 0$ and $\theta_i = \alpha$.

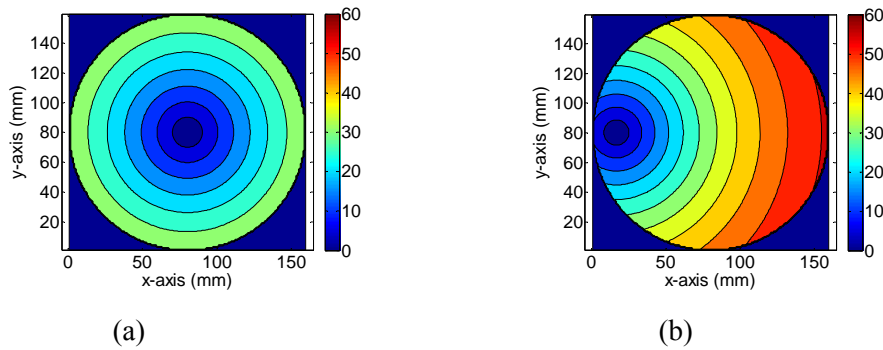


Fig. 6-19 Oblique excitation angles for different feed positions, (a) $\theta_i = 0$, (b) $\theta_i = \alpha$.

It can be seen that as the feed moves along the arc, the excitation angle of each element changes significantly. As a result of the element sensitivity to excitation angles, the reflection phase will change as a function of feed displacement. To minimize the effect of oblique angles of excitation, a simple yet effective approach is to reduce the substrate thickness. Based on the available materials, a 10 mil Rogers 5880 substrate was selected for the design. The reflection

phase versus patch size is given in Fig. 6-20 for various excitation angles.

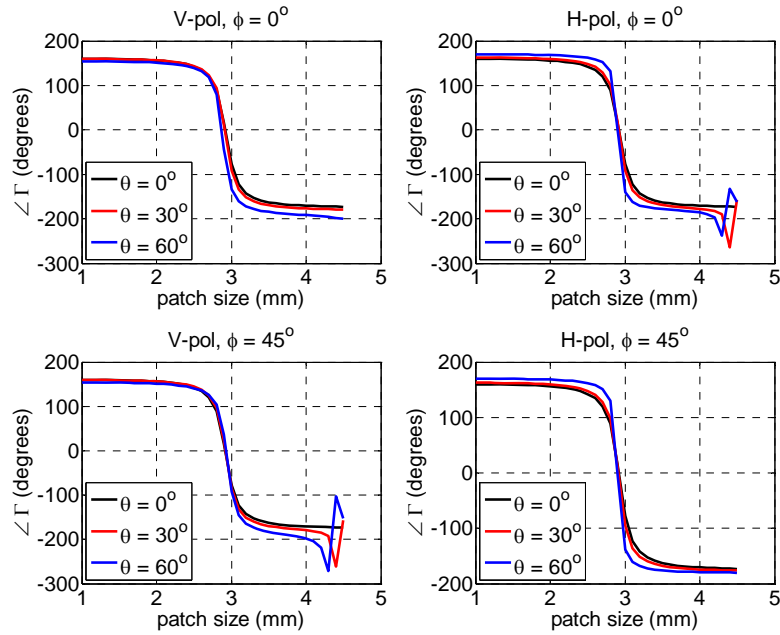


Fig. 6-20 Reflection phase versus patch size for different excitation angles.

To correctly account for the effect of oblique excitation angles, the following procedure was used. First, the patch sizes were determined using the optimized phase distributions under the assumption of normal incidence. In the next stage, the reflection coefficients of the elements were then recalculated with the exact angle of excitation under the local periodicity approximation.

Four different reflectarray designs are studied here: 1) parabolic with a broadside beam, 2) bifocal design, 3) PSO optimized bifocal design, and 4) MOPSO optimized bifocal design. The masks for these four designs are given in Fig. 6-21. The element reflection coefficients for all four designs when the feed is placed at $\theta_i = 0$ are given in Fig. 6-22. The maximum oblique excitation angle in all four designs is observed when the beam is scanned to 30 degrees, corresponding to when the feed antenna is placed at $\theta_i = \alpha$. These results are given in Fig. 6-23.

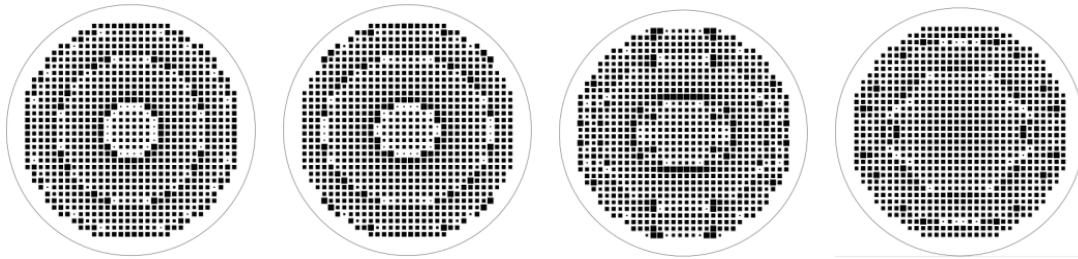


Fig. 6-21 Masks showing the dimensions of patch sizes for each design.

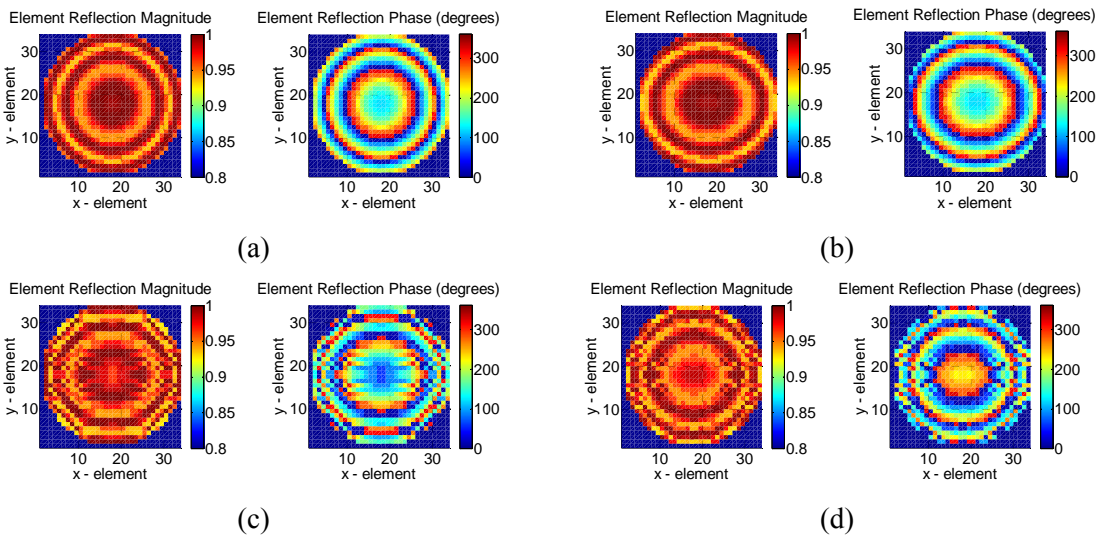


Fig. 6-22 Reflection coefficients of the reflectarray elements when the feed is placed at $\theta_i = 0$, (a) parabolic, (b) bifocal, (c) PSO, (d) MOPSO.

Comparison of the results given in Figs. 6-22 and 6-23 show that although the change in element reflection coefficients is not significant, for an accurate analysis of the beam-scanning performance of the reflectarrays, it is necessary to take the element characteristics into account.

Following the procedure given in [4], the loss budget for all designs is calculated and summarized in Table 6-4. It should be noted that the antenna directivity given in the second column also takes into account the illumination efficiency. From these results it can be seen that due to the increase in oblique excitation angle, the element loss and phase loss show a monotonic increase as the beam is scanned off broadside.

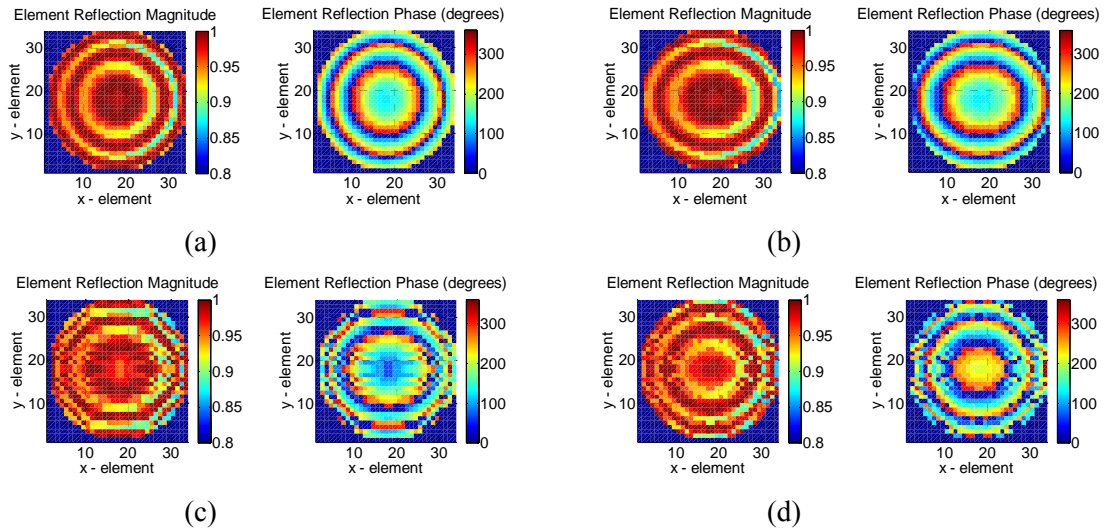


Fig. 6-23 Reflection coefficients of the reflectarray elements when the feed is placed at $\theta_i = \alpha$, (a) parabolic, (b) bifocal, (c) PSO, (d) MOPSO.

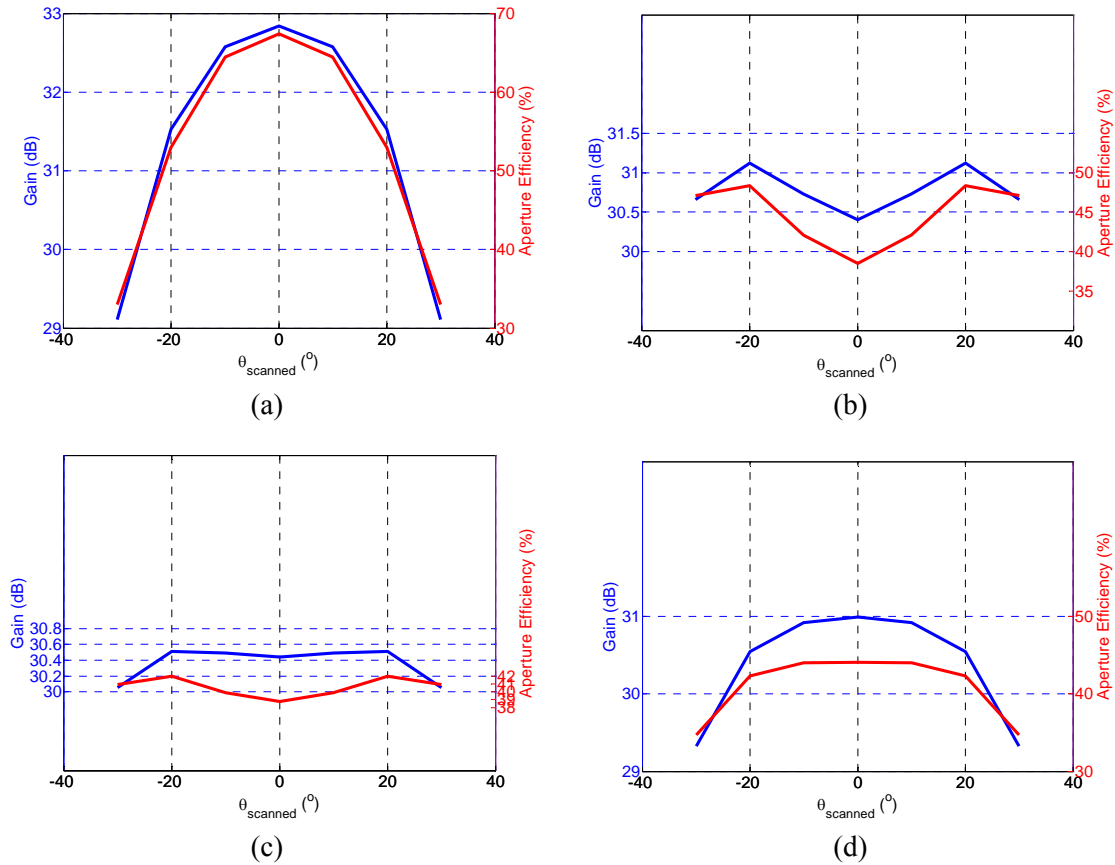


Fig. 6-24 Gain and aperture efficiency versus scan angle, (a) parabolic, (b) bifocal, (c) PSO, (d) MOPSO.

Table 6-4 Loss budget for the beam-scanning reflectarrays.

Parabolic

θ_s	Directivity (dB)	Element Loss (dB)	Phase Loss (dB)	Spillover Loss (dB)	Gain (dB)
30°	30.1345	0.28628	0.2001	0.5378	29.1103
20°	32.3284	0.24972	0.1588	0.3975	31.5224
10°	33.2547	0.23279	0.1244	0.3197	32.5778
0°	33.4779	0.22809	0.1148	0.2949	32.8401

Bifocal

θ_s	Directivity (dB)	Element Loss (dB)	Phase Loss (dB)	Spillover Loss (dB)	Gain (dB)
30°	31.9207	0.31877	0.3876	0.5554	30.6589
20°	31.9971	0.27172	0.1979	0.4046	31.1229
10°	31.3342	0.25088	0.0347	0.3213	30.7273
0°	30.9522	0.24474	0.0056	0.2949	30.4070

PSO

θ_s	Directivity (dB)	Element Loss (dB)	Phase Loss (dB)	Spillover Loss (dB)	Gain (dB)
30°	31.1166	0.3211	0.2075	0.5378	30.0492
20°	31.3127	0.27629	0.1275	0.3975	30.5114
10°	31.1423	0.2552	0.0736	0.3197	30.4938
0°	31.0439	0.24909	0.0619	0.2949	30.4380

MOPSO

θ_s	Directivity (dB)	Element Loss (dB)	Phase Loss (dB)	Spillover Loss (dB)	Gain (dB)
30°	30.6211	0.3429	0.4125	0.5378	29.3279
20°	31.4307	0.29697	0.1888	0.3975	30.5474
10°	31.6787	0.2757	0.1609	0.3197	30.9224
0°	31.7126	0.26948	0.1561	0.2949	30.9921

The gain and aperture efficiency versus scan angle is given in Fig. 6-24. It should be noted here that aperture efficiency is defined as simulated gain over the projected aperture, as discussed in [4].

6.6.2 Fabrication and Measurement of Prototypes

The four reflectarray antennas studied in the previous section have been fabricated and tested using our NSI 2000 planar near-field measurement system. The photographs of the fabricated arrays with 848 square patch elements are shown in Fig. 6-25.

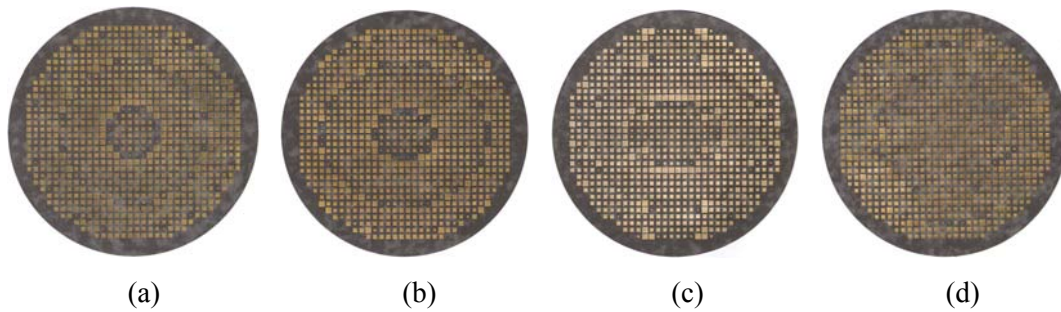


Fig. 6-25 Fabricated beam-scanning reflectarray antennas, (a) parabolic, (b) bifocal, (c) PSO, (d) MOPSO.

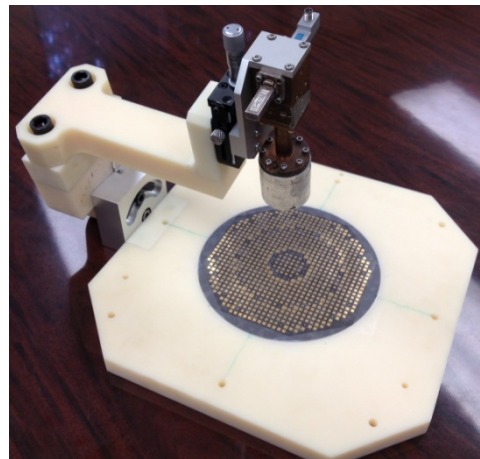
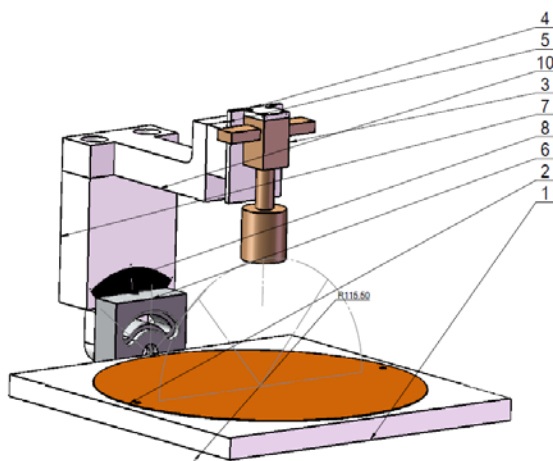


Fig. 6-26 Fabricated beam-scanning reflectarray antenna system.

The centered prime focus LHCP feed horn is mounted on a mechanical alignment system and positioned with an F/D ratio of 0.735. To accurately move the feed along the circular arc, a frame is fabricated that allows for a mechanical movement of the feed. The geometry of the frame and the fabricated beam-scanning reflectarray system are shown in Fig. 6-26. Due to the large size of the feed and alignment system, it is expected that the broadside beam would observe a significant aperture blockage. The beam-scanning performances of the antennas are given in Figs. 6-27 to 6-30 for four discrete beam directions across the 60 degree scan range. It can be seen that the optimized designs show a significant improvement in the scan performance.

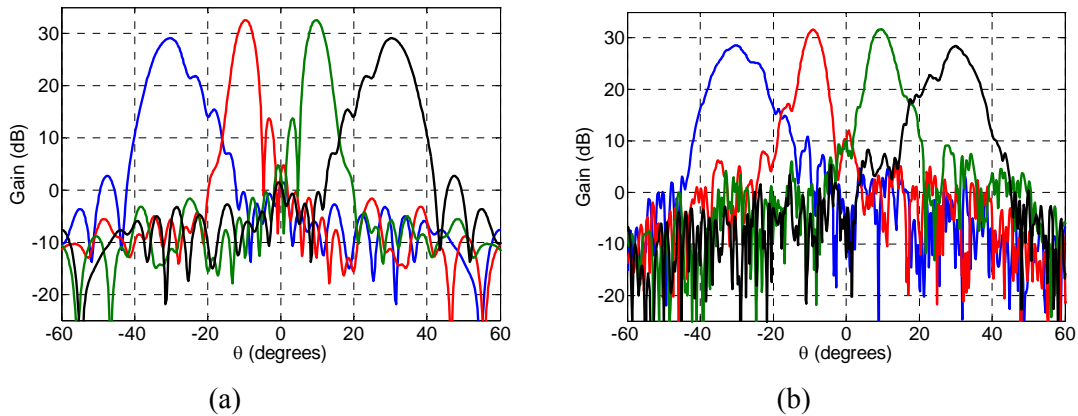


Fig. 6-27 Beam-scanning performance of the parabolic BSRA design: (a) simulated, (b) measured.

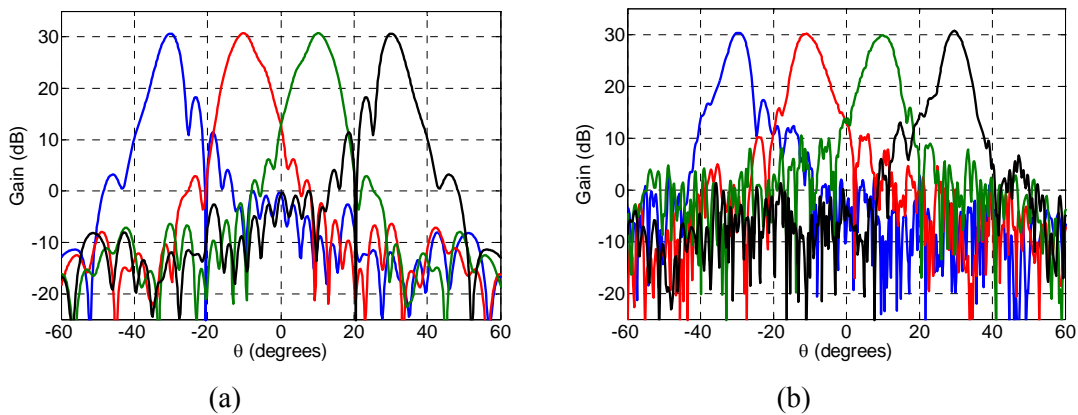


Fig. 6-28 Beam-scanning performance of the bifocal BSRA design: (a) simulated, (b) measured.

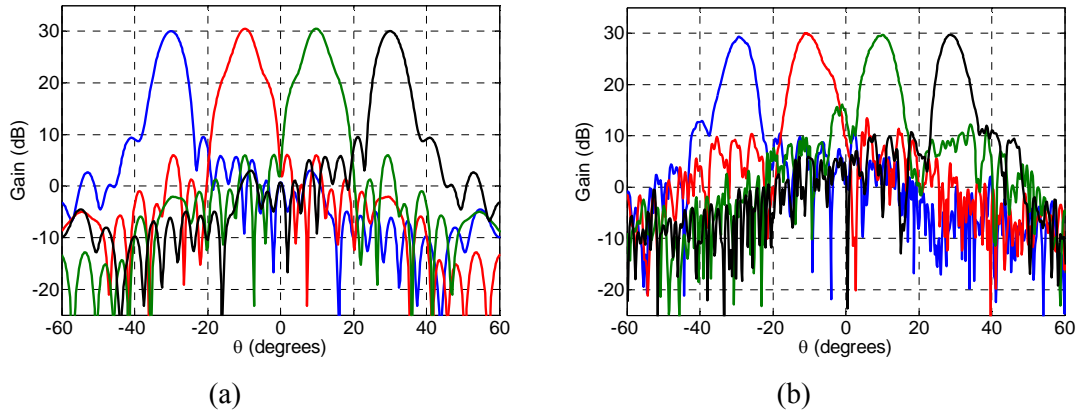


Fig. 6-29 Beam-scanning performance of the PSO BSRA design: (a) simulated, (b) measured.

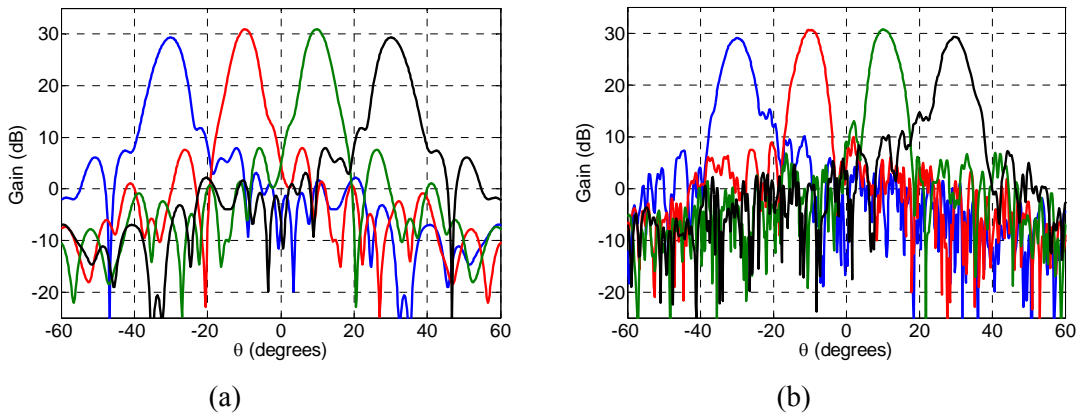


Fig. 6-30 Beam-scanning performance of the MOPSO BSRA design: (a) simulated, (b) measured.

To observe the improvement in the designs in a systematic way, let's first compare the measured performance of the parabolic, bifocal, and PSO designs when the beam is scanned to $+30^\circ$. These results are given in Fig. 6-31. The major problem for beam-scanning with the parabolic design is the high SLL. With the bifocal design, the measured SLL has been reduced by more than 7 dB. A further improvement is observed with the optimized design, where a measured SLL below -18 dB is obtained for the antenna. In the next stage, let's compare the beam-scanning performance of the optimized designs. The measured radiation patterns for the beams scanned to 10° and 30° are given in Fig. 6-32.

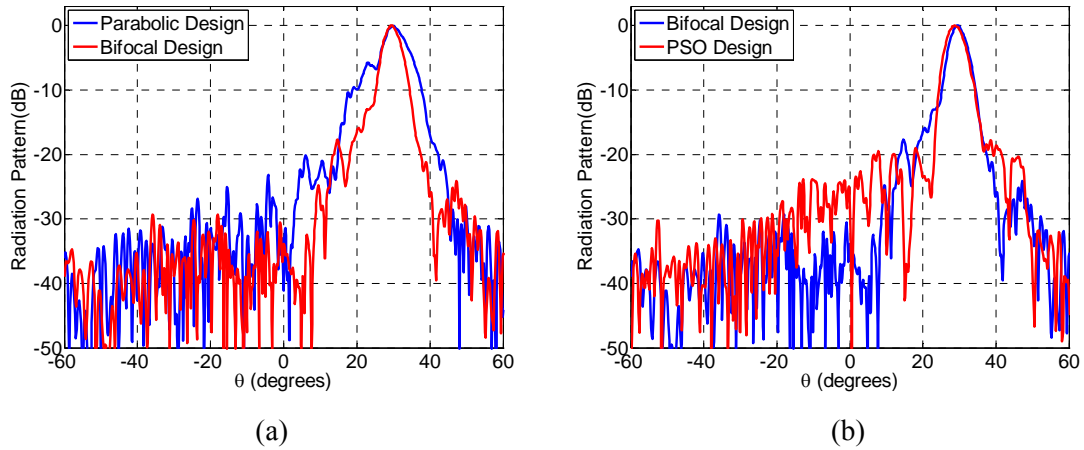


Fig. 6-31 Comparison of the measured radiation pattern for 30 degree scanned beams.

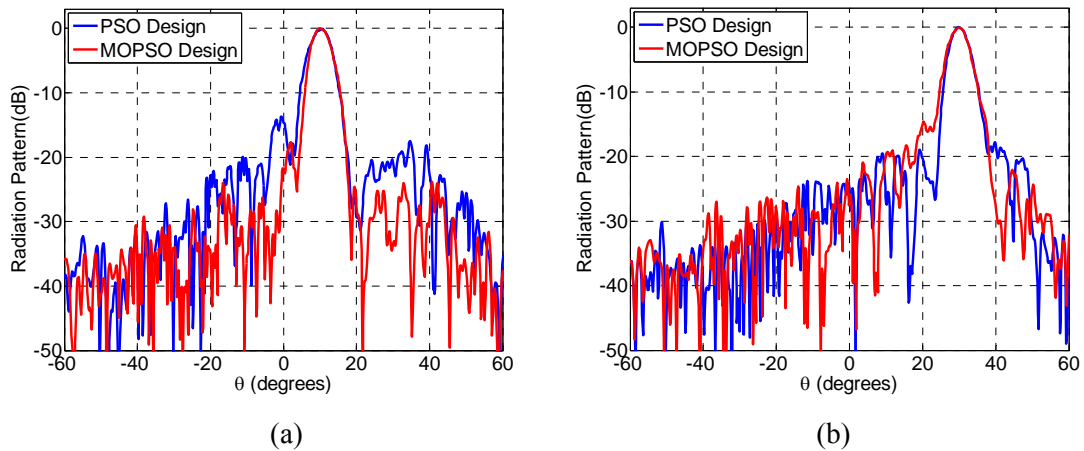


Fig. 6-32 Comparison of the measured beam-scanning performance of the optimized designs: (a) $+10^\circ$ scan, (b) $+30^\circ$ scan.

These results clearly show the improvement of the multi-objective optimized design, where the measured SLL is below -15 dB across the entire scan range.

The measured and simulated gain versus scan angle is shown in Fig. 6-33 for all four designs. It can be seen that a reasonably good agreement between the measured and simulated results are observed for the off broadside beams. The measured broadside beam however suffers from a very large aperture blockage [23], and as a result the peak gain is reduced by about 6 dB. In the

design here, the blockage volume from the horn feed and alignment system, is approximately $7\lambda \times 7\lambda \times 14\lambda$.

As discussed in the previous chapter, to accurately determine the bandwidth of a reflectarray antenna, it is necessary to first ensure that the main beam direction doesn't scan with frequency. For these beam-scanning antennas, the feed offset angle and main beam direction are not equal, due to the DBF, and as such it is expected that a slight beam squint may be observed in these designs. To study this, we measure the main beam direction as a function of frequency for all four designs. These results are given in Fig. 6-34 for the $+10^\circ$ and $+30^\circ$ beams. Due to the symmetry of the array, similar performance should be observed for the other two beams, i.e. -10° and -30° .

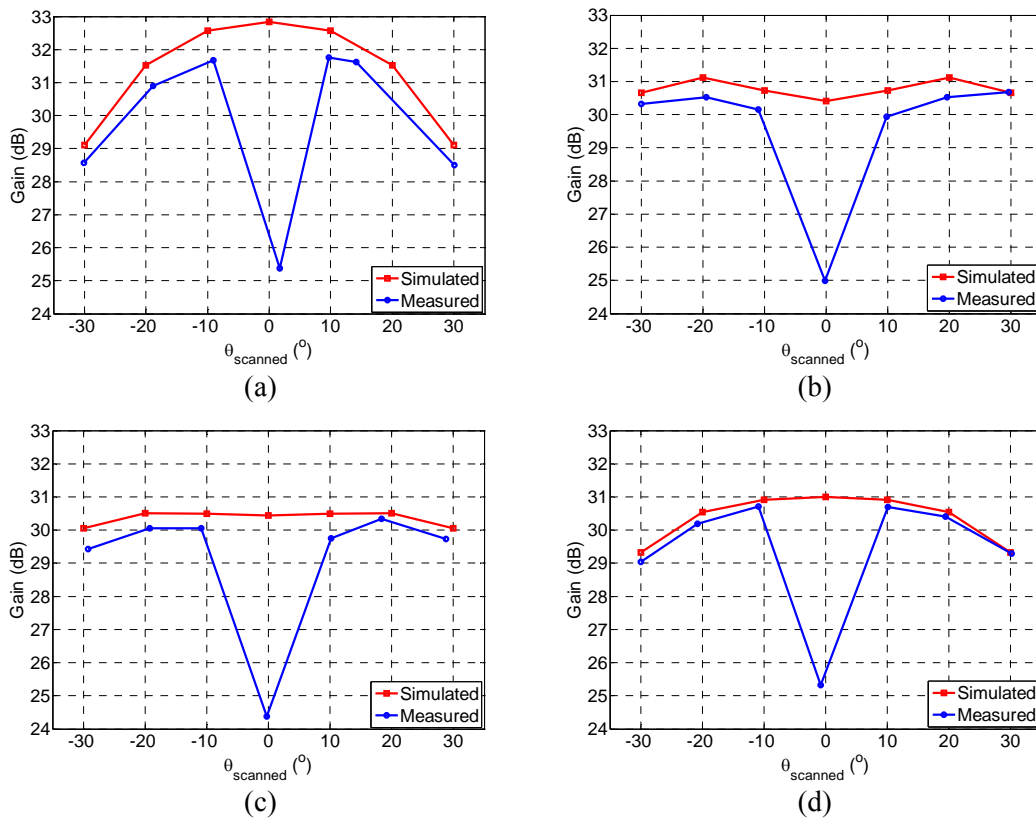


Fig. 6-33 Gain versus scan angle: (a) parabolic, (b) bifocal, (c) PSO, (d) MOPSO.

These results shows that while a slight variation in beam direction is observed in all four designs, this variation is quite small and beam squint is negligible in these systems. As such the bandwidth can be determined based on the gain performance of the antennas. It is important to point out here that in comparison; the bifocal design shows a larger beam squint which again is due to the fact that this design showed a larger BDF.

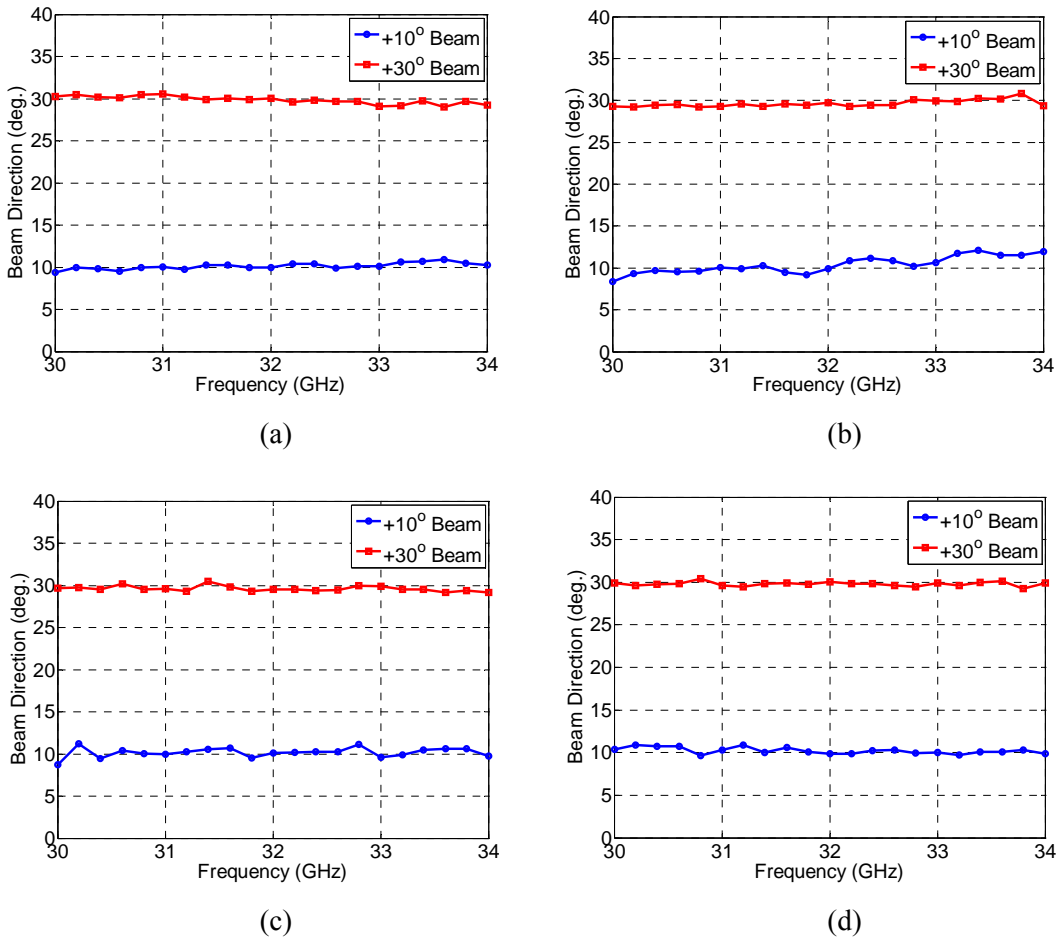


Fig. 6-34 Beam direction versus frequency: (a) parabolic, (b) bifocal, (c) PSO, (d) MOPSO.

The measured gain of the antennas as a function of frequency is given in Fig. 6-35 for all four designs. Similarly these results are only given for the +10° and +30° beams. Here the bandwidth of the reflectarray antennas are defined by the 1 dB gain bandwidth. The measured results show that all four beam-scanning designs show a gain bandwidth around 4 to 5%. This narrow

bandwidth is primarily due to the thin substrate used for the design (10 mil Rogers 5880). These results are summarized in Table 6-5.

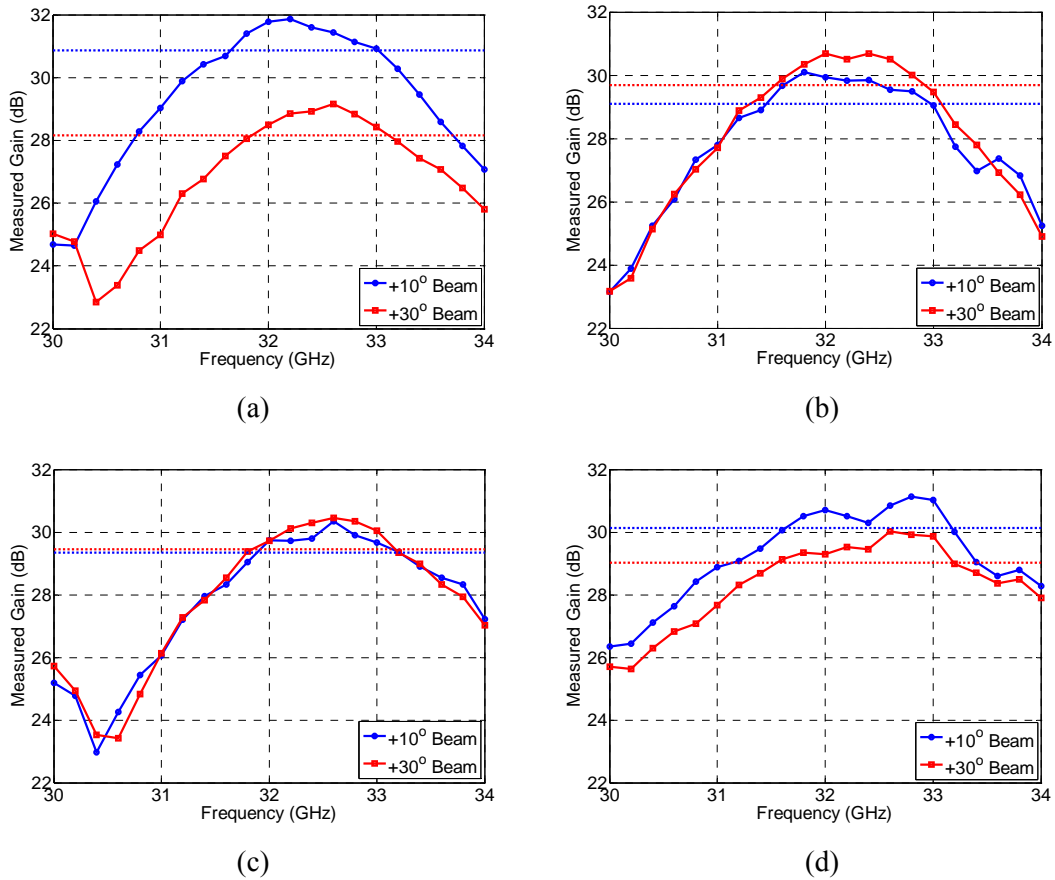


Fig. 6-35 Gain versus frequency: (a) parabolic, (b) bifocal, (c) PSO, (d) MOPSO.

Table 6-5 Measured bandwidth of the beam-scanning reflectarrays.

<i>Design</i>	+10° beam	+30° beam
Parabolic	31.65-33.01 GHz (4.21%)	31.85-33.12 GHz (3.91%)
Bifocal	31.45-32.97 GHz (4.72%)	31.53-32.92 GHz (4.31%)
PSO	31.89-33.20 GHz (4.03%)	31.84-33.17 GHz (4.09%)
MOPSO	31.63-33.17 GHz (4.75%)	31.55-33.19 GHz (5.07%)

CHAPTER VII

CONFORMAL REFLECTARRAY ANTENNAS

In this chapter we investigate the feasibility of designing reflectarray antennas on conformal surfaces. Some practical considerations for surface curvature effects are discussed, and a generalized analysis approach is presented to compute the radiation pattern of conformal reflectarray antennas. Reflectarray antennas on singly-curved conformal cylindrical platforms are studied and radiation characteristics and scanning performance of these designs are compared with their planar counterpart. It is shown that a conformal reflectarray antenna can be a suitable choice for a high-gain antenna where curved platforms are required.

7.1 Advantages of Conformal Array Antennas

As discussed in the previous chapters, planar reflectarray antennas combine the favorable features of both printed arrays and parabolic reflectors and create a low-profile, low-mass, and low-cost antenna. In general, a planar reflectarray antenna imitates the conventional parabolic reflectors, with the added advantage of having a flat surface instead of the curved reflecting surface. The surface of the reflectarray antenna consists of phase changing elements, which create the collimated beam and are usually distributed on a planar aperture. A notable advantage of individual control over the phase of the elements is that, the reflectarray surface does not have to be restricted to a planar geometry.

Several applications require the use of conformal antenna technology. While the need for a conformal antenna system generally depends on the specific application, the advantages can usually be attributed to either mechanical (aerodynamic, hydrodynamic) or electrical benefits [73]. In terms of the mechanical advantages a conformal antenna is designed according to a prescribed shape, which can be some part of an airplane, high-speed train, or other vehicle. The main purpose is to build an antenna that becomes integrated with the structure and causes less disturbance such as extra drag. The electrical advantages of conformal antennas are typically wide angle scanning capabilities. Conformal beam-scanning array antennas can achieve full azimuth and wide elevation coverage, which in most cases is not possible with planar designs.

7.2 Radiation Analysis of Conformal Reflectarray Antennas

7.2.1 Radiation Pattern Calculations

It was shown in chapter 2 that the radiation pattern of a planar reflectarray antenna with thousands of elements could be computed quite efficiently using the classical array theory formulation with proper element excitation. In addition it was shown that the calculated radiation pattern using this approach showed a good agreement with full-wave simulations, where in particular, the main beam direction, beam-width, and side-lobe level match closely with those obtained using full-wave simulations. Therefore the array theory approach is used here to study the radiation characteristics of conformal reflectarrays.

The formulation developed for planar reflectarray antennas can be generalized to analyze the performance of conformal reflectarrays. With the array theory formulation, as long as the elements on the conformal surface are correctly modeled with mutual coupling included, array summation can provide accurate results. Therefore, an important consideration in radiation analysis of conformal designs is the accurate modeling of element radiation characteristics. In

addition to the shape of the element pattern, one should realize that the peak of the element pattern is normal to the local surface, so the peaks will not all point in the same direction for a conformal array [74]. Furthermore, a reflectarray antenna is functioning in the reflection mode, which is different from conventional antenna arrays. Scattering properties of curved surfaces are more complicated than planar surfaces, and in general high order diffraction effects such as generation of creeping waves, and depolarization should be taken into account [75]. Nonetheless, if the conformal surface is not highly curved and edge diffraction is minimized, microwave optic approaches are suitable for the analysis.

The geometry of the conformal reflectarray system is given in Fig. 7-1. The radiation pattern of a conformal reflectarray with $M \times N$ elements can be calculated using the vectorized array summation formula, equation (2-9).

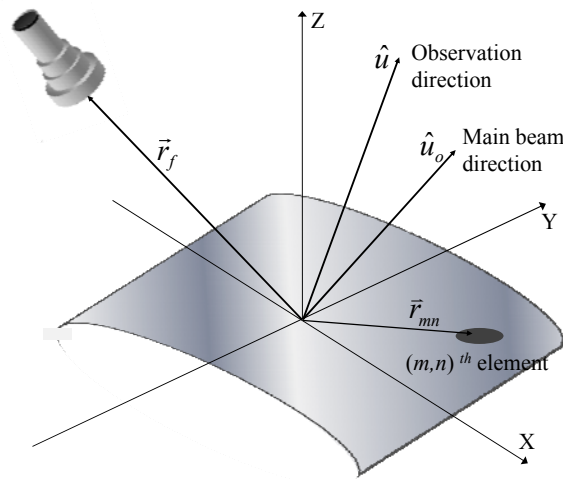


Fig. 7-1 Coordinate system for the conformal reflectarray antenna.

Similar to planar arrays, a cosine q_e model is usually used for the element pattern function A , which in general is not symmetric here due to the surface curvature. Some highly curved conformal arrays may have a $\cos^{1.5}$ behavior in the strong coupling plane and a \cos^1 behavior in the weak coupling plane [63]. As discussed earlier, in these studies the conformal reflectarray

surface is not highly curved, so each unit-cell can be approximated with a planar surface that is tangential to the conformal surface. The element pattern can then be approximated with a symmetric \cos^1 model with its peak normal to the unit-cell surface. Therefore, the important considerations for element pattern modeling are to:

- (1) Determine the exact angle of incidence for each element that controls the receive mode element pattern,
- (2) Determine the orientation of the local cell coordinates with respect to the global coordinates, which controls the transmit mode element pattern.

The transmit element pattern function can be written as

$$A_{mn}(\theta, \varphi) \approx \cos^{q_e} \theta_{local} \cdot e^{jk(\vec{r}_{mn} \cdot \hat{u})}. \quad (7-1)$$

In comparison with planar designs, this function takes into account the effect of surface curvature on the transmit element pattern by using local element coordinates for each radiating element.

As discussed in chapter 2, the element excitation function I , is determined by both the incident field and element property. The element receive pattern is essentially part of the element excitation function, which determines the reflected power from the element based on the angle of excitation and element pattern shape, i.e.,

$$\left| \Gamma_{mn} \right| = \cos^{q_e} \theta_e(m, n). \quad (7-2)$$

While the function here is similar to the planar case, the difference is that for conformal reflectarrays the element angle θ_e depends on both the element location and the local surface orientation.

It is worthwhile to point out here that for planar designs, the element patterns can be obtained using two approaches, namely a unit-cell model and a transmitting antenna model. As an

example, the radiation pattern of a patch element in a periodic media, and a single patch antenna excited with a pin feed are given in Fig. 7-2. In the two designs here the patch dimensions and substrate properties are identical. Note that in the periodic model, the coupling effects of the elements are included in the pattern, where as in the pin feed model, no coupling effects are present. In Fig. 7-2, these results are also compared with the conventional $\cos \theta$ element pattern model.

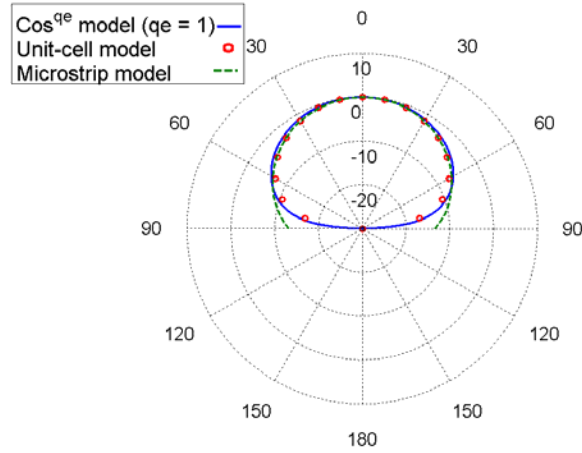


Fig. 7-2 Radiation pattern of a patch element.

It can be seen that a very close agreement is observed between all three patterns, and for these planar elements the $\cos \theta$ model can accurately represent the element pattern performance. While in general for conformal designs a periodic boundary model may not exist, the single patch model on any type of curved platform can be used to characterize the element pattern for conformal designs.

With these approximations, the radiation pattern of a conformal reflectarray antenna can be simplified to the scalar form

$$E(\theta, \varphi) = \sum_{m=1}^M \sum_{n=1}^N \text{Cos}^{q_e} \theta_{local} \text{Cos}^{q_e} \theta_e(m, n) e^{j\phi_{mn}} \frac{\text{Cos}^{q_f} \theta_f(m, n)}{|\vec{r}_{mn} - \vec{r}_f|} e^{-jk(|\vec{r}_{mn} - \vec{r}_f| - \vec{r}_{mn} \cdot \hat{u})}. \quad (7-3)$$

In this equation θ_f is the spherical angle in the feed coordinates and \vec{r}_f is the position vector of the feed. The required phase delay ϕ_{mn} of the mn^{th} element is adjusted to set the main beam in the \hat{u}_o direction.

7.2.2 Gain Calculations

Similar to what was presented in chapter 2 for planar reflectarrays, for an accurate gain calculation it is necessary to determine the overall aperture efficiency of the antenna, where the major influential terms are the spillover and taper efficiency. As discussed earlier, the effect of taper efficiency is taken into account when one calculates the radiation pattern using (7-3). The spillover efficiency, on the other hand, requires some attention. The spillover efficiency (η_s) is defined as the percentage of radiated power from the feed that is intercepted by the reflecting aperture. Mathematically this can be written as

$$\eta_s = \frac{\iint_{\sigma} \bar{P}(\vec{r}) \cdot d\vec{s}}{\iint_{\Sigma} \bar{P}(\vec{r}) \cdot d\vec{s}}, \quad (7-4)$$

where both integrals are fluxes of the Poynting vector $P(r)$ through certain surface areas. The denominator is the total power radiated by the feed; therefore, the integral is performed over the entire surface area of a sphere centered at the feed, denoted by Σ . The numerator is the power incident on the array aperture, so it is evaluated over a portion σ of the sphere, where σ and the array aperture share the same solid angle with respect to the feed. With this model, the denominator in (7-4) will have a simple closed form expression given as

$$\iint_{\Sigma} \bar{P}(\vec{r}) \cdot d\vec{s} = \frac{2\pi}{2q+1}, \quad (7-5)$$

where q is the power of the feed radiation pattern model as discussed in chapter 2. The numerator in (7-4) can be computed numerically for any conformal surface. This is generally the same approach one follows for spillover efficiency calculations of a planar reflectarray, however the difference here is that the integration has to be performed over a curved surface. The gain of the conformal reflectarray antenna is then computed using (2-36).

7.3 Radiation Characteristics of Singly-Curved Conformal Reflectarrays

Low profile printed antennas flush mounted on singly curved surfaces, such as cylinders, represent an important class of conformal arrays that have been used in many experimental radar and communication systems. Cylindrical array antennas are mainly utilized for either full azimuth scanning or sector arrays covering a specific subtended angle. The aim of this study is to investigate the radiation characteristics of reflectarrays on conformal sector cylindrical surfaces. The analysis of this singly-curved canonical problem can provide an insight into many radiation characteristics of conformal reflectarrays. The cross section of the conformal reflectarray system is shown in Fig. 7-3, where concave and convex surfaces are compared with their planar counterpart with the same surface area. In this figure R_c is the radius of the cylinder for the conformal systems, and D represents the physical aperture size.

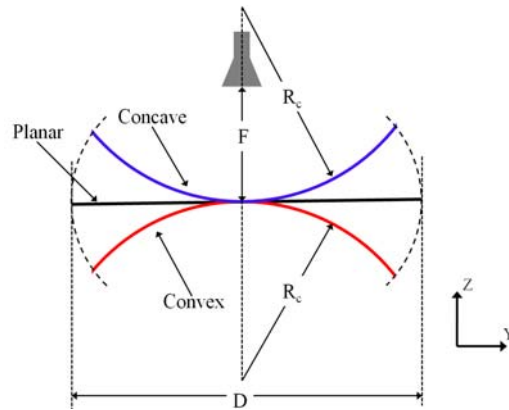


Fig. 7-3 Cross section of the conformal cylindrical reflectarray systems.

7.3.1 Radiation Patterns in the Principal Planes

The numerical approach developed here is applied to the radiation analysis of sector reflectarray antennas mounted on cylindrical surfaces. For a meaningful comparison of the surface curvature effect, the feed properties and the physical aperture size are kept constant, and the only parameter that is changed is the cylinder radius. The reflectarray antennas have a $20\lambda \times 20\lambda$ aperture and are designed to generate a beam in the broadside direction. Ideal phasing elements are used in each design and the element pattern is modeled as a \cos^1 function with no azimuth dependence. It should be noted that the aperture phase distribution for each reflectarray is designed according to its corresponding platform shape. The feed is prime focus, positioned with an $F/D = 0.75$ and the power q of radiation pattern model is 6.5.

The radiation pattern of the reflectarray systems in the curvature plane (yz -plane) is shown in Fig. 7-4 for various cases. The radiation pattern in the xz -plane was similar to the planar case and is not shown here for brevity.

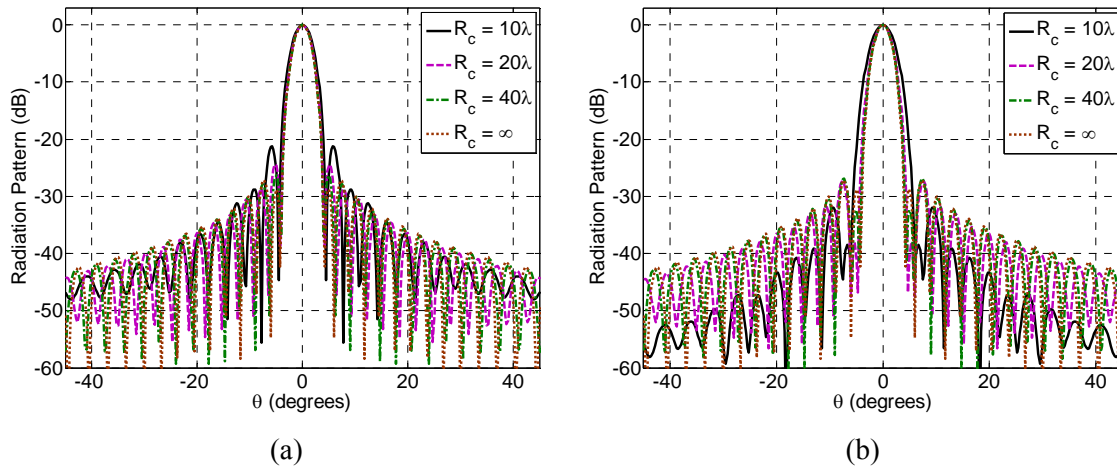


Fig. 7-4. Radiation patterns of cylindrical reflectarrays: (a) concave, (b) convex.

It can be seen that due to the effects of the conformal surface, the radiation patterns show a noticeable difference with planar designs ($R_c \rightarrow \infty$). In particular for the concave design, the side

lobes are higher than the planar case. On the other hand, the convex designs show a lower side-lobe level (SLL), but a much wider beamwidth. For both designs, however, as the cylinder radius increases, the radiation patterns of the conformal designs approach that of a planar case. While the minimum cylinder radius that mimics a planar aperture generally depends on the aperture size, for the cases studied here it is about $R_c = 40\lambda$.

7.3.2 Effects of Conformal Surface on Beamwidth and Side-Lobe Level

The conformal cylindrical systems studied in the previous section were defined based on the size of the cylinder radius (R_c). The aperture size (D) however also plays an important role. For a fixed cylinder radius, a larger aperture means a wider subtended angle ($\alpha = D/R_c$) and a higher level of surface curvature. To study this effect we consider three different aperture sizes and compare the beamwidth and SLL of these designs. The normalized half-power beamwidth (HPBW) in the curvature-plane as a function of cylinder radius is given in Fig. 7-5 for different aperture sizes.

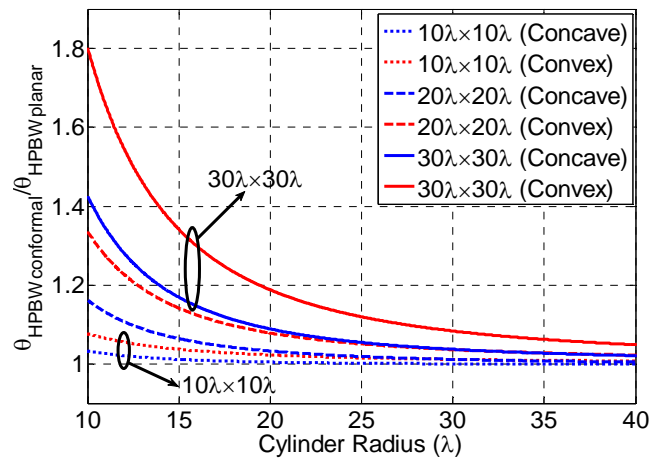


Fig. 7-5. Normalized HPBW in the curvature plane as a function of cylinder radius.

It can be seen that in comparison between the two conformal designs, a convex reflectarray shows a much wider beamwidth. In general however, both conformal designs show defocusing

effects, i.e., a wider beamwidth in comparison with a planar design. This is mainly attributed to the fact that the elements on the conformal surface radiate in the outward (convex) or inward (concave) radial directions of the cylinder, which defocuses the main beam. It should be noted that for a concave design, an optimum position exists for the feed that can achieve maximum gain, which is due to the focusing properties of the conformal surface.

The change in SLL as a function of cylinder radius is given in Fig. 7-6 for different aperture sizes. Comparisons of these results also show that in all cases, for a fixed cylinder radius, as the aperture size increases, the SLL increases for the concave design and decreases for the convex design. In other words, the effect of the conformal surface on the radiation performance becomes more noticeable as the aperture size increases.

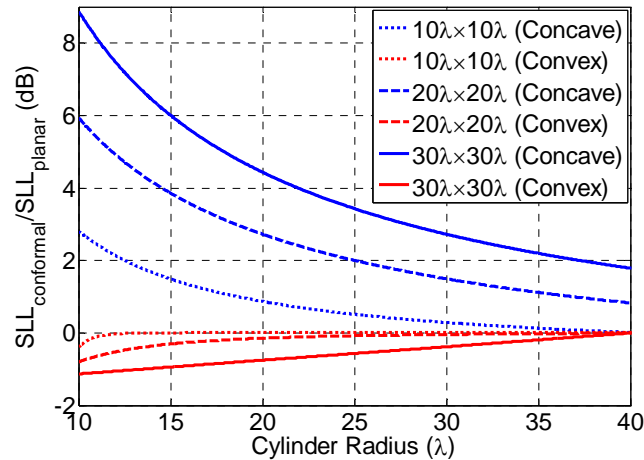


Fig. 7-6. Normalized SLL in the curvature plane as a function of cylinder radius.

The results in Figs. 7-5 and 7-6 indicate that the radiation performance of conformal cylindrical reflectarrays is a function of both cylinder radius and aperture size. However it will be quite advantageous if one can determine the overall performance of the system based on a single conformal parameter. The subtended angle α , takes into account the aperture size, D , which

controls the gain, in addition to the cylinder radius, R_c , which controls the curvature of the conformal surface. As such it can be a suitable measure to evaluate the performance of the system. Table 7-1 summarizes the change in radiation characteristics of some conformal designs with a fixed subtended angle of 1 radian.

Table 7-1 Change in Radiation Performance of Conformal Cylindrical Reflectarrays with $D/R_c = 1$.

Aperture size	Design	$10\lambda \times 10\lambda$	$20\lambda \times 20\lambda$	$30\lambda \times 30\lambda$
HPBW ratio	Concave	0.036	0.033	0.037
	Convex	0.077	0.080	0.083
SLL ratio (dB)	Concave	2.81	2.73	2.73
	Convex	-0.40	-0.25	-0.38

From these results it can be seen that the ratio of the change in HPBW and SLL is almost identical for all three cases. Similar results were observed for other values of subtended angle. In other words it is possible to correctly specify the radiation performance of a conformal reflectarray system based on the value of α . This is quite advantageous from a system design view point, since for any available curved platform the radiation characteristics of the conformal reflectarray can be determined with only one conformal parameter. As an example, for a 10% acceptable increase in HPBW in comparison with a planar design, α is equal to 1.62 and 1.13 radians for concave and convex designs, respectively, for any aperture size.

It is important to point out that the subtended angle (α) decreases as the cylinder radius increases. For the smallest cylinder radius, the aperture size increase corresponds to an increase in α from almost $\pi/3$ to π . Larger apertures will not be practical here since (1) the elements cannot be properly excited (shadow region of feed), and (2) the pattern of the elements at the sector edges point far away from the broadside direction.

7.3.3 Gain and Bandwidth of Conformal Reflectarray Antennas

The reflectarray antenna gain is directly proportional to its projected aperture. Thus for a fixed aperture size, the projected aperture and the corresponding antenna gain of conformal designs will be slightly smaller than for a planar design. For a $20\lambda \times 20\lambda$ aperture with a fixed value of $\alpha = 1$, this will result in a gain reduction of 0.1 and 0.6 dB for concave and convex designs, respectively. While it is possible to mitigate this slight difference in antenna gain by increasing the aperture size, for the bandwidth comparisons here we will compare the normalized antenna gain as a function of frequency.

The bandwidth of the reflectarray antenna is affected by the phase error associated with the spatial delay as well as the bandwidth of elements [7]. While the element bandwidth generally depends on the design methodology, for this comparative study we consider a frequency independent reflection phase for the elements, i.e., only the bandwidth limitation associated with spatial phase delay is taken into account. Fig. 7-7 shows the normalized gain bandwidth of a $20\lambda \times 20\lambda$ reflectarray antenna with planar and conformal apertures ($\alpha = 1$ radian).

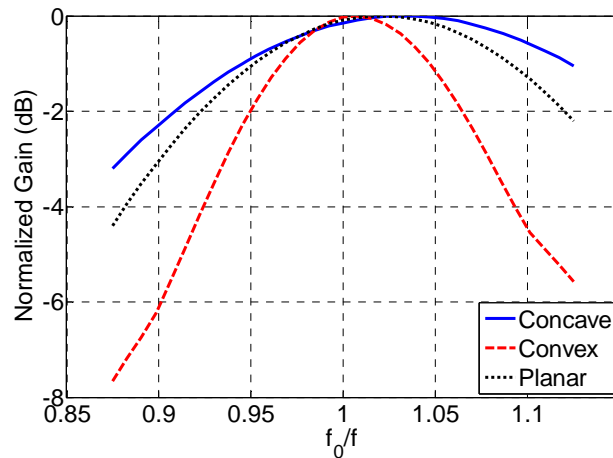


Fig. 7-7. Normalized gain versus frequency for the reflectarray antennas.

It can be seen that a concave design shows a notable improvement in gain bandwidth in

comparison with the planar case. On the other hand, as expected, a convex design shows a reduction in bandwidth.

As discussed earlier, for a concave reflectarray an optimum position exists for the feed so that the antenna achieves its maximum gain. A similar argument is attributed to the bandwidth performance of concave reflectarrays where the maximum bandwidth is attained at a certain radius. To observe the bandwidth performance of these designs as a function of cylinder radius, we study the gain bandwidth of the same $20\lambda \times 20\lambda$ reflectarray as a function of cylinder radius. These results are shown in Fig. 7-8.

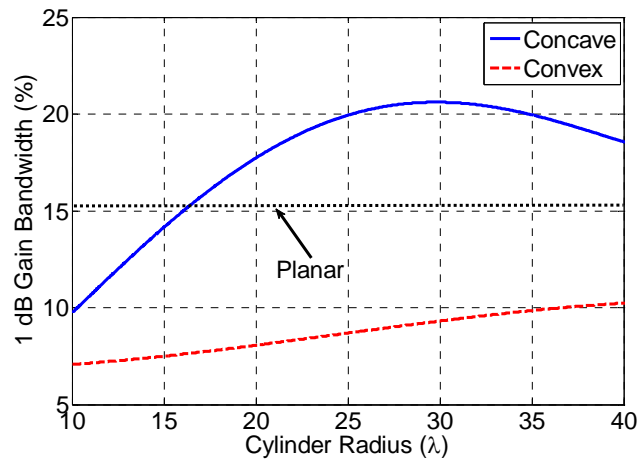


Fig. 7-8. Gain bandwidth of the reflectarray antennas as a function of cylinder radius.

It can be seen that for a convex design, the bandwidth of the reflectarray increases monotonically with R_c . For a concave design however, an optimum subtended angle exists where the antenna achieves the maximum bandwidth. For the design here this optimum subtended angle is 0.67 radians.

7.4 Beam-Scanning Properties of Conformal Reflectarrays

In addition to the mechanical advantages of conformal reflectarrays, a main advantage of

conformal antennas is the capability of achieving wide angle beam scanning. As discussed in chapter 6, a dynamic reflectarray antenna can achieve beam-scanning performance by feed adjustment, aperture phase tuning, or a combination of these techniques. While dynamic feed systems have some unique features, an important consideration in these systems is the sensitivity of the element reflection phase to the angle of excitation. For conformal reflectarrays, the element excitation angle is a function of both feed position and surface curvature. Thus, displacement of the feed phase center will significantly change the element reflection phase, which will degrade the overall performance of the system.

Aperture phase controlled reflectarrays, on the other hand, typically rely on phase shifter technology [64], and are quite suitable for conformal reflectarray systems. Various designs of phase controlled reflectarrays have been demonstrate over the years that can also be implemented for conformal designs. While a continuous phase control is possible with some designs such as varactor diodes, here we focus on the performance of conformal reflectarray antennas using ideal digital phase shifters. For reflectarray antennas with a large number of elements, low-bit quantization phase shifters such as 2 or 3 bits, can achieve good far-field beam scanning [3].

A reflectarray system with an aperture size of $20\lambda \times 20\lambda$ is used for the studies here, and the scanning performances of planar and conformal designs ($\alpha = 2$ radians) are compared. The feed is prime focus, positioned with an $F/D = 0.75$ and the power q of radiation pattern model is 6.5. Lossless 3-bit digital phase shifters covering the complete 2π range are used for the reflectarray elements. For beam-scanning antennas, arguably the most important consideration is the scan loss associated with the system [63]. The scan loss of these reflectarray systems is given in Fig. 7-9.

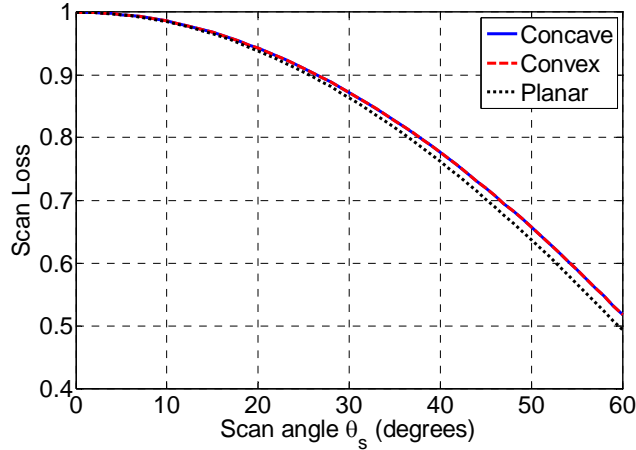


Fig. 7-9. Scan loss of the reflectarray antennas as a function of scan angle.

As expected, these results show that the scan loss of the system can be improved by using conformal platforms for the array; however, this improvement is quite small with sector designs. It should be noted that while systems with larger sectors can improve the scan performance, numerical results showed that this improvement is not significant due. The main reason is that depending on the direction of the scanned beam, only a portion of the total number of elements have an element pattern that is aligned with the direction of the scanned beam. As such, to achieve a good beam-scanning performance, only that portion should be turned on in the system, which is not possible with a single feed. In general, if wide angle scanning is required, a full cylinder or cone has to be used for the system. For the case of a full cylinder reflectarray antenna system, efficient illumination of the antenna would require the use of a circular ring feed array. The cylindrical reflectarray is virtually divided into multiple sectors, where each sector is illuminated by one feed antenna. This design is essentially a hybrid system, which would rely on both aperture phase tuning and feed array (displacement) techniques for beam scanning. The dynamic feed system then illuminates an active sector depending on the beam direction. The concept is essentially analogous to commutating feeds for beam scanning circular arrays which only turn on the elements of the active sector [74].

CHAPTER VIII

CONCLUSIONS

Microstrip reflectarray antennas show momentous promise as a high-gain antenna with low-profile and low-mass features. This new generation of high-gain antenna is a hybrid of two well developed antenna concepts, the reflector antenna and the microstrip antenna array. As such it can offer advantages over both designs; however it is also confronted with new challenges in modeling, design, and practical application. In general, the research on reflectarray antenna is focused on two different aspects, which can be categorized as element level and system level challenges.

8.1 Contributions of this Dissertation

The primary contributions of this dissertation are as follows. On the element level problems two different concepts are proposed and studied.

- Sub-wavelength elements with variable size in reflectarray antenna designs are studied to improve the bandwidth of the antenna while considering practical fabrication tolerances. A new definition of phase error is introduced to analyze the phase performance of reflectarray elements. It is shown that sub-wavelength elements are a suitable solution for broad-band reflectarray antennas. In addition the idea of combining two different broadband techniques for bandwidth improvement of reflectarray antennas is also investigated.

- The loss mechanisms of reflectarray antenna elements at infrared frequency are investigated for potential applications of reflectarrays as CSP systems. The conductor and dielectric loss effects on the reflection magnitude and phase are demonstrated through full wave simulations. It is shown that as a result of the resonance phenomenon, when the material loss increases and the equivalent resistor matches the wave impedance in space, total loss of power occurs. Reflectarray elements using only dielectric materials are proposed to reduce the antenna loss. The low loss optical reflectarrays have many potential applications, such as the highly efficient concentrating solar power systems.

On system level challenges in reflectarray design, three novel concepts are also proposed and studied.

- Different methods for designing single-feed multi-beam reflectarray antennas are investigated and it is shown that for complicated multi-beam reflectarrays, optimization of the antenna is necessary. A local optimization technique, the alternating projection method, is implemented to optimize the performance of multi-beam reflectarray antennas. Required masks, cost definition, and convergence conditions are introduced for multi-beam reflectarrays and a symmetric quad-beam prototype is designed, fabricated, and tested. Furthermore the limitations of this optimization technique for asymmetric multi-beam designs are delineated and a powerful global optimization technique, the particle swarm optimization, is implemented for general multi-beam reflectarray designs. A single-feed quad-beam reflectarray antenna prototype with asymmetric beam directions and beam levels is fabricated and tested.
- Different approaches in the design of beam-scanning reflectarray antennas are reviewed

and the advantages and limitations of these approaches are summarized. From this comparative study it is realized that for moderately wide angle beam-scanning, utilizing a feed displacement technique is more convenient than an aperture phase tuning technique, which requires one to equip every element in the array with a phase control system. In the next stage, a novel aperture phase distribution is proposed for the reflectarray antenna, and is further optimized using a multi-objective PSO technique to improve the beam-scanning performance of the system. A high-gain Ka-band prototype achieving 60 degrees scan range with side-lobe levels below 15 dB is demonstrated.

- The feasibility of designing reflectarray antennas on conformal surfaces is studied numerically. First a generalized analysis approach is presented to compute the radiation pattern of conformal reflectarray antennas. In the next stage, radiation pattern and scanning performance of reflectarray antennas flush mounted on singly-curved cylindrical platforms are studied. The radiation characteristics of these conformal designs are compared with their planar counterpart and it is shown that a conformal reflectarray antenna can be a suitable choice for a high-gain antenna where curved platforms are required

8.2 Future Work

The main focus of this dissertation was on demonstrating the novel features and applications of reflectarray antennas. However, a variety of possible topics remain on both element level and system level problems. On the element level, accurate modeling of the performance of reflectarray phasing elements is of considerable importance. The quasi-periodic approximation of elements in reflectarray antennas may be improved by using surrounded element approaches

[76], rather than the infinite array approach. Furthermore by developing effective optimization routines and utilizing full-wave simulation of the array, the geometrical parameters of the elements in the real reflectarray configuration can also be obtained more accurately. This approach would also take into account the effects of both specular and non-specular reflections from the element, which is necessary for accurate analysis of the reflectarray antenna. Also for the radiation analysis of reflectarray antennas, a notable improvement can be made by taking into account the diffraction at the array edges. In addition, a great deal of interest is still on further improvement of the bandwidth of the reflectarray antenna. In particular for large reflectarrays, bandwidth improvement requires the use of time-delay lines which have not yet been explored in detail for reflectarray antennas.

On the system level, multi-beam reflectarray antennas with multiple feeds can also be studied. Furthermore, the optimum position of the feed antenna in multi-beam systems is also a challenging study. For beam-scanning reflectarray antennas using the feed displacement technique, aperture phase distributions based on the concept of spherical reflectors can be studied for wide-angle beam-scanning. Furthermore a combination of feed displacement and aperture phase tuning techniques in a single design can be studied. It is expected that such a system will be able to achieve a wide-angle beam-scanning performance with a much lower cost. For conformal reflectarrays, an important study is on the accurate modeling of elements on curved platforms. While for the studies presented in this dissertation, a faceted approximation of the surface was deemed acceptable since the structures were not highly curved, in general the effect of element curvature could be taken into account for conformal systems.

BIBLIOGRAPHY

- [1] D. G. Berry, R. G. Malech, and W. H. Kennedy, "The reflectarray antenna," *IEEE Trans. Antennas Propag.*, vol. 11, no. 6, pp. 645–651, Nov. 1963.
- [2] H. R. Phelan, "Spiralphase reflectarray for multitarget radar," *Microwave Journal*, vol. 20, pp. 67–73, July 1977.
- [3] J. Huang and J. A. Encinar, *Reflectarray Antennas*, by Institute of Electrical and Electronics Engineers, John Wiley & Sons, 2008.
- [4] D. M. Pozar, S. D. Targonski, and H. D. Syrigos, "Design of millimeter wave microstrip reflectarrays," *IEEE Trans. Antennas Propag.*, vol. 45, no. 2, pp. 287–296, Feb. 1997.
- [5] A. Yu, "Microstrip reflectarray antennas: Modeling, design and measurement," Ph.D. dissertation, Dept. Elect. Eng., Univ. of Mississippi, Oxford, MS, 2010.
- [6] J. A. Encinar and J. A. Zornoza, "Three-layer printed reflectarrays for contoured beam space applications," *IEEE Trans. Antennas Propag.*, vol. 52, no. 5, pp. 1138–1148, May 2004.
- [7] D. M. Pozar, "Bandwidth of reflectarrays," *Electronics Letters*, vol. 39, no. 21, Oct. 2003.
- [8] J. A. Encinar, "Design of two-layer printed reflectarrays using patches of variable size," *IEEE Trans. Antennas Propag.*, vol. 49, no. 10, pp. 1403–1410, Oct. 2001.
- [9] E. Carrasco, J. A. Encinar, and M. Barba, "Bandwidth improvement in large reflectarrays by using true-time delay," *IEEE Trans. Antennas Propag.*, vol. 56, no. 8, pp. 2496–2503, Aug. 2008.
- [10] P. Nayeri, F. Yang, and A. Z. Elsherbeni, "A broadband reflectarray using sub-wavelength patch elements," *IEEE Antennas and Propagation Society International Symposium*, South Carolina, U.S., 2009.
- [11] D. M. Pozar, S. D. Targonski, and R. Pokuls, "A shaped-beam microstrip patch reflectarray," *IEEE Trans. Antennas Propag.*, vol. 47, pp. 1167–1173, July 1999.
- [12] M. Arrebola, J. A. Encinar, and M. Barba, "Multifed printed reflectarray with three simultaneous shaped beams for LMDS central station antenna," *IEEE Trans. Antennas Propag.*, vol. 56, no. 6, pp. 1518–1527, June 2008.
- [13] S. V. Hum, M. Okoniewski, and R. J. Davies, "Modeling and design of electronically tunable reflectarrays," *IEEE Trans. Antennas Propag.*, vol. 55, no. 8, pp. 2200–2210, Aug. 2007.
- [14] R. B. Dybdal, "Satellite antennas," in *Antenna Engineering Handbook*, J. Volakis, McGraw-Hill, 2007.
- [15] K. K. Chan, and K. Chadwick, "Accurate prediction of finite waveguide array performance based on infinite array theory," *IEEE International Symposium on Phased Array Systems and Technology*, Massachusetts, U.S., Oct. 1996.
- [16] T. B. A. Senior and J. L. Volakis, *Approximate Boundary Conditions in Electromagnetics*, by Institute of Electrical Engineers, Bookcraft Ltd, 1995.

- [17] A. K. Bhattacharyya, *Phased Array Antennas: Floquet Analysis, Synthesis, BFNs, and Active Array Systems*, John Wiley & Sons, 2006.
- [18] P. Hannan, and M. Balfour, "Simulation of a phased-array antenna in waveguide," *IEEE Trans. Antennas Propagat.*, vol. 13, no. 3, pp. 342-353, May 1965.
- [19] H. Mosallaei and K. Sarabandi, "Antenna miniaturization and bandwidth enhancement using a reactive impedance substrate", *IEEE Trans. Antennas Propag.*, vol. 52, no. 9, pp. 2403–2414, Sep. 2004.
- [20] M. Bozzi, S. Germani, and L. Perregrini, "A figure of merit for losses in printed reflectarray elements", *IEEE Antennas Wireless Propag. Lett.*, vol. 3, no. 1, pp. 257–260, 2004.
- [21] P. Nayeri, F. Yang, and A. Z. Elsherbeni, "Single-feed multi-beam reflectarray antennas", *IEEE Antennas and Propagation Society International Symposium*, Toronto, Canada, July 2010.
- [22] Y. Rahmat-Samii, *Reflector Antenna Analysis, Synthesis, and Measurements: Modern Topics*, Lecture Notes, Electrical Engineering Department, University of California at Los Angeles, 2003.
- [23] Y. Rahmat-Samii, "Reflector Antennas", in *Antenna Handbook: Theory, Applications, and Design*, Y. T. Lo and S. W. Lee, Van Nostrand Reinhold, 1988.
- [24] A. Yu, F. Yang, A. Z. Elsherbeni, J. Huang, and Y. Rahmat-Samii, "Aperture efficiency analysis of reflectarray antennas", *Microwave and Optical Technology Lett.*, vol. 52, pp. 364-372, 2010.
- [25] L. Diaz and T. Milligan, *Antenna Engineering Using Physical Optics*, Artech House, 1996.
- [26] J. Huang and R. J. Pogorzelski, "A Ka-band microstrip reflectarray with elements having variable rotation angles", *IEEE Trans. Antennas Propag.*, vol. 46, no. 5, pp. 650–656, May. 1998.
- [27] C. A. Balanis, *Antenna Theory: Analysis and Design*, 3rd Edition, John Wiley & Sons Inc., 2005.
- [28] Y. Rahmat-Samii, "Useful coordinate transformations for antenna applications", *IEEE Trans. Antennas Propag.*, vol. 27, no. 4, pp. 571–574, July 1979.
- [29] A. Ludwig, "The definition of cross polarization", *IEEE Trans. Antennas Propag.*, vol. 21, no. 1, pp. 116–119, Jan. 1973.
- [30] A. W. Love, *Reflector Antennas*, by Institute of Electrical and Electronics Engineers, John Wiley & Sons, 1978.
- [31] Ansoft Designer v6.0, ANSYS Inc., 2011.
- [32] FEKO v 6.1, EM Software & Systems Inc., 2011.
- [33] E. Carrasco, M. Barba and J. A. Encinar, "Reflectarray element based on aperture-coupled patches with slots and lines of variable length", *IEEE Trans. Antennas Propag.*, vol. 55, no. 3, pp. 820–825, March 2007.
- [34] E. Carrasco, M. Barba and J. A. Encinar, "Aperture coupled reflectarray element with a wide range of phase delay", *Electronic Letters*, vol. 42, no. 12, pp. 667-668, June 2006.

- [35] M. R. Chaharmir, J. Shaker, M. Cuhaci, and A. Ittipiboon, "A broadband reflectarray antenna with double square rings", *Microwave and Optical Technology Letters*, vol. 48, no. 7, pp. 1317-1320, July 2006.
- [36] R. E. Hodges, and M. Zawadzki, "A reflectarray antenna for use as interferometric ocean height measurement", *IEEE Aerospace Conference*, March 2005.
- [37] F. Yang and Y. Rahmat-Samii, *Electromagnetic Band Gap Structures in Antenna Engineering*, The Cambridge RF and Microwave Engineering Series, 2008.
- [38] J. Ethier, M.R. Chaharmir, J. Shaker, "Novel approach for low-loss reflectarray designs", IEEE International Symposium on Antennas and Propagation (URSI/APS), Spokane, Washington, USA, July 3 – 8, 2011.
- [39] F. Venneri, S. Costanzo, G. Di Massa, and G. Amendola, "Aperture-coupled reflectarrays with enhanced bandwidth features", *Journal of Electromagnetic Waves and Applications*, vol. 22, 1527-1537, 2008.
- [40] K. C. Kao, and G. A. Hockham, "Dielectric-fibre surface waveguides for optical frequencies", *Proc. IEE*, vol. 113, no. 7, pp. 1151–1158, Jul. 1966.
- [41] P. Mühlischlegel, H. J. Eisler, O. J. F. Martin, B. Hecht, and D. W. Pohl, "Resonant optical antennas," *Science*, vol. 308, pp. 1607-1609, 2005.
- [42] J. M. López-Alonso, B. Monacelli, J. Alda, and G. Boreman, "Uncertainty analysis of the *spatial* responsivity of infrared antennas," *Applied Optics*, vol. 44, pp. 4557-4568, 2005.
- [43] J. C. Ginn, B. A. Lail, and G. D. Boreman, "Phase characterization of reflectarray elements at infrared", *IEEE Trans. Antennas Propag.*, vol. 55, no. 11, pp. 2989–2993, Nov. 2007.
- [44] H. Rajagopalan, and Y. Rahmat-Samii, "Dielectric and conductor loss quantification for microstrip reflectarray: simulations and measurements", *IEEE Trans. Antennas Propag.*, vol. 56, no. 4, pp. 1192–1196, Apr. 2008.
- [45] T. Mandviwala, B. A. Lail, and G. D. Boreman, "Infrared-frequency coplanar striplines: design, fabrication and measurements", *Microwave and Optical Technology Letters*, vol. 47, no. 1, pp. 17–20, Oct. 2005.
- [46] M. A. Ordal, L. L. Long, R. J. Bell, S. E. Bell, R. R. Bell, R. W. Alexander, Jr., and C. A. Ward, "Optical properties of the metals Al, Co, Cu, Au, Fe, Pb, Ni, Pd,Pt, Ag, Ti, and W in the infrared and far infrared", *Applied Optics*, Vol. 22, No. 7, April 1983.
- [47] ANSYS HFSS v13.0, ANSYS Inc., 2011.
- [48] CST Microwave Studio, CST Studio Suite 2011, Computer Simulation Technology AG.
- [49] G. R. Fowles, *Introduction to Modern Optics*, 2nd Edition, 1992.

- [50] M. Bozzi, S. Germani, and L. Peregrini, "Modeling of losses in printed reflectarray elements", *European Microwave Conference*, Oct 2004.
- [51] D. Kajfez, *Dielectric Resonators*, Artech House Antennas and Propagation Library, 1990.
- [52] M. I. Skolnik, *Radar handbook*, McGraw-Hill, 2008.
- [53] P. Balling, K. Tjonneland, L. Yi, and A. Lindley, "Multiple contoured beam reflector antenna systems," *IEEE Antennas and Propagation Society International Symposium*, Michigan, U.S., Jun. 28–Jul. 2, 1993.
- [54] L. Schulwitz and A. Mortazawi, "A compact dual-polarized multibeam phased-array architecture for millimeter-wave radar," *IEEE Trans. Microw. Theory Tech.*, vol. 53, no. 11, pp. 3588–3594, Nov. 2005.
- [55] P. Nayeri, F. Yang, and A. Z. Elsherbeni, "Single-feed multi-beam reflectarray antennas", *IEEE Antennas and Propagation Society International Symposium*, Toronto, Canada, July 2010.
- [56] J. Lanteri, C. Migliaccio, J. Ala-Laurinaho, M. Vaaja, J. Mallat and A. V. Raisanen, "Four-beam reflectarray antenna for Mm-waves: design and tests in far-field and near-field ranges," *EuCAP 2009*, Berlin, Germany, pp. 2532-2535, March 2009.
- [57] R. Vescovo, "Reconfigurability and beam scanning with phase-only control for antenna arrays", *IEEE Trans. Antennas Propag.*, vol. 56, no. 6, pp. 1555-1565, June 2008.
- [58] O.M. Bucci, G. Franceschetti, G. Mazzarella, and G. Panariello, "Intersection approach to array pattern synthesis," *IEE Proceedings*, vol. 137, no. 6, pp. 349-357, Dec. 1990.
- [59] D. W. Boeringer and D. H. Werner, "Particle swarm optimization versus genetic algorithms for phased array synthesis," *IEEE Trans. Antennas Propag.*, vol. 52, no. 3, pp. 397–407, Mar. 2004.
- [60] J. Robinson, and Y. Rahmat-Samii, "Particle swarm optimization in electromagnetics," *IEEE Trans. Antennas Propag.*, vol. 52, no. 2, pp. 397–407, Feb. 2004.
- [61] S. D. Targonski and D. M. Pozar, "Minimization of beam squint in microstrip reflectarrays using an offset feed", *IEEE Antennas and Propagation Society International Symposium*, MD, U.S., July 1996.
- [62] R. J. Mailloux, *Phased Array Antenna Handbook*, 2nd Ed., Artech House, 2005.
- [63] R. C. Hansen, *Phased Array Antennas*, 2nd Ed., John Wiley & Sons, 2009.
- [64] R. R. Romanofsky, "Array phase shifters: theory and technology," in *Antenna Engineering Handbook*, J. Volakis, McGraw-Hill, 2007.
- [65] S. R. Rengarajan, "Scanning and defocusing characteristics of microstrip reflectarrays," *IEEE Antennas Wireless Propag. Lett.*, vol. 9, pp. 163-166, 2010.
- [66] V. Galindo, "Design of dual-reflector antennas with arbitrary phase and amplitude distributions", *IEEE Trans. Antennas Propag.*, vol. 12, no. 4, pp. 403-408, July 1964.

- [67] B. L. J. Rao, "Bifocal dual reflector antenna," *IEEE Trans. Antennas Propag.*, vol. 22, no. 5, pp. 711–714, Sep. 1974.
- [68] T. Li, "A study of spherical reflectors as wide-angle scanning antennas", *IRE Trans. Antennas Propag.*, vol. 7, no. 3, pp. 223-226, July 1959.
- [69] S. V. Hum, and M. Okoniewski, "An electronically tunable reflectarray using varactor diode-tuned elements," *IEEE AP - S/URSI Symposium*, Monterey, California, 2004.
- [70] T. Milligan, *Modern Antenna Design*, 2nd Edition, John Wiley & Sons, 2005.
- [71] C. J. Sletten, *Reflector and Lens Antennas: Analysis and Design Using Personal Computers*, Artech House Inc., 1988.
- [72] W. Menzel, M. Al-Tikriti, and R. Leberer, "A 76 GHz multiple-beam planar reflector antenna," *European Microw. Conf.*, Milano, Italy, Sept. 2002.
- [73] L. Josefsson and P. Persson, *Conformal Array Antenna Theory and Design*, IEEE Press Series on Electromagnetic Wave Theory, John Wiley & Sons, 2006.
- [74] R. L. Haupt, *Antenna Arrays: A Computational Approach*, John Wiley & Sons, 2010.
- [75] T.M. Smith, and S. L. Borison, "Depolarization of a circularly polarized wave by an infinite cylinder", *IEEE Trans. Antennas Propag.*, pp. 796-798, Nov. 1974.
- [76] M. A. Milon, D. Cadoret, R. Gillard, and H. Legay, "Surrounded element approach for the simulation of reflectarray radiating cells," *IET Microwaves, Antennas & Propagation*, vol. 1, no. 2, pp. 289–293, Apr. 2007.

LIST OF APPENDICES

APPENDIX I

FULL-WAVE SIMULATION OF REFLECTARRAY PHASING ELEMENTS

In this appendix, the basic steps to obtain the reflection characteristics of passive reflectarray phasing elements using commercial full-wave electromagnetic analysis softwares will be outlined. The procedures required to obtain the phase range for reflectarray elements will be discussed and numerical results are then presented for Ka-band variable size square patch elements.

AI.1 Method of Moments (Ansoft Designer)

Ansoft Designer [AI.1] is a 2.5-D method of moments (MoM) solver which is very efficient for analysis of single layer periodic structures. It is also possible to analyze multi-layer periodic structures with this solver; however the computational time significantly increases as the number of layers is increased. The geometries of a single layer and double layer square patch in an infinite array model are given in Fig. AI-1.

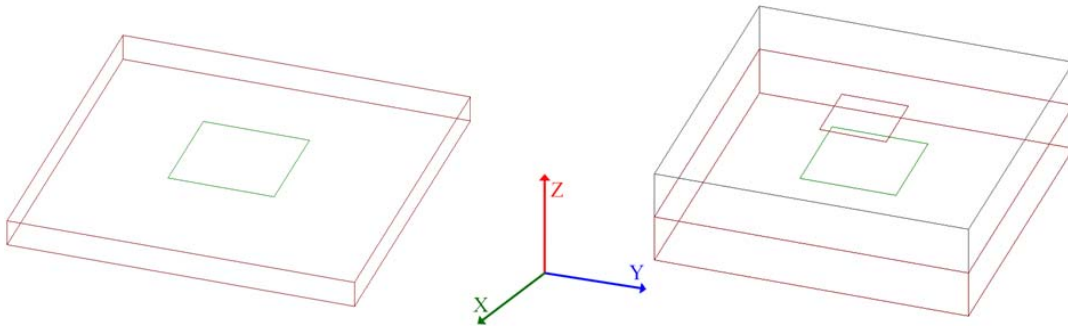


Fig. AI-1. The 3D model of reflectarray unit-cells in Ansoft Designer.

To obtain the reflection characteristics of the phasing elements, a parametric analysis has to be set up, in which one or more of the geometrical parameters of the elements are changed in each simulation, depending on the phase control scheme of the design. It is implicit that for a practical

design where fabrication precision of the manufacturing process is known, this precision value is used throughout this parametric analysis. The reflection coefficients can then be obtained for both polarizations. In this software the V-polarized reflection coefficients refer to an x-directed incident electric field, while the H-polarized coefficients are for a y-directed incident electric field. It should be pointed out that while in some cases it is sufficient to assume normal incidence, it is also possible to change the angle of plane wave incidence for oblique analysis. Also note that as in most MoM solvers; the patch is modeled with a zero thickness here, which is a valid approximation in the microwave range. However at very high frequencies such as in the terahertz range where conductor thickness should be taken into account, this solver is not efficient.

An important consideration in reflectarray element analysis is the proper selection of a phase referencing plane. Typically, in the design procedure, the required reflection phases of the elements are calculated on the top surface of the reflectarray aperture. Therefore, the convenient choice for the reference plane is the aperture surface. In Ansoft Designer, the reflection phase is computed at the top surface of the patch, which is ideally suitable for reflectarray element designs, since no de-embedding will be required here.

AI.2 Finite Element Method (Ansys HFSS)

Ansoft HFSS [AI.2] is a 3-D finite element method (FEM) solver which is very practical for analysis of complicated phasing element configurations. Since this is a 3-D solver conductor thickness can also be modeled very accurately. For periodic electromagnetic structures, such as the reflectarray unit-cells, it is possible to use both the metallic wave-guide [AI.3, AI.4], and the Floquet port [AI.5] analysis methods. While both methods should give the same result, here we

will only discuss the Floquet port method.

For full-wave analysis, once all the layers and patches of the element are modeled, an air box is defined that should completely surround the unit-cell. For a reflectarray element analysis, the top surface of this air box should be placed at a distance about half-wavelength from the top surface of the element and assigned as a Floquet port. The bottom surface can be placed directly beneath the patch and assigned as PEC or as a metal with finite conductivity. The four side boundaries of the air box set the properties of the periodic structure and are named linked boundary conditions in HFSS. Each face of a set of parallel boundaries has to be assigned as either master or slave. The master and slave boundaries for one pair are shown in Fig. AI-2.

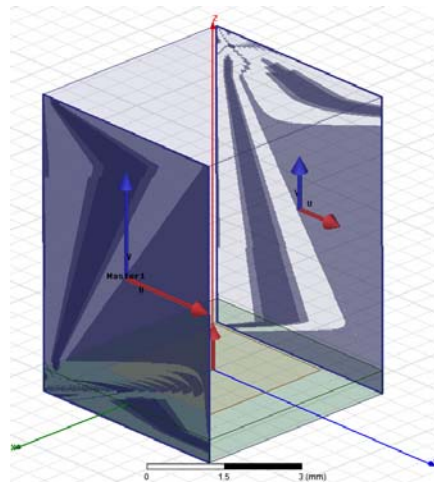


Fig. AI-2. Master and slave boundaries in Ansys HFSS.

The parametric simulations to obtain the reflection characteristics of phasing elements are similar to what was outlined for Ansoft Designer. One notable difference however is the phase reference plane. By default, the reflection coefficients are computed at the Floquet port. To obtain the reflection coefficients on the top surface of the patch, one can use phase de-embedding which can be setup before or after the simulation is completed. The geometry of a single layer square patch element in an infinite array, modeled in Ansys HFSS is given in Fig. AI-3.

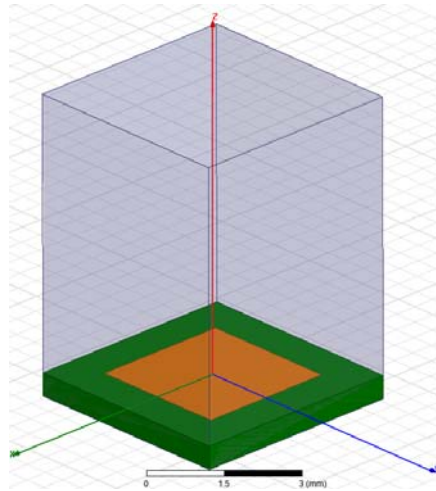


Fig. AI-3. The 3D model of a reflectarray unit-cell in Ansys HFSS.

AI.3 Finite-Integral Time-Domain Method (CST MWS)

CST Microwave Studio (MWS) is a 3-D finite-integral time-domain (FITD) solver that is very efficient for analysis of complicated phasing element configurations. In comparison with Ansys HFSS, for most cases the computational time is much lower and less memory is required for the analysis. Both transient and frequency solvers are available for general electromagnetic simulations; however in the current version [AI.6], periodic media can only be modeled with the frequency solver. The geometry of a single layer square patch element in an infinite array model is given in Fig. AI-4.

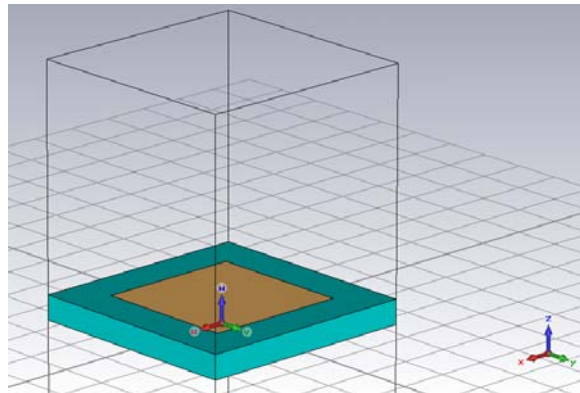


Fig. AI-4. The 3D model of a reflectarray unit-cell in CST MWS.

Similar to the procedure outlined for unit-cell analysis in HFSS, once all the layers and patches are modeled, an air box needs to be defined that completely surrounds the unit-cell. In this software however, when periodic structure analysis is selected, this box will be created automatically. The default setup places the Floquet port at a distance of half-wavelength from the top surface of the structure. To obtain the reflection phase at the top surface of the patch, phase de-embedding has to be used, which has to be setup before the analysis.

AI.4 Simulation Results for a Ka-Band Patch Element

In this section, the three full-wave methods described earlier are used to compute the reflection coefficients of a Ka-band variable size square patch element. The unit-cell size is $4.7 \times 4.7 \text{ mm}^2$ and the substrate is a 20 mil Rogers 5880 which has a dielectric constant of 2.2 and a loss tangent of 0.0009. To obtain a reflection phase response from the elements, the patch size is varied from 1 to 4.5 mm. The reflection coefficients of these elements with normal incidence excitation at 32 GHz are given in Fig. AI-5.

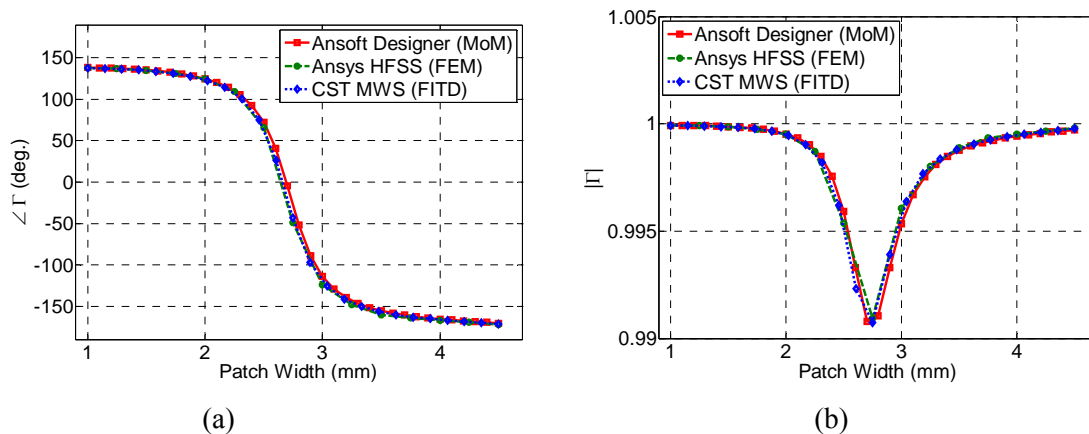


Fig. AI-5. Reflection coefficients of reflectarray phasing elements obtained using different software: (a) reflection phase, (b) reflection magnitude.

It can be seen that a very good agreement is obtained between the three solvers. In comparison,

note that the 3-D solvers (HFSS and CST) show a much closer agreement with each other, and in most cases a very slight difference is observed between the 2.5-D and 3-D solvers.

References

- [AI. 1] Ansoft Designer v6.0, ANSYS Inc., 2011.
- [AI. 2] K. K. Chan, and K. Chadwick., “Accurate prediction of finite waveguide array performance based on infinite array theory,” *IEEE International Symposium on Phased Array Systems and Technology*, Massachusetts, U.S., Oct. 1996.
- [AI. 3] T. B. A. Senior and J. L. Volakis, *Approximate Boundary Conditions in Electromagnetics*, by Institute of Electrical Engineers, Bookcraft Ltd, 1995.
- [AI. 4] P. Hannan, and M. Balfour, “Simulation of a phased-array antenna in waveguide,” *IEEE Trans. Antennas Propagat.*, vol. 13, no. 3, pp. 342-353, May 1965
- [AI. 5] ANSYS HFSS v13.0, ANSYS Inc., 2011.
- [AI. 6] CST Microwave Studio, CST Studio Suite 2011, Computer Simulation Technology AG.

APPENDIX II

MASK GENERATION FOR REFLECTARRAY ANTENNAS

In this appendix, a procedure is outlined for generating the geometry files that are required for fabrication or full-wave simulation of a reflectarray antenna. While a variety of formats are available for geometry files, the most common format for 2-D printed structures is the DXF format, which will be discussed here.

III.1 Data Files for Reflectarray Elements


As discussed throughout this dissertation, once the required phase shift of all the elements on the reflectarray aperture is determined, the element dimensions (or rotation) can be determined from the reflection phase S-curve. In order to input the dimensions and locations of the elements into the software, for fabrication or full-wave simulation, one has to generate a data file containing this information in a format that is recognized by the programs. In this part we outline the procedure used to generate the data files containing the geometrical location and dimensions of the elements. The geometry files are then created using these data files and will be discussed in the next section.

The geometrical location of the reflectarray elements can best be specified by the center position of the unit-cell. Since the geometry files here are 2-D, only the x - and y -locations of each unit-cell center needs to be specified. In our data files, this information is given in the first and second columns, respectively. The next columns contain the geometrical information of the elements. For the variable size patches used in our studies, the patch widths in the x - and y -directions are given in the third and fourth columns, respectively. Similarly for rotated elements, the geometrical data can be included in these columns. Once all these data are organized in a

matrix, the fprintf command in Matlab© is used to write the data in a text file. It is worthwhile to point out here that for a multi-layer configuration, one has to generate a file for each layer. Each layer can then be moved to the correct vertical position in the model.

AII.2 DXF Mask Generation

As mentioned earlier, the DXF file is a very common geometry format for 2-D structures. The overall file organization of a DXF file contains header, classes, tables, blocks, entities, and objects sections. For solid entities, that are required for our designs here, the group codes are given in Fig. AII-1.

 SOLID

The following group codes apply to solid entities.

Solid group codes

Group codes	Description
100	Subclass marker (AcDbTrace)
10	First corner DXF: X value; APP: 3D point
20, 30	DXF: Y and Z values of first corner
11	Second corner DXF: X value; APP: 3D point
21, 31	DXF: Y and Z values of second corner
12	Third corner XF: X value; APP: 3D point
22, 32	DXF: Y and Z values of third corner
13	Fourth corner. If only three corners are entered to define the SOLID, then the fourth corner coordinate is the same as the third. DXF: X value; APP: 3D point
23, 33	DXF: Y and Z values of fourth corner
39	Thickness (optional; default = 0)
210	Extrusion direction (optional; default = 0, 0, 1) DXF: X value; APP: 3D vector
220, 230	DXF: Y and Z values of extrusion direction (optional)

Fig. AII-1. Solid group codes in DXF files.

To generate the DXF file for the variable size rectangular patches, the (x, y, z) coordinates of each vertex has to be computed and imported in the given format. While the computation of the vertex positions is straight forward, by using the data files described earlier, the vertex positioning has to follow the format order. The vertex positions have to be specified in a manner that creates a closed loop with a counter clockwise order. Namely, that is the top left, bottom left,

bottom right, and top right vertices of the rectangle. The DXF file for a patch and the HFSS model are shown in Fig. AII-2.

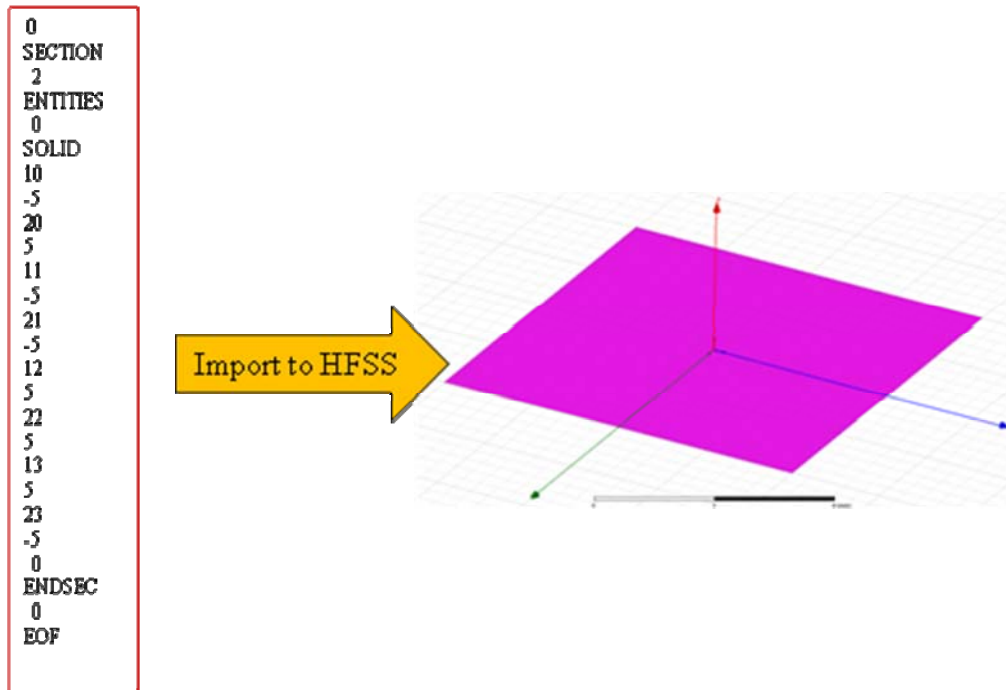


Fig. AII-2. DXF file for a patch and the HFSS model.

It can be seen that the geometry of this single patch can be modeled perfectly in the software. Similarly, using this approach, a full array containing hundreds of elements can easily be imported into any simulation software. Note that however these are geometry files, and once imported the electrical parameters have to be specified for full-wave simulations. Geometry of a full-reflectarray imported into Ansys HFSS is given in Fig. AII-3.

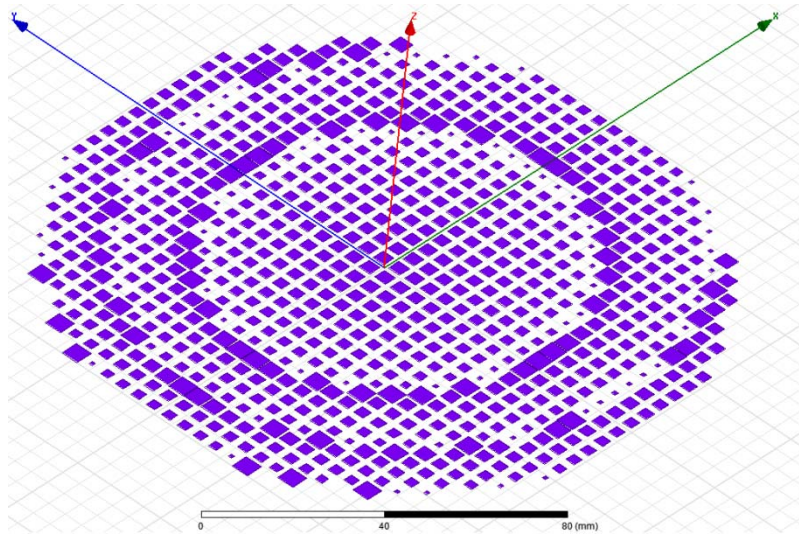


Fig. AII-3. Geometry of reflectarray patch elements modeled in Ansys HFSS.

APPENDIX III

MEASURED HORN ANTENNA PARAMETERS AND ANALYTICAL MODELS

In this appendix, the performance of the feed horn antenna used in the construction of the reflectarray prototypes is presented. The available data sheets and the measurement results obtained at the University of Mississippi are included. An expanded analytical model that includes the cross-polarization of the horn antenna is also presented.

AIII.1 Ka-band Horn Antenna Measurement

The horn antenna used in the studies presented in this dissertation, is a Ka-band circularly polarized corrugated conical horn antenna. A picture of the horn antenna is given in Fig. AIII-1. The antenna has two ports allowing for both right-hand and left-hand circular polarization.

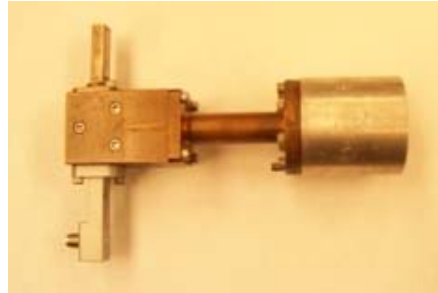


Fig. AIII-1. Ka-band circularly polarized horn antenna.

The radiation pattern of this horn antenna is measured using our NSI-2000 planar near-field measurement system. The near-field electric components are given in Fig. AIII-2 at 32 GHz. While in our studies the far-field characteristics of the horn radiation were used in the analysis, if required, one can also use these fields directly to illuminate the reflector antenna.

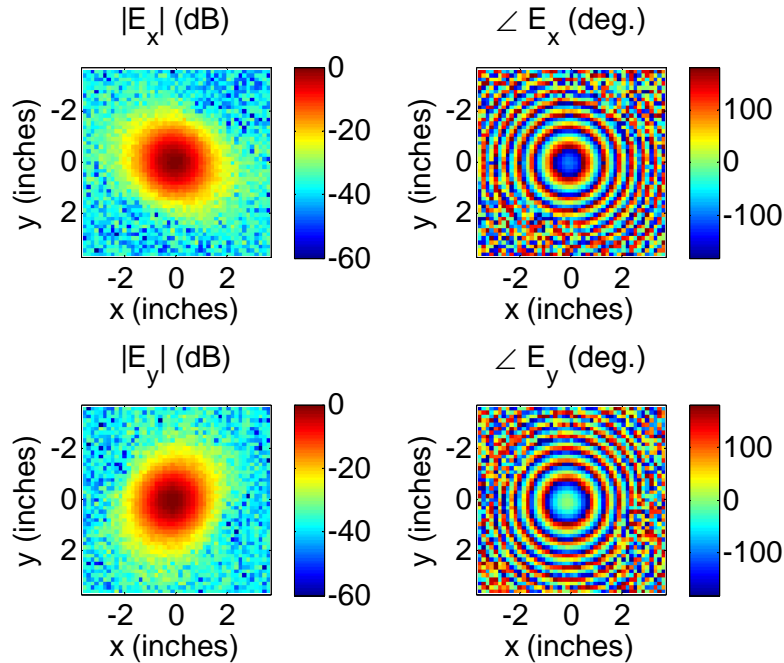


Fig. AIII-2. Measured near-fields of the Ka-band circularly polarized horn antenna.

As discussed in chapter 2 of this dissertation, the common approach to characterize the radiation performance of a feed horn antenna is to use a cosine q radiation pattern model, where the value of the parameter q is determined from the horn measurements. The measured radiation pattern of the horn antenna at 32 GHz is given in Fig. AIII-3, where it is also compared with a cosine q model with $q = 6.5$. It can be seen that, in both planes, the analytical model gives a good representation of the horn pattern. In general if the horn radiation pattern is not symmetric, two different values would be determined here for the two planes. In any case, these values are used in equations (2-6) and (2-7) to represent the radiation pattern of the horn antenna in the analysis.

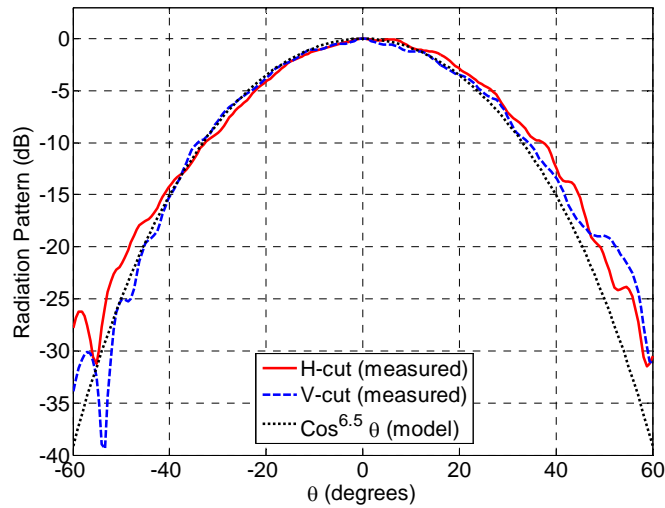


Fig. AIII-2. Measured far-field patterns of the Ka-band circularly polarized horn antenna.

AIII.2 Expanded Analytical Model (Co- and Cross-Polarization Modeling)

The measured radiation pattern of the Ka-band horn antenna shown in the previous section showed a symmetric radiation pattern, which is quite desirable for efficient illumination of a reflector antenna. However, the cross-polarization performance of this horn antenna is not very good. The measured 3-D patterns of the horn antenna are shown in Fig. AIII-3.

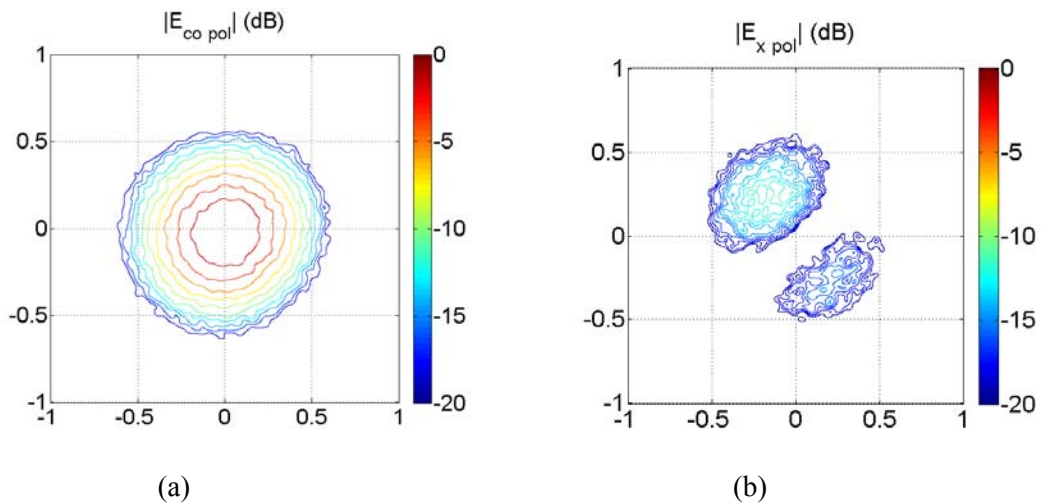


Fig. AIII-3. Measured 3-D radiation pattern of the Ka-band circularly polarized horn antenna.

The results given here clearly show that without modeling the cross-polarized component of the feed radiation pattern, it will not be possible to obtain an accurate estimate of the cross-polarization level of the reflector. While the cross-polarization pattern of the horn is asymmetric, for simplicity here we assume a symmetric cross-polarized model. The measured cross-polarized components in the principal planes and the analytical modeled are given in Fig. AIII-4.

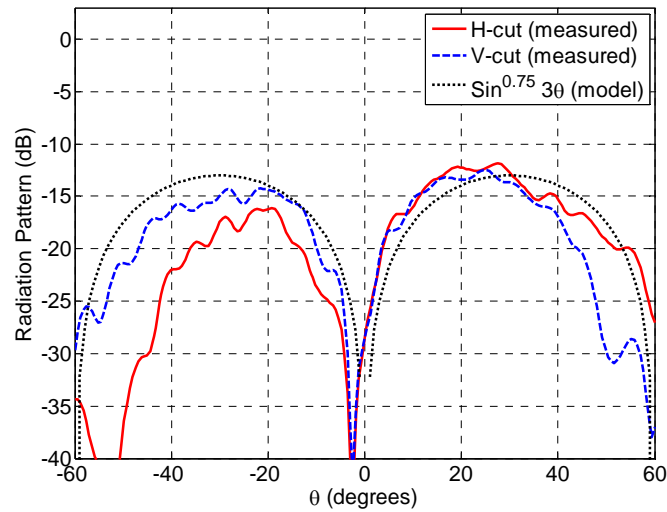


Fig. AIII-4. Measured cross-polarized patterns of the Ka-band circularly polarized horn antenna.

It can be seen that while the asymmetry of the radiation pattern reduces the accuracy of the model here, it still can provide a good estimate of the cross-polarized pattern. It should be noted here that the peak level of 0.18 in the analytical model, was determined from an average value of the cross-polarization in four principal cuts.

APPENDIX IV

DESIGN OF A POTTER HORN ANTENNA FOR REFLECTARRAY FEED

In this appendix, the basic properties of Potter horn antennas are first reviewed, and then a Ka-band horn with a specified radiation pattern model is designed which can be used as a feed for a reflectarray antenna.

AIV.1 Basic Properties of Potter Horn Antennas

As discussed earlier, a feed antenna with a symmetric radiation pattern is usually desired for a reflector feed. However, the conventional pyramidal and conical horn antennas cannot achieve such a radiation performance. While different approaches are available for horn antennas that can enable such a performance [AIV.1], one of the most fundamental methods is to excite higher-order modes in the horn waveguide. Here we will briefly discuss conical horn antennas and higher order mode generation. Conical horn antennas use the dominant TE_{11} mode in the circular waveguide and generate a directive beam with an asymmetric radiation pattern. Unity azimuthal modes of TE_{1m} or TM_{1m} ($m > 1$) can be excited by abrupt or gradual changes in the diameter of the horn or waveguide. This change in diameter will not excite the TE_{nm} or TM_{nm} ($n \neq 1$). The easiest method of exciting higher-order modes with unity azimuthal dependence is to introduce a step change into the diameter of the horn. The abrupt junction will force a break in the smooth current pattern and if the normalized output radius is greater than the cutoff wave-number for the desired mode, some power will be transferred to that mode. The amount of power will depend on both radiuses. In addition changes in the flare angle of a horn will also excite higher-order modes. To achieve a symmetric pattern, a common requirement is to excite a proportion of TM_{11} mode to add to the TE_{11} mode, which is done in the Potter horn antenna [AIV.2]. A cross sectional

geometry of the Potter horn antenna is given in Fig. AIV-1.

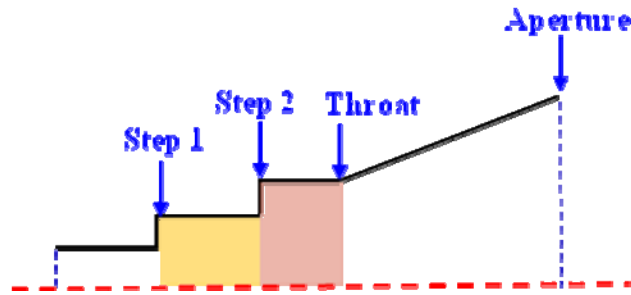


Fig. AIV-1. Cross sectional view of the Potter horn antenna.

While several parameters have to be tuned in a design in order to achieve the desired radiation pattern, some fundamental design rules can be given here. First, the output radius should be greater than 0.6098λ in order to that the TM_{11} mode can propagate; otherwise this mode will be evanescent. In addition the output radius should not be greater than 0.8485λ in order to avoid the propagation of the TE_{12} mode. In addition it is preferable to have the desired amount of TM_{11} power excited (in the flared section of the horn), before this radius is reached. The amount of power that is normally required to be transferred to the TM_{11} mode is between 10 and 20%. For a practical design, an inner radius greater than 0.53λ is required. Since this value is greater than radius of single mode circular waveguides, two steps are needed for a Potter horn. The first junction keeps the power in the TE_{11} mode, and the second junction excites the TM_{11} mode. While in many cases an optimization would be required for the horn design, basically the remainder of the horn design process is to flare the horn so that the aperture diameter will radiate the desired beam-width. The main challenge in the design is that one has to phase the TM_{11} mode so that it is in phase with the TE_{11} mode, while controlling the other constraints.

AIV.2 An Optimized Design with a $\text{Cos}^{6.5}\theta$ Radiation Pattern

As discussed earlier, the Potter horn antenna is a suitable candidate for a reflectarray feed, since it can achieve a symmetric radiation pattern. Depending on the system requirements, one may need to design a feed antenna that can achieve maximum aperture efficiency. In such a case, the optimum value of q , for the feed $\text{cos}^q(\theta)$ radiation pattern model is obtained from the efficiency analysis, and a horn antenna achieving such a pattern has to be designed for the system. In this section we present a design for a Potter horn antenna, that achieves a symmetric radiation pattern with $q = 6.5$ at the center design frequency.

For any design, the initial dimensions of the horn parameters are determined using the design guidelines presented in the previous section; however in most cases it is necessary to tune or optimize these dimensions to achieve the desirable pattern. The particle swarm optimizer (PSO) in FEKO was selected for this task. In total, 7 parameters have to be optimized for this design. The parameters are the radius of the waveguide feed ($R_{\text{waveguide}}$), the radius and length of two wave guide steps ($R_{\text{step1}}, L_{\text{step1}}, R_{\text{step2}}, L_{\text{step2}}$), and the radius and length of the cone ($R_{\text{cone}}, L_{\text{cone}}$). At each fitness evaluation during the optimization, the radiation pattern is computed at a number of discrete points chosen to match the required $\text{cos}^q(\theta)$ pattern and achieve a symmetric pattern in the two principal planes. The optimized dimensions of the Potter horn are given in Table I.

Table AIV-1 Optimized dimensions of the Potter horn antenna.

$R_{\text{waveguide}}$	R_{step1}	L_{step1}	R_{step2}	L_{step2}	R_{cone}	L_{cone}
0.323λ	0.571λ	0.386λ	0.763λ	1.539λ	1.009λ	0.848λ

The electric fields inside the optimized Potter horn are shown in Fig. AIV-2. It can be seen that symmetric aperture fields are generated at the horn aperture which should lead to a symmetric

radiation pattern.

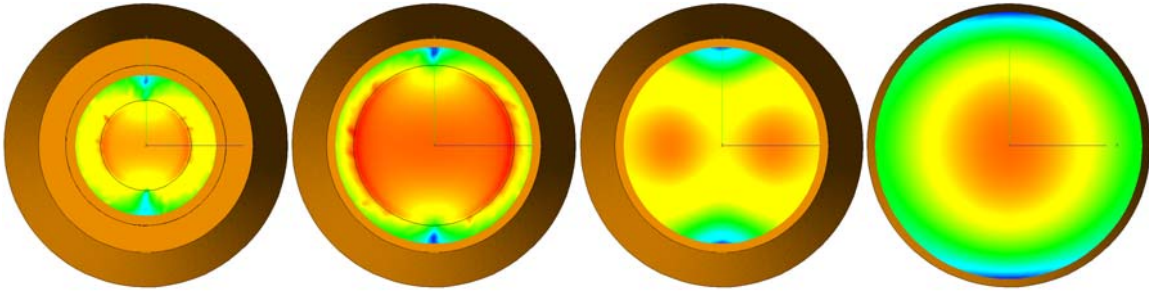


Fig. AIV-2. Electric field magnitude inside the optimized Potter horn antenna.

The normalized radiation pattern of the optimized Potter horn and a comparison with the ideal cosine q model is given in Fig. AIV-3.

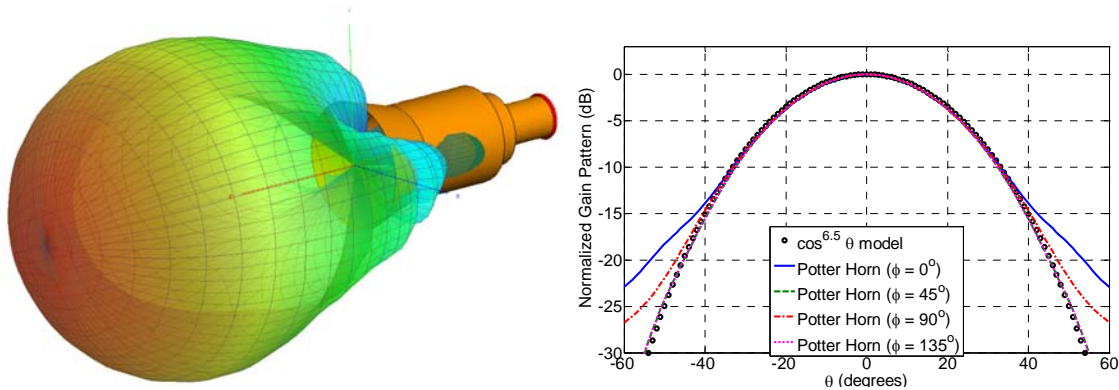


Fig. AIV-3. Normalized radiation patterns of the optimized Potter horn antenna.

It can be seen that the radiation pattern of optimized Potter horn is almost completely symmetric in the four plane cuts, and also matches quite well with the ideal cosine q model up to 40 degrees. Although the beam width requirement for a feed horn design depends on the system parameters, in most cases 40° is sufficient for most cases. It is important to point out that in general multi-mode horns such as the Potter design have a narrow bandwidth, but this should be weighed against the simplicity of the design in comparison with a corrugated horn.

References

- [AIV. 1] D. Oliver, *Microwave Horns and Feeds*, The Institution of Electrical Engineers, 1994.
- [AIV. 2] P. D. Potter, "A new horn antenna with suppressed sidelobes and equal beamwidths", JPL Technical Report No. 32-354, 1963.

APPENDIX V

FULL-WAVE SIMULATION OF REFLECTARRAY ANTENNAS USING FEKO

As discussed earlier in this dissertation, different approaches for analysis of reflectarray radiation pattern have been developed over the years. These numerical approaches provide a fast method to compute the radiation pattern of the reflectarray antenna with a good accuracy; however several approximations are made in the analysis. With these approaches usually a good agreement between measured and simulated results is observed in the pattern shape, but in most cases there are some discrepancies in side-lobe level and cross-polarization levels. In general an accurate analysis of a reflectarray antenna radiation performance requires a full-wave simulation, however this is quite challenging. The electrically large size of the reflectarray antenna aperture, combined with hundreds of elements with dimensions smaller than a wavelength, demands an efficient full-wave technique. Considering the planar geometry of the reflectarray antenna aperture, a surface meshing approach will be more appropriate for this problem. As such, the method of moment (MoM) technique will be more advantageous than other full-wave techniques such as finite element or finite difference, which require volume meshing. In this appendix, a detailed procedure for modeling and full-wave simulation of reflectarray antennas using the commercial software FEKO is presented. A Ka-band reflectarray antenna with 437 elements is designed and simulated. Furthermore a procedure to obtain the phase distribution of the reflectarray using the near-field simulated data is presented. This can be a valuable tool to diagnose and potentially correct elements that are not providing the necessary phase shift.

AV.1 Modeling the Reflectarray Antenna in FEKO and Far-Field Radiation Patterns

The phasing elements used in this study are variable size square patches with a unit-cell

periodicity of $\lambda/2$ (4.6875 mm) at the design frequency of 32 GHz and are fabricated on a 20 mil Rogers 5880 substrate. Both patch and ground plane are modeled as a PEC. The unit-cell model in FEKO is shown in Fig. AV-1 (a). The reflection phase response of the elements is obtained at 12 discrete lengths. The trace of these points usually forms an S-curve, and as such can be approximated with an inverse tangent function. The function used for the interpolation is

$$\psi = -b_l \frac{180}{\pi} \tan^{-1}(a_l(L - L_0)) + c_l. \quad (\text{AV-1})$$

The parameters in this function are obtained using a curve fitting program. For this design these parameters were evaluated to be: $a_l = 4.807$, $b_l = 1.861$, $c_l = -14.84$, $L_0 = 2.653$. The reflection curve response of the reflectarray phasing elements is given in Fig. AV-1 (b).

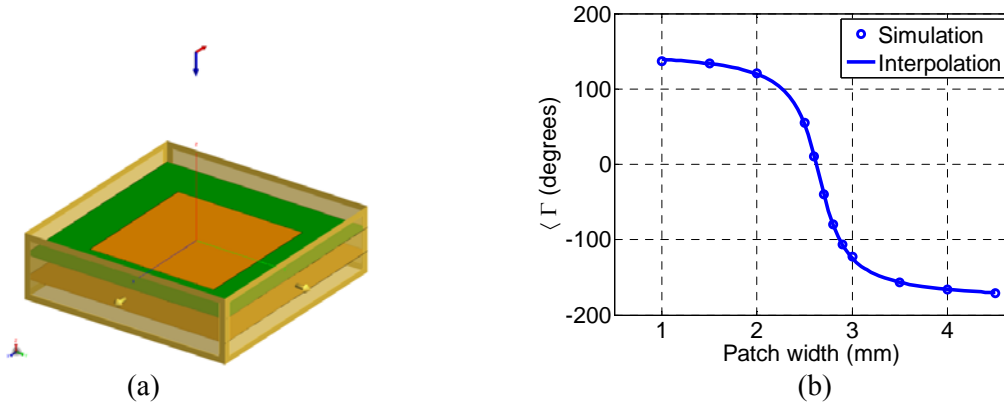


Fig. AV-1. (a) The reflectarray unit-cell model in FEKO. (b) Reflection phase versus patch length for the reflectarray elements.

The reflectarray feed is a Potter horn antenna (see Appendix IV) with an azimuthally symmetric radiation pattern, that can also be modeled with a $\cos^q(\theta)$ function with $q = 6.5$ at 32 GHz. With the feed antenna selected, the next stage is designing the reflectarray antenna system. A circular aperture with a diameter of 12.5λ is selected for the reflectarray which corresponds to 437 square patch elements. For convenience, the geometrical center of the reflectarray is placed at (0, 0, 0). The feed horn is then positioned at $X_{feed} = -38.25 \text{ mm}$, $Y_{feed} = 0 \text{ mm}$, $Z_{feed} = 82.03$

mm , and is pointing toward the geometrical center of the array. The elements phases are then designed to generate a beam in the direction of $(\theta, \varphi) = (25^\circ, 0^\circ)$.

Once the reflectarray system specifications are determined, we can now model the antenna in the software. Modeling the horn, substrate layer and ground plane is straight forward; however modeling the patches requires further attention. Considering the large number of variable size patches in a reflectarray antenna, it would be efficient if one imports the patch elements with a geometry file which contains the location and dimension of each patch. The available version of FEKO can only import parasolid geometry files. While these files also have an ASCII format, and can be created directly, we used third party software to generate the file here. First a DXF file is generated for the reflectarray patch elements as discussed in Appendix II. This file was imported into Ansys HFSS and then exported as a parasolid text file, i.e. *.x_t. It should be noted that for this design, the patch dimensions were determined with a precision of 0.01 mm. The geometry of the reflectarray system modeled in FEKO is shown in Fig. AV-2 (a). For this design 432,278 unknown basis functions need to be calculated by the FEKO method of moments (MoM) solver. Considering the large number of unknowns, the multilevel fast multi-pole method (MLFMM) solver in FEKO was selected for this simulation. In total, the full-wave simulation here required 22.15 GB of memory with a CPU time of 19.94 hours on an 8 core 2.66 GHz Intel(R) Xeon(R) E5430 computer. The simulated 3D radiation pattern of the reflectarray antenna is shown in Fig. AV-2 (b).

The full-wave simulation takes into account all approximations in reflectarray element design and mutual coupling as well as the edge diffraction effects and feed image lobes. Therefore the full-wave simulation here can provide a good measure to observe the performance of the reflectarray elements in the real reflectarray environment. The radiation patterns in the principal

planes (P.P.1 and P.P.2) are given in Fig. AV-3. Here P.P.1 is the xz -plane and P.P.2 is the yz' -plane in the xyz' -coordinate system. This xyz' -coordinate system is obtained by rotating the xyz -coordinate system in Fig. 1, 25° about the y -axis. It can be seen that the main beam is correctly scanned to 25° off-broadside, with side-lobe level below -21.34 dB, which indicates that the phasing elements are providing the necessary phase shift on the reflectarray aperture. The maximum gain of the reflectarray antenna is 28.027 dB, which corresponds to an aperture efficiency of 41.17% with maximum cross-polarization level of -24.01 dB.

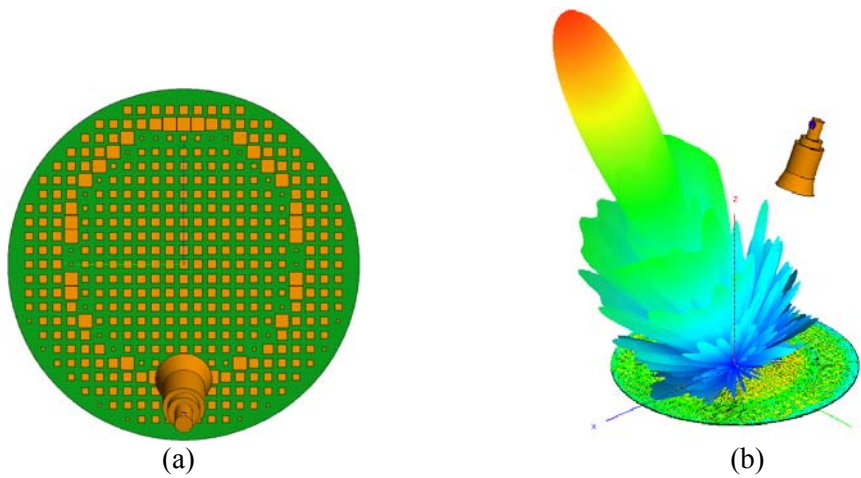


Fig. AV-2. (a) Top view of the reflectarray antenna in FEKO. (b) 3D radiation pattern of the reflectarray antenna simulated in FEKO.

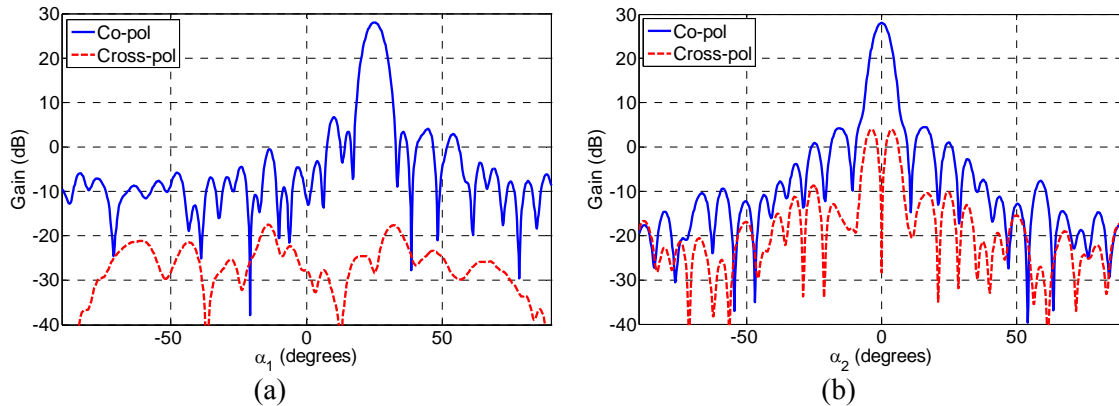


Fig. AV-3. Gain patterns of the reflectarray antenna: (a) P.P.1, (b) P.P.2.

AV.2 Near-Field Study and Aperture Phase Diagnostics

One of the notable advantages of a full-wave simulation is that in addition to calculating the far-field radiation performance, it can also provide the electromagnetic field quantities in the near-field of the reflectarray system. For a reflectarray antenna this can be quite advantageous, since as discussed previously in this dissertation, several approximations are made in the element design, and accurate performance evaluation of the elements would require a near-field analysis. It should be noted that the near-field study here requires analysis of the scattered field. Therefore in addition to the full-wave simulation in the previous section which provided the total field, one must also perform another simulation for the feed antenna only, to obtain the incident fields. Using the scattered near-field data, one can observe the phase shift provided by the phasing elements on the reflectarray aperture. This provides a useful visualization to determine if the phasing elements are designed correctly, and are providing the necessary phase shift. Comparison between the elements ideal phase shift and the quantized phase shift resulted from the full-wave simulation of the reflectarray is given in Fig. AV-4.

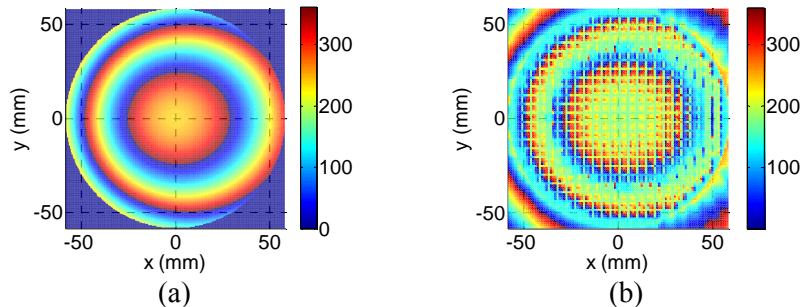


Fig. AV-4. Phase shift on the reflectarray aperture, (a) ideal phase shift, (b) phase shift obtained based on full-wave simulations.

It should be noted that since the feed horn antenna is x -polarized, the phase shift here corresponds to the E_x component. These results clearly indicate that for this design, the phasing elements on the reflectarray aperture are generating a phase shift which creates the collimated

beam. Note that however, the difference in phase shift between the two figures is due to the fact that a finite number of elements are used to generate the phase shift for the reflectarray antenna. In terms of performance diagnostics, if any errors are made in the phasing element design and placement, this study will be able to detect the elements which are not providing the necessary phase shift.

In addition to the scattered fields on the aperture of the reflectarray, a further verification of the proper performance of the reflectarray can be obtained by studying the scattered fields (E_x) in the principal planes of the reflectarray antenna. Since the phasing elements compensate for the spatial delay from the feed horn, a planar phase front must also be observed in the direction of the main beam. The scattered fields in the near-field region of both principal planes are shown in Fig. AV-5.

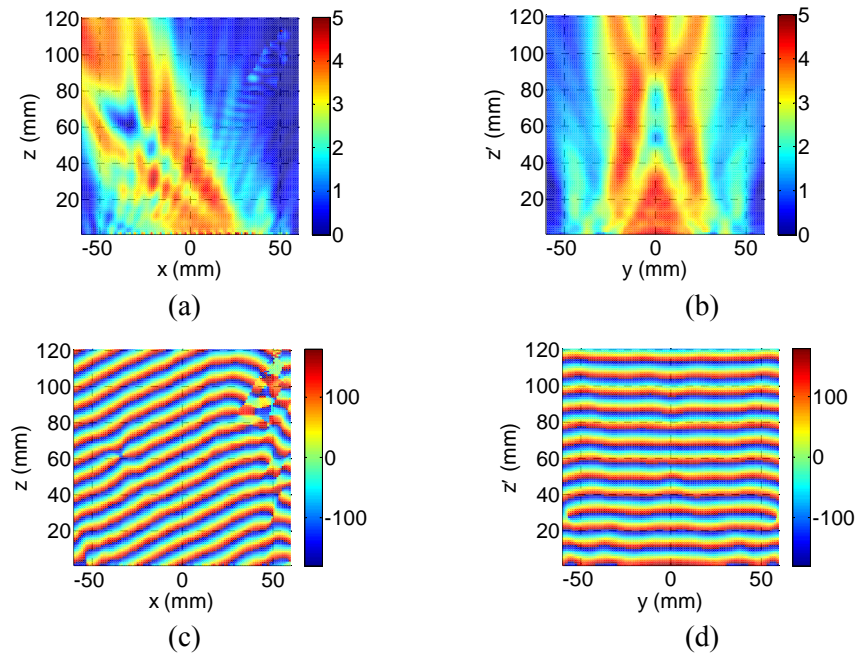


Fig. AV-5. Scattered fields of the E_x component in the principal planes, (a) $|E_x|$ in P.P.1, (b) $|E_x|$ in P.P.2, (c) phase of E_x in P.P.1, (d) phase of E_x in P.P.2.

It can be seen that the phase component of the electric field forms parallel lines in the direction corresponding to the main beam which indicates that the reflectarray antenna is generating a collimated beam. Note that also the shadow of the feed is also observed in the near-field data in P.P.1.

To better illustrate this near-field diagnostic technique for reflectarray antennas, we also designed a reflectarray antenna which randomly distributed fabrication error in a small segment on the aperture. The mask of the ideal design, and the design with random error are given in Fig. AV-6.

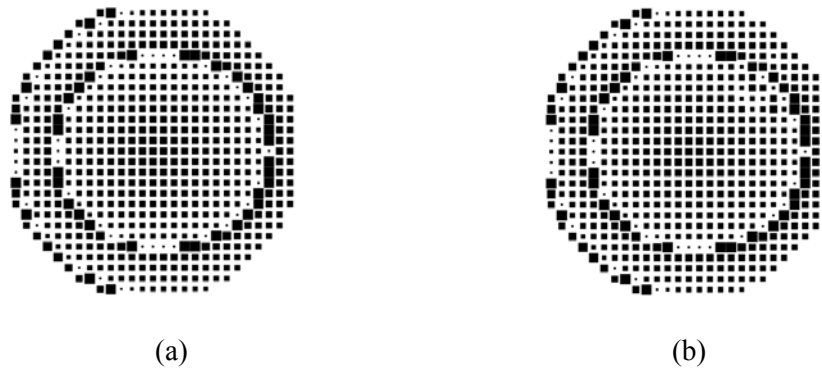


Fig. AV-6. Masks of the simulated reflectarray antennas: (a) ideal fabrication, (b) with random fabrication error.

The error, with a maximum of 1 mm, is randomly distributed in a circle at the top right quadrant of the array. It can be seen from these figures that, in practice it is quite difficult to observe these small fabrication errors, therefore a near-field diagnostic could prove to be quite advantageous. The phase shift of the reflectarray elements are calculated using the full-wave approach and are given in Fig. AV-7., where the aperture phase error associated with the random fabrication error can clearly be observed.

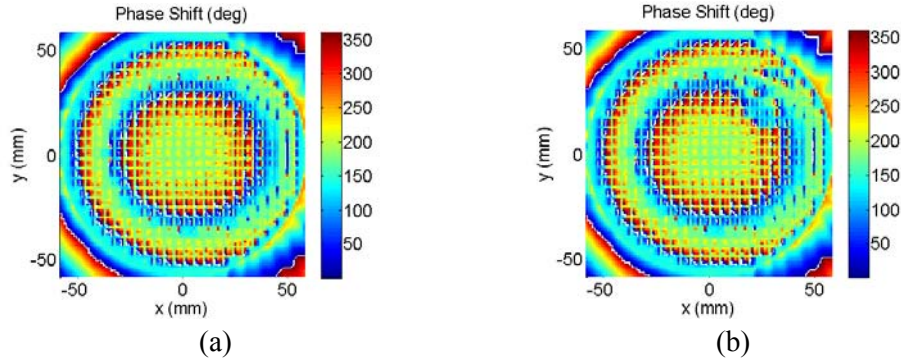


Fig. AV-7. Phase shift on the reflectarray aperture: (a) ideal fabrication, (b) with random fabrication error.

It is worthwhile to point out that while in the study here only 30 elements, i.e. less than 7% of the total number of elements, exhibited phase error, the radiation performance also showed notable degradation. A comparison between the radiation patterns of both designs is given in Fig. AV-8., where it can be seen that in addition to increase in cross-polarization level and some beam deterioration, the maximum gain of the antenna has also been reduced to 27.54 dB. Furthermore, while the gain reduction here is less than 0.5 dB, if such phase error due to fabrication shall be observed in a strongly illuminated region, i.e. the geometrical center of the array, it would correspond to a greater loss.

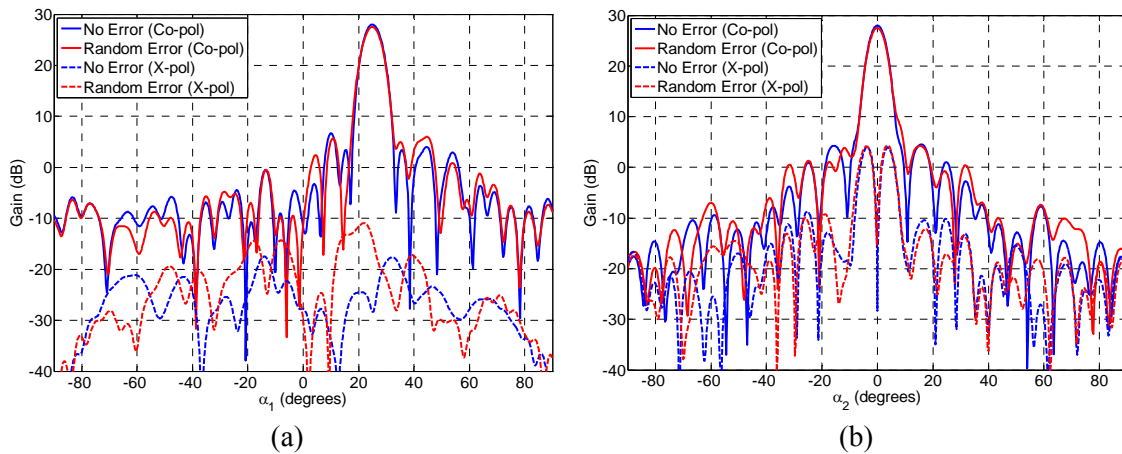


Fig. AV-8. Gain patterns of the reflectarray antenna: (a) P.P.1, (b) P.P.2.

VITA

Payam Nayeri was born in Tehran, Iran. He received the B.S. degree in applied physics from Shahid Beheshti University, Tehran, in 2004, and the M.S. degree in electrical engineering from Iran University of Science and Technology in 2007.

From February 2008 to June 2008, he was a visiting researcher at the University of Queensland, Brisbane, Australia. Since September 2008, he has been a Research Assistant at the University of Mississippi. His research interests include array/reflectarray antennas, multi-beam antennas, optimization methods in electromagnetics, and antenna measurement techniques.

Mr. Nayeri is a member of the IEEE, Sigma Xi and Phi Kappa Phi societies. He has been the recipient of several prestigious awards, including the IEEE Antennas and Propagation Society Doctoral Research Award in 2010, and the University of Mississippi Graduate Achievement Award in Electrical Engineering in 2011.